UNIVERSITY OF LEEDS

Classical and quantum molecular dynamics simulations of dissociation after electron impact in plasma

Ryan Brook

University of Leeds

School of Chemistry

Submitted in accordance with the requirements for the degree of

Doctor of Philosophy

February, 2026

Intellectual Property Statement

The candidate confirms that the work submitted is his own and that appropriate credit has been given where reference has been made to the work of others.

This copy has been supplied on the understanding that it is copyright material and that no quotation from the thesis may be published without proper acknowledgement.

The right of Ryan Brook to be identified as Author of this work has been asserted by him in accordance with the Copyright, Designs and Patents Act 1988.

The first two sections of Chapter 3 contain results and the formulation of the electrophore model that was first published in the Journal of Vacuum Science and Technology A, Volume 43, Page 043003 by R. Brook, O. Bramley, D. V. Makhov, A. Nelson, G. Armstrong, J. Yong, E. Saunders, J. de Viggiani, J. Tennyson, D. V. Shalashillin. The candidate was responsible for writing the python code used to generate all molecular dynamics results, running most of the simulations, graph creation and writing the majority of the paper. The contributions of the other candidates were the development and running of the QEC code, running the Spin Flip dynamics calculations (under the supervision of the candidate), the selection of the molecules and edits of the paper.

The first two sections of Chapter 5 contain equations and results that was first published in The Journal of Chemical Physics in Volume 161, Page 064102 by R. Brook, C. Symonds and D. V. Shalashilin as

part of the special collection on Algorithms and Software for Open Quantum System Dynamics. The candidate was responsible for writing all code concerned with the Full Cloning procedure, the sourcing and running of the code for the test cases, as well as all data collection and graph creation. The candidate was also responsible for writing a large majority of the text in the paper. The other authors were responsible for the conceptualisation of cloning in MCEv1, the writing of the main Fortran MCE code and edits and revisions of the paper.

Acknowledgements

My first expression of gratitude should without a doubt go to my supervisor, Professor Dmitry Shalashilin. His support and guidance began when I joined the research group for my Masters project and has been seemingly endless since. His faith in my work and optimism in me as a researcher has been unmatched, even by my own most of the time. Not only was his support a key step in my starting to pursue a PhD, he has also given me the freedom to pursue and shape my PhD programme exactly in the way that I wanted to and is the main benefactor of the success I have experienced.

I am also grateful for the other members of the Quantum and Classical Molecular Dynamics group at the University of Leeds, particularly Dr. Oliver Bramley and Dr. Dmitry Makhov. Oliver was definitely a role model at the beginning of my PhD and his help with getting acquainted with the workload, existing code and HPC systems at the university was invaluable. Both Oliver and Dmitry have both always been available to answer my many questions and always with warm attitudes. Without them my PhD would not have been as smooth and enjoyable as it was.

I would like to acknowledge the Research Computing team at the University of Leeds. Without them the work contained within this thesis would not be possible as my PhD involved the use of three different HPC clusters that they built and maintained over my four years within the research group. The data in this thesis was generated on ARC3, ARC4 and most recently AIRE.

I would like to say thank you to my family, who has always supported me and my academic ambitions. From a young age I was encouraged to follow both my strengths and my passions which lead me to choosing the degree that I did in what was a rather uncertain time. They have also done excellently at providing a world outside of science that provides perspective on my work and its demands. Finally my deepest thanks go to my partner, Paula, who has been in-

valuable to me when writing this thesis, particularly in the last couple of months as we have settled in our new home together. Her willingness to make my life easier and listen to hours of scientific rambling has not only unbelievably expedited and simplified my writing process but transformed a process famous for being overly stressful into one full of joy. Thank you for being my main motivation.

Abstract

This thesis concerns itself with the application of existing non-adiabatic molecular dynamics methods, namely Ab Initio Multiple Cloning, to a novel application of neutral dissociation of molecules after electronic excitation via electron impact. This process is particularly important in the context of plasma etching of semiconductors, as understanding the dissociation pathways can aid in the design of new precursors that are more environmentally friendly and selective in their etching process. Electronic excitation cross-sections indicate that excitation via electron impact primarily causes population of triplet states. These simulations were performed with Ab Initio Multiple Cloning, though it is also shown that a significant portion of the molecules require only the inclusion of the lowest triplet state, and therefore more computationally efficient standard molecular dynamics are sufficient.

The simulations reveal that analogous to the chromophores that localise photo excitation, there exist certain functional groups, termed electrophores, that localise the excitation via electron impact and therefore also localise the dissociative character of the triplet state. Neutral dissociation pathways are analysed for currently researched plasma precursors. The oxygen atom is identified as playing a key role in the determining of dissociation pathways, with the findings of the molecular dynamic simulations identifying the same weak bonds found in Quadrople Mass Spectrum experiments. The interaction between the oxygen and the C=C bond that was found to be an electrophore previously suggest that a hierarchy of electrophores can be developed. These electrophores can be used to at least qualitatively predict the neutral dissociation pathways of the molecules without the need for simulations.

Finally, the cloning procedure that is the namesake for Ab Initio Multiple Cloning is introduced to the first version of the Multiconfigurational Ehrenfest method. This new extension of can be called Full Cloning MCEv1 as it requires the cloning of the entire basis set.

Full Cloning MCEv1 is benchmarked against the Multiconfigurational Time Dependent Hartree method in the zero temperature regime of the spin boson model, where it showed improved convergence and accuracy.

These results together represent both a theoretical development in the non-adiabatic dynamics community as well as laying the foundation for the application of these methods to a new area of neutral dissociation in plasma etching, supporting the development of cleaner, more selective plasma chemistries.

Contents

1 Introduction **1**

2 Background and Theory **11**

2.1 Introduction 12

2.2 CS and Frozen Gaussians 14

2.2.1 Quantum Harmonic Oscillator 14

2.2.2 Application to MD 17

2.3 Classical molecular dynamics 18

2.4 The MCE method 21

2.4.1 The Coupled CS method 21

2.4.2 Formulation of the MCE method 23

2.4.2.1 Equations for MCEv1 23

2.4.2.2 Equations for MCEv2 25

2.4.2.3 Sampling techniques for the MCE method 26

2.4.3 Ab Initio Multiple Cloning 31

2.5 The Spin Boson Model 33

2.5.1 The MCE method applied to the Spin Boson Model 37

2.5.2 Other methods for solving the Spin Boson Model 39

2.5.2.1 MCTDH 39

2.5.3 MS, FMS and AIMS 42

2.5.4 Multiple Davydov Ansatze 44

2.6 Electronic structure 45

2.6.1 Hartree-Fock 45

2.6.2 Density Functional Theory 47
2.6.3 Basis sets 49
2.6.4 Spin-Flip DFT 51
2.7 Neutral Dissociation 51

3 Neutral dissociation calculations for use in Plasma Etching 59
3.1 Electrophore Model for dissociation after excitation via electron impact 60
3.2 Copmutational details 64
3.2.1 Generation of the initial conditions 64
3.2.2 Propagation equations 65
3.2.3 Results Processing 68
3.3 Simulation of PFAS molecules as potential replacements of C_4F_8 . 68
3.3.1 n-$C_4H_3F_7O$ & i-$C_4H_3F_7O$ 69
3.3.1.1 C-O bonds 73
3.3.1.2 C-C bonds 75
3.3.1.3 C-F bonds 76
3.3.1.4 Temperature dependence 79
3.3.1.5 Comparison to singlet state dissociations 85
3.3.1.6 Comparison to experiment 91
3.3.2 $C_4H_2F_7OH$ 92
3.3.2.1 C-C & C-F bonds 94
3.3.2.2 Temperature dependence 96
3.3.2.3 Comparison to singlet state dissociations 98
3.3.2.4 Comparison to experiment 101
3.3.3 PPVE 101
3.3.3.1 Temperature dependence 107
3.3.3.2 Comparison to singlet state dissociations 110
3.3.3.3 Comparison to experiment 114
3.3.4 Simulations at 1000 K 115
3.3.4.1 The inclusion of Spin-Flip DFT 118
3.4 PIPVE 122

3.5 C_4F_6 . . . 128
3.5.1 1,3-C_4F_6 . . . 128
3.5.2 c-C_4F_6 . . . 130
3.5.3 Basis set dependency . . . 133
3.6 Conclusions . . . 135

4 Testing of triplet state dissociation trends 141
4.1 Computational Details . . . 142
4.2 The impact of the oxygen functional group . . . 143
4.3 The hydrogen buffer . . . 145
4.3.1 The secondary effect of C-H bond dissociations . . . 145
4.3.2 $C_4H_3F_7O$ alcohol isomers . . . 154
4.3.2.1 An issue with inventing isomers . . . 154
4.3.2.2 Functional $C_4H_3F_7O$ alcohol isomers . . . 156
4.4 CH_2F - A potential new electrophore? . . . 165
4.4.1 1,1,2,2,3,3,4-Heptafluoro-1-butanol . . . 165
4.4.2 1,1,2,2,2-pentafluoroethanol . . . 170
4.4.3 1-Fluoropropane . . . 173
4.4.4 1,1,3-Trifluoropropane . . . 177
4.4.5 1,1,4-trifluorobutane . . . 181
4.4.6 1,1,2,2,3,3,4-heptafluorobutane . . . 188
4.5 Interactions of multiple electrophores . . . 196
4.5.1 Propen-1-ol . . . 197
4.5.2 Allyl mehtyl ether . . . 200
4.5.3 PPVE isomer . . . 209
4.6 Conclusions . . . 212

5 Introduction of Cloning to MCEv1 217
5.1 Computational details . . . 219
5.2 Development of the cloning procedure . . . 219
5.2.1 Cross-terms and first applications . . . 222
5.3 MCEv1 vs MCEv2 in the zero temperature Spin Boson Model . . . 228

5.3.1 FC-MCEv1 in the zero temperature regime 238
5.4 Potential conditions for cloning in FC-MCEv1 246
5.5 Conclusions 258

6 Conclusions and outlook **261**

A Programming and algorithms for simulations of Plasma Dissociation **267**
A.1 Program Overview 268
A.2 Folder and File Structure 269
A.3 Program Flow 270
A.4 Preparation of input 271
A.5 Electronic Structure 274
A.6 Processing of output 280
A.7 Checks 281
A.8 An example to run 283

References **285**

List of Figures

2.1 Graphic showing (a) a singular basis function, (b) a swarm of basis functions within the enclosure governed by the compression parameter a_c, and (c) a pancake of basis functions with a focus on the most important modes. 27

2.2 A swarm of trains being guided across PESs (blue) through time via Ehrenfest trajectories (dotted lines). The basis functions within each train follow the same trajectory, reducing the randomness of the swarm and allowing for the reuse of electronic structure information. 28

2.3 CS "bits" (basis functions enclosed by dotted circles) are generated to fully represent the initial wave function. Each "bit" is propagated separately, allowing efficient spotlighting of relevant areas of phase space. 30

2.4 3 example cases of the Spin Boson model where the population difference either oscillates before finding the equilibrium population (solid red line), relaxes to the equilibrium population (dashed green line) or undergoes relocalisation (dashed blue line) 36

2.5 Conceptual cartoon of the Spin–Boson model represented as two harmonic potential energy surfaces. The diabatic wells are identical in shape and separated by an energy offset of 2ϵ corresponding to the bias between the two electronic states. In the unbiased case ($\epsilon = 0$ the wells are degenerate). 37

2.6 The excitation cross sections for two molecules, (a) $C_3H_2F_4$, (b) $C_3H_2F_6$. Molecular cartoons are included on each panel. Taken from reference [118]. 52

2.7 Population of the T2 state for $C_3H_2F_6$ averaged across multiple AIMC trajectories. Taken from reference [118]. 54

2.8 Dissociation kinetics for the molecule $C_3H_2F_6$. AIMC (solid line) with 2 triplet states is compared with standard MD (dashed line) on the lowest triplet state. Taken from reference [118]. 54

2.9 Dissociation kinetics for $C_3H_2F_4$ using standard MD with a simulated temperature of 5000 K. Taken from reference [118]. 55

2.10 Dissociation kinetics for $C_3H_2F_6$ using standard MD across a range of temperatures. Each panel shows the share of broken bonds for 1000 K, 2000 K, 3000 K and 5000 K. Taken from reference [118]. . 57

3.1 Molecular orbital digram showing how the energy gaps between the LOMO and HUMO allow the C=C bond and the oxygen atom to act as an electrophore, localising the triplet state excitation. . . 62

3.2 A schematic of the MD simulation process. A molecule is excited via electron impact (at the electrophore), and given thermal energy. The dissociation of the molecule is then captured through MD. 63

3.3 Excited state cross-sections generated via QEC for i-$C_4H_3F_7O$ after electron impact. 70

3.4 Excited state cross-sections generated via QEC for n-$C_4H_3F_7O$ after electron impact. 70

3.5 Dissociation kinetics of i-$C_4H_3F_7O$ for each bond type, obtained from 400 independent trajectories propagated on the lowest triplet potential energy surface at 5000 K. A dissociation event is defined as the first timestep at which a bond length exceeds 5 Bohr. Kinetics are normalised by the total number of bonds of each type present in the molecule. 72

3.6 Dissociation kinetics of n-$C_4H_3F_7O$ for each bond type over 400 triple state trajectories at 5000 K. A dissociation event is defined as the first timestep at which a bond length exceeds 5 Bohr. Kinetics are normalised by the total number of bonds of each type present in the molecule. 73

3.7 Dissociation kinetics of i-$C_4H_3F_7O$ for each C-O environment over 400 triple state trajectories at 5000 K. A dissociation event is defined as the first timestep at which a bond length exceeds 5 Bohr. Kinetics are normalised by the total number of bonds of each type present in the molecule. 74

3.8 Dissociation kinetics of n-$C_4H_3F_7O$ for each C-O environment over 400 triple state trajectories at 5000 K. A dissociation event is defined as the first timestep at which a bond length exceeds 5 Bohr. Kinetics are normalised by the total number of bonds of each type present in the molecule. 74

3.9 Dissociation kinetics of i-$C_4H_3F_7O$ for each C-C environment over 400 triple state trajectories at 5000 K. A dissociation event is defined as the first timestep at which a bond length exceeds 5 Bohr. Kinetics are normalised by the total number of bonds of each type present in the molecule. 75

3.10 Dissociation kinetics of n-$C_4H_3F_7O$ for each C-C environment over 400 triple state trajectories at 5000 K. A dissociation event is defined as the first timestep at which a bond length exceeds 5 Bohr. Kinetics are normalised by the total number of bonds of each type present in the molecule. 76

3.11 Dissociation kinetics of i-$C_4H_3F_7O$ for each C-F environment over 400 triplet state trajectories at 5000 K. A dissociation event is defined as the first timestep at which a bond length exceeds 5 Bohr. Kinetics are normalised by the total number of bonds of each type present in the molecule. 77

3.12 Dissociation kinetics of n-$C_4H_3F_7O$ for each C-F environment over 400 triplet state trajectories at 5000 K. A dissociation event is defined as the first timestep at which a bond length exceeds 5 Bohr. Kinetics are normalised by the total number of bonds of each type present in the molecule. 77

3.13 The temperature dependence of the dissociation kinetic for C-F (top-left), C-C (top-right), C-H (bottom-left), C-O (bottom-right) in i-$C_4H_3F_7O$. Three temperatures, 3000 K (dotted line), 4000 K (dashed line) and 5000 K (solid line) are compared. 80

3.14 The temperature dependence of the dissociation kinetics for C-F (top-left), C-C (top-right), C-H (bottom-left), C-O (bottom-right) in n-$C_4H_3F_7O$. Three temperatures, 3000 K (dotted line), 4000 K (dashed line) and 5000 K (solid line) are compared. 81

3.15 Temperature dependence of the dissociation kinetics of different C-F environments in the i-$C_4H_3F_7O$ molecule. The plot shows the proportion of total C-F dissociations attributed to each C-F environment. 82

3.16 Temperature dependence of the dissociation kinetics of different C-O environments in the i-$C_4H_3F_7O$ molecule. The plot shows the proportion of total C-O dissociations attributed to each C-O environment. 83

3.17 Temperature dependence of the dissociation kinetics for different C-F environments in the n-$C_4H_3F_7O$ molecule. The plot shows the proportion of total C-F dissociations attributed to each C-F environment. 84

3.18 Temperature dependence of the dissociation kinetics for different C-O environments in the n-$C_4H_3F_7O$ molecule. The plot shows the number of broken C-O bonds in each environment as a percentage of all C-O bonds broken at that temperature. 84

3.19 Temperature dependence of the dissociation kinetics for different C-C environments in the n-$C_4H_3F_7O$ molecule. The plot shows the proportion of total C-C dissociations attributed to each C-C environment. 85

3.20 Count of each bond type breaking first in a trajectory against the average time of that first breakage in the i-$C_4H_3F_7O$ molecule for both the singlet (circles) and triplet state (triangle) trajectories. . 86

3.21 Count of each bond type breaking first in a trajectory against the average time of that first breakage in the n-$C_4H_3F_7O$ molecule for both the singlet (circles) and triplet state (triangle) trajectories. . 86

3.22 Dissociation kinetics of i-$C_4H_3F_7O$ for each bond type over 400 singlet state trajectories at 5000 K 88

3.23 Dissociation kinetics of n-$C_4H_3F_7O$ for each bond type over 400 singlet state trajectories at 5000 K. A dissociation event is defined as the first timestep at which a bond length exceeds 5 Bohr. Kinetics are normalised by the total number of bonds of each type present in the molecule. 89

3.24 Dissociation kinetics of i-$C_4H_3F_7O$ for each C-O environment over 400 singlet state trajectories at 5000 K. A dissociation event is defined as the first timestep at which a bond length exceeds 5 Bohr. Kinetics are normalised by the total number of bonds of each type present in the molecule. 90

3.25 Dissociation kinetics of n-$C_4H_3F_7O$ for each C-O environment over 400 singlet state trajectories at 5000 K. A dissociation event is defined as the first timestep at which a bond length exceeds 5 Bohr. Kinetics are normalised by the total number of bonds of each type present in the molecule. 90

3.26 Structures of n-$C_4H_3F_7O$ and i-$C_4H_3F_7O$ shown in Figure 2 of reference [106] with bonds highlighted to be prone to dissociation represented by dashed lines. 91

3.27 Excited state cross-sections generated via QEC for $C_4H_2F_7OH$ after electron impact. 93

3.28 Dissociation kinetics of $C_4H_2F_7OH$ for each bond type over 400 triplet state trajectories at 5000 K. A dissociation event is defined as the first timestep at which a bond length exceeds 5 Bohr. Kinetics are normalised by the total number of bonds of each type present in the molecule. 93

3.29 Dissociation kinetics of $C_4H_2F_7OH$ for each C-C bond environment over 400 triplet state trajectories at 5000 K. A dissociation event is defined as the first timestep at which a bond length exceeds 5 Bohr. Kinetics are normalised by the total number of bonds of each type present in the molecule. 95

3.30 Dissociation kinetics of $C_4H_2F_7OH$ for each C-F bond environment over 400 triplet state trajectories at 5000 K. A dissociation event is defined as the first timestep at which a bond length exceeds 5 Bohr. Kinetics are normalised by the total number of bonds of each type present in the molecule. 95

3.31 The temperature dependence of the dissociation kinetics for O-H (top-left), C-C (top-right), C-F (bottom-left), C-H (bottom-right) bonds in $C_4H_2F_7OH$. Three temperatures, 3000 K (dotted line), 4000 K (dashed line) and 5000 K (solid line) are compared. 97

3.32 Dissociation kinetics of $C_4H_2F_7OH$ for each bond type over 400 singlet state trajectories at 5000 K. A dissociation event is defined as the first timestep at which a bond length exceeds 5 Bohr. Kinetics are normalised by the total number of bonds of each type present in the molecule. 98

3.33 Dissociation kinetics of $C_4H_2F_7OH$ for each C-C bond environment over 400 singlet state trajectories at 5000 K. A dissociation event is defined as the first timestep at which a bond length exceeds 5 Bohr. Kinetics are normalised by the total number of bonds of each type present in the molecule. 99

3.34 Dissociation kinetics of $C_4H_2F_7OH$ for each C-F bond environment over 400 singlet state trajectories at 5000 K. A dissociation event is defined as the first timestep at which a bond length exceeds 5 Bohr. Kinetics are normalised by the total number of bonds of each type present in the molecule. 100

3.36 Dissociation kinetics of PPVE for each bond type over 372 triplet state trajectories at 5000 K. A dissociation event is defined as the first timestep at which a bond length exceeds 5 Bohr. Kinetics are normalised by the total number of bonds of each type present in the molecule. 102

3.35 Excited state cross-sections generated via QEC for PPVE after electron impact. 102

3.37 Dissociation kinetics of PPVE for each C-O bond environment over 372 triplet state trajectories at 5000 K. A dissociation event is defined as the first timestep at which a bond length exceeds 5 Bohr. Kinetics are normalised by the total number of bonds of each type present in the molecule. 103

3.38 Dissociation kinetics of PPVE for each C-C bond environment over 372 triplet state trajectories at 5000 K. A dissociation event is defined as the first timestep at which a bond length exceeds 5 Bohr. Kinetics are normalised by the total number of bonds of each type present in the molecule. 104

3.39 Dissociation kinetics of PPVE for each C-F bond environment over 372 triplet state trajectories at 5000 K. A dissociation event is defined as the first timestep at which a bond length exceeds 5 Bohr. Kinetics are normalised by the total number of bonds of each type present in the molecule. 105

3.40 The proportions of the conditions under which the bonds in the 'active region' of PPVE dissociate. Each bar shows the percentage of the bond that breaks before others in the 'active region' (dark blue), after the C#3-O bond (red), after C#4-O (pink) or after the C=C bond (light blue). 106

3.41 The temperature dependence of the dissociation kinetics for C-F (top-left), C=C (top-right), C#3-O (bottom-left), C#4-O (bottom-right) in bond types in PPVE. Three temperatures, 3000 K (dotted line), 4000 K (dashed line) and 5000 K (solid line) are compared. 108

3.42 Temperature dependence of the dissociation kinetics of different C-F environments in the PPVE molecule. The plot shows the proportion of total C-F dissociations attributed to each C-F environment. 109

3.43 Dissociation kinetics of PPVE for each bond type over 400 singlet state trajectories at 5000 K. A dissociation event is defined as the first timestep at which a bond length exceeds 5 Bohr. Kinetics are normalised by the total number of bonds of each type present in the molecule. 110

3.44 Count of each bond type breaking first in a trajectory against the average time of that first breakage in the PPVE molecule for both the singlet (circles) and triplet state (triangle) trajectories. 111

3.45 Dissociation kinetics of PPVE for each C-O bond environment over 400 singlet state trajectories at 5000 K. A dissociation event is defined as the first timestep at which a bond length exceeds 5 Bohr. Kinetics are normalised by the total number of bonds of each type present in the molecule. 112

3.46 Dissociation kinetics of PPVE for each C-C bond environment over 400 singlet state trajectories at 5000 K. A dissociation event is defined as the first timestep at which a bond length exceeds 5 Bohr. Kinetics are normalised by the total number of bonds of each type present in the molecule. 113

3.47 Dissociation kinetics of PPVE for each C-F bond environment over 400 singlet state trajectories at 5000 K. A dissociation event is defined as the first timestep at which a bond length exceeds 5 Bohr. Kinetics are normalised by the total number of bonds of each type present in the molecule. 113

3.48 Dissociation kinetics of PPVE for each bond type over 876 triplet state trajectories at 1000 K. A dissociation event is defined as the first timestep at which a bond length exceeds 5 Bohr. Kinetics are normalised by the total number of bonds of each type present in the molecule. 116

3.49 Dissociation kinetics of i-$C_4H_3F_7O$ for each bond type over 100 triplet state trajectories at 1000 K. The regular timestep of 10 atomic time units (solid line) is compared with a timestep of 30 atomic units (dotted line). 117

3.50 Dissociation kinetics of n-$C_4H_3F_7O$ for each bond type over 100 triplet state trajectories at 1000 K. The regular timestep of 10 atomic time units (solid line) is compared with a timestep of 30 atomic units (dotted line). 118

3.51 Dissociation kinetics of PPVE for each bond type over 372 triplet state trajectories at 5000 K. Spin-Flip DFT (dotted line) is compared with standard DFT (solid line). 119

3.52 Dissociation kinetics of i-$C_4H_3F_7O$ for each bond type over 400 triplet state trajectories at 5000 K. Spin-Flip DFT (dotted line) is compared with standard DFT (solid line). 120

3.53 Dissociation kinetics of n-$C_4H_3F_7O$ for each bond type over 400 triplet state trajectories at 5000 K. Spin-Flip DFT (dotted line) is compared with standard DFT (solid line). 121

3.54 Dissociation kinetics of $C_4H_2F_7OH$ for each bond type over 400 triplet state trajectories at 5000 K. Spin-Flip DFT (dotted line) is compared with standard DFT (solid line). 122

3.55 Dissociation kinetics of PIPVE for each bond type over 392 triplet state trajectories at 5000 K. A dissociation event is defined as the first timestep at which a bond length exceeds 5 Bohr. Kinetics are normalised by the total number of bonds of each type present in the molecule. 123

3.56 Dissociation kinetics of PIPVE for each C-O bond environment over 392 triplet state trajectories at 5000 K. A dissociation event is defined as the first timestep at which a bond length exceeds 5 Bohr. Kinetics are normalised by the total number of bonds of each type present in the molecule. 125

3.57 Dissociation kinetics of PIPVE for each C-C bond environment over 392 triplet state trajectories at 5000 K. A dissociation event is defined as the first timestep at which a bond length exceeds 5 Bohr. Kinetics are normalised by the total number of bonds of each type present in the molecule. 125

3.58 Dissociation kinetics of PIPVE for each C-F bond environment over 392 triplet state trajectories at 5000 K. A dissociation event is defined as the first timestep at which a bond length exceeds 5 Bohr. Kinetics are normalised by the total number of bonds of each type present in the molecule. 126

3.59 Dissociation kinetics of 1,3-C_4F_6 for each bond type over 382 triplet state trajectories at 5000 K. A dissociation event is defined as the first timestep at which a bond length exceeds 5 Bohr. Kinetics are normalised by the total number of bonds of each type present in the molecule. 129

3.60 Dissociation kinetics of 1,3-C_4F_6 for each C-C bond environment over 382 triplet state trajectories at 5000 K. A dissociation event is defined as the first timestep at which a bond length exceeds 5 Bohr. Kinetics are normalised by the total number of bonds of each type present in the molecule. 130

3.61 Dissociation kinetics of c-C_4F_6 for each bond type over 382 triplet state trajectories at 5000 K. A dissociation event is defined as the first timestep at which a bond length exceeds 5 Bohr. Kinetics are normalised by the total number of bonds of each type present in the molecule. 131

3.62 Dissociation kinetics of c-C_4F_6 for each C-C bond environment over 382 triplet state trajectories at 5000 K. A dissociation event is defined as the first timestep at which a bond length exceeds 5 Bohr. Kinetics are normalised by the total number of bonds of each type present in the molecule. 132

3.63 Dissociation kinetics of c-C_4F_6 for each C-F bond environment over 382 triplet state trajectories at 5000 K. A dissociation event is defined as the first timestep at which a bond length exceeds 5 Bohr. Kinetics are normalised by the total number of bonds of each type present in the molecule. 132

3.64 Dissociation kinetics for 1,3-C_4F_6 at 5000 K, comparing the 6-31+G*, cc-pVDZ, STO-2G, def2-SVP and def2-SVP basis sets. . . 134

4.1 Dissociation kinetics of methanol for each bond type, obtained from 100 independent trajectories propagated on the lowest triplet potential energy surface at 5000 K. A dissociation event is defined as the first timestep at which a bond length exceeds 5 Bohr. Kinetics are normalised by the total number of bonds of each type present in the molecule. 144

4.2 Dissociation kinetics of propanol for each bond type over 400 lowest triplet state trajectories at 5000 K. A dissociation event is defined as the first timestep at which a bond length exceeds 5 Bohr. Kinetics are normalised by the total number of bonds of each type present in the molecule. 146

4.3 Dissociation kinetics of propanol for each C-H bond environment over 400 lowest triplet state trajectories at 5000 K. A dissociation event is defined as the first timestep at which a bond length exceeds 5 Bohr. Kinetics are normalised by the total number of bonds of each type present in the molecule. 147

4.4 Dissociation kinetics of $C_2OF_3H_3$ for each bond type over 250 lowest triplet state trajectories at 5000 K. A dissociation event is defined as the first timestep at which a bond length exceeds 5 Bohr. Kinetics are normalised by the total number of bonds of each type present in the molecule. 148

4.5 Dissociation kinetics of $C_2OF_3H_3$ for each C-O bond environment over 250 lowest triplet state trajectories at 5000 K. A dissociation event is defined as the first timestep at which a bond length exceeds 5 Bohr. Kinetics are normalised by the total number of bonds of each type present in the molecule. 149

4.6 Dissociation kinetics of $C_3H_5F_3$ for each bond type over 200 lowest triplet state trajectories at 5000 K. A dissociation event is defined as the first timestep at which a bond length exceeds 5 Bohr. Kinetics are normalised by the total number of bonds of each type present in the molecule. 150

4.7 Dissociation kinetics of $C_3H_5F_3$ for each C-H bond environment over 200 lowest triplet state trajectories at 5000 K. A dissociation event is defined as the first timestep at which a bond length exceeds 5 Bohr. Kinetics are normalised by the total number of bonds of each type present in the molecule. 151

4.8 Dissociation kinetics of $C_3H_5F_3$ for each C-C bond environment over 200 lowest triplet state trajectories at 5000 K. A dissociation event is defined as the first timestep at which a bond length exceeds 5 Bohr. Kinetics are normalised by the total number of bonds of each type present in the molecule. 152

4.9 Change from initial energy for a triplet state trajectory of 1,2,3,3,4,4,4-Heptafluoro-1-butanol at 5000 K. The removal of the atom from the propagation occurs at timestep 64. 155

4.10 Change from initial energy for a triplet state trajectory of 1,1,3,3,4,4,4-Heptafluoro-1-butanol at 5000 K. The removal of the atom from the propagation occurs at timestep 60. 156

4.11 Dissociation kinetics of $C_4H_2F_7$-2-OH for each bond type over 400 triple state trajectories at 5000 K. A dissociation event is defined as the first timestep at which a bond length exceeds 5 Bohr. Kinetics are normalised by the total number of bonds of each type present in the molecule. 157

4.12 Dissociation kinetics of iso-$C_4H_2F_7OH$ for each bond type over 400 triple state trajectories at 5000 K. A dissociation event is defined as the first timestep at which a bond length exceeds 5 Bohr. Kinetics are normalised by the total number of bonds of each type present in the molecule. 158

4.13 Dissociation kinetics of $C_4H_2F_7$-2-OH for each C-C bond environment over 400 triple state trajectories at 5000 K. A dissociation event is defined as the first timestep at which a bond length exceeds 5 Bohr. Kinetics are normalised by the total number of bonds of each type present in the molecule. 159

4.14 Dissociation kinetics of iso-$C_4H_2F_7OH$ for each C-C bond environment over 400 triple state trajectories at 5000 K. A dissociation event is defined as the first timestep at which a bond length exceeds 5 Bohr. Kinetics are normalised by the total number of bonds of each type present in the molecule. 160

4.15 Dissociation kinetics of $C_4H_2F_7$-2-OH for each C-F bond environment over 400 triple state trajectories at 5000 K. A dissociation event is defined as the first timestep at which a bond length exceeds 5 Bohr. Kinetics are normalised by the total number of bonds of each type present in the molecule. 161

4.16 Dissociation kinetics of iso-$C_4H_2F_7OH$ for each C-F bond environment over 400 triple state trajectories at 5000 K. A dissociation event is defined as the first timestep at which a bond length exceeds 5 Bohr. Kinetics are normalised by the total number of bonds of each type present in the molecule. 162

4.17 The comparison of the average C-F dissociation yields for three different molecules, $C_4H_2F_7$-2-OH, iso-$C_4H_2F_7OH$ and the original $C_4H_2F_7OH$ isomer studied in section 3.2. 164

4.18 Dissociation kinetics of 1,1,2,2,3,3,4-Heptafluoro-1-butanol for each bond type over 200 lowest triplet state trajectories at 5000 K. A dissociation event is defined as the first timestep at which a bond length exceeds 5 Bohr. Kinetics are normalised by the total number of bonds of each type present in the molecule. 166

4.19 Dissociation kinetics of 1,1,2,2,3,3,4-Heptafluoro-1-butanol for each C-C bond environment over 200 lowest triplet state trajectories at 5000 K. A dissociation event is defined as the first timestep at which a bond length exceeds 5 Bohr. Kinetics are normalised by the total number of bonds of each type present in the molecule. . 167

4.20 Dissociation kinetics of 1,1,2,2,3,3,4-Heptafluoro-1-butanol for each C-F bond environment over 200 lowest triplet state trajectories at 5000 K. A dissociation event is defined as the first timestep at which a bond length exceeds 5 Bohr. Kinetics are normalised by the total number of bonds of each type present in the molecule. . 168

4.21 Dissociation kinetics of C_2F_5OH for each bond type over 100 lowest triplet state trajectories at 5000 K. A dissociation event is defined as the first timestep at which a bond length exceeds 5 Bohr. Kinetics are normalised by the total number of bonds of each type present in the molecule. 171

4.22 Dissociation kinetics of C_2F_5OH for each C-F bond environment over 100 lowest triplet state trajectories at 5000 K. A dissociation event is defined as the first timestep at which a bond length exceeds 5 Bohr. Kinetics are normalised by the total number of bonds of each type present in the molecule. 172

4.23 Dissociation kinetics of 1-C_3H_7F for each bond type over 200 lowest triplet state trajectories at 5000 K. A dissociation event is defined as the first timestep at which a bond length exceeds 5 Bohr. Kinetics are normalised by the total number of bonds of each type present in the molecule. 174

4.24 Dissociation kinetics of 1-C_3H_7F for each C-H bond environment over 200 lowest triplet state trajectories at 5000 K. A dissociation event is defined as the first timestep at which a bond length exceeds 5 Bohr. Kinetics are normalised by the total number of bonds of each type present in the molecule. 175

4.25 Dissociation kinetics of 1-C_3H_7F for each C-C bond environment over 200 lowest triplet state trajectories at 5000 K. A dissociation event is defined as the first timestep at which a bond length exceeds 5 Bohr. Kinetics are normalised by the total number of bonds of each type present in the molecule. 176

4.26 Dissociation kinetics of 1,1,3-$C_3H_5F_3$ for each bond type over 200 lowest triplet state trajectories at 5000 K. A dissociation event is defined as the first timestep at which a bond length exceeds 5 Bohr. Kinetics are normalised by the total number of bonds of each type present in the molecule. 178

4.27 Dissociation kinetics of 1,1,3-$C_3H_5F_3$ for each C-C bond environment over 200 lowest triplet state trajectories at 5000 K. A dissociation event is defined as the first timestep at which a bond length exceeds 5 Bohr. Kinetics are normalised by the total number of bonds of each type present in the molecule. 179

4.28 Dissociation kinetics of 1,1,3-$C_3H_5F_3$ for each C-F bond environment over 200 lowest triplet state trajectories at 5000 K. A dissociation event is defined as the first timestep at which a bond length exceeds 5 Bohr. Kinetics are normalised by the total number of bonds of each type present in the molecule. 180

4.29 Dissociation kinetics of 1,1,3-$C_3H_5F_3$ for each C-H bond environment over 200 lowest triplet state trajectories at 5000 K. A dissociation event is defined as the first timestep at which a bond length exceeds 5 Bohr. Kinetics are normalised by the total number of bonds of each type present in the molecule. 181

4.30 Dissociation kinetics of 1,1,4-$C_4H_7F_3$ for each bond type over 200 lowest triplet state trajectories at 5000 K. A dissociation event is defined as the first timestep at which a bond length exceeds 5 Bohr. Kinetics are normalised by the total number of bonds of each type present in the molecule. 182

4.31 Dissociation kinetics of 1,1,4-$C_4H_7F_3$ for each C-C bond environment over 200 lowest triplet state trajectories at 5000 K. A dissociation event is defined as the first timestep at which a bond length exceeds 5 Bohr. Kinetics are normalised by the total number of bonds of each type present in the molecule. 183

4.32 Dissociation kinetics of 1,1,4-$C_4H_7F_3$ for each C-F bond environment over 200 lowest triplet state trajectories at 5000 K. A dissociation event is defined as the first timestep at which a bond length exceeds 5 Bohr. Kinetics are normalised by the total number of bonds of each type present in the molecule. 184

4.33 Dissociation kinetics of 1,1,4-$C_4H_7F_3$ for each C-H bond environment over 200 lowest triplet state trajectories at 5000 K. A dissociation event is defined as the first timestep at which a bond length exceeds 5 Bohr. Kinetics are normalised by the total number of bonds of each type present in the molecule. 185

4.34 Dissociation kinetics of 1,1,4-$C_4H_7F_3$ for each bond type over 200 lowest triplet state trajectories at 3000 K. A dissociation event is defined as the first timestep at which a bond length exceeds 5 Bohr. Kinetics are normalised by the total number of bonds of each type present in the molecule. 187

4.35 Dissociation kinetics of 1,1,4-$C_4H_7F_3$ for each C-C bond environment over 200 lowest triplet state trajectories at 3000 K. A dissociation event is defined as the first timestep at which a bond length exceeds 5 Bohr. Kinetics are normalised by the total number of bonds of each type present in the molecule. 188

4.36 Dissociation kinetics of 1,1,4-$C_4H_7F_3$ for each C-F bond environment over 200 lowest triplet state trajectories at 3000 K. A dissociation event is defined as the first timestep at which a bond length exceeds 5 Bohr. Kinetics are normalised by the total number of bonds of each type present in the molecule. 189

4.37 Dissociation kinetics of 1,1,4-$C_4H_7F_3$ for each C-H bond environment over 200 lowest triplet state trajectories at 3000 K. A dissociation event is defined as the first timestep at which a bond length exceeds 5 Bohr. Kinetics are normalised by the total number of bonds of each type present in the molecule. 190

4.38 Dissociation kinetics of $C_4H_3F_7$ for each bond type over 200 lowest triplet state trajectories at 5000 K. A dissociation event is defined as the first timestep at which a bond length exceeds 5 Bohr. Kinetics are normalised by the total number of bonds of each type present in the molecule. 191

4.39 Dissociation kinetics of $C_4H_3F_7$ for each C-C bond environment over 200 lowest triplet state trajectories at 5000 K. A dissociation event is defined as the first timestep at which a bond length exceeds 5 Bohr. Kinetics are normalised by the total number of bonds of each type present in the molecule. 192

4.40 Dissociation kinetics of $C_4H_3F_7$ for each C-H bond environment over 200 lowest triplet state trajectories at 5000 K. A dissociation event is defined as the first timestep at which a bond length exceeds 5 Bohr. Kinetics are normalised by the total number of bonds of each type present in the molecule. 194

4.41 Dissociation kinetics of $C_4H_3F_7$ for each C-F bond environment over 200 lowest triplet state trajectories at 5000 K. A dissociation event is defined as the first timestep at which a bond length exceeds 5 Bohr. Kinetics are normalised by the total number of bonds of each type present in the molecule. 195

4.42 Dissociation kinetics of propen-1-ol for each bond type over 414 lowest triplet state trajectories at 5000 K. A dissociation event is defined as the first timestep at which a bond length exceeds 5 Bohr. Kinetics are normalised by the total number of bonds of each type present in the molecule. 197

4.43 Dissociation kinetics of propen-1-ol for each C-H bond environment over 414 lowest triplet state trajectories at 5000 K. A dissociation event is defined as the first timestep at which a bond length exceeds 5 Bohr. Kinetics are normalised by the total number of bonds of each type present in the molecule. 198

4.44 Average populations of 400 triplet state multiple trajectory Ehrenfest trajectories for propen-1-ol at 5000 K starting at state 1 (left) and state 2 (right). 199

4.45 Dissociation kinetics of propen-1-ol for each bond type over 414 triplet state multiple trajectory Ehrenfest trajectories at 5000 K with the population beginning in state 1. 200

4.46 Dissociation kinetics of propen-1-ol for each bond type over 400 triplet state multiple trajectory Ehrenfest trajectories at 5000 K with the population beginning in state 2. 201

4.47 Dissociation kinetics of allyl methyl ether for each bond type over 376 lowest triplet state trajectories at 5000 K. A dissociation event is defined as the first timestep at which a bond length exceeds 5 Bohr. Kinetics are normalised by the total number of bonds of each type present in the molecule. 202

4.48 Dissociation kinetics of allyl methyl ether for each bond type over 314 multiple state Ehrenfest triplet state trajectories at 5000 K with the population beginning in state 2. 203

4.49 Dissociation kinetics of allyl methyl ether for each C-H bond environment over 376 lowest triplet state trajectories at 5000 K. A dissociation event is defined as the first timestep at which a bond length exceeds 5 Bohr. Kinetics are normalised by the total number of bonds of each type present in the molecule. 205

4.50 Dissociation kinetics of allyl methyl ether for each C-H bond environment over 314 multiple state Ehrenfest triplet state trajectories at 5000 K with the population beginning in state 2. 206

4.51 Dissociation kinetics of allyl methyl ether for each C-O bond environment over 376 lowest triplet state trajectories at 5000 K. A dissociation event is defined as the first timestep at which a bond length exceeds 5 Bohr. Kinetics are normalised by the total number of bonds of each type present in the molecule. 207

4.52 Dissociation kinetics of allyl methyl ether for each C-O bond environment over 314 multiple state Ehrenfest triplet state trajectories at 5000 K, with the populations beginning in state 2. 208

4.53 Dissociation kinetics of the PPVE isomer for each bond type over 314 lowest triplet state trajectories at 5000 K. A dissociation event is defined as the first timestep at which a bond length exceeds 5 Bohr. Kinetics are normalised by the total number of bonds of each type present in the molecule. 210

4.54 Dissociation kinetics of PPVE isomer for each C-C bond environment over 314 lowest triplet state trajectories at 5000 K. A dissociation event is defined as the first timestep at which a bond length exceeds 5 Bohr. Kinetics are normalised by the total number of bonds of each type present in the molecule. 211

4.55 Dissociation kinetics of PPVE isomer for each C-O bond environment over 314 lowest triplet state trajectories at 5000 K. A dissociation event is defined as the first timestep at which a bond length exceeds 5 Bohr. Kinetics are normalised by the total number of bonds of each type present in the molecule. 211

4.56 Dissociation kinetics of PPVE isomer for each C-F bond environment over 314 lowest triplet state trajectories at 5000 K. A dissociation event is defined as the first timestep at which a bond length exceeds 5 Bohr. Kinetics are normalised by the total number of bonds of each type present in the molecule. 212

5.1 Spin Boson case with parameters, $\epsilon = 0$, $\omega_c = 2.5$, $\beta = 5$, and $\alpha_k = 0.09$. Comparison of MCEv1 cloned propagations with (dashed) and without (dotted) the inclusion of cross terms to the MCTDH benchmark (solid line). Both MCEv1 propagations performed with $N_{bf} = 50$ basis functions and M = 50 bath modes and converged with 64 repeats. 224

5.2 Symmetrical well Spin Boson case with $\omega_c = 2.5$, $\beta = 5$, and $\alpha_k = 0.09$. Comparison of MCEv1 cloned propagations with three cloning events (dotted), nine cloning events (dashed) and without (dotted-dashed) cloning to the MCTDH benchmark (solid line). All MCEv1 propagations were performed with $N_{bf} = 1$ basis function and M = 50 bath modes and converged with 64 repeated randomly selected "bits." 227

5.3 Symmetrical well Spin Boson case with $\omega_c = 10$, $\beta = 5000$ (as an estimation of infinity), and $\alpha_k = 0.05$. The MCEv1 propagation was performed with $N_{bf} = 200$ basis function and M = 200 bath modes and converged with 64 repeated randomly selected "bits." . 229

5.4 Symmetrical well Spin Boson case with $\omega_c = 10$, $\beta = 5000$ (as an estimation of infinity), and $\alpha_k = 0.1$. The MCEv2 propagations were performed with $N_{bf} = 200$ basis function and M = 200 bath modes and the MC-MCEv2 propagation had an initial basis set size of $N_{bf} = 200$ basis function and M = 200 bath modes and allowed for 4 cloning events. All propagations were converged with 64 repeated randomly selected "bits." 231

5.5 Symmetrical well Spin Boson case with $\omega_c = 10$, $\beta = 5000$ (as an estimation of infinity), and $\alpha_k = 0.1$. The MCEv1 propagation was performed with $N_{bf} = 200$ basis function and M = 200 bath modes and converged with 64 repeated randomly selected "bits." . 232

5.6 Symmetrical well Spin Boson case with $\omega_c = 10$, $\beta = 5000$ (as an estimation of infinity), and $\alpha_k = 0.1$. The MCEv2 propagations were performed with $N_{bf} = 200$ basis function and M = 200 bath modes and the MC-MCEv2 propagation had an initial basis set size of $N_{bf} = 200$ basis function and M = 200 bath modes and allowed for 4 cloning events. All propagations were converged with 64 repeated randomly selected "bits." 234

5.7 Symmetrical well Spin Boson case with $\omega_c = 10$, $\beta = 5000$ (as an estimation of infinity), and $\alpha_k = 0.4$. The MCEv2 propagations were performed with $N_{bf} = 200$ basis function and M = 200 bath modes and the MC-MCEv2 propagation had an initial basis set size of $N_{bf} = 200$ basis function and M = 200 bath modes and allowed for 4 cloning events. All propagations were converged with 64 repeated randomly selected "bits." 236

5.8 Symmetrical well Spin Boson case with $\omega_c = 10$, $\beta = 5000$ (as an estimation of infinity), and $\alpha_k = 0.5$. The MCEv2 propagations were performed with $N_{bf} = 200$ basis function and M = 200 bath modes and the MC-MCEv2 propagation had an initial basis set size of $N_{bf} = 200$ basis function and M = 200 bath modes and allowed for 4 cloning events. All propagations were converged with 64 repeated randomly selected "bits." 238

5.9 Symmetrical well Spin Boson case with $\omega_c = 10$, β =5000 (as an estimation of infinity), $\alpha_k = 0.4$. MCEv1 (dotted), FC-MCEv1 (dashed) were compared to the MCTDH benchmark (full line). MCEv1 had parameters: $N_{bf} = 200$ basis functions and M = 200 bath modes. FC-MCEv1 had parameters: $N_{bf} = 200$ basis functions and M = 100 bath modes. All runs converged with 64 repeats or randomly selected "bits". 240

5.10 Symmetrical well Spin Boson case with $\omega_c = 10$, β =5000 (as an estimation of infinity), $\alpha_k = 0.55$. MCEv1 (dotted), FC-MCEv1 (dashed) were compared to the MCTDH benchmark (full line). MCEv1 had parameters: $N_{bf} = 200$ basis functions and M = 200 bath modes. FC-MCEv1 had parameters: $N_{bf} = 200$ basis functions and M = 100 bath modes. All runs converged with 64 repeats or randomly selected "bits". 242

5.11 Symmetrical well Spin Boson case with $\omega_c = 20$, β =5000 (as an estimation of infinity), $\alpha_k = 0.4$. MCEv1 (dotted), FC-MCEv1 (dashed) were compared to the MCTDH benchmark (full line). MCEv1 had parameters: $N_{bf} = 200$ basis functions and M = 200 bath modes. FC-MCEv1 had parameters: $N_{bf} = 200$ basis functions and M = 100 bath modes. All runs converged with 64 repeats or randomly selected "bits". 244

5.12 Symmetrical well Spin Boson case with $\omega_c = 20$, β =5000 (as an estimation of infinity), $\alpha_k = 0.5$. MCEv1 (dotted), FC-MCEv1 (dashed) were compared to the MCTDH benchmark (full line). MCEv1 had parameters: $N_{bf} = 200$ basis functions and M = 200 bath modes. FC-MCEv1 had parameters: $N_{bf} = 200$ basis functions and M = 100 bath modes. All runs converged with 64 repeats or randomly selected "bits". 246

5.13 Symmetrical well Spin Boson case with $\omega_c = 10$, β =5000 (as an estimation of infinity), $\alpha_k = 0.7$. MCEv1 shows propagation without cloning for different basis set sizes, compared to the MCTDH benchmark (full line). All runs converged with 64 repeats or randomly selected "bits". 248

5.14 Symmetrical well Spin Boson case with $\omega_c = 20$, β =5000 (as an estimation of infinity), $\alpha_k = 0.7$. MCEv1 propagation without cloning is shown for basis sets with $N_{bf} = 50$ and differing number of bath modes, compared to the MCTDH benchmark (full line). All runs converged with 64 repeats or randomly selected "bits". . . 250

5.15 Symmetrical well Spin Boson case with $\omega_c = 20$, β =5000 (as an estimation of infinity), $\alpha_k = 0.7$. Propagation without cloning for basis sets with 50 (blue), 150 (red) and 250 (green) basis functions and 150 bath modes, compared to the MCTDH benchmark (black). All runs converged with 64 repeats or randomly selected "bits". . . 251

5.16 A comparison of different observables of the breaking force for the case with parameters $\omega_c = 20$, β =5000 (as an estimation of infinity), $\alpha_k = 0.7$. The MCEv1 propagation was performed with $N_{bf} = 150$ and 150 bath modes and 64 'bit-by-bit' repeats. 253

5.17 A comparison of different breaking forces for the case with parameters $\omega_c = 20$, β =5000 (as an estimation of infinity), $\alpha_k = 0.7$. The MCEv1 propagation was performed with $N_{bf} = 50$, 150 and 250 basis functions, 150 bath modes and 64 'bit-by-bit' repeats. . 254

5.18 Symmetrical well Spin Boson case with $\omega_c = 20$, β =5000 (as an estimation of infinity), $\alpha_k = 0.7$. MCEv1 and FC-MCEv1 had parameters: $N_{bf} = 150$ basis functions and M = 150 bath modes. Both the angular and standard form of FC-MCEv1 cloned when 25% of basis functions had a breaking force over 0.149. 255

5.19 Symmetrical well Spin Boson case with $\omega_c = 20$, β =5000 (as an estimation of infinity), $\alpha_k = 0.7$. Both the angular and standard form of FC-MCEv1 had the Full Cloning event at 5 a.t.u.. 257

A.1 Flowchart of the generalised steps for the Plasma dissociation code. The most relevant file for each step is contained within brackets. . 271

A.2 A screen grab of the inputs.json file used for the 1,1,4-trifluorobutane molecule presented in section 4.3.5 284

List of Tables

3.1 Distances from fluorine atoms to hydrogen atoms for fluorines attached to C#1 and C#3 (in Bohr). 78
3.2 Comparison of bond-breaking behaviour and yield between spin-flip and standard DFT methods. 120

4.1 Spin populations on atoms and bonds for the ground state equilibrium geometry for the molecule 1,1,2,2,3,3,4-Heptafluoro-1-butanol. 169

Abbreviations

1,1,3-C3H5F3	1,1,3-Trifluoropropane
1,1,4-C4H7F3	1,1,4-trifluorobutane
1,3 C4F6	Hexafluoro-1,3-butadiene
1-C3H7F	1-Fluoropropane
2-C4F6	Hexafluoro-2-butyne
AIMC	Ab Initio Multiple Cloning
a.t.u	Atomic Time Units
BO	Born-Oppenhiemer approximation
$C_2F_3OH_3$	trifluoromethyl methyl ether
C_2F_5OH	1,1,2,2,2-pentafluoroethanol
$C_3H_5F_3$	1,1,1-trifluoropropane
$C_4H_2F_7$-2-OH	1,1,1,3,4,4,4-heptafluorobutan-2-ol
$C_4H_2F_7OH$	2,2,3,3,4,4,4-heptafluoro-1-butanol
C4H3F7	1,1,2,2,3,3,4-heptafluorobutane
c-C4F6	Hexafluorocyclobutene
CCS	Coupled Coherent States
CS	Coherent States
DFT	Density Functional Theory
FC-MCEv1	Full Cloning MCEv1
FG	Frozen Gaussian
GTOs	Gaussian Type Orbitals
GWP	Global Warming Potential
HEOM	Hierarchical Equations Of Motion
HOMO	Highest Occupied Molecular Orbital
i-$C_4H_3F_7O$	1,1,1,2,3,3,3-heptafluoro-2-methoxypropane
iso-$C_4H_2F_7OH$	fluoromethyl hexafluoroisopropanol
IVR	Initial Value Representation
LUMO	Lowest Unoccupied Molecular Orbital
MCE	Multi-Configurational Ehrenfest Method
MCEv1	Multiconfigurational Ehrenfest Method Version 1
MCEv2	Multiconfigurational Ehrenfest Version 2
MCTDH	Multi-Configurational Time Dependent Hartree
MD	Molecular Dynamics
mDa	Multiple Davydov Ansatz
mDa2	Multi-D2 Ansatz
ML-MCTDH	Multi-Layer MCTDH
MQC-IVR	Mixed Quantum Classical Initial Value Representation

MS	Multiple Spawning
NAMD	Non-Adiabatic Molecular Dynamics
n-$C_4H_3F_7O$	1,1,1,2,2,3,3-heptafluoro-3-methoxypropane
PES	Potential Energy Surface
PIPVE	Perfluoro(isopropyl vinyl)ether
PPVE	Perfluoropropylvinyl Ether molecule
QHO	Quantum Harmonic Oscillator
STOs	Slater Type Orbitals
TDSE	Time-Dependent Schrodinger Equation

Chapter 1

Introduction

1. INTRODUCTION

Since its inception (arguably as early as the 1920s [1]), computational chemistry has served as an indispensable tool for chemists in all fields, and never more so than in the present day. These disciplines of chemistry contain but are not limited to drug discovery [2, 3], medicine [4], organic chemistry [5, 6], biochemistry, and plasma research [7, 8]. Though by no means a complete or finished field [9], it allows for calculations to support or expand experimental findings, and can act to provide information where experiments are highly demanding in terms of time or resources [10].

In accordance with Moore's law [11], recent advancements in hardware have allowed for leaps and bounds in computational power. As technology moves towards exascale power supercomputers and the long-awaited quantum processors [12–15], larger and previously inaccessible computational projects are currently feasible. However as the transistors that power our technology move closer and closer to the atomic scale, Moore's law may begin to fail. Fortunately, the development of computational chemistry has progressed through other avenues, namely in the form of new software and theories [16], with impressive advancements being made within the last couple decades [17]. As with all areas involving technology, there has also been a large push in recent years towards the utilisation of artificial intelligence and neural networks to aid in computational research [18–20]. Computational chemistry is evolving to become a rather central tool throughout chemistry in general and this can be best highlighted by observing the increasing number of open-source codes [21–23], learning materials and recent developments that aim to integrate the field with the general education of chemistry [24–30].

A particularly influential subfield of computational chemistry, which enables chemists to calculate the process of a reaction and to visualise the motion of molecules over time, is that of molecular dynamics (MD) [31, 32]. As modern experiments are becoming increasingly complex, it has become frequent for the results to be paired with MD simulations in order to provide interpretation and perspective [31, 33] as the experimental results alone can often be challenging to fully analyse. The accuracy of these accompanying simulations is then corroborated with the experiment by comparing an experimental observable with

one calculated by the dynamics. At its foundation, MD often employs the Born-Oppenheimer approximation (BO) [34], which permits the separation of electronic and nuclear motion (due to the large mass difference between a nucleus and an electron), leading to the generation of the Potential Energy Surface (PES), a conceptual multi-dimensional landscape relating the energy of a molecule to the position of the constituent atoms. Understanding this idea allows for the visualisation of molecular processes as the molecule travelling through this PES. In this perspective, the PES is a description of the behaviour of the system: the optimised ground geometry of the molecule can be found by locating the minimum of the molecule's lowest PES [35], and the energy barriers surrounding that minimum geometry can provide insights into the stability and reactivity of the compound. The largest differences between the various MD methods are in the handling of this PES, and the motion of the molecule. In classical MD [17, 36, 37], empirical and experimental data surrounding a molecule (bond angles, intramolecular forces etc.) can be applied in order to construct a static force-field that approximates the PES. Using the forces derived from this forcefield allows for the application of standard Newton's laws of motion to the molecule to move the atoms. The forcefield can then be applied again to the new geometry of the molecule to find the new corresponding forces. The repetition of this process allows for the motion of a molecule to be captured and analysed in detail. The pre-calculated nature of this force field, along with the simplicity of Newtonian mechanics allows for the efficient simulation of very large molecular systems over long time frames.

The primary limitation for classical MD then lies with the accuracy of this approximation of the PES to the real structure [16]. The static nature of the classical forcefield while advantageous in its construction, also carries with it certain constraints, and as a result classical forcefields are therefore incapable of processing events that would alter the electronic structure of the molecule, such as the change in number of atoms and multiplicity of the molecule after a bond dissociation or the shift in electronic density in charge transfer processes. While there are some methods developed to act as a work-around for the static

nature of the constructed forcefield [38, 39], it is natural to turn to a more robust way of describing the PES. One such approach would be the use of a quantum mechanical theory such as Density Functional Theory (DFT) [40], which uses the total electron density in order to relate the geometry of the nuclei directly to the electronic energies and forces on an ab initio basis. This allows for the PES to be sampled 'on-the-fly' instead of constructing the PES for every specific geometry allowing a quantum treatment of dynamics.

Quantum MD [41] on the other hand inherently incorporates quantum effects by allowing the nuclei of the system to evolve as a wavefunction through the solving of the time-dependent Schrödinger equation (TDSE). The use of the TDSE allows for the quantum effects neglected by classical MD, such as zero point energy and coherence, to emerge automatically. However, solving this TDSE for any case beyond an extremely primitive system is almost never feasible. The computational cost of finding the solution to the equation scales exponentially with the size of the system, encountering the ever famous 'curse of dimensionality' [42]. Another challenge posed when simulating molecular systems is that often more than one electronic state is required, inevitably leading to electronic transitions. In these non-adiabatic regimes, the BO approximation, the underpinning idea allowing the formulation of the PES in classical MD no longer functions, requiring the treatment of the electrons to also be quantum in nature. This formalisation leads to the aptly-called non-adiabatic molecular dynamics (NAMD), where nuclear and electronic motion are now coupled.

These computationally demanding quantum calculations severely limit the dimensions of the systems that can be considered. As a natural response, semiclassical methods have emerged, attempting to straddle the accuracy of quantum methods with the computational efficiency of classical MD. Some of the earliest yet still practical semiclassical work is that of Miller's in 1970 [43], where he rewrote the scattering matrix to contain purely classical terms in an attempt to faithfully reproduce previously calculated quantum mechanical transition probabilities. Continuing with the idea of achieving quantum results while relying on classical terms, the Initial Value Representation (IVR) [44, 45] family was

developed with the key aim of eliminating a problem faced by many early semiclassical methods.

IVR achieves this by using the average over the initial conditions for the classical trajectories to replace the boundary value problem. This issue had prohibited early semiclassical theories from being computationally feasible, due to the requirement of heavily computationally expensive root search algorithms (that remain being improved in terms of efficiency through recent years [46]). As with all things, IVR methods are not without their weaknesses, including difficulty handling important quantum effects like tunnelling [47] and the oscillatory nature of multiple interfering paths resulting in a dynamic sign problem [48]. A modern IVR method that attempts to correct these issues is mixed quantum classical initial value representation (MQC-IVR) [49, 50], an example worth highlighting due to its capture of the semiclassical ideal. MQC-IVR achieves this by utilising a transformation of variables from double Herman-Kluk IVR [51, 52] (a more expensive quantum IVR) through a modified Fillinov filtration. The extent of this transformation can then be given through a mode-dependent matrix of smaller matrices controlling the displacement of each mode in terms of phase space. A null matrix therefore yields the original Herman-Kluk IVR, but with careful choice of coefficients the most problematic modes can be dampened, significantly reducing the oscillations that can lead to the dynamic sign problem while still providing a high level of accuracy to the vital modes. The result is a flexible method that is capable of providing similar levels of accuracy that approach that of double Herman-Kluk IVR while also being capable of simulating the dynamics of systems that are much larger and normally left to more classical versions of IVR, such as Linearised IVR [53–55].

Although IVR and other semiclassical methods serve as an important bridge between classical and quantum MD, there have also been other significant advances in the field. Multi-configurational Time Dependent Hartree (MCTDH) [56] is a successful method which employs single-particle functions that evolve through variationally derived equations of motion, allowing for a formally exact quantum treatment of the system. However, these variational propagation equa-

tions are very computationally demanding as they encounter a scaling issue, with their complexity increasing rapidly with the dimensionality of the system studied. This is the primary limiting factor for MCTDH to simulate high-dimensional systems, though later expansions to the method have further pushed back this limit [57]. Another widely used method is Trajectory Surface Hopping [58] which is sometimes referred to as the 'workhorse of computational chemistry' employing an ensemble of independent trajectories guided classically, which 'hop' between different PES based on stochastic selection rules.

A common theme in NAMD is that of the trajectory guided basis set [59]. This is due to the efficiency afforded by bypassing the need for a large number of grid points as the trajectories cause the basis functions to act as a 'spotlight', highlighting only the necessary area of phase space, allowing for a much more compacted and efficient basis set. The methods involving this technique can then be differentiated by the construction of the wavefunction and the choice of how to guide the basis functions. Having a multi-set ansatz (a separate set of nuclear basis functions for each electronic state) combined guiding the Gaussians with classical trajectories leads to the Full Spawning class of methods [60–62]. If these classical equations of motion are instead derived variationally, then the method is that of the variational multi-configurational Gaussian [63, 64]. Reducing the multi-set ansatz to a single-set and replacing the Gaussian wave packet with Coherent States (CS) then results in the multiple Davydov ansatz (mDa) [65, 66]. Finally, if one maintains the use of CS but instead derives their equations of motion from Ehrenfest dynamics instead of from the full variational principal the multi-configurational Ehrenfest method (MCE) [67, 68] is produced, the method developed by the group of Shalashilin over the past decades, and the method chosen for the NAMD simulations performed in this thesis.

The development of MCE began with Shalashilin and Child publishing the Coupled Coherent states (CCS) method in 2000 [69, 70], where it was compared extensively with the work of Hernan and Kluk. CCS in fact takes advantage of many prevalent ideas from the semiclassical communities [63] and uses 'Frozen Gaussian' CS to simulate systems. The ansatz used in CCS is constructed as

a sum of CS weighted by quantum amplitudes, with the trajectories guided by the Hamiltonian averaged over the entire wavefunction and the equations for the quantum amplitudes derived from the variational principle. The computational advantages of CCS allow it to access higher dimensionality systems [71] and find applications reproducing spectra, with more recent advancements extending the method to fermionic systems[72, 73]. Another natural extension of CCS is to consider more than one electronic state, with each having a quantum amplitude of its own, yielding the Multi-Configurational Ehrenfest method version 1 (MCEv1) [68]. The MCEv1 method similarly offers great scalability into higher dimensionality. Multiconfigurational Ehrenfest version 2 (MCEv2) [67] introduces an extra coefficient into the ansatz that separates the intra- and inter-configurational coupling. While this difference in construction makes the method harder to converge in model systems [74], it opens up the method to applications in AIMD leading to Ab Initio Multiple Cloning (AIMC) [75], where both the nuclear and electronic parts of the wavefunction are calculated 'on-the-fly', usually employing DFT to calculate electronic properties of the molecular structure, including SCF energy and forces.

AIMC, as with most successful NAMD methods, has been repeatedly applied to simulating photochemical processes [62, 76–79]. In fact, it could be argued that photochemistry has been the main focus of the NAMD community. This is due to photochemistry's wide and continually growing range of applications, from the design of efficient solar cells [80–83], to the complex mechanisms that determine atmospheric chemistry, often instigated by a photon from the sun, as well as numerous use cases in organic and biological chemistries [84–87]. The correct handling of a photo-excited molecule requires the simulation of multiple coupled excited states that often undergo non-adiabatic processes as a route of relaxation. This reason has served as a motivation for many methods to extend beyond the BO regime, such as the spawning procedure into the Full Multiple Spawning framework or the introduction of cloning into AIMC, to handle the regions of phase space with high non-adiabatic coupling. For years, these methods have aided experimental photo-chemists with data exploring finer resolutions, further-

ing the explanation of mechanisms and recently answering a challenge to predict the results of an upcoming experiment regarding cyclobutanone photochemistry [88–102].

While a lot of NAMD methods and techniques were developed because of and for photochemistry, there is no reason outside of tradition these methods are not applied to other areas of chemistry. One such area that the author hopes will be a prominent area is that of neutral dissociation following electronic excitation after electron impact. This process has a wide range of applications particularly important to the semiconductor industry where it has been labelled 'one of the least studied yet most important' concept of advancing the science of plasma etching [103, 104]. Plasma excited by electron impact is used to generate fluorinated radicals which are used to etch into silicon wafers in order to create accurately designed semiconductors. The precursors used to form this plasma unfortunately often have a high global warming potential (GWP) leading to environmental concerns [105, 106], for which the industry is currently addressing with multiple process control techniques, such as atomic layer etching [103, 107]. As the size of the etching and silicon wafers decreases, industry is also motivated to find new reagents with greater selectivity allowing for more efficient and complex circuits, and there is a great interest in the search [8, 108–113], including within theoretical disciplines [7, 114–117].

From a NAMD perspective, many techniques and methods developed for photochemistry can be applied with minimal modifications [118]. The largest difference between simulating these processes is the establishment of initial conditions as excitation via electron impact often excites to the triplet state (due to the lack of selection rules), leading to very different dynamics from the singlet state populated via photo-excitation. This thesis aims to show that MD can be applied to the problem of neutral dissociation, producing results backed by experiment. Preliminary rules of neutral dissociation extracted from these MD simulations in the triplet state will be laid out. It is the hope of the author of this thesis that the results here will lay the foundation that the NAMD community will continue to improve upon, aiding the semiconductor community in designing plasma that

is more effective, selective and environmentally friendly.

The structure of this thesis is as follows. Chapter 2 summarises the genesis of MD based on CS, leading to the development of multiple different methods. The chapter ends with the discussion of a paper presenting the novel application of MD methods to neutral dissociation on the triplet state. Chapter 3 contains multiple MD simulations of molecules that have been studied experimentally in the plasma etching context. The key finding of these simulation is that there exist certain functional groups localise the excitation to the triplet state. These functional groups are analogous to the chromophores in photochemistry and are given the name electrophores due to their high electron density. The "electrophore model" is then constructed via preliminary dissociation rules generated via analysis of dissociation pathway trends of multiple molecules. Chapter 4 continues with the "electrophore model" via the testing of these rules with the simulation of additional molecules that are selected particularly in relation to the rules. The necessity of the inclusion of non-adiabatic effects for molecules with multiple electrophores is also explored. Finally, Chapter 5 concerns the theoretical development of the cloning procedure into MCEv1 and presents several cases where the cloning procedure leads to convergence of zero temperature spin boson model that were previously unattainable.

Chapter 2

Background and Theory

2.1 Introduction

Quantum mechanics fundamentally revolves around the Schrödinger equation, both in its time-independent,

$$\hat{H}|\Psi\rangle = E|\Psi\rangle, \tag{2.1}$$

and its time dependent form,

$$i\hbar\frac{\partial\psi}{\partial t} = -\frac{\hbar^2}{2m}\nabla^2\psi + V\psi, \tag{2.2}$$

The total energy of a system is contained within the Hamiltonian. This operator includes terms for the kinetic energy of both nuclei ($\hat{T}_n$) and electrons ($\hat{T}_e$), the Coulomb attraction between electrons and nuclei ($\hat{V}_{ne}$), and the repulsive interactions between both electrons ($\hat{V}_{ee}$) and between nuclei ($\hat{V}_{nn}$),

$$\hat{H} = \hat{T}_e + \hat{T}_n + \hat{V}_{ne} + \hat{V}_{ee} + \hat{V}_{nn}, \tag{2.3}$$

where:

$$\hat{T}_e = -\sum_I \frac{1}{2}\nabla_I^2, \qquad \text{(Electronic kinetic energy)} \tag{2.4}$$

$$\hat{T}_n = -\sum_A \frac{1}{2M_A}\nabla_A^2, \qquad \text{(Nuclear kinetic energy)} \tag{2.5}$$

$$\hat{V}_{ne} = -\sum_{i,A} \frac{Z_A}{|r_I - r_A|}, \qquad \text{(Electron-nuclear attraction)} \tag{2.6}$$

$$\hat{V}_{ee} = \sum_{i<j} \frac{1}{|r_I - r_J|}, \qquad \text{(Electron-electron repulsion)} \tag{2.7}$$

$$\hat{V}_{nn} = \sum_{A<B} \frac{Z_A Z_B}{|r_A - r_B|}, \qquad \text{(Nucleus-nucleus repulsion)} \tag{2.8}$$

The indices are separated into A and B for nuclear parts, and i and j for the electronic indices. Any summations containing these indices represent a sum over the total number of nuclei and electrons depending upon the corresponding index. Knowledge of the Hamiltonian of the system is vital as it is required for the evolution of the wavefunction from any given initial state. As all information

is contained within the Schrödinger equation, the change in a system can be understood through the time evolution of the Schrödinger equation from the wavefunction from some initial state at t = 0.

$$|\Psi(t)\rangle = e^{-i\hat{H}t/\hbar}|\Psi(0)\rangle, \tag{2.9}$$

Unfortunately for the quantum chemistry community, the TDSE is not capable of being solved exactly for any system beyond the simplest within a reasonable computational time frame. For this reason, chemists often turn to the BO approximation that utilises the mass difference between electrons and nuclei to assume that the electronic rearrangements with respect to the nuclei can be assumed to be instant. Within this perspective, the nuclei can be seen to be frozen when considering and calculating the electronic information. Due to this simplification, $\hat{T}_n$ vanishes as the nuclear positions (and therefore $\hat{V}_{nn}$) become constants. This is often presented as the electronic hamiltonian,

$$\hat{H}_{elec} = \hat{T}_e + \hat{V}_{ne} + \hat{V}_{ee}, \tag{2.10}$$

Then the nuclear parts of the system can be guided via trajectories with the electronic information being updated at every timestep via an electronic structure theory, such as DFT. The methods for solving the TDSE can then be categorised into the choices made to guide the nuclei, with classical, semiclassical and quantum variants. Within all three categories, it is common to employ a trajectory guided nuclear basis set ($\phi(t)$) with quantum amplitudes ($C_k(t)$) weighting the different electronic states ($\chi(t)$),

$$|\Psi(t)\rangle = \sum_k C_k(t)|\chi_k(t)\rangle|\phi(t)\rangle, \tag{2.11}$$

An incredibly useful choice for these nuclear basis functions is that of CS [119], which are quantum objects that have advantageous classical-like properties. Their non-orthogonal yet over complete nature also allows for a highly flexible and efficient representation of nuclear wavefunctions across a range of dynamical regimes.

2.2 CS and Frozen Gaussians

The concept of a CS can be said to be intrinsic to quantum mechanics itself, originally introduced by Schrödinger in 1926 [120], and were then rediscovered decades later within the field of quantum optics [121–123]. CS are said to have 3 routes of derivation and therefore definitions,

1. CS are unique quantum states that satisfy the Heisenberg uncertainty principle.

2. CS can be taken to be the set of eigenvalues of the harmonic-oscillator lowering operator.

3. CS can be found by taking the vacuum state of the harmonic oscillator and applying the displacement operator.

Conceptually, the first definition is easiest to understand. Heisenberg's uncertainty principle states that for any quantum object it is impossible to know exactly both the position and momentum. In fact, the extent to which one can know these quantities is bounded such that,

$$(\Delta x)^2(\Delta p)^2 = (1/2)^2, \tag{2.12}$$

in atomic units. While it is indeed possible for the uncertainty to be any degree above it, CS are objects that satisfy this minimum possible bound. It is important to note that as an infinite pair of numbers can be multiplied together to give this same bound, the 'circular' pair with $\Delta p = 1/2$ and $\Delta x = 1/2$ is often referred to as CS. Other states satisfying the limit of the uncertainty principle with unequal uncertainties are referred to as squeezed states, which themselves have a myriad of applications [124–135].

2.2.1 Quantum Harmonic Oscillator

Interestingly the other two definitions are based within the context of the Quantum Harmonic Oscillator (QHO). The QHO is well studied due to it being exactly solvable analytically while still having applications across quantum mechanics, often

used to approximate smooth potentials. The one dimensional case of the QHO has the hamiltonian,

$$\hat{H}_{QHO} = \frac{\hat{p}^2}{2m} + \frac{1}{2}m\omega^2\hat{x}^2, \tag{2.13}$$

where $\hat{p}$ and $\hat{x}$ are the momentum and position operators respectively, m is the mass of the particle and ω is the angular frequency. This Hamiltonian is analogous to that of the classical harmonic oscillator,

$$E = \frac{mv^2}{2} + \frac{kx^2}{2}, \tag{2.14}$$

In order to more easily conceptualise the QHO, a change of variables is often used. Linear combinations of the position and the momentum operators give rise to the ladder operators,

$$\hat{a} = \sqrt{\frac{m\omega}{2\hbar}}(\hat{x} + \frac{i}{m\omega}\hat{p}), \tag{2.15}$$

$$\hat{a}^\dagger = \sqrt{\frac{m\omega}{2\hbar}}(\hat{x} - \frac{i}{m\omega}\hat{p}), \tag{2.16}$$

The ladder operators are also often presented with the number operator, $\hat{N}$,

$$\hat{N} = \hat{a}^\dagger\hat{a}, \tag{2.17}$$

The prefactors in Eqns. 2.15, 2.16 are chosen to produce clean commutations between the three operators:

$$[\hat{a}, \hat{a}^\dagger] = 1, \tag{2.18}$$

$$[\hat{N}, \hat{a}] = -\hat{a}, \tag{2.19}$$

$$[\hat{N}, \hat{a}^\dagger] = \hat{a}^\dagger, \tag{2.20}$$

Then when a combination of the operators are applied to a given eigenstate of $|\lambda\rangle$ (with corresponding eigenvalue λ) we get,

$$\hat{N}\hat{a}|\lambda\rangle = \hat{a}\hat{N}|\lambda\rangle - \hat{a}|\lambda\rangle = (\lambda - 1)\hat{a}|\lambda\rangle, \tag{2.21}$$

$$\hat{N}\hat{a}^\dagger|\lambda\rangle = \hat{a}\hat{N}|\lambda\rangle + \hat{a}^\dagger|\lambda\rangle = (\lambda + 1)\hat{a}^\dagger|\lambda\rangle, \tag{2.22}$$

showing that both $\hat{a}|\lambda\rangle$ and $\hat{a}^\dagger|\lambda\rangle$ are eigenstates of $\hat{N}$ with eigenvalues of $\lambda - 1$ and $\lambda + 1$. Therefore the ladder operators acting as on an eigenstate λ can be written as,

$$\hat{a}|\lambda\rangle = \sqrt{\lambda}|\lambda - 1\rangle, \tag{2.23}$$

$$\hat{a}^\dagger|\lambda\rangle = \sqrt{\lambda + 1}|\lambda + 1\rangle, \tag{2.24}$$

with the appropriate norm preserving prefactors. Therefore $\hat{a}$ can be seen as a lowering operator that lowers the system one eigenstate 'down the ladder', and likewise $\hat{a}$ as a raising operator that raises the system one eigenstate 'up the ladder'. As the raising and lowering operators were first defined in terms of the position and momentum operators, it is possible to instead write the position and momentum operators in terms of raising and lowering operators,

$$\hat{x} = \sqrt{\frac{\hbar}{2m\omega}}(\hat{a} + \hat{a}^\dagger), \tag{2.25}$$

$$\hat{p} = -i\sqrt{\frac{\hbar m\omega}{2}}(\hat{a} - \hat{a}^\dagger), \tag{2.26}$$

After substitution into the QHO Hamiltonian (Eqn. 2.13) and subsequent rearranging, the Hamiltonian can be written as,

$$\hat{H}_{QHO} = \hbar\omega(\hat{a}^\dagger\hat{a} + \frac{1}{2}), \tag{2.27}$$

With this formalism for the QHO framework in mind, it is now possible to return the definitions for CS presented at the beginning of the subsection. The second definition states that CS are eigenstates of the lowering operator (Eqn. 2.15), meaning CS are the states such that,

$$\hat{a}|z\rangle = z|z\rangle, \tag{2.28}$$

The displacement operator uses a complex number and then shifts the position of the system by the real part while shifting momentum by the imaginary part,

$$\hat{D}(z) = e^{z\hat{a}^\dagger - z^*\hat{a}}, \tag{2.29}$$

The final definition of the CS states that they can be found by the displacement operator acting upon the ground state of the QHO,

$$\hat{D}(z)|0\rangle = |z\rangle, \tag{2.30}$$

As can be seen in Eqns. 2.28,2.30, both of the definitions use a complex number, z, to construct the CS. The choice of z is free, meaning that every complex number, z, can form a 'label' for a corresponding CS, $|z\rangle$. The label of the CS then resembles the centres of the CS within phase space,

$$z(t) = \frac{\gamma^{1/2}q + i\left(\frac{\gamma^{-1/2}}{\hbar}\right)p}{\sqrt{2}}, \tag{2.31}$$

where a one-dimensional CS is written,

$$\langle x|z\rangle = \left(\frac{\gamma}{\pi}\right)^{1/4} \exp\left[-\frac{\gamma}{2}(x-q)^2 + \frac{ip(x-q)}{\hbar} + \frac{ipq}{2\hbar}\right], \tag{2.32}$$

where γ is the inverse width parameter, and the last term of the equation being a phase factor, ensuring normalisation and phase-space consistency. CS also have a useful property of forming a multi-dimensional CS simply by forming a product of multiple one-dimensional CS,

$$|z_k(t)\rangle = \prod_{m=1}^{M} |z_k^{(m)}(t)\rangle, \tag{2.33}$$

2.2.2 Application to MD

Outside of the context of the QHO, CS retain their usefulness as their minimum uncertainty is maintained through time evolution, leading to them often being

called the 'most classical' quantum object and being applied in a wide range of fields [136–141]. While a singular CS is sufficient to describe the motion of the QHO, it is almost always the case that an ensemble is required to simulate more complicated systems. Within MD, a 'Frozen Gaussian' is a CS given by Eqn. 2.32 with the width parameter kept constant, as to 'freeze' the width. This concept is often traced back to the seminal work by Heller [142], though the idea of using multiple Gaussians had been seen even earlier, where two Gaussians were successful in simulating exciton-photons [143]. While Gaussians with varying width ('Thawed') have found applications [144–147], FGs are arguably the more popular variant. In practice a relatively small (especially compared to a grid basis) ensemble of FGs can simulate a system with a high number of degrees of freedom.

2.3 Classical molecular dynamics

Classical MD, as the name suggests, performs simulations of the movement of molecules based upon the classical mechanics perspective. This provides information on how the individual atoms within a system interact allowing for the transformation of the concept of a mechanism into a 'molecular movie' furthering chemists' understanding as the transfer of energy and momentum within the molecule can be fully visualised. Conceptually each atom of a molecule can be treated as a point moving through space according to Newton's equation of motion, which is simply,

$$\frac{dR^2}{d^2t}M = F = -\nabla V, \tag{2.34}$$

Where - $\nabla V represents either the gradient of a force field or the result of a quantum mechani$

In order to properly propagate the path of the molecule, it is necessary to understand the evolution of the forces, particularly how they relate to a change in molecular structure. The task of attributing this relationship is traditionally ascribed to forcefields, which can relate molecular features such as bond angles and length to the forces experienced by each atom. There are many such force-

fields designed that have become increasingly popular within the MD community such as the AMBER [148, 149] forcefield designed to model proteins. There has also recently been a significant increase in the use of machine learning models that replace the chemical intuitions such as Leonard-Jones potentials with generated machine learning forcefields [150, 151]. While a machine learning forcefield can reach chemical accuracy for certain systems, it often requires thousands to millions of Ab Initio calculations from which to extrapolate. A common solution to this issue is that of active learning [152], whereby a forcefield can iteratively select geometries that are sufficiently different from its current training set to revert back to Ab Initio calculations before adding that result into its own training set, both preventing the forcefield from giving an unfounded answer and increasing its own boundaries while being in use for classical trajectories. Another weakness of forcefields is solved by so-called reactive forcefields, which allow for the change of molecule connectivity such as after a bond dissociation event. This is implemented via a forcefield such as ReaxFF [39, 153], which is constructed to allow for the dynamic calculation of the bond order between all atoms generating a forcefield that is much more complex than its non-reactive counterparts.

In practice, in order to limit computational cost, a large molecule is often partitioned into several sections which are then treated as the interacting parts. An insightful review of classical MD [16] summarises five main resolutions. The first two are sub-atomic which are dominated by quantum effects and so are often off-limits to study through classical MD. The last three are atomistic, supra-atomistic and supra-molecular. A key part of the process of this simplification is the selection of relevant degrees of freedom to preserve. The degrees of freedom that are removed should be of a large enough quantity that any potential loss in accuracy compared to simulating the full dimensionality of the system is offset by the gain in computational cost. It is also natural to remove any degree of freedom that is known prior to simulation to not have any effect on the intended observable. Another key concept in the viability of classical MD is that of sampling. Sampling can be used as an answer to the rare event problem [154, 155], where the processes that are of interest in the simulation do not occur read-

ily enough to be studied with statistical relevance, causing a large portion of the computational resources to be spent on gathering non-relevant data. Umbrella sampling [156, 157], for example, consists of sampling from multiple harmonic (umbrella potentials) that are partitioned across the target double well, that allows for trajectories that are encouraged to overcome free-energy barriers. Boxed molecular dynamics [155, 158] is an interesting sampling technique that is applied as the trajectory is propagating, not in the initial conditions. By exactly inverting the velocity of each atom once a molecule reaches a preset boundary, it is possible to confine the molecule within a specific area without significantly perturbing the total energy or electronic structure of the molecule. This means that a much larger portion of the trajectory can be dedicated to simulating non-equilibrium spaces that might otherwise not be frequently occupied. While the original formation of boxed molecular dynamics limited the method to focusing on simple observables, new extensions have recently been developed that greatly generalised the concept. Development of these sampling techniques to address the rare event problem has lead to various other solutions, such as the insertion of 'fake' degrees of freedom to better 'steer' the trajectory [159–161] and remains to this day a very active field of study [155].

Classical MD has found applications in a wide range of fields within chemistry, including but not limited to combustion [37], low temperature plasma [162] and perhaps most commonly biological molecules [163]. While it has proven itself useful over several decades, it is undoubted that any approximation comes at the cost of at least some accuracy. For example when the systems of interest to be simulated are sufficiently small, it is common for the most processes to be quantum in nature and therefore require the quantum effects (such as tunnelling) that are not inherently included within a classical forcefield. Simulations that require frequent changes in molecular connectivity and charge density also pose a challenge to a classical forcefield. The most conceptually straightforward way to rectify these issues is to include quantum effects via Ab Initio quantum calculations such as DFT, producing mixed classical-quantum molecular dynamics or even full quantum molecular dynamics.

2.4 The MCE method

2.4.1 The Coupled CS method

The Coupled CS (CCS) method was first presented by Shalashilin in 2000 [69] (though it did rely and build upon previous work [164–166]) with the aim of propagating an ensemble of CS representing a wavefunction exactly, replacing the necessity of evaluating the van-Kleck propagator. The CCS method begins by expressing the wavefunction in the coherent-state representation via insertion of the position-space identity. The equations themselves begin with writing the wavefunction in terms of the CS basis,

$$\langle z|\psi\rangle = \int dx \, \langle z|x\rangle\langle x|\psi\rangle, \tag{2.35}$$

where z still represents the complex coherent state. This Husimi representation forms the basis of CCS where the overall wavefunction is projected onto each CS and then weighted with the overlap between said CS and the position eigenstate. For clarity and ease in later equations, the Hamiltonian is also often ordered such that raising operators precede lowering operators,

$$\hat{H}(z) = \hat{H}(\hat{a}, \hat{a}^\dagger) = \hat{H}_{ord}(\hat{a}^\dagger, \hat{a}), \tag{2.36}$$

which immediately has the beneficial consequence that an element of the matrix of the overlap can now be written,

$$\langle z|\hat{H}|z'\rangle = \langle z|z'\rangle\hat{H}_{ord}(z^*, z'), \tag{2.37}$$

where the overlap of 2 CS is given as,

$$\langle z|z'\rangle = e^{z^*z' - \frac{|z|^2}{2} - \frac{|z'|^2}{2}}, \tag{2.38}$$

and the identity operator for the CS is given as,

$$\hat{I} = \sum_{k,l} |z_k\rangle(\Omega^{-1}_{kl})\langle z_l|, \tag{2.39}$$

where Ω_{kl} is the overlap matrix given by the elements,

$$\Omega_{kl} = \langle z_k | z_l \rangle, \tag{2.40}$$

The ansatz of CCS can then be written as,

$$|\psi(t)\rangle = \sum_k C_k(t)|z_k(t)\rangle = \sum_k D_k(t) e^{\frac{iS_k(t)}{\hbar}} |z_k(t)\rangle, \tag{2.41}$$

where the quantum amplitude $C_k(t)$ is often rewritten in terms of the classical action $S_k(t)$, in order to separate rapidly varying phase from the smooth amplitude in the form of a pre-exponential factor $D_k(t)$,

$$D_k(t) = \sum_l \langle z_l(t)|\psi(t)\rangle e^{\frac{i(S_l(t) - S_k(t))}{\hbar}} (\Omega^{-1})_{kl}(t), \tag{2.42}$$

where,

$$C_l(t) = \langle z_l(t)|\psi(t)\rangle e^{\frac{iS_l(t)}{\hbar}}, \tag{2.43}$$

All of these equations allow for the derivation of the equations of motion for CCS in terms of the classical action, CS and quantum amplitudes,

$$\frac{dS(t)}{dt} = \frac{i\hbar}{2} \sum_J (z_J^* \dot{z}_J - z_J \dot{z}_J^*) - \hat{H}_{ord}(z^*, z), \tag{2.44}$$

$$\frac{dz_J}{dt} = \frac{-i}{\hbar} \frac{\partial \hat{H}_{ord}(z_J^*, z_J)}{\partial z_J^*}, \tag{2.45}$$

$$\frac{dC_l}{dt} = -\frac{i}{\hbar} \sum_k \langle z_l | z_k \rangle \delta^2 \hat{H}_{ord}(z_l^*, z_k) D_k e^{\frac{i(S_k - S_l)}{\hbar}}, \tag{2.46}$$

where,

$$\delta^2 \hat{H}_{ord}(z_l^*)(z_k) = \hat{H}_{ord}(z_l^*)(z_k) - \hat{H}_{ord}(z_l^*)(z_l) - \frac{\partial \hat{H}_{ord}(z_l^*)(z_l)}{\partial z_J}(z_k - z_J), \tag{2.47}$$

The strengths of the CCS method then lies with how closely Eqn. 2.45 mimics classical trajectories with the difference being that $\hat{H}_{ord}$ contains quantum corrections, allowing the method to naturally incorporate quantum effects. In this

sense the method is capable of propagating quantum states along classical-like trajectories. With the help of sampling tricks [167], CCS has been applied to many systems [70, 71, 168–171]. Since its inception, CCS has also had multiple extensions developed [72, 73, 172], such as re-derivation of the equations within the context of fermionic CS, showing that the simple concepts behind the method allow for a flexible framework that can scale nicely with high dimensionality.

2.4.2 Formulation of the MCE method

2.4.2.1 Equations for MCEv1

The MCE methods can then be seen as an expansion of the CCS method to incorporate multiple electronic states. The ansatz for the first version of MCE [68] is as follows,

$$|\Psi(t)\rangle_{\mathrm{MCEv1}} = \sum_{n,l=1}^{N,L} \left(a_{ln}|\chi_l\rangle\right)|z_k(t)\rangle, \tag{2.48}$$

where N is the number of basis functions and L the number of electronic states. While in theory L can be set to however many states are required to simulate a system, in practice (and for this thesis), L is often set to two, a ground state ($|0\rangle = |\psi_0^{system}\rangle$) and excited state ($|1\rangle = |\psi_1^{system}\rangle$). In this case the ansatz for MCEv1 becomes,

$$|\Psi(t)\rangle_{\mathrm{MCEv1}} = \sum_{k=1}^{K} \left(a_{1k}|1\rangle + a_{0k}|0\rangle\right)|z_k(t)\rangle, \tag{2.49}$$

where $|z_k\rangle$ is an ensemble of 'Frozen Gaussian' CS. Similarly to CCS, the CS are evolved through the equation,

$$i\frac{dz_k}{dt} = \frac{\partial H^{\mathrm{Ehr}}}{\partial z_k^*}, \tag{2.50}$$

where the ordered Hamiltonian ($\hat{H}_{ord}$) of Eqn. 2.45 is replaced with, the Ehrenfest Hamiltonian (H^{Ehr}), which is found by averaging the ordered Hamiltonian over the system configuration, n.

$$H^{\text{Ehr}} = \frac{|a_{1n}|^2\langle z_k|\hat{H}_{11}|z_k\rangle + |a_{0n}|^2\langle z_k|\hat{H}_{00}|z_k\rangle + 2\,\text{Re}\left(a_{0n}^* a_{1n}\langle z_k|\hat{H}_{10}|z_k\rangle\right)}{|a_{1n}|^2 + |a_{0n}|^2}, \quad (2.51)$$

The computationally inexpensive Ehrenfest trajectory shown in Eqn. 2.50 results in the basis set of MCE being guided by a pseudo-PES that is constructed by the quantum average of all the PES considered in the system. The quantum amplitudes that weight the impact an electronic state has on the wavefunction evolve with equations derived variationally from the Lagrangian,

$$\sum_k a_{1k}\langle z_J|z_k\rangle - \langle z_J|z_k\rangle H^{(11)}(z_J^*, z_k) - \langle z_J|z_k\rangle H^{(12)}(z_J^*, z_k)a_{2k} + i\left((z_J^* - z_k^*)\dot{z}_k + \frac{\dot{z}_k z_k^*}{2} - \frac{z_k \dot{z}_k^*}{2}\right)\langle z_J|z_k\rangle a_{1k} = 0, \quad (2.52)$$

which can be somewhat simplified by the introduction of the classical action (similar to as done in CCS) and rewriting the quantum amplitudes a_r,

$$a_r = d_r e^{iS_r}, \quad (2.53)$$

so that Eqn. 2.52 becomes,

$$\sum_k i\,\dot{d}_{rk} e^{iS_{rk}}\langle z_J|z_k\rangle = \sum_k \langle z_J|z_k\rangle\,\delta^2 H'^{(rr)}(z_J^*, z_k) d_{rk} e^{iS_{kr}} + \sum_k \sum_{s\neq r} \langle z_J|z_k\rangle\, H^{(rs)}(z_J^*, z_k)\, d_{sk} e^{iS_{sk}}, \quad (2.54)$$

where the classical action S_r and $\delta^2 H'^{(rr)}$ are given by

$$S_r = \int \left[i\frac{\dot{z}z^* - z\dot{z}^*}{2} - \langle z|H^{(rr)}|z\rangle \right] dt, \quad (2.55)$$

$$\delta^2 H'^{(rr)} = H^{(rr)}(z_J^*, z_k) - H^{(rr)}(z_k^*, z_k) - iH^{(rr)}(z_J^* - z_k^*)\dot{z}_k, \quad (2.56)$$

respectively. A strength and perhaps key defining point of MCEv1 is that the equations for the evolution of the amplitudes effectively couple not only each

quantum amplitude but also each configuration and therefore trajectory. A limiting factor of almost all trajectory guided methods is that once the basis set has travelled sufficiently far along the trajectory, the basis sets begin to uncouple weakening the methods ability to accurately simulate the system. The advantage of MCEv1 then lies in that while the trajectories are computationally inexpensive to calculate, the way that they are coupled ensures that they 'push' one another and as such stay coupled in the physically relevant areas of phase space for longer. In it's original paper, MCEv1 was shown capable of matching the benchmark simulating 2000 degrees of freedom with only 200 configurations.

2.4.2.2 Equations for MCEv2

The second formulation of the MCE method (MCEv2) was presented only a year later [67]. The ansatz for this method is very similar to the first iteration,

$$|\Psi(t)\rangle_{\text{MCEv2}} = \sum_{n=1}^{N} D_k \left(a_{1n}|1\rangle + a_{0n}|0\rangle\right)|z_k(t)\rangle, \tag{2.57}$$

where it in fact only differs by the introduction of the configurational amplitude, D_k, which separates the inter- and intra-configurational coupling. While the inter-configurational coupling was said to be an advantage, this separated nature of MCEv2 was designed for ease of implementation of Ab Initio MD, which was later created as Ab Initio Multiple Cloning (AIMC) [75]. While the propagation of the CS nuclear basis remains unchanged, the additional amplitude changes the equations for the evolution of a_r,

$$\frac{da_r}{dt} = i\left[i\frac{\dot{z}z^* - z\dot{z}^*}{2} - \langle z|H^{(rr)}|z\rangle\right]a_r - i\sum_{s\neq r}\langle z|H^{(rs)}|z\rangle a_r, \tag{2.58}$$

which under the usual transformation gives,

$$\frac{dd_r}{dt} = -i\sum_{s\neq r}\langle z|H^{(rs)}|z\rangle d_s e^{i(S_s - S_r)}, \tag{2.59}$$

The derivation of the new amplitudes is rather dense but finally results in,

$$\sum_I \langle \phi_J(t)|\phi_I(t)\rangle \frac{dD_I(t)}{dt} = -i\sum_I \Delta^2\langle H\rangle_{ji} D_I(t), \tag{2.60}$$

where the elements of $\Delta^2\langle H\rangle$ are,

$$\sum_I \Delta^2\langle H\rangle_{ij} = \langle \phi_J(t)|\hat{H}|\phi_I(t)\rangle - \langle z_J(t)|z_I(t)\rangle H_{ji} - i\langle \phi_J(t)|\ \phi_I(t)\rangle (z_J^* - z_I^*)\dot{z}_I, \tag{2.61}$$

where,

$$\langle \phi_J(t)|\hat{H}|\phi_I(t)\rangle = \langle z_J|\hat{H_{11}}|z_I\rangle a_{1j}^* a_{1i} + \langle z_J|\hat{H_{22}}|z_I\rangle a_{2j}^* a_{2i} + \langle z_J|\hat{H_{12}}|z_I\rangle a_{1j}^* a_{2i} + \langle z_J|\hat{H_{21}}|z_I\rangle a_{2j}^* a_{1i}, \tag{2.62}$$

and,

$$H_{ji} = a_{1j}^*\langle z_J|\hat{H_{11}}|z_I\rangle a_{1i} + a_{1j}^*\langle z_J|\hat{H_{12}}|z_I\rangle a_{2i} + a_{2j}^*\langle z_J|\hat{H_{21}}|z_I\rangle a_{1i} + a_{2j}^*\langle z_J|\hat{H_{22}}|z_I\rangle a_{2i}, \tag{2.63}$$

It is important to note that the coupling matrix $\Delta^2\langle H\rangle$ will always have small elements and zero diagonal elements. The introduction of the D_k amplitude due to having the effect of separating the coupling between configurations and the coupling between the quantum amplitudes in a single configuration also allows for the trajectory of each configuration to be run individually, with the calculations of D_k constructing the whole basis being calculated as post-processing. This ability to run trajectories on separate hardware at separate times is a great advantage when it comes to MCE's application to Ab Initio MD.

2.4.2.3 Sampling techniques for the MCE method

While MCE is a computationally efficient method, the key to maintaining the efficiency and accuracy across several different systems is apt use of different sampling techniques [74, 167]. Before propagation, while the basis set is being calculated, it is best to form a "swarm" of CS functions around the first basis

function generated, ensuring that they are sufficiently coupled while still entirely representing the initial wavefunction ($|\Psi_0\rangle = |z_0\rangle$). The size of the swarm is controlled via the compression parameter, a_c, which can be iterated upon until a basis set with sufficient norm has been found. The distribution of the CS within the swarm is given by the equation,

$$F(z_k) \propto e^{-a_c|z_k - z_0|^2}, \tag{2.64}$$

In certain cases, it is possible to partition the bath of the system into more and less important modes. With this priority realised, the degrees of freedom which are most relevant can be assigned more CS via adjustment of the compression parameter for each individual mode. The spherical swarm shown in Fig. 2.1b then becomes a more "pancake" style distribution shown in Fig. 2.1c. These types of distributions allow both MCEv1 and MCEv2 to sample initial conditions more accurately and efficiency.

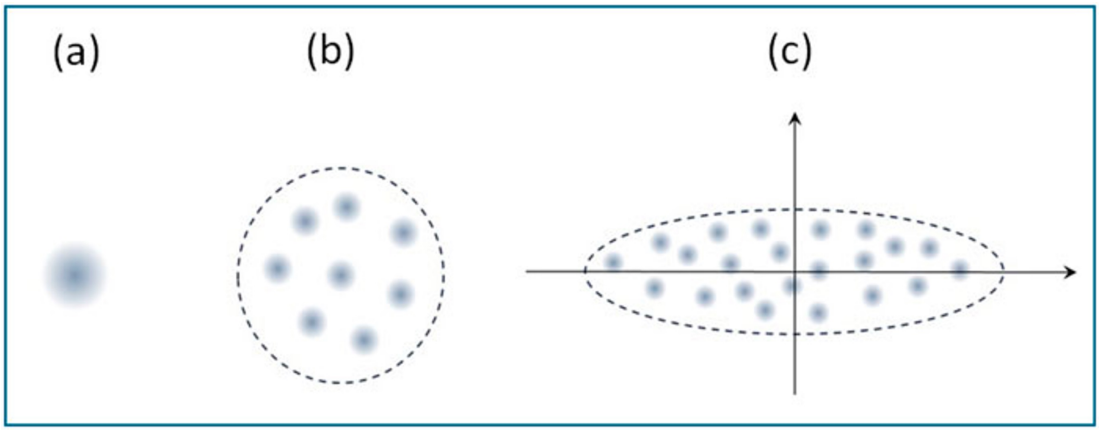

Figure 2.1: Graphic showing (a) a singular basis function, (b) a swarm of basis functions within the enclosure governed by the compression parameter a_c, and (c) a pancake of basis functions with a focus on the most important modes.

As with all methods that involve Ab Initio MD, the calculations for electronic structure constitute a large portion of the computational expense. A line of basis

functions following the same trajectory (henceforth referred to as trains with the concept displayed in Fig. 2.2) were therefore introduced into MCEv2 in order to have a larger basis at a negligible cost due to the train allowing all basis functions on the same trajectory to reuse the same electronic structure information. The rigid nature of the trains also partially prevents the decrease in convergence seen when using swarm initial sampling. Similar to the compression parameter for swarms, trains also have a spacing parameter which determines how much a basis function on the train is time-shifted along the trajectory.

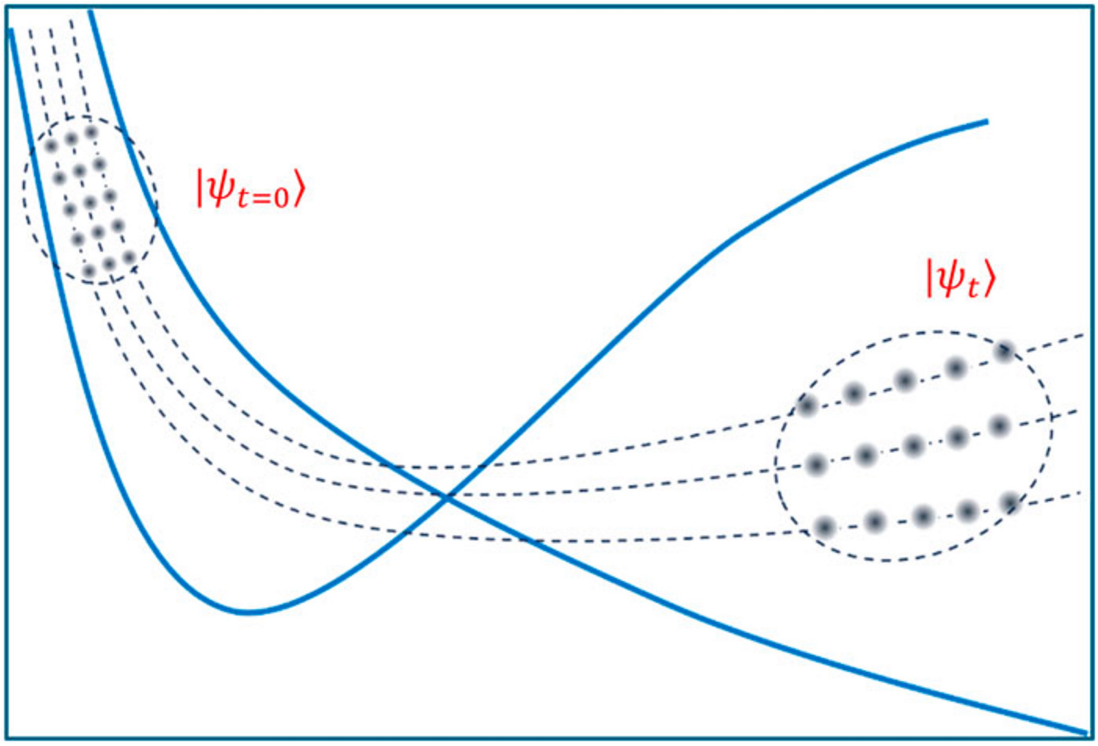

Figure 2.2: A swarm of trains being guided across PESs (blue) through time via Ehrenfest trajectories (dotted lines). The basis functions within each train follow the same trajectory, reducing the randomness of the swarm and allowing for the reuse of electronic structure information.

In practice, this spacing parameter for basis set trains is found by first creating swarm of basis functions with the lowest compression parameter that generates a

basis set with unitary norm. This number of basis functions then grows by creating a train for each CS of the swarm with the spacing generally being determined as the largest spacing that maintains the norm of the basis set as a whole. These conditions are derived from the fact that for MCEv2, the norm of each individual configuration (and therefore the whole basis set) needs to be 1.

Once the basis set is generated successfully, it is possible to propagate several basis sets in parallel. If these different basis sets differ only via the initial conditions in the phase space components of the CS then an average of these different basis sets (often referred to as 'repeats') will in fact mimic the results of a larger basis set. This allows for many repeats with small basis sets to be performed, usually in parallel, reducing both the computational cost and the need for excessive hardware. For many cases, including the Spin Boson model, the way to separate the overall wavefunction into several "bits" of smaller basis functions is found through the Harmonic Oscillator density operator, $\hat{\rho}$, of the M CS, given by

$$\hat{\rho} = \int |z_{\text{bath}}\rangle\rho(z_{\text{bath}})\langle z_{\text{bath}}|\frac{d^2 z_{\text{bath}}}{\pi^M} = \prod_{m=1}^{M}\int |z^{(m)}\rangle\rho(z^{(m)})\langle z^{(m)}|\frac{d^2 z^{(m)}}{\pi}, \tag{2.65}$$

In this equation, $d^2 z^{(m)} = \frac{dp^{(m)}dq^{(m)}}{2}$ represents the standard phase space integration measure for the harmonic oscillator for the m-th CS associated with the m-th bath mode. z_{bath} is the usual product of one-dimensional CS multiplied together to form a multi-dimensional 'bath' CS. Within the context of a harmonic oscillator it is possible to use a product of one-dimensional operators to deconstruct Eqn. 2.65. This operator is itself a product of 1D density operators,

$$\rho(z^{(m)}) = \sigma^{(m)} e^{-\sigma^{(m)}|z^{(m)}|^2}, \tag{2.66}$$

The key parameter introduced here is $\sigma^{(m)}$, representing the density matrix. The width of this matrix is given by the interaction of the frequency of the bath mode ($\omega^{(m)}$) and temperature,

$$\sigma^{(m)} = e^{\beta\omega^{(m)}} - 1, \tag{2.67}$$

where β is the inverse temperature parameter, $\beta = \frac{1}{k_b T}$. These repeats can then be propagated as swarms (and trains in the case of MCEv2) as shown in Fig. 2.3, before being averaged to present the results of the larger basis set being approximated.

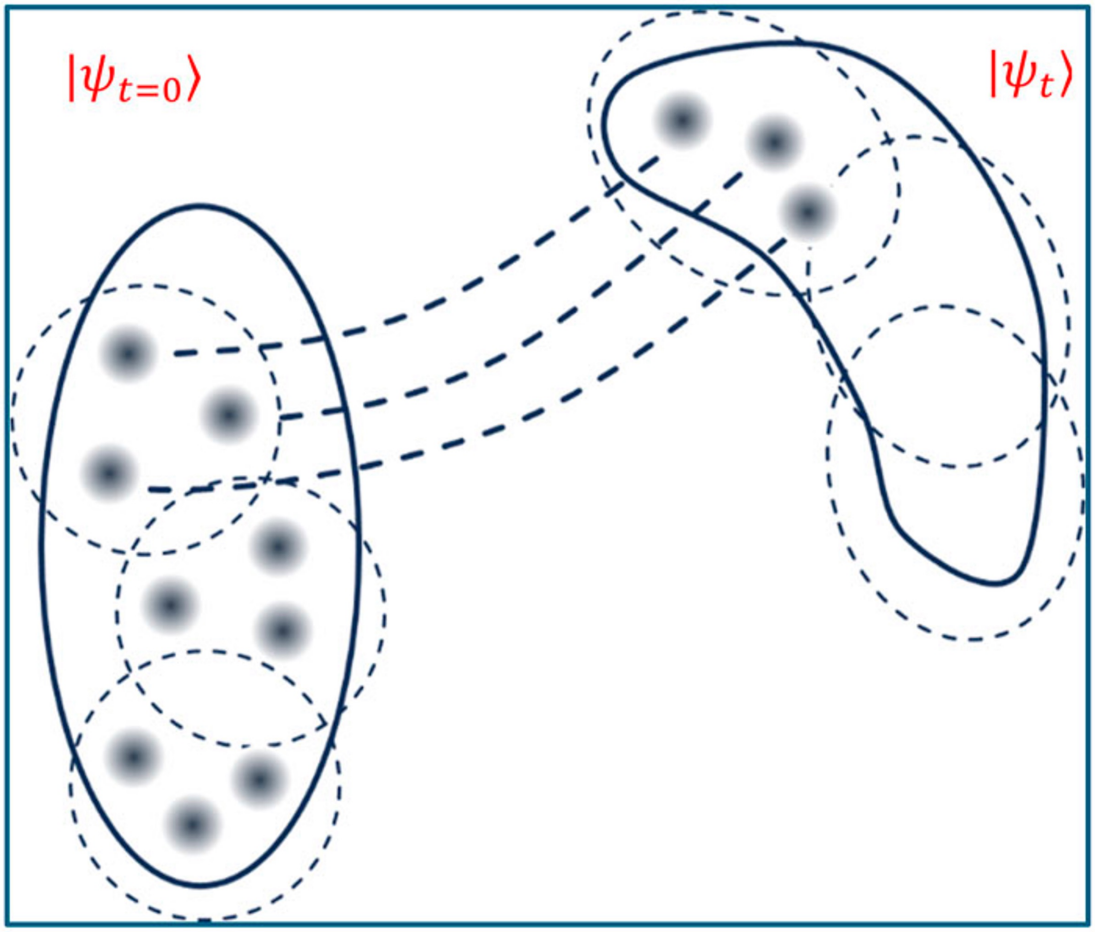

Figure 2.3: CS "bits" (basis functions enclosed by dotted circles) are generated to fully represent the initial wave function. Each "bit" is propagated separately, allowing efficient spotlighting of relevant areas of phase space.

The initial conditions of the "bits" are sampled from a distribution around a given point in phase space, usually the origin $(q, p) = (0, 0)$. Each "bit" is later propagated using a swarm basis set, as shown in Fig. 2.3. All "bits" can be

propagated in parallel, making MCE highly efficient. The "bit-by-bit" propagation has been successfully used for both MCEv1 and MCEv2.

2.4.3 Ab Initio Multiple Cloning

The AIMC method is the Ab Initio extension of MCEv2, taking the ansatz shown in Eqn. 2.57. While AIMC makes use of all of the sampling techniques mentioned in the previous section, it was the introduction of cloning that allowed the method to accurately simulate non-adiabatic processes of molecules. The Ehrenfest trajectories that guide AIMC report a great computational cost reduction over variational trajectories due to moving the basis set along a quantum averaged psuedo-PES. This simplification works well when the PES are separated but after crossing a region of non-adiabatic crossing, it's possible the averaged PES may not accurately represent the whole nature of the diverging 'true' PES. Therefore the guiding Ehrenfest force may become unphysical and misguide the basis set and while a sufficiently large number of trajectories and repeats could still average to the correct result, it is computationally unviable. To rectify this, cloning allows for the Ehrenfest trajectories to bifurcate in a similar fashion to the wavefunction. Basis functions that are being misguided can be identified via investigation of the breaking force for each electronic state I,

$$F^{br}_{I,n} = (a^n_I)^* a^n_I \Big[\nabla_r V_I - \sum_J (a^n_I)^* a^n_I \nabla_r V_J\Big], \tag{2.68}$$

which is the difference between the averaged force and the force on the electronic state I for basis function n weighted by the population of the given electronic state, in order to only include electronic states with relevant population. The breaking force for each PES can then be transformed into acceleration via multiplication with the inverse mass matrix. An increase in this breaking acceleration means that the difference between the Ehrenfest force and the true forces is rapidly increasing, suggesting that the approximation no longer holds. When a basis function is no longer accurately guided an additional basis function is created with identical CS and the amplitudes of both the new and misguided basis

functions become,

$$|\psi'_k\rangle = |\chi_k\rangle \left(\frac{a_I^k}{|a_I^k|}|\psi_I\rangle + \sum_{J\neq I} 0|\psi_J\rangle \right), \tag{2.69}$$

$$|\psi''_k\rangle = |\chi_k\rangle \left(0|\psi_I\rangle + \sum_{J\neq I} \frac{1}{\sqrt{1-|a_I^k|^2}} a_J^k|\psi_J\rangle \right), \tag{2.70}$$

with both I and J representing different electronic states. From the normalisation factors in Eqn. 2.69 it is clear that the summation of the two new basis functions, $|\psi'_k\rangle, |\psi''_k\rangle$, results in the original basis function meaning that at the timestep of cloning the wavefunction as a whole remains unchanged. However, the basis size has now been incremented by one and the problematic average of the PES for that original problematic basis function has now been separated across multiple basis functions and so the resulting dynamics will differ. In order to make the cloning procedure generally applicable to a wide range of systems, an effort was made to establish three main conditions of cloning,

1. In order for both of the amplitudes of generated clones to be negligible, cloning should only concur when there is significant population on more than one PES. To measure this the width function is defined for each basis function such that,

$$W = \frac{1}{\sum_k |a_k^{(I)}|^4}, \tag{2.71}$$

therefore cloning should occur when this width function exceeds 2, suggesting that there is population in multiple states.

2. By quantifying the difference between the Ehrenfest force, F_{Ehr} and the force acting upon the most populated electronic state, F_{max}, as a pseudo angle, it is possible to clone only trajectories that are significantly misguiding the basis function. If we define this pseudo angle θ^n as,

$$\theta^n = arccos\left(\frac{2F_{Ehr}^n F_{max}^n}{|F_{Ehr}^n|^2 |F_{max}^n|^2} \right), \tag{2.72}$$

and then set a condition for cloning to be when $\theta^n = \frac{\pi}{12}$, then clones will be only be generated when there is significant difference in the Ehrenfest force and the max force, suggesting that the trajectory is not being guided physically.

3. When a trajectory passes through a conical intersection, it is possible that the previous conditions for cloning can be triggered multiple times, leading to an excessive yet unhelpful growth of the basis set. To limit this, cloning should only occur in regions where the electronic states are weakly coupled. To define these regions we clone only when the following expression,

$$\frac{|\sum_{I,J}(a_I^n)^* a_J^n d_{IJ}^{(n)}(V_I^{(n)} - V_J^{(n)})}{|\sum_I |a_I^{(n)}|^2 \nabla_{R_n} V_I^{(n)}}, \tag{2.73}$$

is below a certain threshold, often given to be 0.05.

While these cloning conditions are not perfectly suitable for each system and have their own limits, they are generally applicable to a wide range of cases. AIMC has successfully been applied to multiple different photochemical processes including electronic and vibrational energy transfer between two- and three-ring linear poly(phenylene ethynylene) units [76], relaxation of pyridine [173], the photodynamics of ethene [75], vibrationally mediated photodissociation for pyrrole [77, 174, 175] and most recently a prediction challenge for the ultrafast electron diffraction of photo-excited gas-phase cyclobutanone [88]. The method has also been implemented in multiple MD packages [173, 176].

2.5 The Spin Boson Model

The Spin Boson model is a famous model of open quantum systems [177, 178], which can be applied to many different fields [179–190]. As the Spin Boson model consists of two quantum distinct energy wells, it is also possible to frame the model in the context of computational chemistry, with one well being seen as a donor state and the other an acceptor state. The bath of the Spin Boson

model can then be seen as a bath of the nuclear vibrational degrees of freedom. Within this perspective it is possible to stage the many different regimes of the Spin Boson model as a testing ground for newly developed dynamics methods and their extensions. Many such methods have been tested against the Spin Boson model, though it is challenging to formulate a method that performs well for all regimes including those of high coupling strength, high dimensionality and low temperature. The description of the Spin Boson model begins with its Hamiltonian,

$$\hat{H} = \begin{bmatrix} H_B + H_C + \epsilon & \Delta \\ \Delta & H_B - H_C - \epsilon \end{bmatrix}, \tag{2.74}$$

where the diagonal Hamiltonian elements consists of sums of H_b (the Hamiltonian of the bath), H_C (the Hamiltonian of the coupling between the bath and the system) and ϵ (the energy bias parameter, i.e. twice the gap between the zero-point energy of the wells.) The off diagonal Hamiltonian element is Δ, the tunnelling parameter. In practice, Δ is often set to 1 and used as a scaling factor for the other parameters. The rest of the information for a case of the Spin Boson model is contained with the bath's spectral density function. A linear power law relation between the frequency and spectral density (though others exist) is said to be Ohmic. The Ohmic spectral density of the Spin Boson model is given by,

$$J(\omega) = \frac{\pi}{2} \sum_m \frac{(C^{(m)})^2}{2(\omega^{(m)})^2} \delta(\omega - \omega^{(m)}), \tag{2.75}$$

In order to make the spectral density more computationally practical and easy to discretize (as well as to better represent other systems), a cut-off function is often applied which changes the behaviour of the spectral density around and after a characteristic frequency, ω_c. The exponential cut-off applied in this thesis presents an exponential decay after the characteristic frequency. When the exponential cut-off is applied it is possible to write the spectral density in terms of the kondo parameter, a_k,

$$J_{exp}(\omega) = \frac{\pi}{2}\alpha_k \omega e^{\frac{-\omega}{\omega_c}}, \tag{2.76}$$

While the exponential cut-off is the most popular when testing MCE, others exist that better suit specific systems. Examples of this include the Drude-Laurentz (Debye) [**Lindoy**, 191–193] cut off,

$$J_{DL}(\omega) = 2\pi\lambda\omega\frac{\Omega}{\Omega^2 + \omega^2}, \tag{2.77}$$

and the Brownian oscillator [194],

$$J_{BO}(\omega) = \frac{\Omega\gamma\lambda}{(\omega^2 - \omega_c^2)^2 + \gamma^2\omega^2}, \tag{2.78}$$

where γ^2 is the dampening parameter. The decay of the Drude-Laurentz cut-off is elongated compared to the exponential cut-off, leading to a spectral density that naturally includes higher frequencies of the bath, which is useful for solvent dynamics. The underdamped Brownian oscillator has a heavy oscillating nature which is often applied to photosynthetic complexes and nano-mechanical systems. Both of these cut-offs can present challenges to different methods, with the long tail of the Drude-Laurentz cut-off suggesting there is a long bath correlation time and that numerical truncation of the bath may prove difficult. The oscillations in the Brownian oscillator can cause issues for path integrals and methods that rely on weak coupling approximations.

While the Spin Boson model is indeed very varied and can present many different cases, within the Ohmic exponential cut off regime, the cases can be partitioned into three main categories of population transfer (which are exemplified in Fig. 2.4), based on the coupling parameter (α_k). When the coupling between the system and the bath is sufficiently weak, the population transfer takes the form of a large number of oscillations with the amplitudes inversely proportional to α_k. If the wells are symmetrical to the point where the zero-point energies are equal ($\epsilon = 0$), then these oscillations will eventually dampen to an

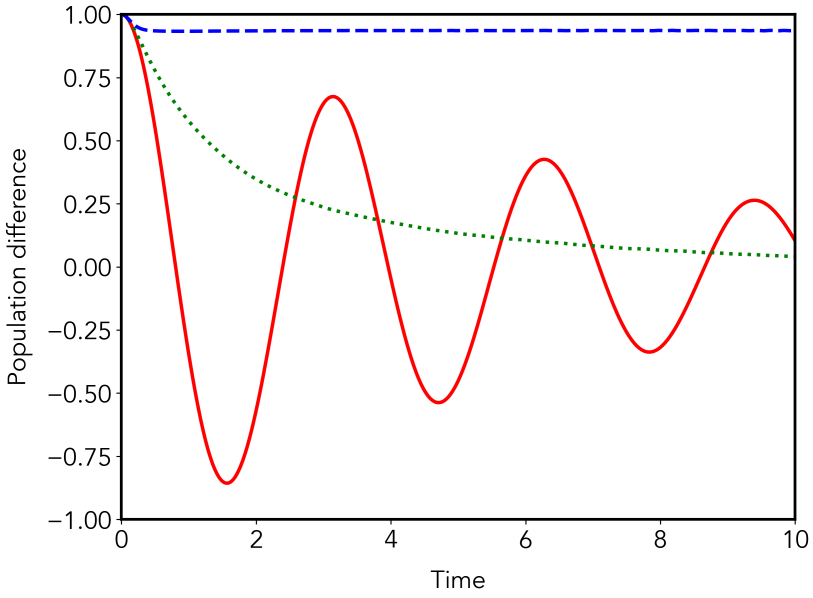

Figure 2.4: 3 example cases of the Spin Boson model where the population difference either oscillates before finding the equilibrium population (solid red line), relaxes to the equilibrium population (dashed green line) or undergoes relocalisation (dashed blue line)

equilibrium population where each well is equally populated. As the coupling increases, the rate of population transfer slows until the oscillations disappear and the resulting population transfer is that of a smooth relaxation to the equilibrium population. Finally, with sufficiently strong coupling, it is possible for the Spin Boson model to undergo relocalisation, where only a small portion of the initial population is transferred rather quickly before establishing stability. Ideally a method developed for MD would be capable of accurately converging several different regimes across multiple different cut-offs for the Spin Boson model.

In the computational chemistry community, the Spin Boson model is often thought of as two PES in the form of identical wells, as demonstrated in Figure 2.5. The parameter ϵ can then be thought of as the height difference between the two wells, representing half the shift in zero-point energy. While harder to represent on a cartoon, the other parameters can also be conceptualised this way with

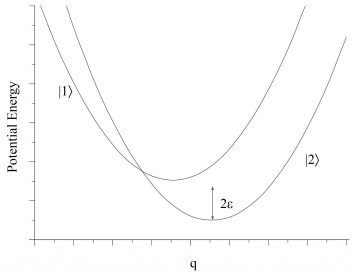

Figure 2.5: Conceptual cartoon of the Spin–Boson model represented as two harmonic potential energy surfaces. The diabatic wells are identical in shape and separated by an energy offset of 2ϵ corresponding to the bias between the two electronic states. In the unbiased case ($\epsilon = 0$ the wells are degenerate).

the coupling α_k being a measure of the degree to which each electronic state displaces the surrounding environment. In this picture, increasing the system–bath coupling corresponds to increasing the separation between the minima of the two potential wells, leading to a larger reorganisation of the bath following a change in the electronic state. Strong coupling therefore results in significant dressing of the system by the environment and enhances non-adiabatic and dissipative effects. The characteristic frequency of the bath, ω_C, controls the curvature of the wells and thus the timescale on which the environment responds to changes in the system. High characteristic frequencies correspond to a rapidly responding (stiff) bath, leading to dynamics that are closer to the Markovian limit, while low characteristic frequencies represent a slow bath that retains memory of the system's past evolution. In this way, the characteristic frequency contains and controls the degree of non-Markovian behaviour present in the dynamics. Within this thesis, only wells with equal bias are investigated ($\epsilon = 0$), a range of characteristic frequencies and coupling strengths are considered.

2.5.1 The MCE method applied to the Spin Boson Model

When MCE is applied to the Spin Boson model it is necessary to discretize the continuous bath into modes in order to generate the CS basis functions. This is

done by rewriting the exponential cut off spectral density shown in Eqn. 2.76 in the form,

$$C^{(m)^2} = w_m \frac{2J_{exp}(\omega^{(m)})}{\pi\rho(\omega^{(m)})}, \tag{2.79}$$

The density of the frequency, $\rho(\omega)$ is itself given by

$$\int_0^{\omega^{(m)}} d\omega\rho(\omega) = m, m = 1, ..., M, \tag{2.80}$$

where,

$$\rho(\omega) = a\frac{J_{exp}(\omega)}{\omega}, \tag{2.81}$$

where the prefactor, a, is

$$a = \frac{2M}{\pi\alpha_k\omega_c(1 - e^{\frac{-\omega_{max}}{\omega_c}})}, \tag{2.82}$$

and ω_{max} is the largest bath frequency considered in the system. It is worth noting that the form of Eqn. 2.81 is a convenient choice as it has been shown that given a sufficient number of modes, the functional choice has been shown to be irrelevant in terms of accuracy [195], only in terms of number of modes required for convergence. Under this choice of discretization, it is now possible to write the coupling coefficients, C_m, between the bath and the system as,

$$C^{(m)} = \omega^{(m)}\sqrt{\frac{\alpha_k\omega_c}{M}(1 - e^{\frac{-\omega_{max}}{\omega_c}})}, \tag{2.83}$$

Finally the frequencies of the bath is given as,

$$\omega^{(m)} = -\omega_c ln\left[1 - \frac{m}{M}(1 - e^{\frac{-\omega_{max}}{\omega_c}})\right], \tag{2.84}$$

While the Hamiltonian given in Eqn. 2.74 is indeed the general form, MCE requires that any Hamiltonian it is applied to be of the form $\hat{H}(z, z^*)$. This highlights another strength of MCE because as CS can be defined in terms of the annihilation operator, the two Hamiltonians $\hat{H}_B$ and $\hat{H}_C$ can be rewritten as,

$$\langle z_J|\hat{H}_B|z_k\rangle = \langle z_J|z_k\rangle \sum_m \omega^{(m)}(z_J^{*(m)} z_k^{(m)} + \frac{1}{2}), \tag{2.85}$$

$$\langle z_J|\hat{H}_C|z_k\rangle = \langle z_J|z_k\rangle \sum_m \frac{C^{(m)}}{\sqrt{2\omega^{(m)}}}(z_J^{*(m)} + z_k^{(m)}), \tag{2.86}$$

where z_J, z_k are multi-dimensional CS and $z_J^{(m)}, z_k^{(m)}$ are the m-th mode of said multi-dimensional CS. It is also worth noting that for MCEv2, the breaking force that is central to the conditions of cloning depends on the difference in potential energy of the electronic states. As this difference is always constant in the Spin Boson model, the equation for the breaking force is reduced to merely being dependent on the amplitudes. This results in the breaking force for configuration, n, in the Spin Boson model as,

$$F_{SB,n}^{br} = |a_{1n}a_{2n}|^2, \tag{2.87}$$

The maximum breaking force can then be found when the amplitudes are exactly split between the two wells presenting an image of an Ehrenfest configuration straddled between two electronic states giving a maximum value of 0.25. For this reason, the standard cloning condition for an Ehrenfest configuration within the MCEv2 approach to the Spin Boson model is to clone when $F_{SB}^{br} > 0.249$.

2.5.2 Other methods for solving the Spin Boson Model

2.5.2.1 MCTDH

The multiconfigurational time dependent Hartree (MCTDH) approach [56] is a method often applied to the Spin Boson model that is capable of solving the model exactly [57, 196, 197]. It does this by writing the wavefunction as the following ansatz,

$$|\psi(t)\rangle = \sum_J A_J(t)|\phi_J(t)\rangle = \sum_{J_1} ... \sum_{J_m} A_{J_1,J_2,...,J_m}(t)\Pi_{k=1}^M|\varphi_{j_k}^k(t)\rangle, \tag{2.88}$$

where $|\varphi_{jk}^{k}(t)\rangle$ are single particle functions. These basis functions are a convenient tool in MCTDH as they are each capable of representing multiple degrees of freedom. MCTDH also stands out among the other methods considered in this thesis as the method does indeed solve the wavefunction with a grid basis, allowing it to be numerically exact and for that reason has served as a benchmark for many other methods, including MCE. However, as with all grid-based methods, the problematic scaling with degrees of freedom can be computationally prohibitive. Due to its reliance on a full configuration interaction over all possible single particle function combinations, the MCTDH method exhibits exponential scaling with system dimensionality. For a system with a given M modes and a given n single particle functions required per mode, the resulting terms are of n^m length. Therefore when applied to molecular systems it is common for MCTDH to simulate a reduced dimensionality model.

That is not to say that the MCTDH cannot be applied to systems of high dimensionality. In fact the Multi-layer MCTDH (ML-MCTDH) [57, 198–200] does so by replacing the necessity for the full configurational interaction across all single particle functions by representing the single particle functions not by the combination of primitive basis functions but instead by their own basis set of single particle functions (which themselves are represented by a primitive basis set). This process can be repeated several times giving multiple layers, allowing for the partitioning of weakly coupled degrees of freedom and greatly reducing the number of cross terms required for calculation. Weak coupling typically arises when interactions between subsets of coordinates are small compared to their internal dynamics, for example when different vibrational groups evolve on distinct timescales or are spatially separated. For a system with six degrees of freedom and four single particle functions assigned to each degree, standard MCTDH requires a total of $4^6 = 4096$ configurations. If these six degrees of freedom are able to partitioned into two groups of three then the number of configurations reduces to only $4^3 + 4^3 = 128$ configurations, a total reduction of 32x. The ML-MCTDH ansatz is then given by

$$|\varphi_n^k(t)\rangle = \sum_I B_I^{k,n}(t)|u_I^k(t)\rangle$$
$$\equiv \sum_{i_1}\sum_{i_2}\cdots\sum_{i_{Q(k)}} B^{k,n}_{i_1,i_2,\ldots,i_{Q(k)}} \prod_{q=1}^{Q(k)} |v_{i_q}^{(k,q)}(t)\rangle, \tag{2.89}$$

Single hole functions are then defined to show how the groups forming the wavefunction interact by fixing the group that defines the function and then projecting the whole wavefunction across the remaining degrees of freedom. On the first layer this is written as,

$$|\Psi_n^k(t)\rangle = \sum_{j1}\ldots\sum_{j=k-1}\sum_{j=k+1}\ldots\sum_{jp}(t)A_{j1,\ldots jk-1,jk+1,\ldots,jp}\Pi_{l\neq k}^p|\varphi_{jl}^l(t)\rangle, \tag{2.90}$$

for subsequent layers, concise writing of the single hole functions requires exploiting their relation to the layer above,

$$|g^{(k,q)}_{L(i),n,r}(t)\rangle = \sum_r |v_r^{(k,q)}(t)\rangle|g^{(k,q)}_{L(i+1),n,r}(t)\rangle, \tag{2.91}$$

Each layer of the ML-MCTDH method requires its own equation of motion. As with standard MCTDH this is found via the application of the variational principle with respect to the coefficients of that layer to the overall wavefunction,

$$i|\dot{\Psi}\rangle_{L1coeff}(t) = \hat{H}(t)|\Psi(t)\rangle, \tag{2.92}$$

ML-MCTDH has been successful in simulating systems with other 1000 degrees of freedom as well as multiple challenging regimes of the Spin Boson model. MCTDH as a framework has also been applied to many cases as well through the use of multiple extensions such as MCTDH-F [201–203], MCTDH-B [204–208], MCTDH-X [209, 210] and G-MCTDH [211–215].

2.5.3 MS, FMS and AIMS

The multiple spawning (MS) framework [61] is a collection of 'Frozen Gaussian' trajectory based methods that propagate via classical evolution of the phase space centres of the CS on a single PES while propagating the amplitudes in a quantum manner. The basic form of the MS ansatz is given by,

$$\Psi(R, r, t) = \sum_{I=1}^{N(t)} C_I(t)\, \chi_I(R; t)\, \phi_{s_I}(r; R) \tag{2.93}$$

It is important to note here that the index for the electronic states, χ is the same as the index for the physical states, φ. This is because, contrary to MCE, the MS framework operates with a multi-set ansatz where each electronic state has an associated nuclear basis set. The quantum amplitudes are evolved through the equations,

$$\frac{dC_I(t)}{dt} = -\frac{i}{\hbar} \sum_J \left(S^{-1}\right)_{IJ} \left[H_{IJ} - i\hbar\, (\dot{S})_{IJ}\right] C_J(t), \tag{2.94}$$

using the inverse of the overlap matrix (S^{-1}) and the matrix representation of the time derivative operator ($\dot{S}$) given by the equations,

$$S_{IJ} = \langle \chi_I \mid \chi_J \rangle_R, \tag{2.95}$$

$$\dot{S}_{IJ} = \left\langle \chi_I \middle| \frac{\partial}{\partial t} \chi_J \right\rangle_R, \tag{2.96}$$

and the Hamiltonian matrix in Eqn. 2.94 has the elements,

$$H_{IJ} = \langle \chi_I \phi_{s_I} \mid \hat{H} \mid \chi_J \phi_{s_J} \rangle, \tag{2.97}$$

The MS framework derives its name from the spawning procedure used to dynamically grow the basis set. When a basis function enters a region of high

non-adiabatic coupling, a child basis function is spawned on the electronic state not occupied by the basis function. Conceptually, the idea is very similar to the procedure of AIMC and in fact was the direct inspiration for cloning. Similar to AIMC, the fact that MS methods can begin simulations with small basis sets that increase only when the current basis set is inadequate is a large computational advantage. In practice the basis function undergoing the spawning is propagated to the phase space where the coupling is strongest, and then an exact copy of said basis function is created in terms of classical energy, phase space position and momentum, adjusting the velocity only. An effort is also made to limit the overlap between the basis set and the new child basis function. Then both the parent and the child basis function are back propagated in line with the whole basis set before basis set propagation begins with the additional basis function. The spawning procedure was originally developed for the same reason as cloning in AIMC, to allow the basis set to accurately follow a wavefunction undergoing non-adiabatic processes. However, this condition is not found when MS is applied to the Spin Boson model as the coupling between the two wells remains constant regardless of phase space position. A modification of the spawning procedure was developed for the Spin Boson model that maintained the overlap of the basis functions on the other well. When a basis function was found to have no overlap over a certain defined threshold (see Eqn. 2.98) then the spawning procedure was called and a child basis function is created with sufficient overlap, allowing the method to accurately simulate the zero-temperature Spin Boson model [216]. To quantify this overlap, the following equation is used:

$$O_I = Max_J |\langle \chi^i | \chi^j \rangle|, \tag{2.98}$$

The MS framework is an excellent example of how a method is developed around a novel idea (multiple spawning in Full MS) before being extended to an Ab Initio method in the form of Ab Initio multiple spawning [62, 217–219] and that method being continuously iterated and updated to increase efficiency and expand the range of systems considered with scholastic selection Ab Initio multiple spawning [220] and Ab Initio multiple spawning with informed stochastic

selection [221] being recently published.

2.5.4 Multiple Davydov Ansatze

A group of methods with great resemblance to MCE is the Multiple Davydov Ansatze (mDA) methods, which allows application to similar systems (including the Spin Boson model [222]) and straightforward transference of developments and extensions. There exists in fact a hierarchy of the methods (hDA) [65, 66] and the original formulations can be traced back to the 1970s with the concept of Davydov's solition [223–225]. The largest similarity between the mDA and MCE is that the MCEv1 ansatz in Eqn. 2.49 is structurally also the ansatz for the multi-D2 Ansatz (mD2A). While the equations for the evolution of the quantum amplitudes also employs the same equations in both methods, the methods differ in the propagation of the CS nuclear basis set. The mD2A method uses fully variationally derived trajectories for the nuclear basis set where MCE opts for the computationally cheaper Ehrenfest trajectories. This fully variational approach would suggest that the mD2A will be able to match the results of MCEv1 with a significantly reduced number of configurations, though not at the same computational cost as the Ehrenfest configurations scale better in terms of dimensionality. These findings were corroborated when both MCEv1 and mD2A were compared to a Hierarchical equations of motion (HEOM) [226] (which is itself a method presented for solving the Spin Boson model [227–230]) benchmark when investigating a one-dimensional Holstein molecular crystal model [231]. Both methods matched accurately with MCE often requiring hundreds of modes compared to the fully quantum variational basis set of mD2A requiring under 60 configurations (referred to as multiplicity by the authors of the paper). The beneficial scaling of MCE however proved to be an advantage as it was able to employ a basis set of thousands of modes when the cases where approaching the computational limit of HEOM, which was computationally prohibitive for mD2A.

2.6 Electronic structure

2.6.1 Hartree-Fock

While Ab Initio MD methods are flexible in the variety of systems to which they can be applied, this is dependent on the fact that the electronic structure information supplied is accurate. This then requires a suitable choice of electronic structure theory, which similarly to the choice of NAMD methods is a balance between accuracy and computational cost. However, unlike for the molecular dynamic community, there exists a hierarchy of electronic structure methods, often presented as a ladder.

Hartree-Fock [232–235] serves as the bottom rung and is a foundational method of electronic structure theory. It operates within the BO approximation and attempts to solve the electronic Schrödinger equation,

$$\hat{H}_{elec}|\Psi_{elec}\rangle = E_{elec}|\Psi_{elec}\rangle, \tag{2.99}$$

To do this, an assumption is made that the many electron equation in Eqn. 2.99 can be represented by a series of one-electron equations of the form,

$$h(x_I)\chi(x_I) = \epsilon_J\chi(x_I), \tag{2.100}$$

For this transformation to occur, it requires also the deconstruction of the electronic Hamiltonian into many one electron Hamiltonians. From inspection of Eqn. 2.99, it is simple to imagine this deconstruction of the kinetic energy to simply be the kinetic energy term of the single electron, and the second term representing the attraction between nuclei and electrons can also simply be re-written to the attraction between the nuclei and a given electron. However the last term, the electron-electron repulsion by definition cannot be written in terms of one electron as it is determined by the distance between multiple electrons. To bypass this, the mean field approximation is invoked and the electron-electron repulsion is written as the repulsion between a single electron and the average of all other electrons. Combining these three deconstructed terms yields the Fock operator given by,

$$\hat{f} = -\frac{1}{2}\nabla_I^2 - \sum_A \frac{Z_A}{r_{iA}} + v^{HF}(x_I), \tag{2.101}$$

where $v^{HF}(x_I)$ is the mean-field repulsion experienced by the single electron x_I. The electron Hamiltonian can then be rewritten as a sum of the Fock operator applied to each single electron,

$$\hat{H}_{elec} = \sum_I \hat{f}(x_I), \tag{2.102}$$

and so the single electron Schrodinger equation can be now written as,

$$\hat{f}(x_I)\chi(x_I) = \epsilon\chi(x_I), \tag{2.103}$$

For this simplification to hold, the total electronic wavefunction (consisting of num_{elec} electrons) must be able to be written as a series of single electron wavefunctions. The natural assumption would be to write them as a simple product, known as a Hartree product,

$$\Psi_{HP} = \chi_I(x_1)\chi_I(x_2)...\chi_I(x_N), \tag{2.104}$$

where N is the total number of electrons. This assumption fails however as Eqn. 2.104 violates the Pauli exclusion principle and the anti-symmetrical property required of the wavefunction. In actuality the Hartree-Fock method has to write the wavefunction as a so called slater determinant [236],

$$\Psi_{SD}(x_1, x_2, \ldots, x_N) = \frac{1}{\sqrt{N!}} \begin{vmatrix} \chi_1(x_1) & \chi_2(x_1) & \cdots & \chi_N(x_1) \\ \chi_1(x_2) & \chi_2(x_2) & \cdots & \chi_N(x_2) \\ \vdots & \vdots & \ddots & \vdots \\ \chi_1(x_N) & \chi_2(x_N) & \cdots & \chi_N(x_N) \end{vmatrix}, \tag{2.105}$$

Within this representation, each spin-orbital is shown by columns with each row containing information about only one electron. This approximation of the wavefunction is not perfect, with Hartree-Fock ignoring dispersion interactions and struggling to properly account for bond-breaking events. The scaling of the

Hartree-Fock method can also seen through the growth of these slater determinants, with the method scaling to the order $O(n^4)$, where n is the number of basis functions. Constructing a more accurate wavefunction via employing a linear combination of slater determinant results in the configuration interaction method, the next rung of the hierarchical ladder. While more accurate it is also significantly more expensive as N electrons and M spin-orbitals requires a wavefunction written in terms of $\frac{M!}{N!(M-N)!}$ slater determinants, each of which require the calculations of many two electron integrals.

2.6.2 Density Functional Theory

Another route to obtaining electronic structure information is through DFT [40], based on two foundational principles set by Hohenberg and Kohn [237],

1. The ground state properties of a system can be found via the systems electron density, $\rho(x, y, z)$.

2. The correct ground state density for any given system is one that minimises the total energy.

As the first principle states, any property of a system can be found through the electron density, allowing us to write the total energy to be minimised as a functional of the electron density, $E(\rho(x, y, z))$. This immediately proposes a reduction in computational cost as it reduces the degrees of freedom from being the position of each atom to simply the three spatial dimensions of the density, however the challenge still remains to minimise the energy functional in order to find the correct electron density. The electron function is of course now also expressed in terms of electron density,

$$E[\rho] = T[\rho] + V_{ne}[\rho] + V_{ee}[\rho], \tag{2.106}$$

The minimisation of this function is not a trivial task, mostly due to the large number of unknown factors in terms of the kinetic energy and electron-electron interactions. The solution to this was proposed by Kohn and Sham, where they

replace the system of interacting electrons with another of 'non-interacting electrons' that is still capable of producing the correct density [238]. This Kohn-Sham equation has the form (with (x,y,z) being replaced with the usual position vector r),

$$\left[-\frac{1}{2}\nabla^2 + v_{ne}(r) + v_H(r) + v_{xc}(r)\right]\psi_I(r) = \epsilon_I\psi_I(r), \tag{2.107}$$

where v_{ne} is the typical nuclear-electron attraction, v_H is the mean field electron-electron (as in Hartree-Fock) potential and v_{xc} is the exchange correlation potential. These terms are given by,

$$V_{ne}[\rho] = \int v_{ne}(r)\,\rho(r)\,dr, \tag{2.108}$$

$$v_H(r) = \int \frac{\rho(r')}{|r-r'|}\,dr', \tag{2.109}$$

$$v_{xc}(r) = \frac{\delta E_{xc}[\rho]}{\delta\rho(r)}, \tag{2.110}$$

where E_{xc} is itself a functional representing the exchange-correlation that accounts for quantum effects not captured by the other terms, being best described as the term that captures the unknowns. This functional is therefore itself an unknown and must be approximated with many different popular choices available. All terms of the Kohn-Sham equation are dependent on the electron density and so in order to accurately solve this equation an accurate yet efficient form of the density is required. This is done by writing the electronic density as a summation of basis functions,

$$\rho(r) = \sum_I |\psi_I(r)|^2, \tag{2.111}$$

where $\psi_I(r)$ are the non-interacting Kohn-Sham orbitals. Two of the main choices that separate different DFT calculates are then the basis set and the exchange functional. While not every basis set is apt for simulating every system, there are general trends that the larger the basis set and the more complete its

formulation, the more accurate the resulting calculations, though at an increased computational cost.

2.6.3 Basis sets

In order to make the electronic Schrödinger equation tractable, molecular orbitals are expressed as linear combinations of predefined functions known as basis functions, which together form a basis set. By increasing the flexibility of this basis (through either increasing the complexity or number of basis functions), the wavefunction can be represented with increasing accuracy, at the expense of additional computational cost. The simplest basis set that can be constructed is that each orbital is represented by a singular basis function, often called a minimal basis set. To originally do this Slater type orbitals (STO) [239] were employed of the form,

$$\chi_{n,l,m}(r,\theta,\phi) = N_{n,l,m,\zeta} Y_{l,m}(\theta,\phi) r^{n-1} e^{-\zeta r}, \tag{2.112}$$

where $N_{n,l,m,\zeta}$ is the normalisation constant, $Y_{l,m}(\theta,\phi)$ describes the angular dependence of the orbital and $r^{n-1}e^{-\zeta r}$ is the radial part. STOs are often referred to as a natural basis set as they take a similar form to the hydrogen atom functionals and so have a decrease in probability as the distance between the electron and the nucleus increases along with satisfying Kato's cusp condition [240, 241] (meaning that the wavefunction has a discontinuity in its derivative at the position of the nucleus).

While these basis functions are based on some chemical truth, they are often computationally cumbersome. To rectify this the STOs can be written as a linear combination of primitive Gaussian type orbitals [242] (GTOs) creating the STO-nG basis sets, where n is the number of GTOs used to approximate each STO. The total electronic wavefunction can then be written as a sum of GTOs,

$$\Psi = \sum_{i}^{STO} (\sum_{J}^{n} c_J G_j^i), \tag{2.113}$$

where G_j^i is the primitive GTO basis function for the i-th STO. GTOs take the form

$$G_{n,l,m}(r,\theta,\psi) = N_n r^{n-1} e^{\alpha r^2} Y_l^m(\theta,\psi), \tag{2.114}$$

The minimal choice of a single STO to represent each orbital is called single-ζ. There is of course the possibility of using any given number, n, leading to n-ζ basis sets, where each orbital is represented by n basis functions. It is also possible to construct a basis set that has a split valence, meaning that there is a set number of primitive GTOs for each electron within an inner shell, and each electron in the valence shell is represented with higher than single-ζ. Split valence basis sets built upon GTOs can be identified via the label N-MPG, where N is the number of primitive GTOs used for the orbitals in the inner shell, M is the number of primitive GTOs for the inner valence function and P is how many primitive GTOs are assigned to the outer valence. The label can also be presented with asterisks, with one signifying the inclusion of d-type polarization functions for heavy atoms and two signifying the inclusion of p polarization functions for each hydrogen atom. Diffuse functions have very slow decay with respect to distance allowing for accurate description of electron density far from the nucleus which is useful for simulating bond-breaking events. Polarization functions are included to increase the flexility in the angular momentum of the basis set, which can benefit the description of lone pairs and bond breaking.

A very commonly used basis set is "6-31+G*" developed by Pople [243], taken as a good compromise between accuracy and computational cost. The label can be decomposed into (6,3,1,+,*), which can then be understood as follows,

1. 6: 6 primitive GTOs are assigned to the core orbitals.
2. 31: the valence orbitals are assigned 3 GTOs as part of the 'tight' valence function with an additional GTO forming the 'loose' valence function.
3. +: The inclusion of + adds diffuse functions to all non-hydrogen atoms.
4. *: A single asterisk includes d-type polarization functions for heavy atoms.

2.6.4 Spin-Flip DFT

In the current day, DFT is arguably the most popular approach for solving the electronic wavefunction, with new functionals being published each year [40]. However it is not without its limitations. When considering (particularly multiple) excited states, it is possible that standard DFT functionals and methods are not stable enough for application to simulations that undergo significant structural changes such as bond breaking events. Similar issues can occur when simulating systems that exhibit strong static correlation due to DFT's reliance on the exchange-correlation functional. The Spin-Flip approach [244] has a long history of applications and functions [205, 245–252] via using a more stable reference state of higher multiplicity (accessible via a single excitation that flips the spin of an electron) to accurate calculate the PES of the target lower spin state, which may be accessible due to strong correlation effects. For example, a triplet states can be utilised to create a stable PES for a singlet diradical, a system that is known to cause issues for standard DFT.

2.7 Neutral Dissociation

Most NAMD methods have been applied to some form of photophysics [253, 254]. Last year the community built around photochemical MD took part in a challenge to predict the outcome of a cyclobutanone experiment, with many submissions [88–102]. While there is no denying the applications of photochemistry in almost every field of chemistry, from increasing efficiency of solar cells [81, 82] to photo catalysis unlocking new reaction pathways [84–87, 90, 255], it is possible that there are many unsolved areas of chemistry that are overlooked. It is the opinion of the author of this thesis that neutral dissociation after excitation via electron impact particularly with regards to plasma is one of those areas. The MD study of neutral dissociation after excitation via electron impact is a very recent, hopefully emerging field of investigation [118]. The free electron is capable of transferring not only energy but also angular momentum, resulting in possible excitation to many excited states. As for most fluorine-containing organic molecules the

lowest excited state is triplet, it is possible to say that electron impact often excites molecules to the lowest triplet state, and there are no selections rules such as the ones found in photochemistry. To verify this assumption it is possible to run calculations employing Quantemol's UKMOL+R method to calculate the electronic state excitation cross-sections for electron impact [256]. To this end, our group previously investigated two molecules, $C_3H_2F_6$ and $C_3H_2F_4$.

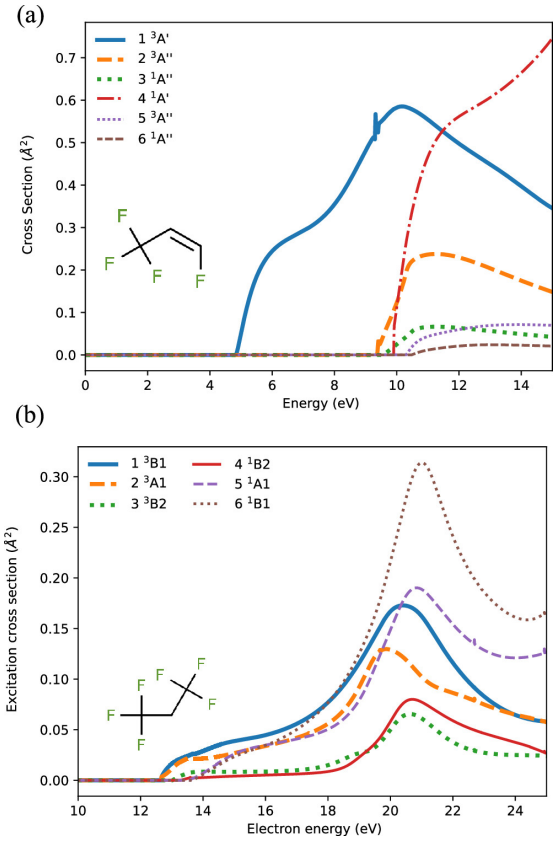

Figure 2.6: The excitation cross sections for two molecules, (a) $C_3H_2F_4$, (b) $C_3H_2F_6$. Molecular cartoons are included on each panel. Taken from reference [118].

Fig. 2.6 shows how for $C_3H_2F_4$, the triplet states are very convincingly the dominant spin states, due to the large cross-section that exists around 5 eV, which can be accredited to the presence of the double carbon-carbon bond (C=C). However the $C_3H_2F_6$ molecule, without the C=C bond, presents with two lowest

cross-sections that appear almost degenerate at the lowest energy that have less clear separations. The assumption that triplets states are still dominant even in this circumstance is supported by the fact the three lowest occurring cross-sections correspond to triplet states and the total cross-section for the triplet states is larger than for singlet states at low energy.

As the assumption that only the lowest triplet state is needed not necessarily held for this molecule, AIMC was used to calculate NAMD trajectories, considering the two lowest triplet states with the population of such trajectories shown in Fig. 2.7. When the molecule began on the highest triplet state (T2), the population declined rapidly to the lowest triplet state (T1) within the first 50 fs of simulation, and the transfer appears to curtail around a population of 0.2. Likewise when the simulation begins with the molecule in the T1 state, there is a quick initial transfer to the T2 state before the populations arrive at practically the same equilibrium with a T2 population of approximately 0.2. This finding supports the fact that even for a molecule that has multiple close lying triplet states, its dissociation pathways can still be investigated under the assumption that the dynamics need only include the lowest. As NAMD involves a force calculation for each electronic state as well a separate DFT calculation for the electronic coupling, the computational savings are roughly that of three times (as the cost of the nuclear propagation equations are negligible when compared to the DFT calculations).

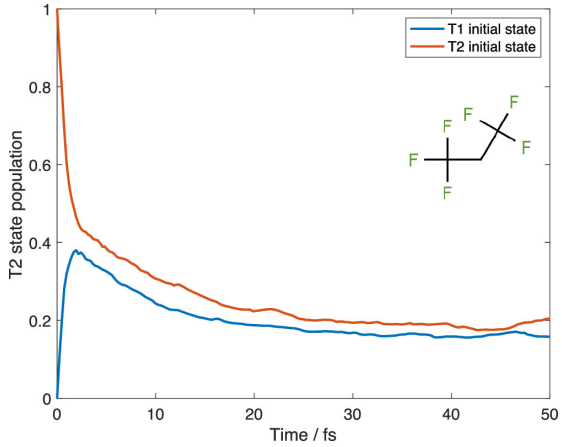

Figure 2.7: Population of the T2 state for $C_3H_2F_6$ averaged across multiple AIMC trajectories. Taken from reference [118].

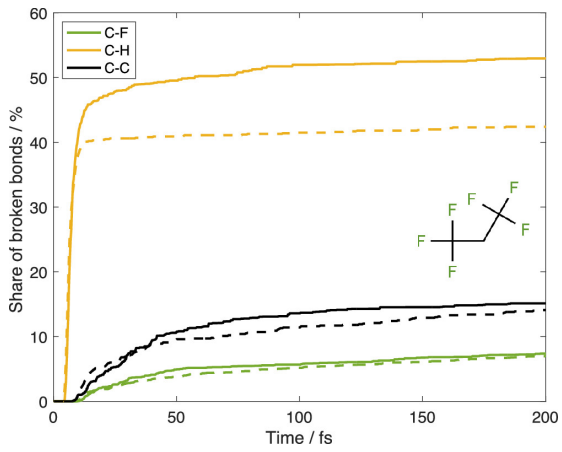

Figure 2.8: Dissociation kinetics for the molecule $C_3H_2F_6$. AIMC (solid line) with 2 triplet states is compared with standard MD (dashed line) on the lowest triplet state. Taken from reference [118].

The AIMC trajectories that were run were compared with those of standard MD with their dissociation yields plotted in Fig. 2.8. For both the C-C and the C-F bond types in the molecule, there was very good agreement between both methods, with both finding a share of broken bonds for each type of approximately 15 and 8 percent respectively. However, the last bond type in the molecule, C-H does present a different dissociation yield with the inclusion of the second

triplet state increasing the share of broken bonds by approximately 10%. The reason for this difference can be inferred from the dissociation kinetics themselves. For both C-C and C-F the dissociation kinetics are an almost logarithmic with an initial increase around 10 fs before the rate of dissociation slows down and continues steady for the rest of the propagation. The dissociation kinetics for the C-H, however, have over 90% of the dissociations occur within the first 10 fs. This means that the majority of the dissociations occur while the molecule is still relaxing to the lowest triplet state, causing the disparity seen between the two methods. The understanding of this occurrence allowed for the dynamics to be performed on the lowest triplet state only under the two following main assumptions:

1. The electron impact excites the molecule into a triplet state.
2. Any population on a higher triplet relaxes to the lowest triplet state within a time frame that can be taken to be instant.

Under these assumptions standard MD was also run for the molecule with the double bond, $C_3H_2F_4$.

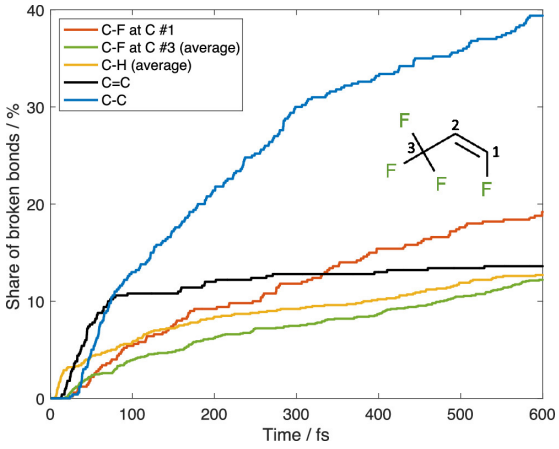

Figure 2.9: Dissociation kinetics for $C_3H_2F_4$ using standard MD with a simulated temperature of 5000 K. Taken from reference [118].

The dissociation kinetics for the $C_3H_2F_4$ molecule in Fig. 2.9 is rather different than the $C_3H_2F_6$ counterpart. The bond type with the highest share of broken

bonds is no longer the C-H bond but instead the C-C bond, accounting for 40%. Also interesting is that for the initial propagation of approximately 40 fs the dissociation rate of the C=C bond is actually higher than that of the C-C bond, suggesting that at least immediately after excitation the C=C bond is weaker than the C-C bond. The conclusion drawn from this finding is that it's possible the excitation is localised around this double bond. That is to say that the energy gap between the highest occupied molecular orbital (HOMO) of the sigma bond and the lowest unoccupied molecular orbital (LUMO) of the anti-bonding orbital results in the lowest triplet state. The dissociative character of the excitation then causes initial dissociations of the C=C bond. This theory is further supported by the separation of the share of broken bonds for the two C-F environments. The C-F at C#1 (a double bonded carbon) presents a much higher dissociation yield, which follows the theory of excitation being localised on the C=C bond before the dissociative character of the triplet state impacts closer bonds first.

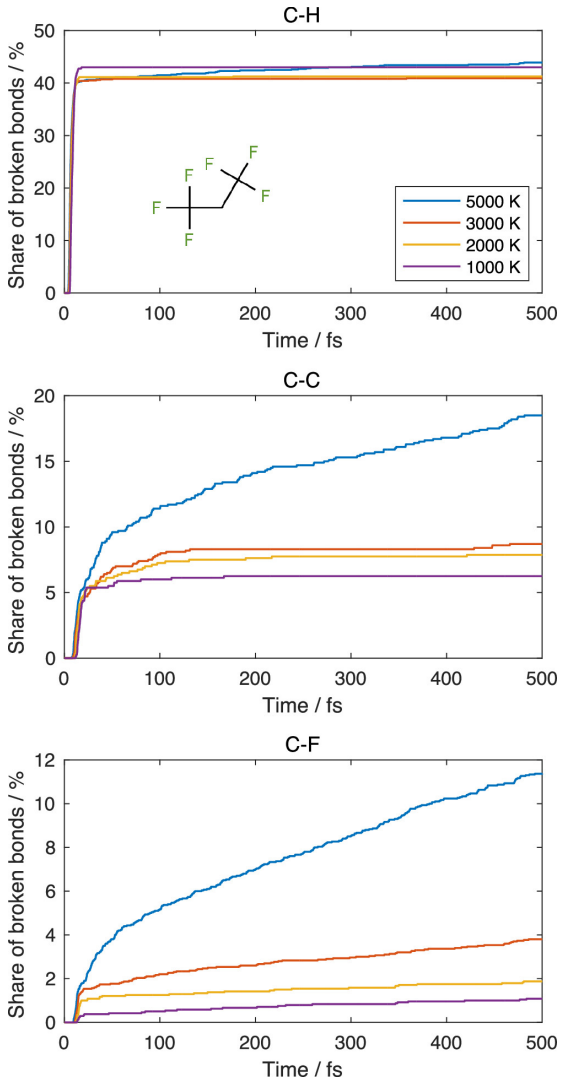

Figure 2.10: Dissociation kinetics for $C_3H_2F_6$ using standard MD across a range of temperatures. Each panel shows the share of broken bonds for 1000 K, 2000 K, 3000 K and 5000 K. Taken from reference [118].

The simulation temperature of 5000 K is too high for direct applications to industrial plasma. In order to investigate the temperature dependence of neutral dissociation and how large the trends differ when approaching low temperature the MD of $C_3H_2F_6$ after electron impact was also performed at simulated temperatures of 1000 K, 2000 K, 3000 K and 5000 K with the dissociation yields of

several bond types across these temperatures shown in Fig. 2.10. The overall trends between the bond types remains the same, with the dissociation kinetics of C-H bonds appearing independent of the temperature, suggesting that the C-H bond is very weak in the triplet state. The initial rate of dissociation for the C-C bond halves between 1000 K and 5000 K with there being almost no dissociations of the C-C bond after 10 fs, meaning all the C-C bond breaking events occur as part of the initial excitation and the generated initial momentum of the trajectory. A similar effect occurs with the C-F bonds but to a larger extent, to where at 1000 K they make up less than a percent of the share of broken bonds.

The investigation of these two molecules through MD has laid a very important foundation for the investigation of neutral dissociation in plasma after excitation via electron impact. It also serves as a proof-of-concept that affordable yet accurate dynamics of this process can be achieved when applying simplifying assumptions. C=C bonds dissociating more rapidly than single bonds as found in the MD simulations has been reported a few times experimentally but not investigated thoroughly [257]. The application of MD allows for the investigation of many molecules within an efficient time frame due to removing the need of redesigning the experiment. This tool can therefore be used to discover similar trends among functional groups and molecules, ultimately aiding in the design of a rule set for triplet state dissociation, a thus far understudied field in the MD community.

Chapter 3

Neutral dissociation calculations for use in Plasma Etching

While the plasma industry has many applications, particularly in areas of medicine [258, 259], this thesis concentrates entirely on the application of plasma to the semiconductor industry, where the plasma is used for two main processes, silicon etching and deposition. Both processes require efficient generation of specific radicals. For silicon etching, fluorine-containing radicals are required to remove the substrates from the wafer and etch the required pattern. In order to generate this fluorine radical containing plasma, industry often turns to the use of PFAS molecules, which are environmentally concerning. Therefore there exists a two-fold motivation behind the search for replacement plasma precursors, namely that they are more environmentally friendly but also more selective in their processes. This search can be expedited by a better understanding of the dissociation pathways of PFAS molecules. As it is unable to be studied through experiments, neutral dissociations remain a large gap in the knowledge base. MD simulations could provide insights into these otherwise hidden processes and help understand the mechanisms and determining factors of the neutral dissociation pathways. Potential replacements for certain plasma precursors molecules that have been historically popular with industry, such as C_4F_8, have been investigated in recent years, comparing wafer etch rates to scout for plasma options with a lower global warming potential. Their dissociation pathways were also analysed via mass spectrometry, providing insight into the dissociation of the important plasma molecules. If MD simulations can reproduce key findings from these experiments and identify trends of neutral dissociation, it would present a big step forward for the plasma community, as well as provide a whole new area of investigation for the MD community.

3.1 Electrophore Model for dissociation after excitation via electron impact

As discussed in section 2.7, there has been a recent novel application of NAMD to neutral dissociation in plasma [118]. In this paper it was shown that for the molecules considered the triplet states were dominant, an effect which has been

found in other theoretical studies of plasma [113]. The most interesting finding of the paper is proximity to double carbon-carbon bonds (C=C) increases the dissociation yield of a bond relative to other bonds of the same type. In fact, at the beginning of the propagation, the rate of dissociation of the C=C bond was higher than the single bond equivalent (C-C). This suggests that the energy gap between the π-orbital of the double bond and the corresponding anti-bonding orbital localises the excitation of the molecule to the C=C bond. This localisation can be seen as the electron impact excitation equivalent to the chromophore groups within photo-excitation. These groups that localise the electron impact excitation are similarly determined by specific energy gaps and often involve areas of high electron density and therefore can be named electrophores. An atom that could play the role of an electrophore is the oxygen atom. The lone pairs on the oxygen atom present a similar energy gap to the C=C bond and in essence the oxygen atom electrophore can be conceptualised as doubled bonded to itself. Fig. 3.1 shows how the excitation of the electron from the π-orbital in a C=C bond is fairly similar to that of the excitation of the non-bonding orbitals in a C-O-C bond.

Molecules containing oxygen have been investigated as plasma molecule replacements [**RN759**, 105, 106, 260] and as such understanding of how oxygen affects the neutral dissociation pathways of these molecules would be a great boon to the plasma industry. Understanding electrophores and the role they play can serve a key role in the prediction of neutral dissociation pathways due to the localisation of excitation. It is important to identify what can serve as an electrophore, and how electrophores affect the neutral dissociation of the molecule. To the best of the author of this thesis' knowledge, there is only one other MD investigation into triplet state dissociation after electron impact [116], but the study is not regarding a industry relevant molecule. To this end, this chapter attempts to establish some foundational preliminary trends for triplet state neutral dissociation in plasma through the lens of the electrophore model.

To achieve this, ab initio MD simulations will be run for several molecules. It is worth noting that the vast majority of the molecules considered in this

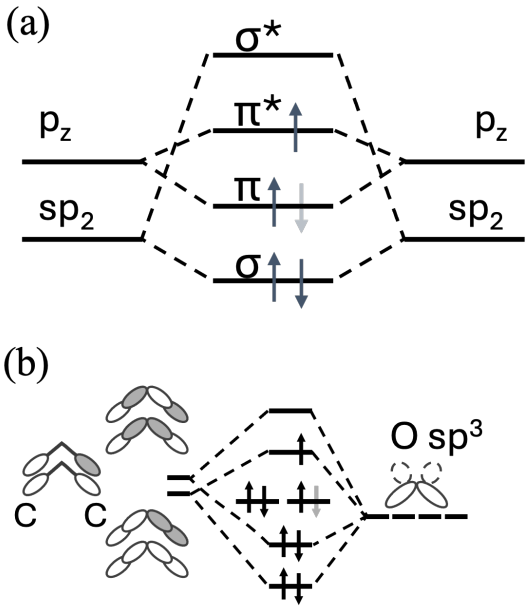

Figure 3.1: Molecular orbital digram showing how the energy gaps between the LOMO and HUMO allow the C=C bond and the oxygen atom to act as an electrophore, localising the triplet state excitation.

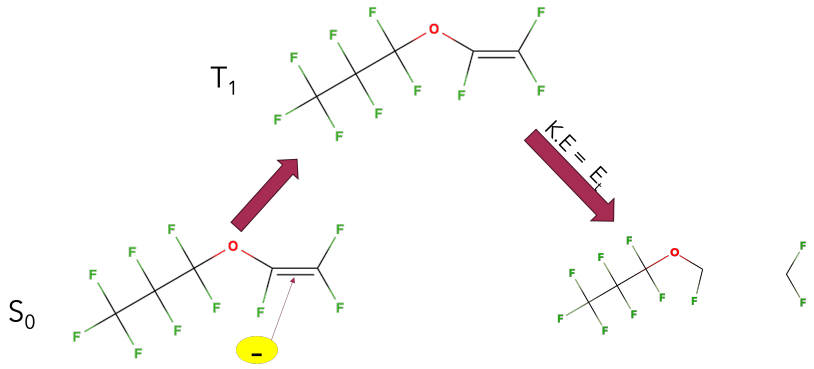

Figure 3.2: A schematic of the MD simulation process. A molecule is excited via electron impact (at the electrophore), and given thermal energy. The dissociation of the molecule is then captured through MD.

thesis will be simulated applying the assumption that, due to the presence of an electrophore separating the presence of the lowest triplet and the behaviour of higher triplet states relaxing rapidly, only the lowest triplet state is required to accurately propagate the trajectories. Therefore while both methodology and the code to run the simulations have been developed with AIMC in mind, the method more closely resembles the classical MD presented in Section 2.3 than the MCE family of methods.

Conceptually, a molecule is excited instantly to the lowest triplet state and given appropriate thermal energy to generate the momenta. Once initial conditions have been generated, the molecule is then propagated on the lowest triplet state using a standard Verlet algorithm for 500 femtoseconds (fs). A bond is taken to be broken once its bond length exceeds 5 Bohr, enabling the analysis of the dynamics, showcasing both dissociation yield and the corresponding dissociation kinetics. Further information on the propagation and the code used to perform the simulations can be found in the appendix. A cartoon of the procedure is shown in Fig. 3.2.

3.2 Copmutational details

All electronic structure calculations presented in this thesis were performed using DFT as implemented in QChem. The triplet excited states were described using standard DFT or SF-TDDFT depending on the molecule's requirements. Unless otherwise directly stated in the section, all calculations employed the B3LYP functional with the 6-31G*+ basis set (unless otherwise stated in section 3.5.3.

3.2.1 Generation of the initial conditions

To generate appropriate initial conditions, the initial excitation of the molecule is assumed to be vertical in a Franck-Condon sense, meaning that the equilibrium geometry of the singlet state is an appropriate starting geometry for all trajectories. Once the equilibrium geometry is obtained from an optimising electronic structure calculation, the vibrational modes are sampled to generate initial momentum based on the Boltzmann distribution at the specified temperature. Therefore the momentum for each atom can be written as,

$$P_{j,k} = m_j * \sum_{i}^{n_{mod}} A_{j,i} * v_{i,k} \tag{3.1}$$

where i is the mode index and j the atom index. $A_{j,i}$ is the three dimensional mode displacement matrix. The mode space velocities, $v_{i,K}$ are generated randomly and scaled in accordance with the temperature and the effective mass of the modes, $M_{eff,i}$,

$$v_{i,k} = r_{n,i,k} = \sqrt{\frac{2T}{M_{eff,i}}}, r_{n,i,k} \sim \mathcal{N}(0,1) \tag{3.2}$$

where,

$$M_{eff,i} = \sum_{j}^{n} m_j ||A_{j,i}||^2 \tag{3.3}$$

It is important to note that temperature enters the dynamics exclusively through the sampling of the initial nuclear momenta. As a result, any invest-

igation into temperature effects requires regeneration of the initial conditions rather than modification of the propagation algorithm itself.

3.2.2 Propagation equations

The propagation algorithms used throughout this thesis is based on algorithms developed within AIMC. The computational implementation can be split into two main sections. The first is a preliminary step that updates both the position and momentum of the molecule. The second is a correction step that adjusts the momentum only. There are several equations and processes however that are shared between steps. The first being the construction of the electronic Hamiltonian. This Hamiltonian is a Hermitian matrix with dimensions equal to the number of PES considered and where the diagonal elements take the form,

$$\hat{H}^{ii}_{elec} = E_{SCF}(i) + 77.67785291 \tag{3.4}$$

where the $E_{SCF}(i)$ is the calculated SCF energy for the $i-th$ electronic state. The other matrix elements takes the form

$$\hat{H}^{ij}_{elec} = -i(\sum V * C_{ij}) \tag{3.5}$$

$$\hat{H}^{ji}_{elec} = -\hat{H}^{ij}_{elec} \tag{3.6}$$

Where V is the velocity of the atoms (in bohr units per atomic time unit) and C_{ij} are the coupling matrix elements relating to $i-th$ and $j-th$ electronic state. For all MD simulations considered in this thesis outside of section 4.4, all of the molecules are simulated on only the lowest triplet PES and so the electronic Hamiltonian collapses to a vector with the value of Eqn. 3.4. A second order Magnus expansion is needed to estimate the time evolution operator by taking an input of two electronic Hamiltonians,

$$U_{mag2}(\hat{H}_{elec,1}, \hat{H}_{elec,2}, \Delta t) = e^{\hat{H}_{\Delta t}\Delta t} * e^{\hat{H}_{tr}*\Delta t} \tag{3.7}$$

where, $\hat{H}_{tr}$ is the trace matrix found by calculating the average of the diagonal values of the two electronic Hamiltonians multiplied through the identity matrix,

$$\hat{H}_{tr} = \sum_{i} (\hat{H}^{ii}_{elec,1} + \hat{H}^{ii}_{elec,2}) I \tag{3.8}$$

and $\hat{H}_{\Delta t}$ is the average traceless Hamiltonians throughout the timestep given by,

$$\hat{H}_{\Delta t} = \frac{\hat{H}_{elec,1} + \hat{H}_{elec,2}}{2} - \hat{H}_{tr} \tag{3.9}$$

It is worth mentioning that $\hat{H}_{\Delta t}$ remains a matrix and so the current implementation for matrix exponentiation is the Padé approximation. The final object shared between both propagation steps is the Ehrenfest force vector which is calculated as a function of the amplitudes, forces, energy and the coupling of the molecule.

$$F_{Ehr} = \sum_{i}^{N_{States}} f_i * A_i + \sum_{i} \sum_{i \neq j} 2Re(A_i A_j)(E_i - E_j) * C_{ij} \tag{3.10}$$

Where A_i is the amplitude for the i-th electronic state, E_i is the SCF energy for the i-th electronic state and f_i are the forces calculated via electronic structure.

The preliminary propagation step occurs before the electronic structure is run in that timestep and so the data is used is the electronic structure generated in the last timestep as it pertains to the current geometry of the molecule. As a result the second order magnus expansion of the time evolution operator is based entirely on a singular electronic Hamiltonian resulting in the evolution of the amplitudes being given by,

$$A^p = U_{mag2}(\hat{H}_{elec,1}, \hat{H}_{elec,1}, \Delta t) A^0 \tag{3.11}$$

The preliminary propagation step ends with the updating of the coordinates and the momentum according to the Verlet algorithm,

$$X^p = X^0 + V^0 \Delta t + \frac{F^0_{Ehr}}{2M} (\Delta t)^2 \tag{3.12}$$

$$P^p = P^0 + F_{Ehr}\Delta t \tag{3.13}$$

The correcting propagation step occurs after the calculation of the electronic structure for the timestep. In order to accurately capture the evolution of the amplitudes throughout the timestep it is common to split the timestep into ten slices in order to properly calculate the Ehrenfest force. The final force vector used to correct the momentum is a sum of these slices.

$$F_{Ehr}^{Corr} = \sum_{s}^{10} F_{Ehr,s} \tag{3.14}$$

To begin iterating over the slices, temporary values are first established,

$$A^{temp} = U_{mag2}(\hat{H}_{elec,1}, \hat{H}_{elec,1}, \frac{\Delta t}{20})A^0 \tag{3.15}$$

$$E_{SCF}^{temp} = 0.95E_{SCF}^{p} + 0.05E_{SCF}^{0} \tag{3.16}$$

$$f^{temp} = 0.95f^{p} + 0.05f^{0} \tag{3.17}$$

$$C^{temp} = 0.95C^{p} + 0.05C^{0} \tag{3.18}$$

the rest of the slices are then calculated by adjusting the weights of the original and preliminary values,

$$\hat{H}_{elec,s} = \frac{s\hat{H}_{elec,2} + (10-s)\hat{H}_{elec,1}}{10} \tag{3.19}$$

$$A^s = U_{mag2}(\hat{H}_{elec,s}, \hat{H}_{elec,s}, \frac{\Delta t}{10})A^0 \tag{3.20}$$

$$E_{SCF}^{s} = (0.1s + 0.05)E_{SCF}^{p} + (0.95 - 0.1s)E_{SCF}^{0} \tag{3.21}$$

$$f^{temp} = (0.1s + 0.05)f^{p} + (0.95 - 0.1s)f^{0} \tag{3.22}$$

$$C^{temp} = (0.1s + 0.05)C^p + (0.95 - 0.1s)C^0 \tag{3.23}$$

Once all slices have been calculated and summed to find the correcting force vector, the momentum is then corrected,

$$P^1 = P^0 + F_{Ehr}^{Corr}\Delta t \tag{3.24}$$

The values that have been calculated at the end of the timestep (including the electronic structure forces) then become the starting point of the next timestep and used for the preliminary propagation step. This propagation loop continues until the final timestep has been reached.

3.2.3 Results Processing

Once a trajectory has been finished, the coordinates are scanned in order to find the first timestep at which a bond exceeds a length of 5 Bohr. These timesteps are then collated and organised into both specific bond and bond type. The plotting of the number of dissociation occurrences over the number of that bond type present as a function of time allows for the inspection of dissociation patterns and identification of weak bonds. The general sequence is to plot the dissociations of each bond type (eg. C-C vs C-F vs C-O) before later investigating individual bond environments (grouping all C-F bonds based on which carbon they are bonded to). Unless otherwise stated, all dissociation kinetics shown in this chapter use the dissociation definition and normalisation described in the caption of Figure 3.5.

3.3 Simulation of PFAS molecules as potential replacements of C_4F_8

C_4F_8 (specifically the cyclic isomer, octafluorocyclobutane) has been used in the plasma industry in order to etch silicon wafers, specifically in the deep reactive ion etching (DRIE) processes. The CF_x radicals formed by its dissociation allow

for the formation of a film that is both appropriately selective and capable of high anisotropic etching, causing deep but narrow etching sites. This is a huge advantage in a field whose advancements continually demand the plasma be able to etch smaller and smaller features onto the silicon wafer. However while successful, C_4F_8 is also a potent greenhouse gas, with a global warming potential (GWP) exceeding 8,000 and an atmospheric lifetime spanning thousands of years, prompting the industry to develop processes to limit the environmental effects. One such process is atomic layer etching (ALE), which offers precise, layer-by-layer material removal while reducing the volume of etchant gases required [103, 107]. However another solution would be to replace the C_4F_8 precursor with a molecule with a lower GWP but similar effectiveness in terms of silicon wafer etching. Such molecules (particularly those containing oxygen) are currently being investigated by experimental groups. It is from these investigations into potential replacements that the molecules simulated in this chapter are sourced with the aim of establishing trends and investigating whether the oxygen atom truly acts as an electrophore in practice along with any other trends observed in the dissociation pathways.

3.3.1 n-$C_4H_3F_7O$ & i-$C_4H_3F_7O$

The molecules 1,1,1,2,2,3,3-heptafluoro-3-methoxypropane (n-$C_4H_3F_7O$) and 1,1,1,2,3,3,3-heptafluoro-2-methoxypropane (i-$C_4H_3F_7O$) are two of three isomers of $C_4H_3F_7O$ that have been investigated as low GWP replacements for C_4F_8 and other standard plasma ingredients [106, 260]. The two molecules are positional ether isomers that differ by the position of the oxygen atom, with n-$C_4H_3F_7O$ having the oxygen atom at the end of the carbon chain, and i-$C_4H_3F_7O$ having the oxygen atom in the centre of the molecule.

The QEC calculations performed for i-$C_4H_3F_7O$ in Fig. 3.3 show that excitation to the triplet state after electron impact is heavily dominant as the two lowest cross-sections observed corresponding to triplet states, with the lowest triplet state having a higher cross section across all energy ranges considered. For the case of n-$C_4H_3F_7O$ in Fig. 3.4, the lowest lying cross-section corresponds

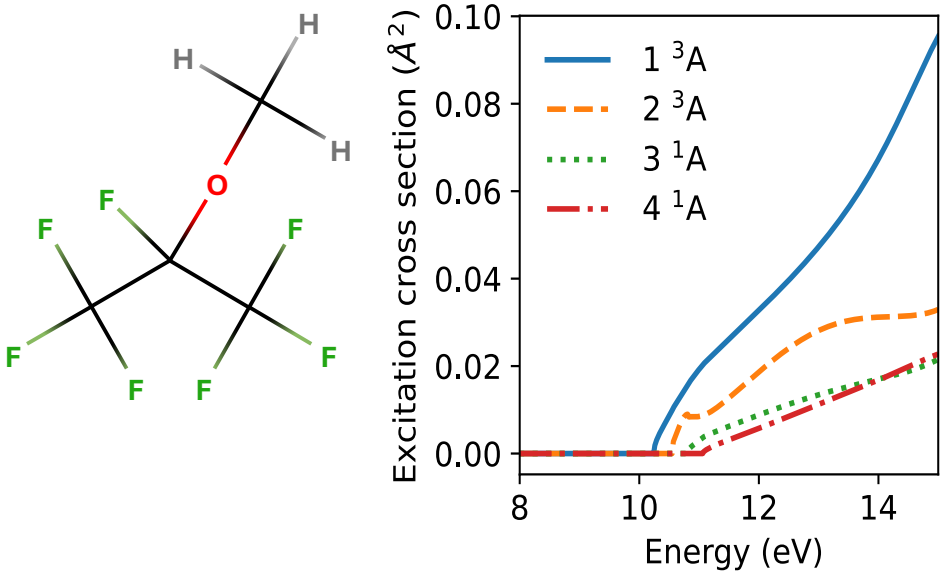

Figure 3.3: Excited state cross-sections generated via QEC for i-$C_4H_3F_7O$ after electron impact.

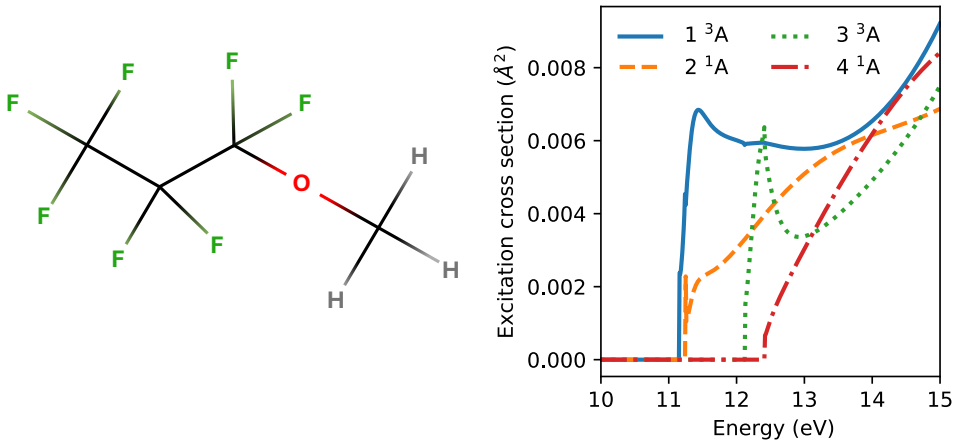

Figure 3.4: Excited state cross-sections generated via QEC for n-$C_4H_3F_7O$ after electron impact.

to a triplet state, with the second lowest being attributed to a singlet. However, at least up to 15 eV, the triplet states cross-sections are dominant across the energy range, with a significant gap between both triplet states. Knowing this it is possible to continue the two main assumptions of Section 2.7 and perform the dynamics only on the lowest triplet state. These fluoroether isomers are of interest due to the high number of fluorine bonds present in the molecules, suggesting that there is potential for a wide range of fluorine containing radicals to be formed upon dissociation after excitation via electron impact. The fact that the molecules contain an oxygen atom contributes to the low GWP and is also a point of interest due to the potential role of an electrophore that the atom could play in determining the dissociation pathways from the triplet state. Upon initial inspection of the molecules and application of the electrophore model, we can assume that the dissociation pathways undertaken after excitation to the triplet state via electron impact will differ, as the key difference between the two isomers is also the key aspect of determining dissociation, namely the position of the electrophore.

While the dissociation profiles of the two molecules are fairly similar, there still remain several differences. The dissociation yields of almost all bond types are higher in i-$C_4H_3F_7O$ (shown in Fig.3.5) when compared to n-$C_4H_3F_7O$ (shown in Fig.3.6) with the exception of the C-C bonds. In both isomers, the C-H bonds dissociate often and almost always within the first 25 fs, after which the dissociation kinetics plateau significantly. In n-$C_4H_3F_7O$, the C-H bonds have a dissociation yield of 27% increasing to 35% in the more symmetrical i-isomer. As multiple bonds breaking on the same atom is discouraged, in i-$C_4H_3F_7O$ roughly one C-H bond dissociates per trajectory. While the C-O and C-C bonds have high dissociation yields in both isomers (with them breaking approximately equally in n-$C_4H_3F_7O$ by 500 fs), the C-O bonds do break notably earlier in the propagation, suggesting that the localisation of the triplet state is in fact around the oxygen atom and therefore its dissociative character affects oxygen containing bonds first before spreading throughout the molecule. The dissociation yield of the C-O bonds also increases to 43% in the i-isomer compared to 35% in the n-

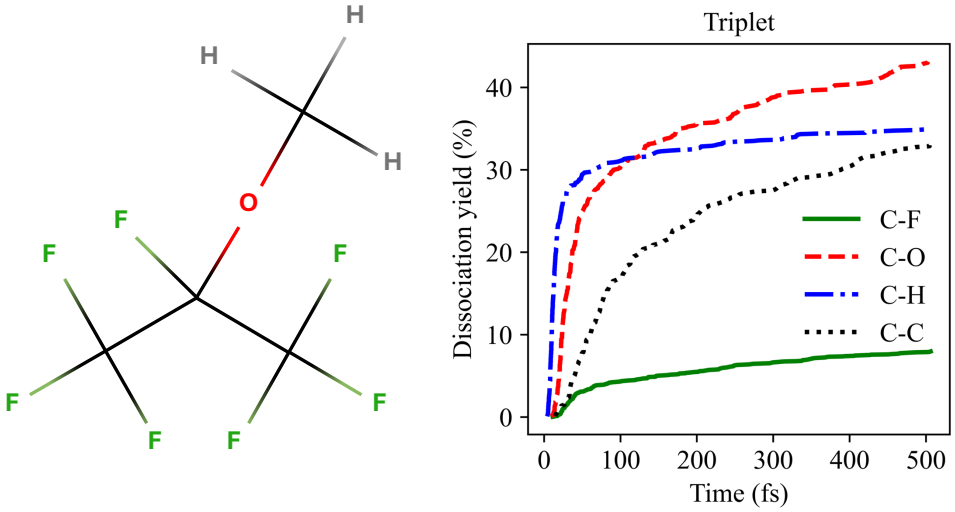

Figure 3.5: Dissociation kinetics of i-$C_4H_3F_7O$ for each bond type, obtained from 400 independent trajectories propagated on the lowest triplet potential energy surface at 5000 K. A dissociation event is defined as the first timestep at which a bond length exceeds 5 Bohr. Kinetics are normalised by the total number of bonds of each type present in the molecule.

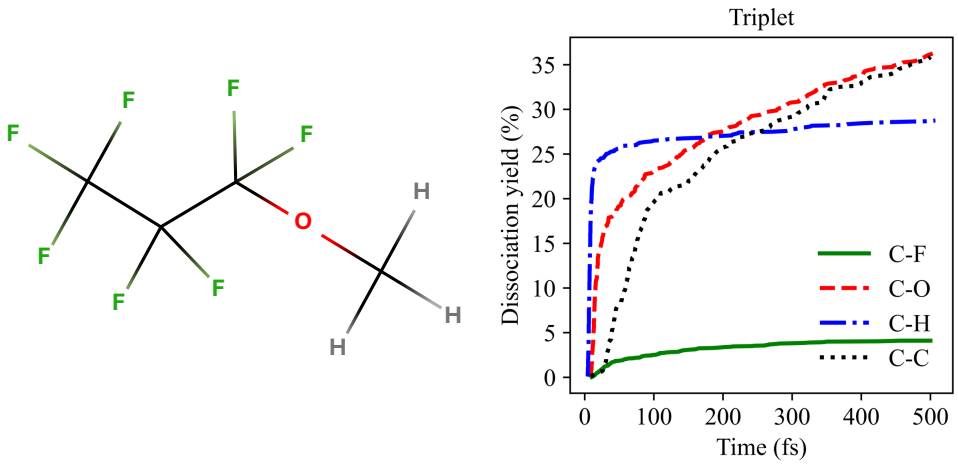

Figure 3.6: Dissociation kinetics of n-$C_4H_3F_7O$ for each bond type over 400 triple state trajectories at 5000 K. A dissociation event is defined as the first timestep at which a bond length exceeds 5 Bohr. Kinetics are normalised by the total number of bonds of each type present in the molecule.

isomer. The C-F bonds are the bonds with the lowest dissociation yield in both molecules, though it does double from 4.1% in n-$C_4H_3F_7O$ to 8% in i-$C_4H_3F_7O$. The overall increase in the number of dissociations can be attributed to the central electrophore in i-$C_4H_3F_7O$ having more nearby bonds to affect.

3.3.1.1 C-O bonds

Not only do the overall dissociation yields of the C-O bonds in each molecule differ, there are also differences in the individual dissociation yield of each C-O bond within both molecules. Fig. 3.7 shows that the dissociation of the C#2-O bond accounts for over 60% of the C-O dissociations in i-$C_4H_3F_7O$, with a dissociation yield of 55% where as for n-$C_4H_3F_7O$ (see Fig. 3.8) the two C-O bonds in the molecule dissociate approximately equally with dissociation yields of 35%. This difference can be explained via the central oxygen changing the resulting radical created following the cleavage of the C#2-O bond, as having the radical in the centre of the carbon chain is more stable than the radical

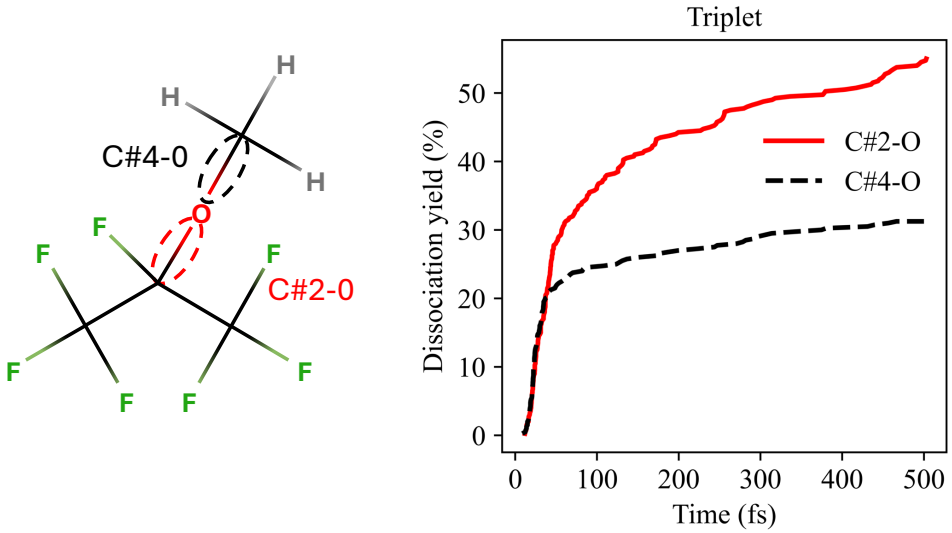

Figure 3.7: Dissociation kinetics of i-$C_4H_3F_7O$ for each C-O environment over 400 triple state trajectories at 5000 K. A dissociation event is defined as the first timestep at which a bond length exceeds 5 Bohr. Kinetics are normalised by the total number of bonds of each type present in the molecule.

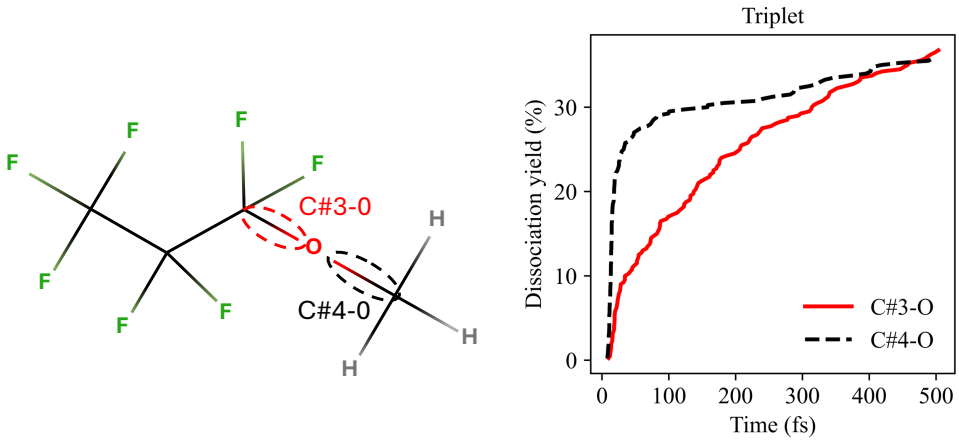

Figure 3.8: Dissociation kinetics of n-$C_4H_3F_7O$ for each C-O environment over 400 triple state trajectories at 5000 K. A dissociation event is defined as the first timestep at which a bond length exceeds 5 Bohr. Kinetics are normalised by the total number of bonds of each type present in the molecule.

forming on the terminal carbon, as is the case after the C#3-O bond dissociates in the n-isomer. In fact, the dissociations of the C#4-O bonds are similar in both molecules with dissociations yields of 31% and 33% for i-$C_4H_3F_7O$ and n-$C_4H_3F_7O$ respectively. The kinetics of the C#4-O bond are also similar with the majority of bond dissociation events occurring within the beginning of the propagation. This is due to the fact that in both molecules, the dissociation of the C#4-O bond is competing with the C-H bonds which dissociate rapidly. As it is discouraged for a single atom to experience multiple dissociation events within the same trajectory, the C-H bonds act as a limiter for the dissociation of the C#4 bond in both molecules.

3.3.1.2 C-C bonds

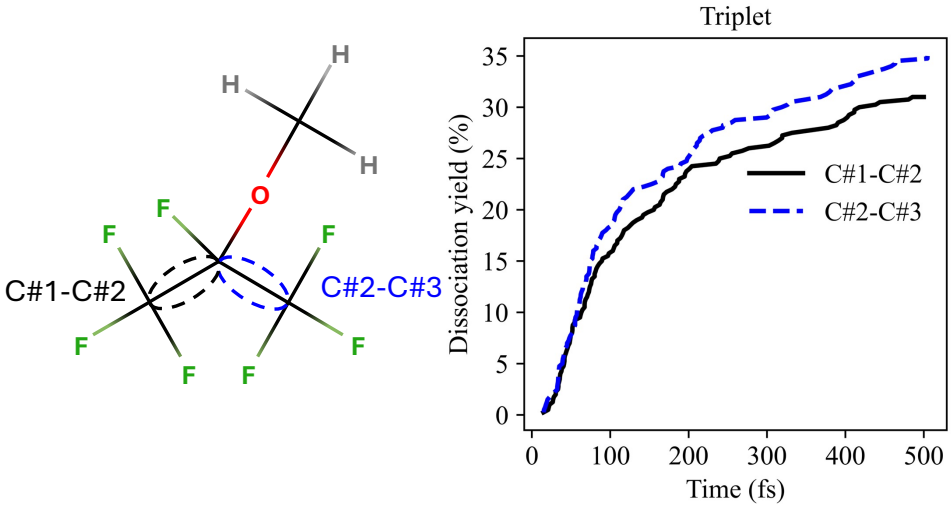

Figure 3.9: Dissociation kinetics of i-$C_4H_3F_7O$ for each C-C environment over 400 triple state trajectories at 5000 K. A dissociation event is defined as the first timestep at which a bond length exceeds 5 Bohr. Kinetics are normalised by the total number of bonds of each type present in the molecule.

The symmetrical isomer i-$C_4H_3F_7O$ predictably shows approximately equal dissociation of the two C-C bonds in Fig. 3.9. There is no difference between

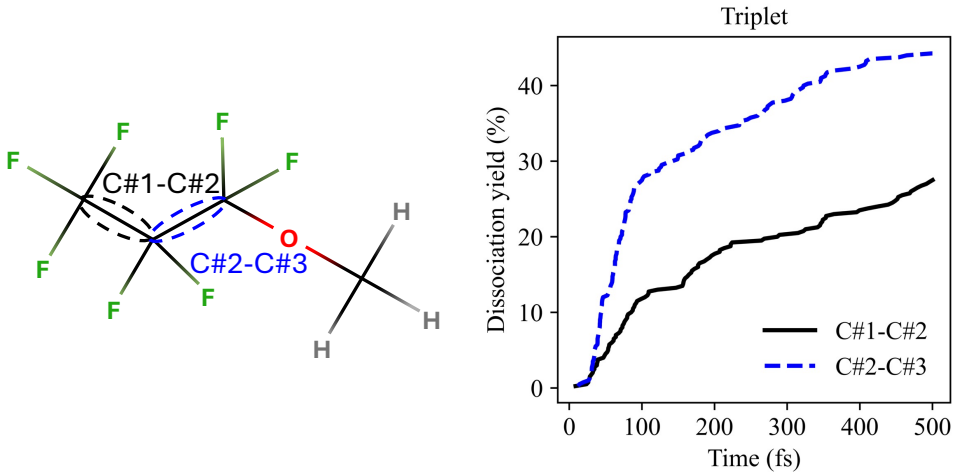

Figure 3.10: Dissociation kinetics of n-$C_4H_3F_7O$ for each C-C environment over 400 triple state trajectories at 5000 K. A dissociation event is defined as the first timestep at which a bond length exceeds 5 Bohr. Kinetics are normalised by the total number of bonds of each type present in the molecule.

the dissociation of the two bonds during the initial propagation and at 500 fs the C#2-C#3 bond represents 53% of the C-C dissociations in i-$C_4H_3F_7O$. The n-$C_4H_3F_7O$ molecule presents a more interesting case as there is a significant difference between the dissociation yields of the two C-C bonds shown in Fig. 3.10. The C#2-C#3 bond accounts for over 60% of the dissociations in the n-isomer. This makes sense in accordance with the electrophore model as the triplet state excitation is localised around the electrophore oxygen atom. This results in its dissociative character more greatly affecting the bonds closest to the oxygen atom and also causing the dissociations to occur more rapidly with the C#2-C#3 bond experiencing more dissociations within 100 fs than the C#1-C#2 bond dissociates across the whole propagation of 500 fs.

3.3.1.3 C-F bonds

Likewise the dissociation yields of the individual C-F environments in both molecules can be predicted via their proximity to the oxygen atom. For i-$C_4H_3F_7O$,

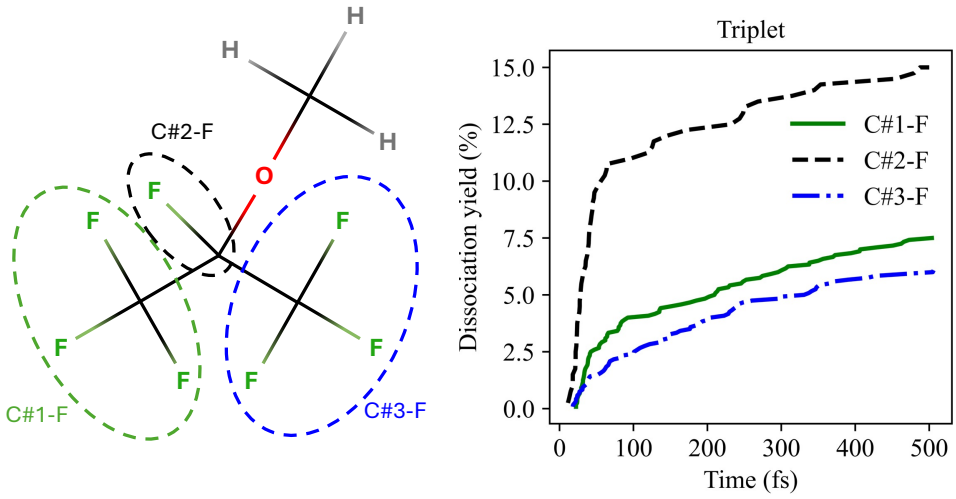

Figure 3.11: Dissociation kinetics of i-$C_4H_3F_7O$ for each C-F environment over 400 triplet state trajectories at 5000 K. A dissociation event is defined as the first timestep at which a bond length exceeds 5 Bohr. Kinetics are normalised by the total number of bonds of each type present in the molecule.

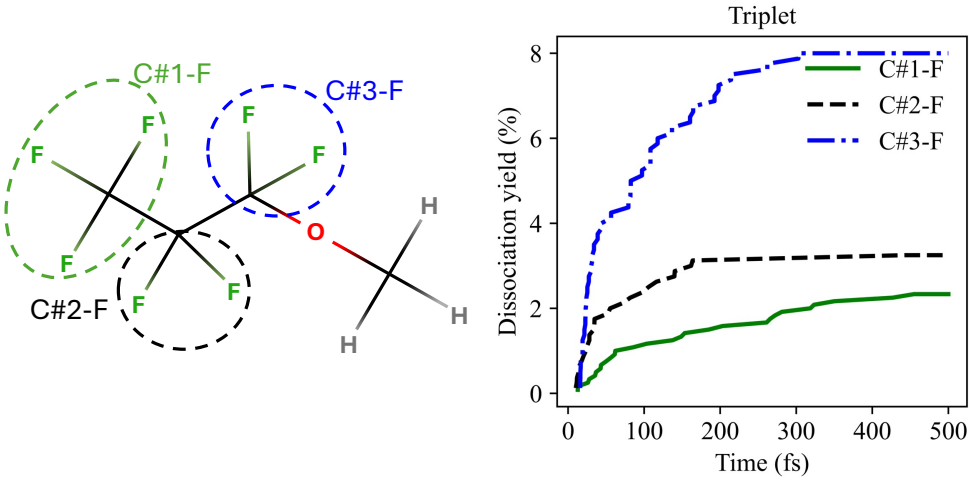

Figure 3.12: Dissociation kinetics of n-$C_4H_3F_7O$ for each C-F environment over 400 triplet state trajectories at 5000 K. A dissociation event is defined as the first timestep at which a bond length exceeds 5 Bohr. Kinetics are normalised by the total number of bonds of each type present in the molecule.

Fig. 3.11 shows that the fluorine atom bonded to the C#2 carbon is very close to the electrophore oxygen atom and therefore the environment has the highest dissociation yield, with a relatively high yield of 15%, with the single bond representing 27% of all C-F dissociations in i-$C_4H_3F_7O$. However the other two environments, C#1-F and C#3-F are not symmetrical despite appearing so in the molecule cartoon, due to an artefact of the simulations. As each trajectory begins with the optimised singlet state geometry, the molecule begins from a 'frozen' state, contrary to the real world where the bonds surrounding C#2 would be constantly rotating. Table 3.1 shows that the C#1-F group has consistently less distance between the fluorines and the methyl group. This steric factor influences dissociations causing the C#1-F environment to dissociate slightly more than the C#3-F. This theory is further supported by the fact that the fluorine bonded C#1 with the shortest difference to the hydrogens has the highest dissociation yield of all C-F bonds barring the C#2-F fluorine. As the C-F bond is rather strong in the triplet state, the dissociation yield of each fluorine in the C#1-F and C#3-F is not that large, with yields of 7.5% and 6% respectively.

Table 3.1: Distances from fluorine atoms to hydrogen atoms for fluorines attached to C#1 and C#3 (in Bohr).

Fluorine Group	**Distance 1**	**Distance 2**	**Distance 3**	**Average**
F attached to C#1	6.13	6.81	10.07	7.67
F attached to C#3	9.79	9.47	10.80	10.02

The n-$C_4H_3F_7O$ isomer has a much simpler profile in terms of C-F dissociations in Fig. 3.12. The order for the environments is determined entirely by the proximity to the electrophore. The C#3-F environment on the carbon bonded to the oxygen atom accounts for 52% of all C-F dissociations. It is also important to take into account not only the number of dissociations in a vacuum but also within the context of the dissociation pathways. The dissociation of a bond can heavily discourage the breaking of another bond involving those same atoms. Within this perspective, it is possible to further state the power of proximity to the electrophore on the dissociation of neighbouring bonds as the C-F environments

that dissociate the most are bonded to the carbons who already experience a higher number of dissociations due to more dissociative C-C and C-O bonds. In the case of i-$C_4H_3F_7O$, the C#2-F environment has a much higher dissociation yield while bonded to the central carbon which can experience either C-C bond breaking (as opposed to the other C-F environments only competing with one C-C bond each) as well as the C#2-O bond which has the highest dissociation yield in the molecule.

3.3.1.4 Temperature dependence

The temperature of simulations being 5000 K is vital for the molecules to dissociate rapidly enough to generate a sufficiently populated dataset to allow discussion of dissociation pathways. However this temperature is not reasonably suited to be a direct comparison to experimental temperatures. In order to investigate whether the trends found in the 5000 K simulations continue, it is possible to find the temperature dependence of the molecules via additional simulations at 4000 and 3000 K for which the dissociation yields are shown in Fig. 3.13 and 3.14 for i-$C_4H_3F_7O$ and n-$C_4H_3F_7O$ respectively. As an increase in temperature greatly increases the initial kinetic energy of the molecules, it is unsurprising that the 5000 K simulations resulted in the highest number of dissociations. This trend continues with 4000 K dissociating more than the 3000 K trajectories, with a few exceptions. In n-$C_4H_3F_7O$, there is an increased number of C-H dissociations compared to at 3000 K. Fig. 3.8 seems to confirm that the initial dissociations of the C#4-O bond are competing with the C-H bonds and a reduction of that bond breaking via a decrease in temperature allows for more C-H dissociations to be the first bond broken on C#4. The same effect can be seen in i-$C_4H_3F_7O$ as the reduction in C-O and C-C bonds allow for a greater number of dissociations of the C-H and C-F bonds at 3000 K than 4000 K. In both molecules, the rapid initial dissociation character of the C-H and C-O bonds is preserved, suggesting that the localisation around the oxygen atom is not temperature dependent and is in fact a product of being an electrophore.

There are not only shifts in the dissociation yields at different temperatures,

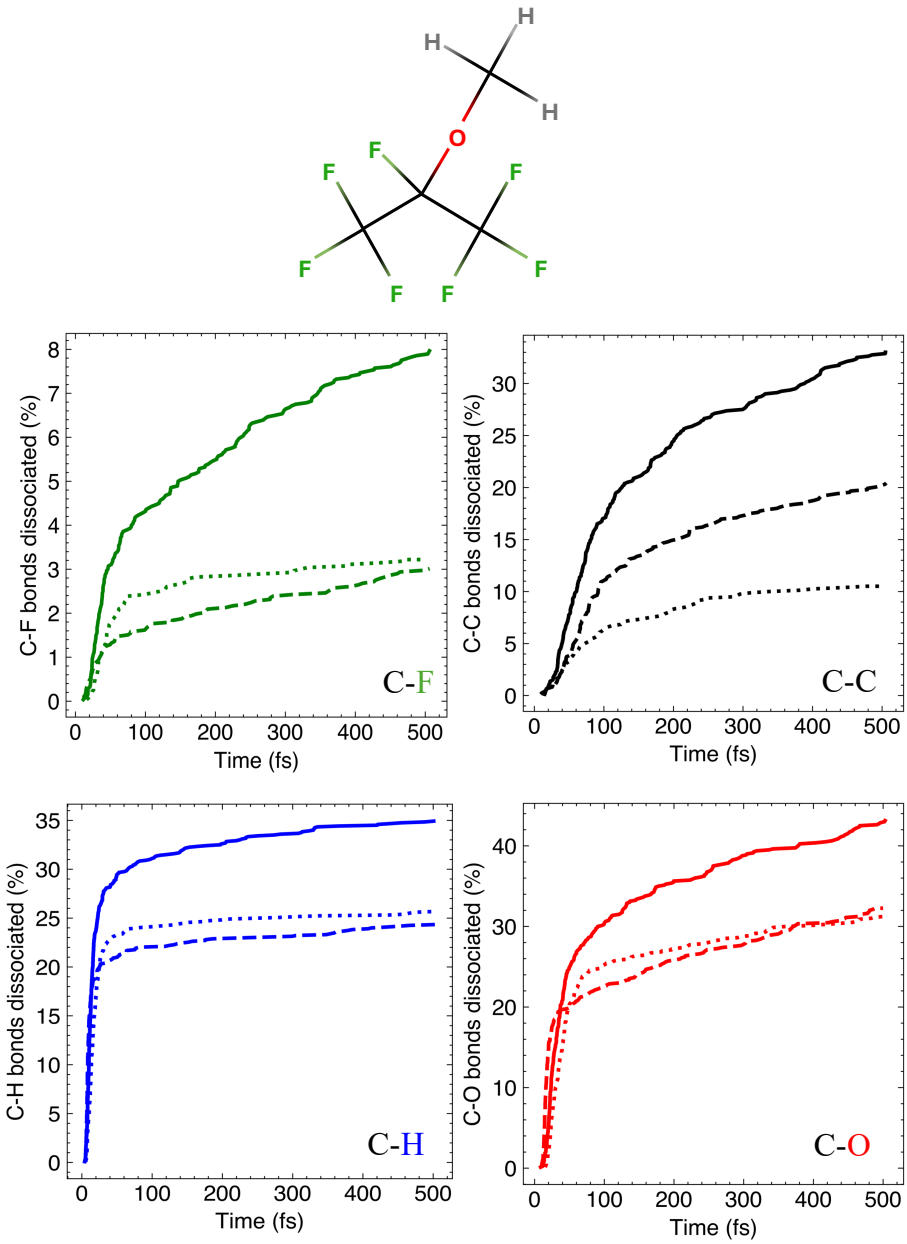

Figure 3.13: The temperature dependence of the dissociation kinetic for C-F (top-left), C-C (top-right), C-H (bottom-left), C-O (bottom-right) in i-$C_4H_3F_7O$. Three temperatures, 3000 K (dotted line), 4000 K (dashed line) and 5000 K (solid line) are compared.

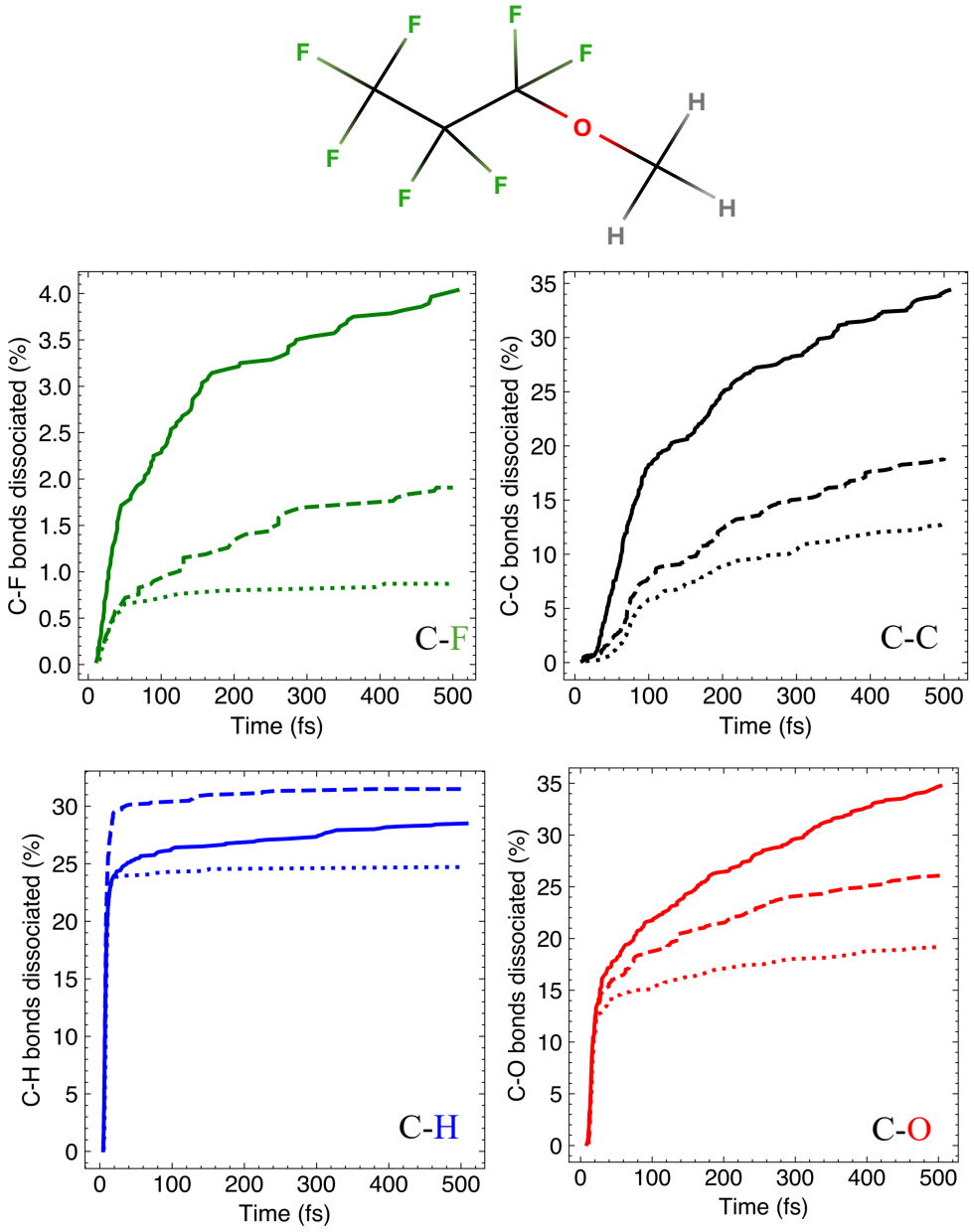

Figure 3.14: The temperature dependence of the dissociation kinetics for C-F (top-left), C-C (top-right), C-H (bottom-left), C-O (bottom-right) in n-$C_4H_3F_7O$. Three temperatures, 3000 K (dotted line), 4000 K (dashed line) and 5000 K (solid line) are compared.

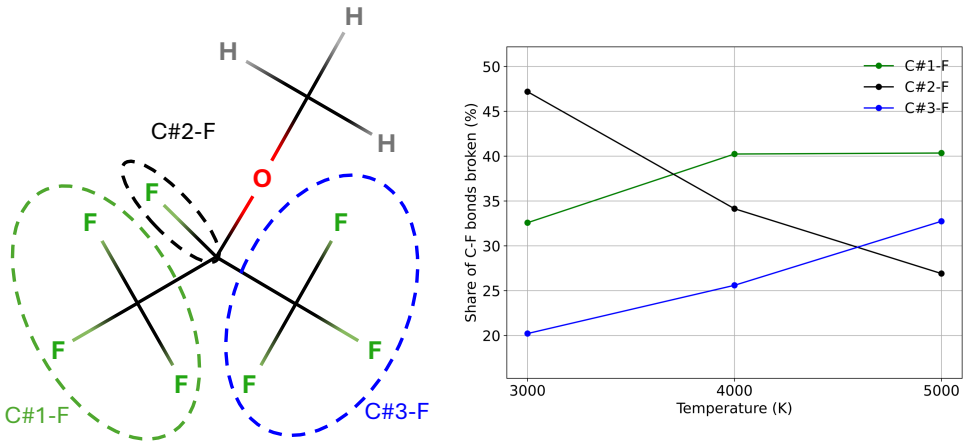

Figure 3.15: Temperature dependence of the dissociation kinetics of different C-F environments in the i-$C_4H_3F_7O$ molecule. The plot shows the proportion of total C-F dissociations attributed to each C-F environment.

there are also changes within the bond types, with each individual environment accounting for a different proportion of dissociations. For the dissociated C-F bonds in Fig. 3.15, the methyl group steric factor discussed earlier causes the C#1-F group to dissociate more than the C#3-F group at all temperatures. Due to the higher number of fluorines in each CF_3 group, they have a higher proportion of C-F dissociations than the C#2-F fluorine at 5000 K. However as the temperature decreases it becomes harder for a C-F bond to dissociate and so the C#2-F singular bond closest to the electrophore increases to 47% of all C-F bond dissociations,

The dissociations in the C-O environments in i-$C_4H_3F_7O$ also have shifting proportions across the different temperatures in Fig. 3.16. While the C-O bonds do move to dissociating more evenly at 4000 K, the difference in dissociation shifts back to almost approximately the same propagation seen at 5000 K when the temperature is further decreased to 3000 K. In fact the dissociation yield of the C#2-O bond increases when the temperature decreases from 4000 K to 3000 K. The increase in the proportion of C#4-O bonds at 4000 K can be seen due to the dissociation yield of the C-H decreasing by over 10% which at 5000 K was acting as a limiting factor of C#4-O dissociation. This increase could

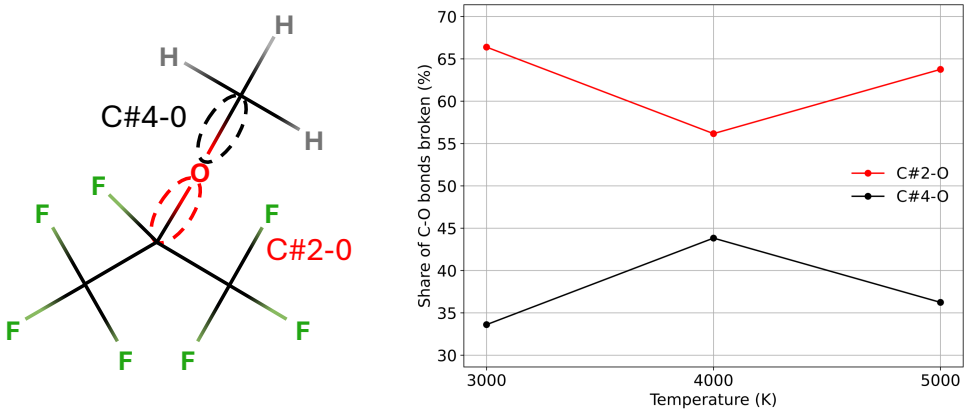

Figure 3.16: Temperature dependence of the dissociation kinetics of different C-O environments in the i-$C_4H_3F_7O$ molecule. The plot shows the proportion of total C-O dissociations attributed to each C-O environment.

happen due to the fact that there are significantly decreased numbers of C-C and C-F dissociations meaning there is more opportunity for the C#2-O bond to dissociate.

Fig. 3.17 shows the proportion of dissociated C-F environments for n-$C_4H_3F_7O$. The share of dissociated C-F bonds being C#3-F is roughly maintained across all temperatures within the range of 50-55%, and the general environment order is also identical. In fact the share of C#2-F dissociations increases to 42% as the temperature decreases along with the significant decrease of C#1-F dissociations to only 10%. As the dissociation yield of C-F bonds decreases to only 1% at 3000 K, and the furthest C-F environment from the electrophore dissociates only twice across 400 trajectories, the dissociation of the C-F bonds at low temperatures appears to be determined entirely by the dissociative localisation of the electrophore.

Similarly as in the case of i-$C_4H_3F_7O$, the change in temperature affects which C-O bond breaks more often shown in Fig. 3.18. At 5000 K the two bonds break approximately evenly but as the temperature decreases, the C#4-O bond accounts for more and more C-O dissociations, likely due to the lower number of dissociations of the C-H bonds that were previously preventing further disso-

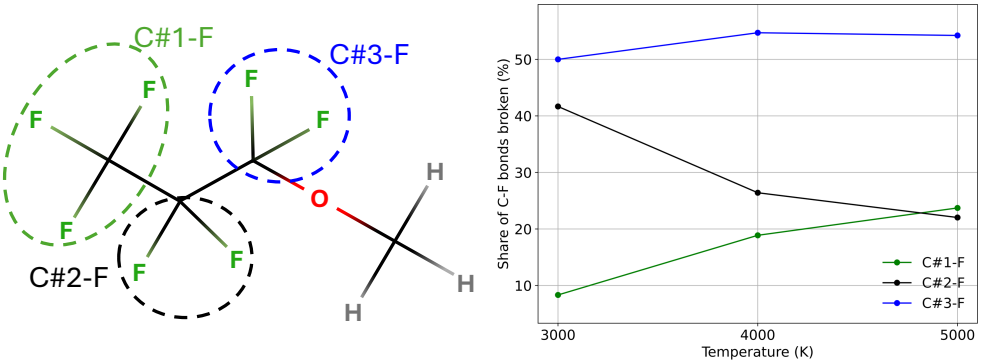

Figure 3.17: Temperature dependence of the dissociation kinetics for different C-F environments in the n-$C_4H_3F_7O$ molecule. The plot shows the proportion of total C-F dissociations attributed to each C-F environment.

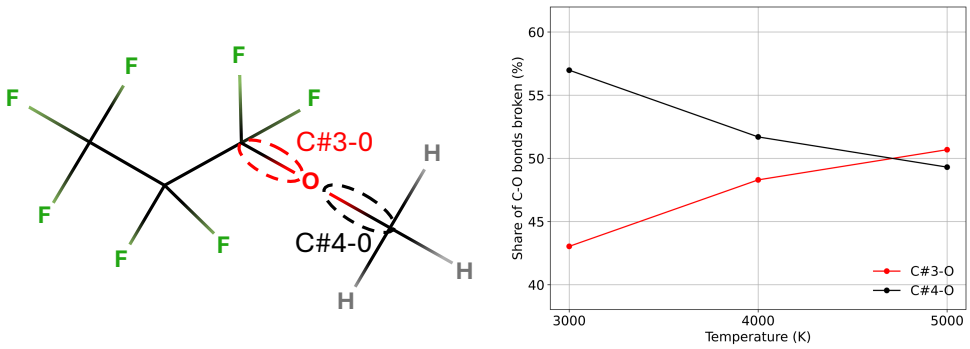

Figure 3.18: Temperature dependence of the dissociation kinetics for different C-O environments in the n-$C_4H_3F_7O$ molecule. The plot shows the number of broken C-O bonds in each environment as a percentage of all C-O bonds broken at that temperature.

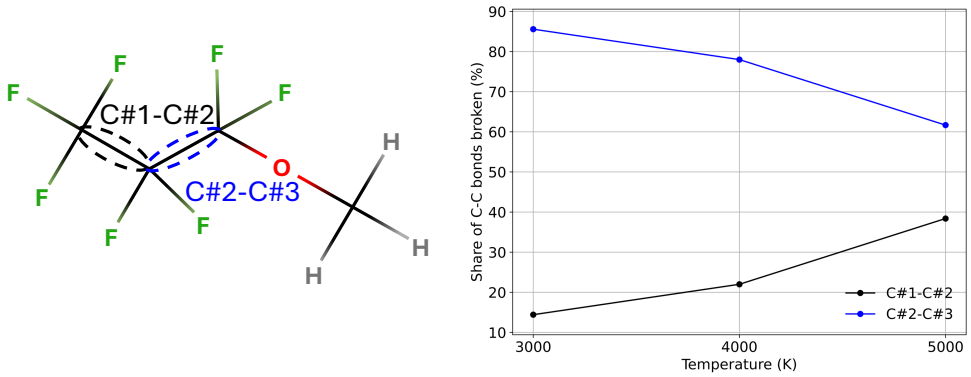

Figure 3.19: Temperature dependence of the dissociation kinetics for different C-C environments in the n-$C_4H_3F_7O$ molecule. The plot shows the proportion of total C-C dissociations attributed to each C-C environment.

ciations of bonds including the C#4 carbon. Even at the lowest temperature of 3000 K this difference is not large with the C#4-O accounting for 56% of the C-O dissociations. This is not the case for the C-C bonds in Fig. 3.19 however as the reduction of temperature dramatically shifts the proportions to the C#2-C#3 bond accounting for almost 90% of the C-C dissociations at 3000 K. This is another example of how the effect of the electrophore on the dissociation pathways of the molecule becomes more visible as the temperature of the simulations are lowered.

3.3.1.5 Comparison to singlet state dissociations

Fig. 3.20 and Fig. 3.21 analyse both the frequency by which each bond type dissociates first in a trajectory, and the average time for this first dissociation event. When investigating the first bond broken in each trajectory, it is clear to see the disparity in the first dissociation times between the singlet and triplet state. For the triplet state, all bond types have an average first break time at or below 25 fs. In contrast the quickest bond type breaking first in the singlet state for both molecules is the C-H bond with average times of 86.7 fs in i-$C_4H_3F_7O$ and 32.2 fs in n-$C_4H_3F_7O$, with all other bond types having an average time of over 150 fs.

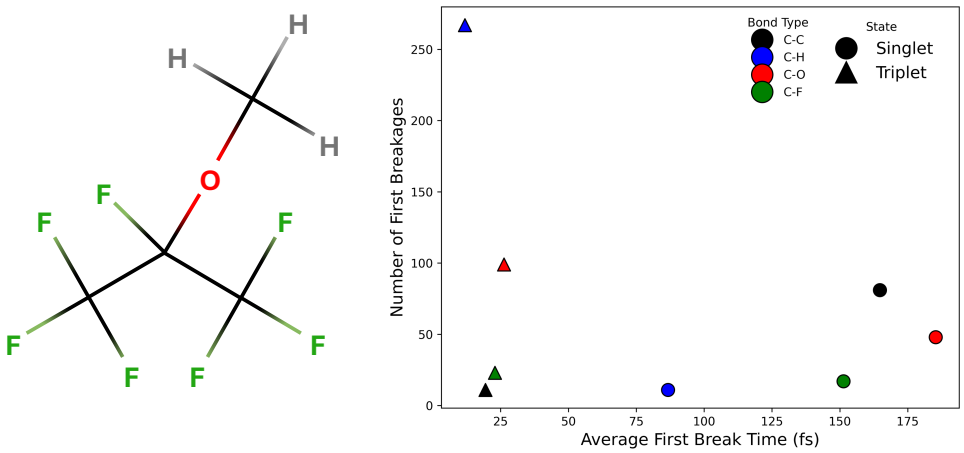

Figure 3.20: Count of each bond type breaking first in a trajectory against the average time of that first breakage in the i-$C_4H_3F_7O$ molecule for both the singlet (circles) and triplet state (triangle) trajectories.

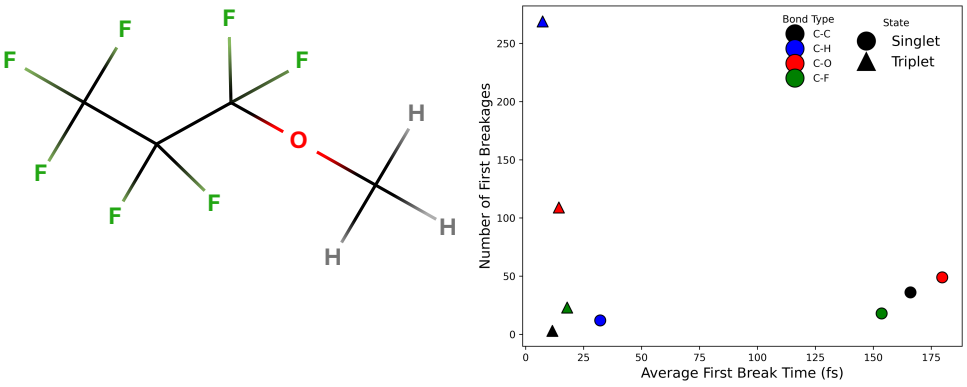

Figure 3.21: Count of each bond type breaking first in a trajectory against the average time of that first breakage in the n-$C_4H_3F_7O$ molecule for both the singlet (circles) and triplet state (triangle) trajectories.

Out of the 400 trajectories run for i-$C_4H_3F_7O$ in the singlet state, only 157 trajectories had any dissociations leading to an average number of dissociations of 0.94, with only 104 trajectories having a second dissociation event. Every single trajectory in the triplet state had at least one dissociation, with an average number of bonds broken per trajectory of 3.12, and 365 out of 400 trajectories having more than one bond broken. In the triplet state, the C-H bonds break readily and rapidly to the extent that other bonds are unlikely to break first, therefore it is important to note that the only other bond type that has meaningful number of dissociations first in the trajectory is the C-O bonds, with 99 trajectories having a C-O bond break first. The reason for this being that the oxygen atom is the electrophore that localises the triplet state causing it to have an increased number of initial dissociations before the dissociative character spreads to the neighbouring bonds.

The n-isomer also has very similar trends in the singlet state, with only 115 singlet state trajectories having any dissociation events, and only 73 of those having second dissociation events. There was once again a much lower average number of bonds broken per trajectory, 0.6 for the singlet state compared to 2.6 in the triplet state. Even counting only the trajectories that did dissociate gives a lower average of 2.1 dissociation events per trajectory. In the triplet state, again the C-O bond is the most broken first in a trajectory barring the C-H bonds, further supporting the electrophore localisation theory.

The dissociation yields for each bond type from the singlet state MD trajectories for the i-$C_4H_3F_7O$ molecule are presented in Fig. 3.22. The most notable difference between the dissociation kinetics of the i-$C_4H_3F_7O$ molecule on the singlet and the triplet states is the dissociation of the C-H bond. In the triplet state, the C-H bonds have a dissociation yield of 35%, which considering the molecule contains a CH_3 group, means approximately one C-H bond dissociates per trajectory. In the singlet state, the C-H bonds have a dissociation yield of only 4.3%, again suggesting that the C-H bond is much weaker within the triplet state. The C-C and the C-O bonds are bond types with relatively high dissociation yields in both states. The C-O bonds have a dissociation yield of 43% in

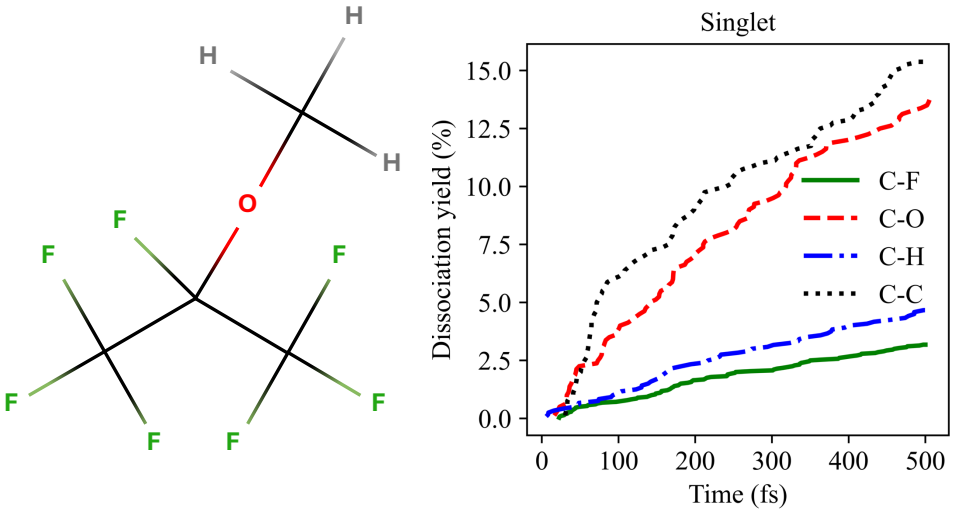

Figure 3.22: Dissociation kinetics of i-$C_4H_3F_7O$ for each bond type over 400 singlet state trajectories at 5000 K

the triplet state and 13.8% in the singlet state. The C-C bonds have the largest dissociation yield in the singlet state at 15.3% under half of the yield of 33% in the triplet state. In both states, the lowest dissociation yield belongs to the C-F bonds, due to their bond strength.

The dissociation yields of the n-$C_4H_3F_7O$ molecule greatly decrease when the dissociation is simulated in its singlet state with the results shown in Fig. 3.23. With the exception of the C-H bonds, the bond order is mostly preserved albeit with there being a relatively much larger gap between the dissociation yields of the C-O and the C-C bonds. The C-F dissociation yield decreases by more than half from 5% to only 2%, while the bonds with the highest dissociation yield are the C-O bonds at 10%, which is a 3.5x reduction from the dissociation yield found in the triplet state.

Interestingly while all the dissociation yields for both molecules increase when in the triplet state, there is also a change in the kinetics, with the dissociations being less linear due to the dissociative character of the triplet state. With the exception of the C-H bonds, the bond type most affectd by this change is the C-O bonds that have the sharpest initial breaking, due to the role played by the

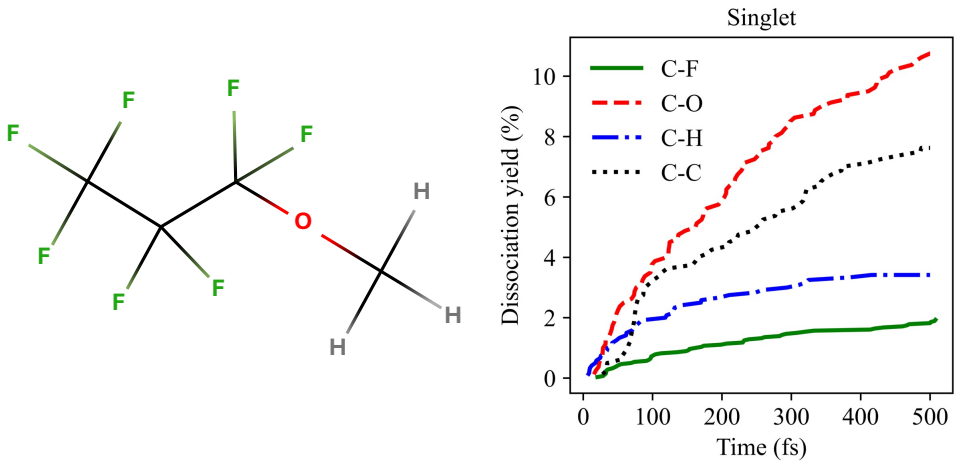

Figure 3.23: Dissociation kinetics of n-$C_4H_3F_7O$ for each bond type over 400 singlet state trajectories at 5000 K. A dissociation event is defined as the first timestep at which a bond length exceeds 5 Bohr. Kinetics are normalised by the total number of bonds of each type present in the molecule.

oxygen atom as an electrophore.

While the overall dissociation yields presented for the C-O bond type in Figs. 3.22 & 3.23 are correct in regards to the trajectories, Figs. 3.24 & 3.25 show that perhaps they are not the most faithful average of the two bonds present in each molecule. In the singlet state, even when the simulated temperature is as high as 5000 K, the C#4-O bonds are truly dominant in both molecules accounting for over 85% of the C-O dissociations. The dissociation yields are also very high considering the triplet state with dissociation yields of 25% and 20% for i-$C_4H_3F_7O$ and n-$C_4H_3F_7O$ respectively. This is contrary to the dissociations in the triplet state where the C-O bonds dissociate evenly in the n-isomer and where the C#2-O bond breaks more often in the i-isomer. A partial explanation for this could be the almost complete absence of C-H dissociations in the singlet state removing what appears to be the main limiting factor of the C#4-O bond. In the singlet state, the oxygen is not acting as an electrophore and so the molecule does not experience any localisation and as such the C-O bonds could simply dissociate based on bond strength. The C#4-O bond can then be seen as favoured as the

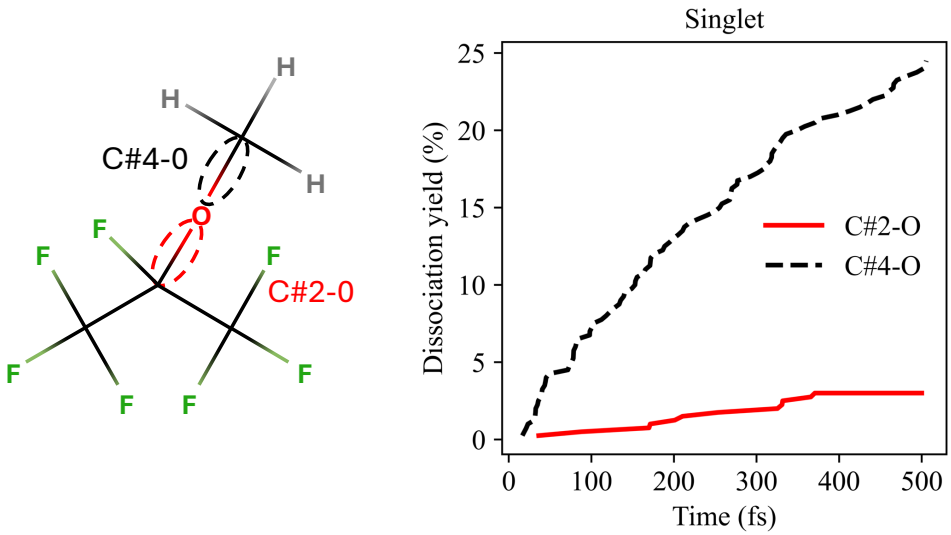

Figure 3.24: Dissociation kinetics of i-$C_4H_3F_7O$ for each C-O environment over 400 singlet state trajectories at 5000 K. A dissociation event is defined as the first timestep at which a bond length exceeds 5 Bohr. Kinetics are normalised by the total number of bonds of each type present in the molecule.

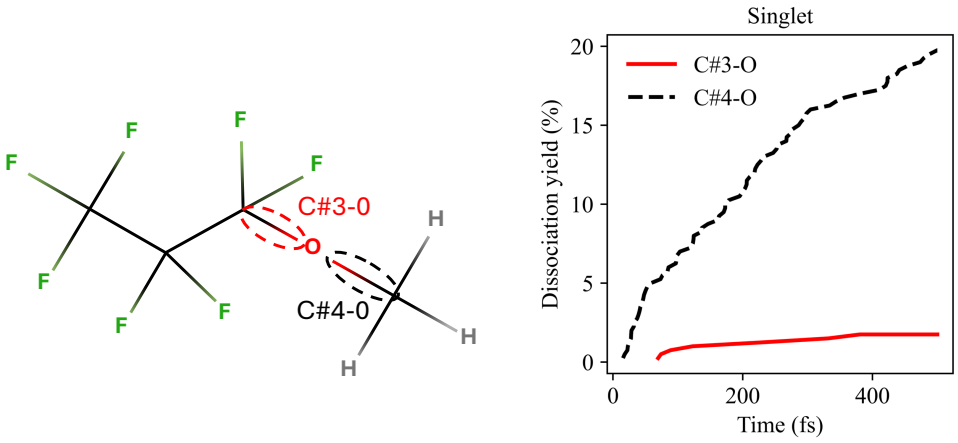

Figure 3.25: Dissociation kinetics of n-$C_4H_3F_7O$ for each C-O environment over 400 singlet state trajectories at 5000 K. A dissociation event is defined as the first timestep at which a bond length exceeds 5 Bohr. Kinetics are normalised by the total number of bonds of each type present in the molecule.

perfluoro group is extremely electron withdrawing which conversely weakens the C#4-O bond. The C#4-O dissociation is also favoured thermodynamically as the C_3F_7O radical formed is significantly more stable than the CH_3O radical formed via the dissociation of the C#2-O bond due to the negative hyper conjugation [261] with the oxygen's lone pairs, allowing for the delocalisation of the electrons across the many available σ^* orbitals of the fluorine atoms.

3.3.1.6 Comparison to experiment

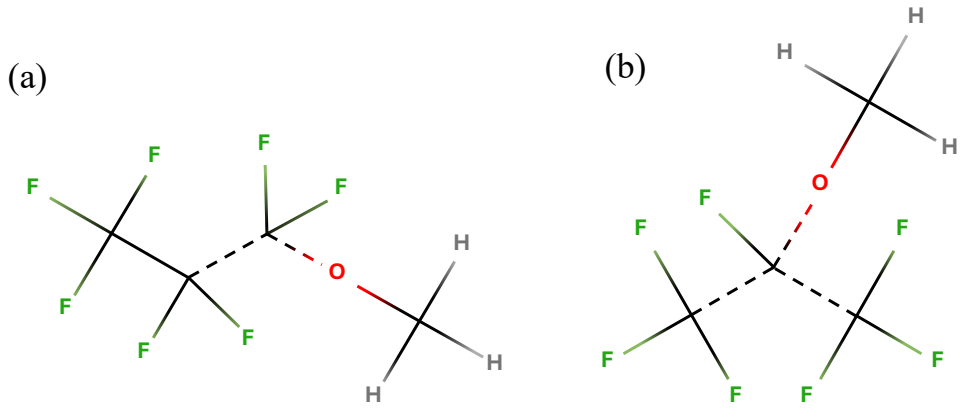

Figure 3.26: Structures of n-$C_4H_3F_7O$ and i-$C_4H_3F_7O$ shown in Figure 2 of reference [106] with bonds highlighted to be prone to dissociation represented by dashed lines.

Both of these molecules were investigated as potential plasma ingredients and within this experimental study, mass spectrometry was used to identify the weak bonds for this molecule in plasma [106]. While neutral dissociation is only a single process of many that occur within a plasma reactor, this data can be used to support the dissociation pathways found in the MD simulations performed as well as the overall assumption that neutral dissociation in plasma after electron impact is mainly via the triplet state. For instance, the mass spectrometry has a large hydrogen peak, which can be explained via the results of the triplet state MD simulations showing that the C-H bond is very weak in the triplet state, but barely dissociates in the singlet state. Fig. 3.26 shows the weak bonds that

were highlighted in the paper as dashed lines. It is also interesting to note that while a small CH_3 peak was shown in the data, only the C-O bond to the carbon chain has been highlighted as dissociative. This is further evidence of triplet state dominated dissociations as in the singlet state, the C-O bond to the methyl group was heavily dominant; only in a triplet state can the C-O bond to the carbon chain be shown to be dissociative.

The fragments found at the end of the simulations also matches well with the findings of the experimental paper. In both spectra there is a significant highlighted CF_3 peak which was the second most common radical produced in the simulations of i-$C_4H_3F_7O$ for multiple temperatures (after only atomic hydrogen) and the fifth most common for n-$C_4H_3F_7O$. The fact the C-C bonds are highlighted differently in Fig. 3.26 can also be explained by the electrophore model as the central electrophore leads to dissociation of both C-C bonds and overall more bond dissociations due to being closer to more bonds, a phenomenon also noted by the authors of the experimental paper.

3.3.2 $C_4H_2F_7OH$

2,2,3,3,4,4,4-heptafluoro-1-butanol ($C_4H_2F_7OH$) is the final of the $C_4H_3F_7O$ isomers that were considered as a potential replacement for C_4F_8 [260]. This isomer is of interest because the electrophore oxygen atom in this isomer is engaged in a different functional group, an alcohol. Whether the oxygen continues to be an electrophore when not part of a C-O-C group and if so, whether the effects of the electrophore change can be investigated by the dissociation pathways found through the MD simulations. As with the other oxygen containing atoms, the cross-section that appears at the lowest energy range considered within Fig. 3.27 corresponds to a triplet state, with a sufficient energy gap until the next cross-section appears. While this second lowest state is a singlet state, the triplet states are clearly dominant until at least 15 eV, meaning that our assumption of performing standard MD on the lowest triplet state only remains valid for this molecule.

The most notable and unique aspect of the dissociation yields of the alcohol

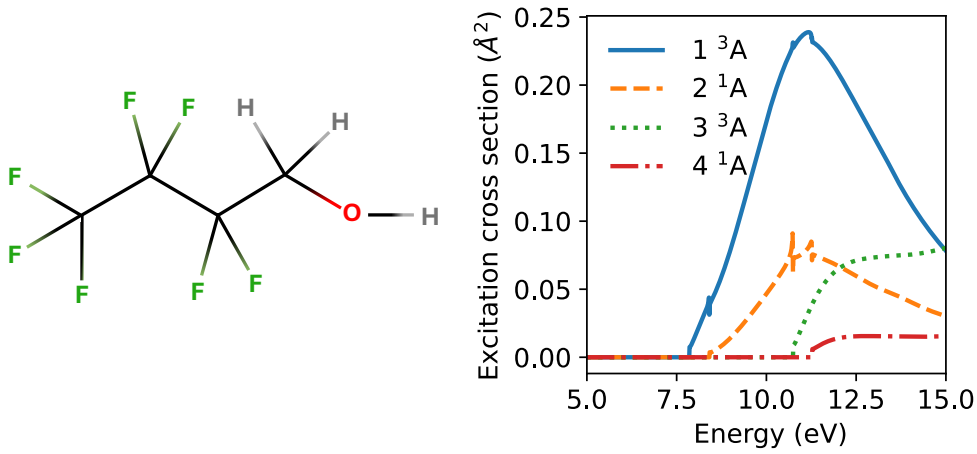

Figure 3.27: Excited state cross-sections generated via QEC for $C_4H_2F_7OH$ after electron impact.

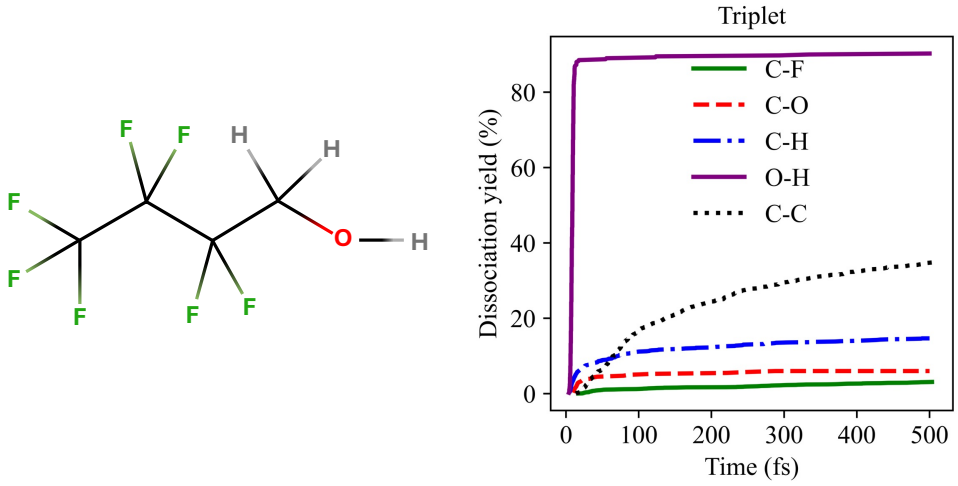

Figure 3.28: Dissociation kinetics of $C_4H_2F_7OH$ for each bond type over 400 triplet state trajectories at 5000 K. A dissociation event is defined as the first timestep at which a bond length exceeds 5 Bohr. Kinetics are normalised by the total number of bonds of each type present in the molecule.

isomer in Fig. 3.28 is the very dominant dissociation of the O-H bond. The C-H bond has been shown to be rather weak in the triplet state (as is partially the case for this molecule) and so it is logical that a hydrogen atom bonded to an electrophore would also dissociate readily. The bond breaks almost always with an average dissociation time of 8.6 fs and dissociates in over 90% of trajectories, most often being the first bond broken (86% of the time) and actually accounts for a third of all dissociation events across all trajectories of the molecule. The other bond type with a significant number of first dissociations within a trajectory is C-H with a dissociation yield of 15%, significantly lower than the other $C_4H_3F_7O$ isomers. The other great change in the dissociation kinetics for this new functional group isomer is the dissociation of the C-O bond which previously was a dominant bond in the dissociation pathways of the ethers, now only having a yield of 6%. This is explained as natural consequence of the O-H bond dissociating readily producing a radical oxygen which is discouraged from undergoing additional bond breaking events. The C-F dissociation yield is also the lowest of the $C_4H_3F_7O$ isomers considered, potentially due to the hydrogens on the C#4 carbon acting as a form of buffer, creating distance between the electrophore oxygen atom and the fluorines and reducing the capability of transferring the dissociative character of the triplet state excitation (that is localised by the electrophore) to the C-F environments. Interestingly, the average C-C dissociation yield remains rather high at 35%. As there is one more C-C bond in this isomer than those considered before, this means that on average slightly more than one C-C bond is broken per trajectory.

3.3.2.1 C-C & C-F bonds

While the initial localisation of the triplet state very clearly travels to the O-H bond, the effect of the position of the electrophore can still be seen in the dissociation yields of the different C-C and C-F environments. For instance Fig. 3.29 shows the C-C bond closest to the electrophore, C#3-C#4, accounts for over 55% of all C-C bonds with a dissociation yield of 60%. This yield is likely so high due to being adjacent to the electrophore while also being in a molecule where

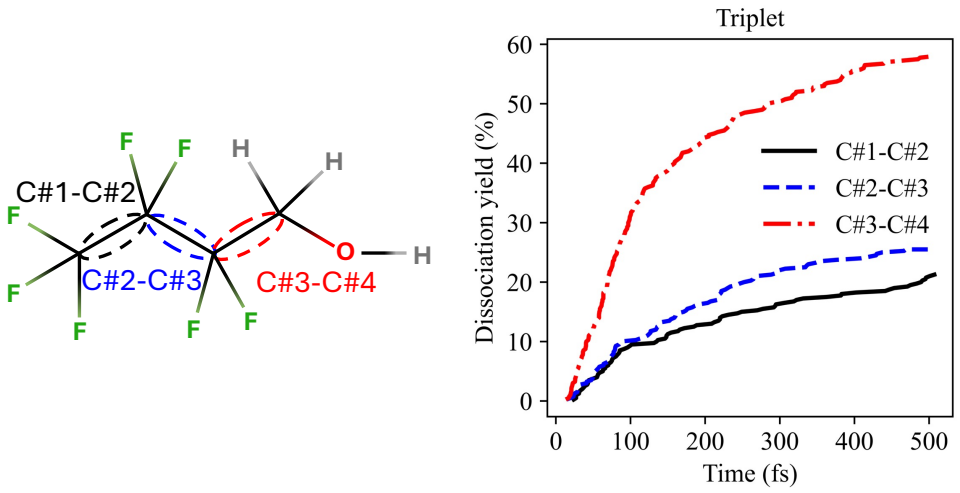

Figure 3.29: Dissociation kinetics of $C_4H_2F_7OH$ for each C-C bond environment over 400 triplet state trajectories at 5000 K. A dissociation event is defined as the first timestep at which a bond length exceeds 5 Bohr. Kinetics are normalised by the total number of bonds of each type present in the molecule.

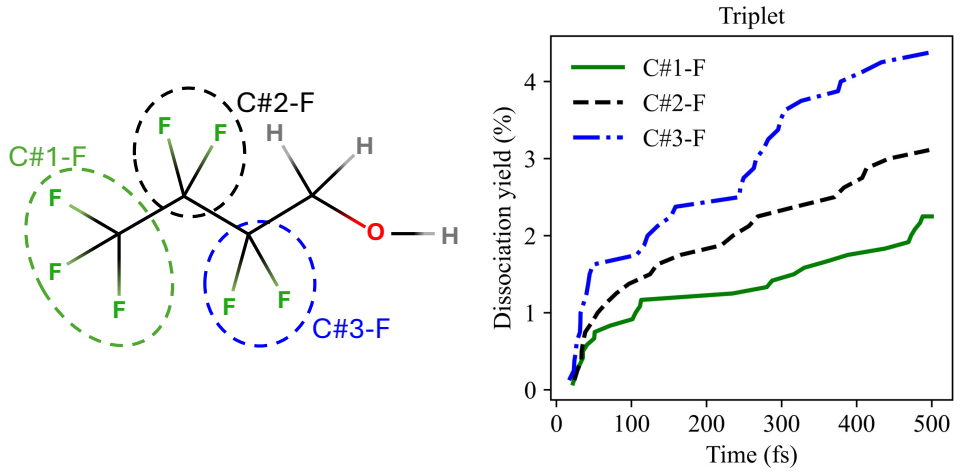

Figure 3.30: Dissociation kinetics of $C_4H_2F_7OH$ for each C-F bond environment over 400 triplet state trajectories at 5000 K. A dissociation event is defined as the first timestep at which a bond length exceeds 5 Bohr. Kinetics are normalised by the total number of bonds of each type present in the molecule.

the C-O bond almost never dissociates. Combining this also with the lower than previously observed C-H bond yield means that the C#3-C#4 bond is rather uncontested in terms of dissociations. The other two C-C bonds dissociate less than half as often, maintaining the order of dissociation yields corresponding to the distance from the electrophore. The same trend is seen in Fig. 3.30 in the C-F environments with the C#3-F environment dissociating most often accounting for 40% of the C-F dissociations though with a very small dissociation yield of only 4%. The largest dissociation yield of a bond type environment being so low reinforces the need of running a large number of trajectories in order to create a sufficient resolution in the data from which conclusions can be drawn. It is also important to note that due to the presentation of the dissociation yields it is not clear the C#1-F and C#2-F environments contribute roughly an equal number of dissociations due to the different number of fluorines within each environment resulting in different dissociation yields of 3.1% and 2.3%, while both environments actually account for approximately 14% of the C-F dissociations.

3.3.2.2 Temperature dependence

As in the case of the $C_4H_3F_7O$ ether isomers, additional trajectories were preformed at lower temperatures of 3000 K and 4000 K, with the overall dissociation yields for all bond types shown in 3.31. The O-H bond that was shown to dominate the dissociation pathways in Fig. 3.28 does so even more as the temperature is decreased because the dissociation yield remains practically unchanged and in fact increases very slightly at 3000 K. The O-H bond is therefore the weakest bond so far considered and therefore its dissociation can be said to be barrierless only in the triplet state. However the rest of the bond types do have significant reductions in dissociation yields to the point where at 3000 K, the singular O-H bond accounts for over 60% of all dissociations in the molecule. The strongest case to make for this is with the C-F bonds, which had a small average dissociation yield is only 3% at 5000 K. When the temperature is reduced to 3000 K, the C-F dissociations become almost non-existent, with the only C-F environment experiencing any dissociations is C#3-F, the closest to the electrophore. However due to

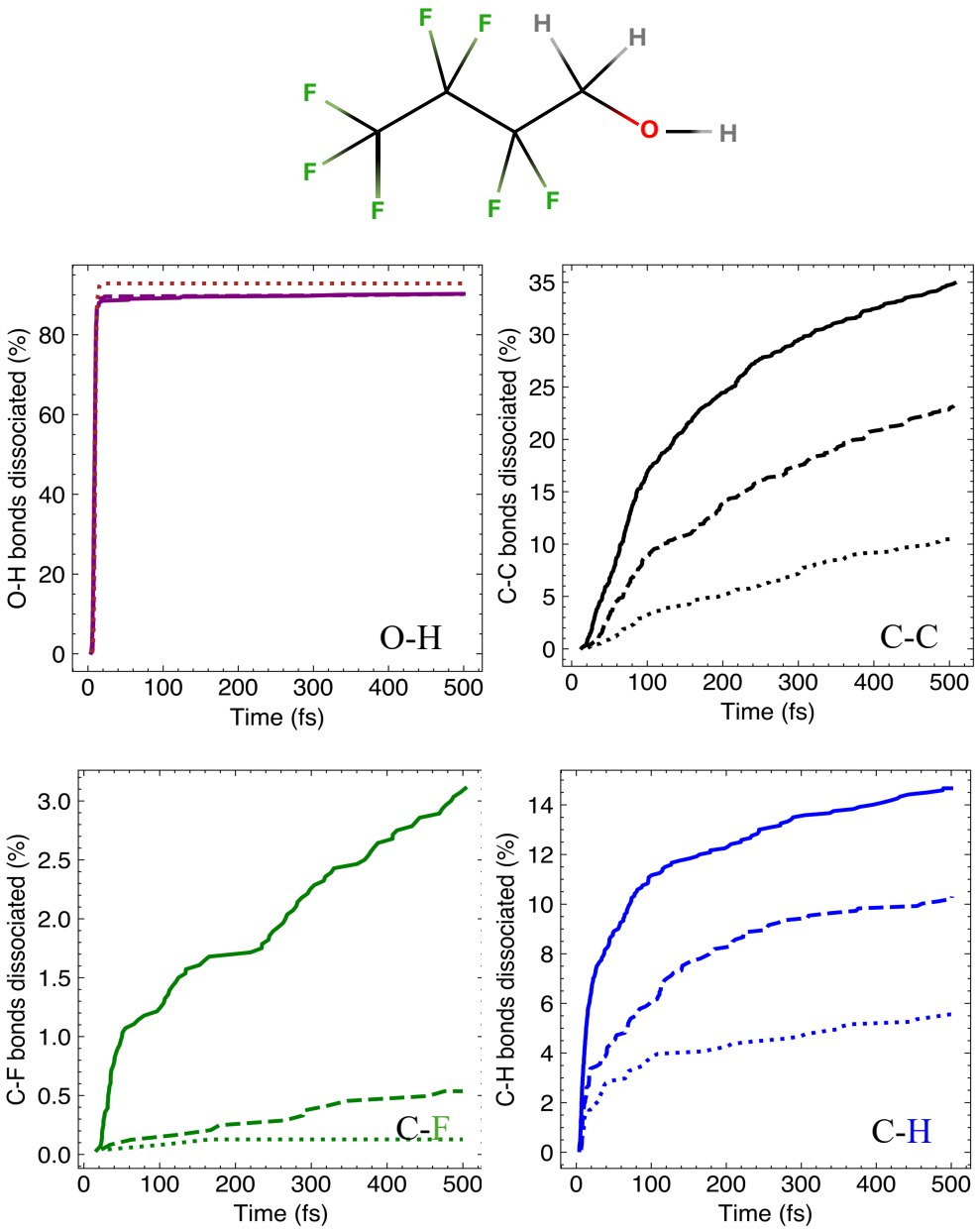

Figure 3.31: The temperature dependence of the dissociation kinetics for O-H (top-left), C-C (top-right), C-F (bottom-left), C-H (bottom-right) bonds in $C_4H_2F_7OH$. Three temperatures, 3000 K (dotted line), 4000 K (dashed line) and 5000 K (solid line) are compared.

the hydrogen buffer on the C#4 carbon that separates the electrophore from the fluorines, there are only 3 dissociations across 400 trajectories, significantly fewer than observed in the ether isomers without this increased electrophore distance in the previous section. The C-C and the C-H bonds undergo a fairly regular reduction in dissociation yield with regards to the temperature. The dissociation yields decrease by fairly equal amounts between 5000 K to 4000 K and 4000 K to 3000 K, with final dissociation yields of 10%. The C-H bonds however show a much stronger temperature dependence than seen in the ether isomers. This is probably due to the fact that excitation to the triplet state still results in a rapid dissociation of the O-H bond and so the dissociative character of the triplet state has caused a bond dissociation event on the other side of the oxygen atom and so the dissociation is not being expedited by the initial localisation of the triplet state to the same extent as in the ether molecules.

3.3.2.3 Comparison to singlet state dissociations

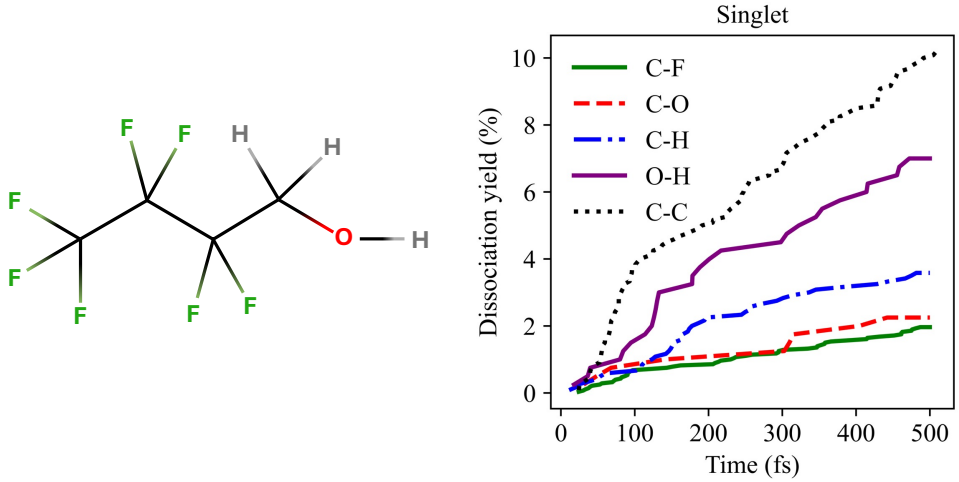

Figure 3.32: Dissociation kinetics of $C_4H_2F_7OH$ for each bond type over 400 singlet state trajectories at 5000 K. A dissociation event is defined as the first timestep at which a bond length exceeds 5 Bohr. Kinetics are normalised by the total number of bonds of each type present in the molecule.

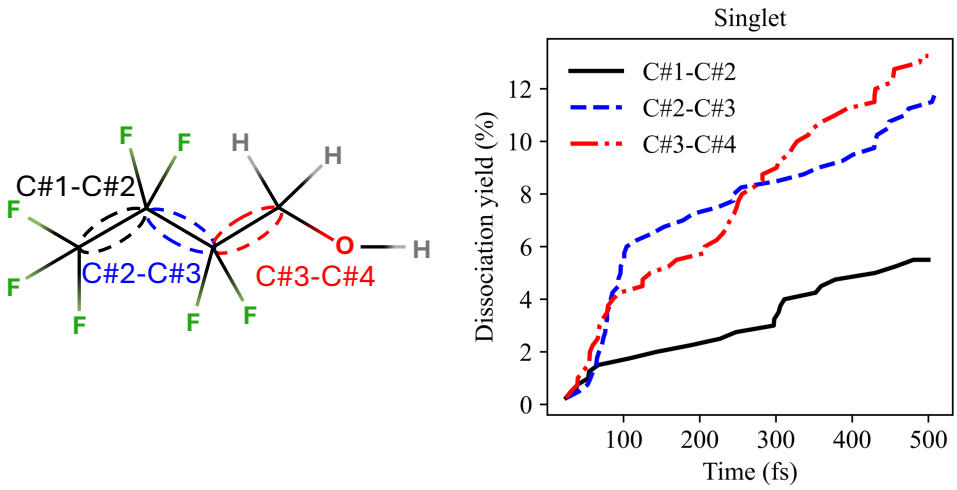

Figure 3.33: Dissociation kinetics of $C_4H_2F_7OH$ for each C-C bond environment over 400 singlet state trajectories at 5000 K. A dissociation event is defined as the first timestep at which a bond length exceeds 5 Bohr. Kinetics are normalised by the total number of bonds of each type present in the molecule.

The dissociation pathways of the singlet state vary significantly compared to that of the triplet state. The defining feature of the dissociation of the alcohol in the triplet state was the rapid dissociation of the O-H bond, which in the singlet state has a dissociation yield of just 7% in Fig. 3.32, an over 10x reduction. All other bond types also have a reduction in dissociation yields with the highest now belonging to the C-C bonds at 10%. The C-O and C-F bonds have a significant reduction as well with the dissociations yield of the C-O bonds being only 2.2%, having only 9 dissociation events across 400 trajectories. It is interesting to note that when comparing to the C-O bond dissociation yields in the ether isomers, it can be shown that the alcohol functional has the same effect of lowering the C-O dissociation yield in the singlet state. All bonds (and again, most notably the O-H bond) have also become more linear in their dissociations, losing the initial spike of dissociations that happen due to the triplet state, with a higher percentage of the dissociations happening later in the propagation.

The C-C bonds in the singlet state do not have the clear delineation based

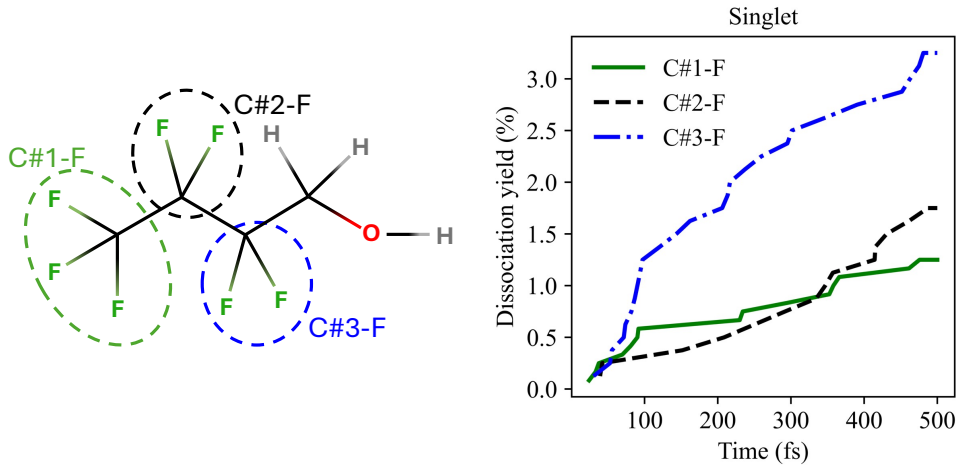

Figure 3.34: Dissociation kinetics of $C_4H_2F_7OH$ for each C-F bond environment over 400 singlet state trajectories at 5000 K. A dissociation event is defined as the first timestep at which a bond length exceeds 5 Bohr. Kinetics are normalised by the total number of bonds of each type present in the molecule.

on the proximity to the oxygen atom that was seen in the triplet state as shown in Fig. 3.33, as the oxygen is not acting as an electrophore. The C#2-C#3 and C#3-C#4 bonds have very similar dissociation yields with the C#2-C#3 bond dissociating more rapidly during the initial propagation, though both final yields were smaller than in the triplet state with final yields of only 13% and 11.8% for the C#3-C#4 and C#2-C#3 bonds respectfully. Similar to the triplet state however, the C#1-C#2 bond is the least dissociated with very few initial dissociations. The C-F environments in Fig. 3.34 do in fact maintain the same order as in the triplet state with the C#3-F environment dissociating the most with a dissociation yield of 3.1%, only a slight decrease from the triplet state. The dissociation yields of the other environments also decrease by around or less than a percentage though the initial dissociation yield of the C#1-F environment does outpace the yield for the C#2-F group. This shows that while the triplet state caused a significant increase for all bond types for all molecules considered thus far, the hydrogens acting as a buffer in $C_4H_2F_7OH$ severely limit the increase in dissociations expected due to the distance between the fluorine environments

and the electrophore.

3.3.2.4 Comparison to experiment

Despite being presented in the same paper as the ether $C_4H_3F_7O$ isomers [106], this alcohol molecule did not have any highlighted bonds present. This could be due to the significantly lower number of C-O dissociations found in the simulations. The C-O peak in the mass spectra data was also larger than the one found in the ether isomers, which is supported by our finding that due to the dissociation of the O-H bond and the C#3-C#4 bond (which is the most broken of the C-C bonds), the C-O bond almost never dissociates, unlike the other molecules considered where it is one of the main dissociated bonds. The experimental authors also comment that this molecule experienced fewer dissociation events which was noted by the MD simulations as the alcohol molecule had far fewer bonds broken than the ether isomers.

3.3.3 PPVE

The perfluoropropylvinyl ether molecule (PPVE) is interesting due to having two adjacent functional groups that have been shown to act as electrophores. While the presence of two electrophores might suggest two triplet states with cross-sections appearing at low electron eV, the QEC calculations found only one triplet state with an energy range of up to 20 eV in Fig. 3.35, and only one singlet state with a cross section at a much higher energy of around 14 eV. Interestingly the cross sections for the other oxygen containing molecules had the lowest lying cross-section at higher energies, normally over 8 eV where as the triplet state cross-section is around 6 eV for PPVE. This value is more akin to the cross-sections produced for the $C_3H_2F_4$ molecule presented in Fig. 2.6, suggesting that the cross-section found for PPVE corresponds to the presence of the C=C bond over the presence of the oxygen atom. Considering that there is only one triplet state over a wide energy range, it is possible that the excited state forms some form of resonance structure with the triplet state excitation localised around both the C=C bond and the oxygen atom.

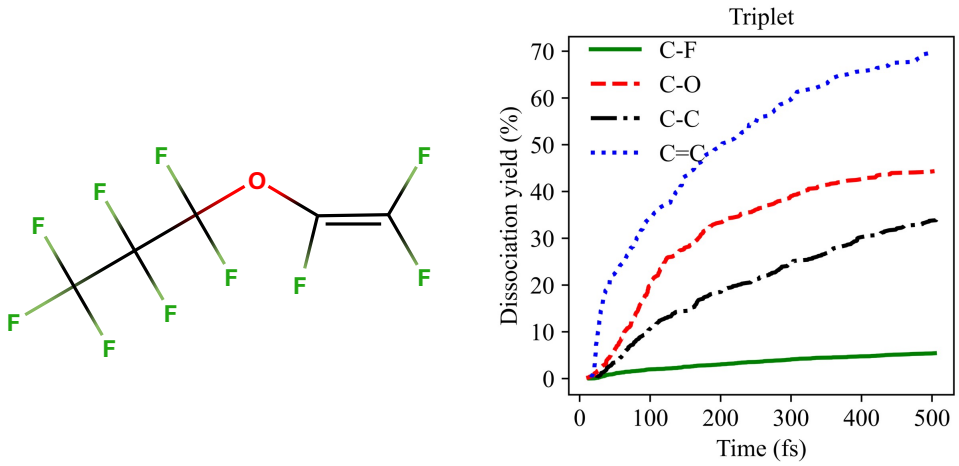

Figure 3.36: Dissociation kinetics of PPVE for each bond type over 372 triplet state trajectories at 5000 K. A dissociation event is defined as the first timestep at which a bond length exceeds 5 Bohr. Kinetics are normalised by the total number of bonds of each type present in the molecule.

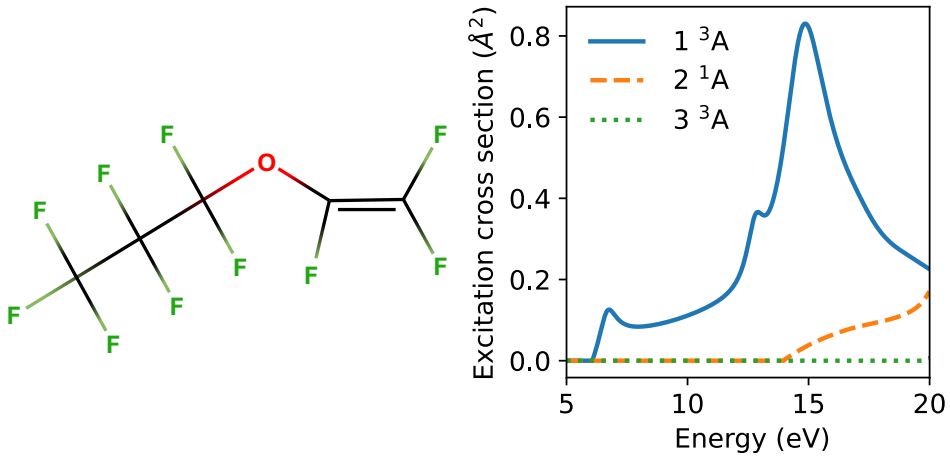

Figure 3.35: Excited state cross-sections generated via QEC for PPVE after electron impact.

Fig. 3.36 shows that as the oxygen atom is once again an ether and not an alcohol functional group, the C-O bonds dissociate often, with a dissociation yield of 41%. However the most dominant bond type in PPVE is the C=C bond with

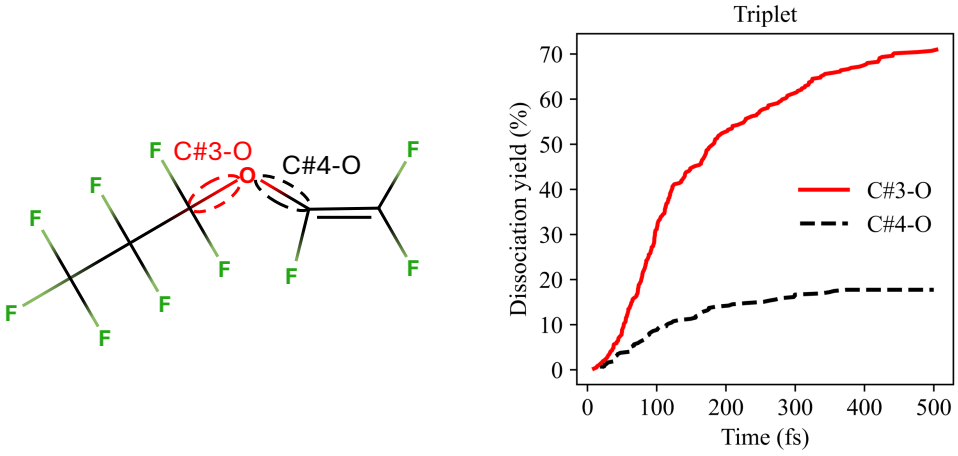

Figure 3.37: Dissociation kinetics of PPVE for each C-O bond environment over 372 triplet state trajectories at 5000 K. A dissociation event is defined as the first timestep at which a bond length exceeds 5 Bohr. Kinetics are normalised by the total number of bonds of each type present in the molecule.

a dissociation yield of 70%, slightly more than double the overall dissociation yield of the C-C bond at 34%. This means that the number of dissociations of the C=C bond is higher than the number of dissociations of both C-C bonds combined. Despite having three more fluorine atoms than the $C_4H_3F_7O$ isomers, the number of dissociations of the C-F bond is roughly equal to that of the i-$C_4H_3F_7O$ molecule, with an average dissociation yield of 5.3%.

The individual dissociation yields of the C-O bonds in PPVE are vastly different as shown in Fig. 3.37. The average dissociation yield of 41% shown in Fig. 3.36 is greatly under representing the 70% dissociation yield of the C#3-O bond, the highest dissociation yield of any C-O bond across the molecules considered and is an equivalent yield to the C=C bond. The C#4-O bond however has a much lower yield of 20%, accounting for only 22% of the general C-O bond dissociations. It appears that the presence of the double bond significantly impacts the stability of the radical and therefore heavily directs which C-O bond dissociates. This factor combined with the C#3-O bond involving a potential electrophore causes this bond to be the most dissociated in PPVE, accounting

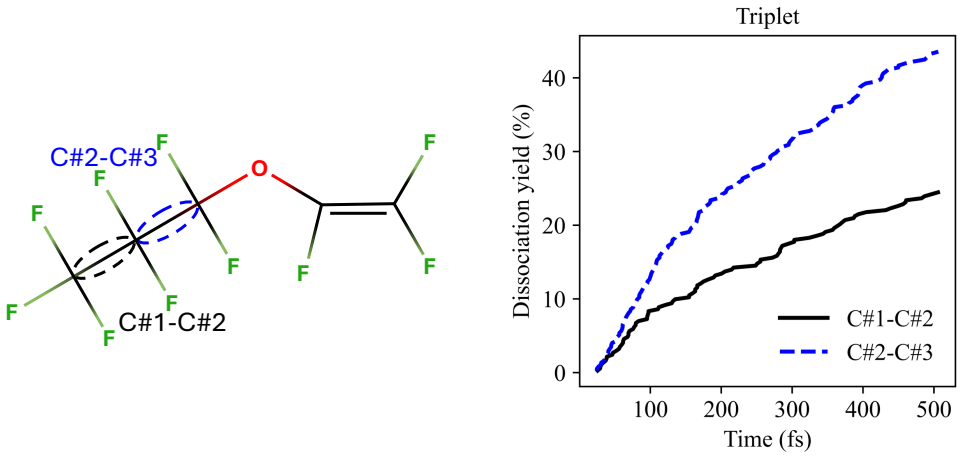

Figure 3.38: Dissociation kinetics of PPVE for each C-C bond environment over 372 triplet state trajectories at 5000 K. A dissociation event is defined as the first timestep at which a bond length exceeds 5 Bohr. Kinetics are normalised by the total number of bonds of each type present in the molecule.

for over a quarter of all dissociation events. It is worth that while the C#3-O bond is incredibly dissociative, neither of the dissociation kinetics of the C-O bonds present with the initial rapid dissociations found in the dissociations of the C#4-O found in the other ethers in this section. As the C=C does have a much higher number of initial dissociations, this suggests that while both the C=C and the oxygen atom can act as an electrophore that the C=C is the more dominant electrophore and is the part of the PPVE molecule that localises the triplet state excitation.

As with previous molecules, the effect of the electrophore localisation can be seen in order of the dissociations of the different bond environments. The C-C bond closest to the electrophore, C#2-C#3, has a dissociation yield of 41% and accounts for 60% of the C-C dissociations in the PPVE molecule as shown in Fig. 3.38. This increased dissociative character is apparent even at initial times, and continues throughout propagation. It is also important to note the context of the dissociation pathways as opposed to simply comparing the bonds in a vacuum. The C#3-O bond is the most dissociated bond in the molecule

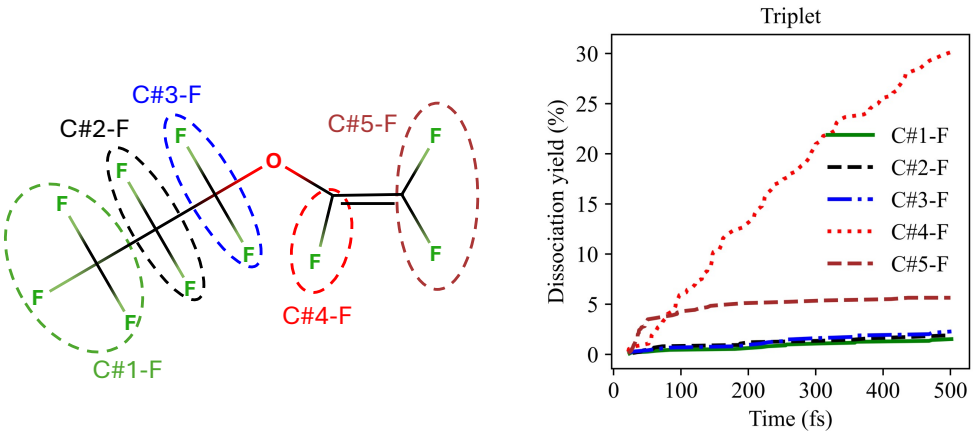

Figure 3.39: Dissociation kinetics of PPVE for each C-F bond environment over 372 triplet state trajectories at 5000 K. A dissociation event is defined as the first timestep at which a bond length exceeds 5 Bohr. Kinetics are normalised by the total number of bonds of each type present in the molecule.

and despite also being a bond involving the third carbon, the C#2-C#3 bond dissociates directly following the dissociation of the C#3-O bond 22.5% of the time which accounts for 28% of the C#2-C#3 bond dissociation events. This again suggests the dissociative character of the electrophore persists after the breaking of the C-O bond.

The dissociation yields of the C-F environments in PPVE as in Fig. 3.39 present perhaps thus far the clearest evidence of the electrophore effect. The C#4-F bond that experiences proximity to both the oxygen atom and the C=C bond has by far the highest dissociation yield seen for a C-F bond environment of 30%. This a dissociation yield six times higher than the next environment, C#5-F which contain the fluorines on the other side of the double bond, also being adjacent to an electrophore. Surprisingly the C#3-F environment which also has close proximity to an electrophore cannot be picked out from the rest of the environments. This is due to being positioned on the carbon that experiences both the C#2-C#3 and the C#3-O dissociations both of which are very dissociative, discouraging the breaking of the C#3-F bonds.

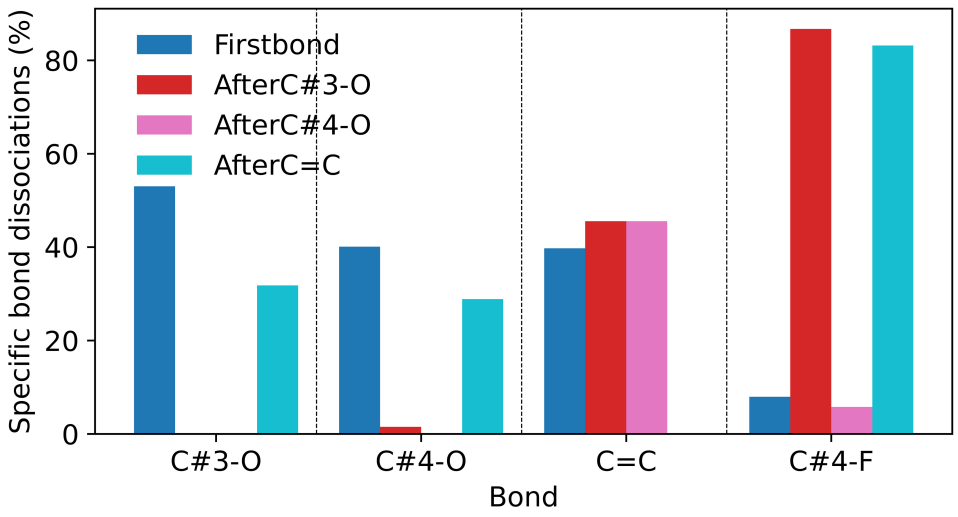

Figure 3.40: The proportions of the conditions under which the bonds in the 'active region' of PPVE dissociate. Each bar shows the percentage of the bond that breaks before others in the 'active region' (dark blue), after the C#3-O bond (red), after C#4-O (pink) or after the C=C bond (light blue).

Dissociation pathways are important to be understood and therefore information can also be gleaned not only from how often a bond breaks, but also which bonds breaks first in a trajectory, and how a specific bond breaking influences the dissociation rate of another. This can be seen clearly within the PPVE molecule as both C-O bonds only break in the same trajectory once. Similarly, which C-O bond breaks affects the most likely second bond to dissociate. When the C#3–O bond breaks first, the C=C bond is the most likely to break next, occurring in 38.4% of such events. Conversely, if the C#4–O bond is the first to dissociate then the C#2–C#3 bond becomes the predominant next dissociation, appearing in 46.38% of cases, while the C=C bond dissociates much less frequently (only 7.25% of the time). Additionally, when the C=C bond breaks initially, it tends to facilitate subsequent cleavage at the C#3–O bond significantly more often than at the C#4–O bond — with respective occurrences of 32.77% compared to 8.94%.

Therefore, it is significant if a bond dissociates often specifically after other neighbouring bonds which is detailed in Fig. 3.40 for the bonds in the 'active

region'. Due to its proximity to both electrophores, the C#4-F bond is so dissociative to the extent that a majority (over 95%) of the dissociations of the bond occur after the dissociation of another bond. For instance, the C#4-F bond breaks after 28.6% of the C#3-O dissociations, making these two bonds dissociating in this order one of the most common dissociation pathways. The dissociation of the C=C bond which contains the carbon of the C#4-F bond also does not prevent the C#4-F bond dissociation, with the C#4-F bond dissociating after 26% of the C=C dissociations. The only bond that seemingly discourages the C#4-F bond dissociations is the C#4-O bond, which after its dissociation the C#4-F bond breaks only thrice across all 400 trajectories. In order to have more certainty, many more trajectories would have to be run as the C#4-O bond has a much lower dissociation yield than both the C#3-O and the C=C bonds which limits the study of the pathways after this dissociation. The fact that the C#4-F bond breaks after other bonds is also reflected in the average breaking time of the C#4-F bond at 237.8 fs, almost double the breaking times of the C=C, C#3-O and C#4-O bonds with average times of 146.3, 152.3, 132.2 fs respectively. This region surrounding the two electrophores can be seen as the 'active region' of the molecule, as the breaking of a bond does not necessarily discourage the breaking of a second bond involving the same atom as all of the bonds in the active region have a significant percentage of dissociations after another bond on the same carbon.

3.3.3.1 Temperature dependence

The temperature dependence of the active region shows that the different bonds are affected by different extents by the reduction of the temperature, visible through the dissociation yields presented in Fig. 3.41. The C#4-F bond has a severe decrease in dissociation yield from 30% at 5000 K to just 7% at 3000 K. The C=C bond also shows significant reductions as the temperature is dropped, more so when at the lowest temperature of 3000 K where the dissociation yield is lowered to 22%. At 4000 K, the dissociation yields of the C-O bonds are relatively barely lowered. There is however a large difference between their changes in

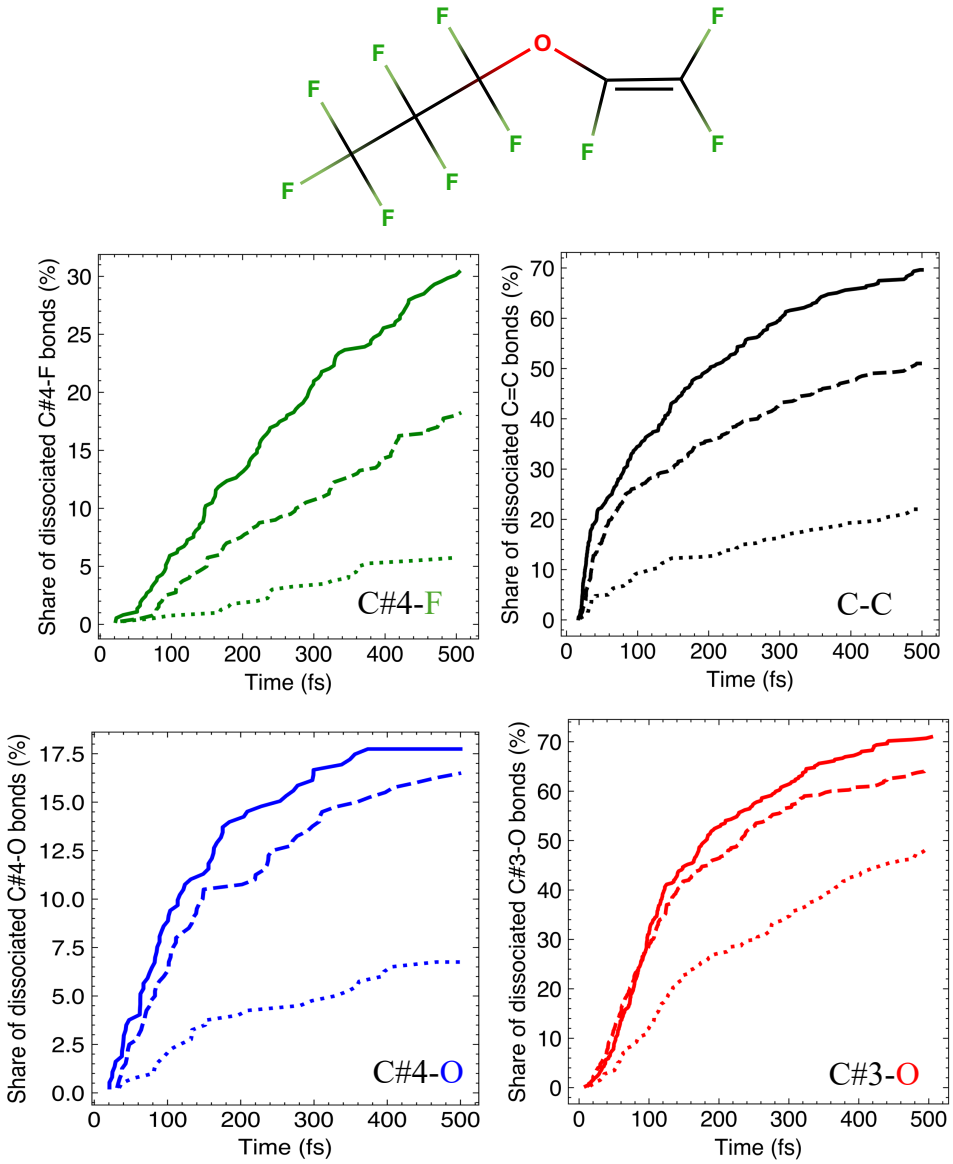

Figure 3.41: The temperature dependence of the dissociation kinetics for C-F (top-left), C=C (top-right), C#3-O (bottom-left), C#4-O (bottom-right) in bond types in PPVE. Three temperatures, 3000 K (dotted line), 4000 K (dashed line) and 5000 K (solid line) are compared.

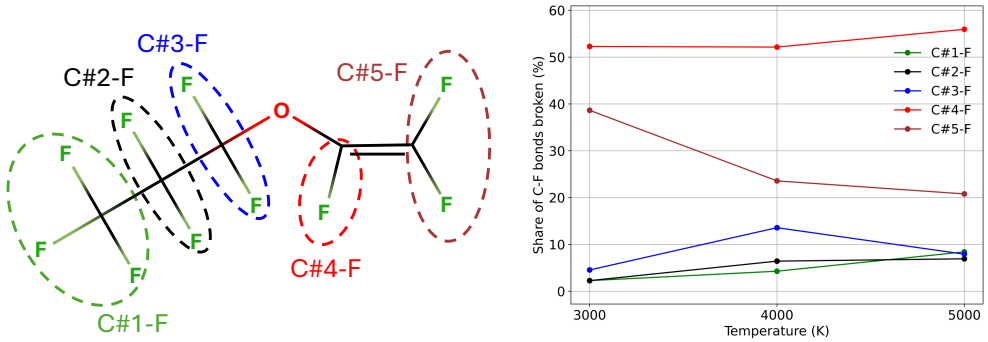

Figure 3.42: Temperature dependence of the dissociation kinetics of different C-F environments in the PPVE molecule. The plot shows the proportion of total C-F dissociations attributed to each C-F environment.

dissociation yields reductions at 3000 K, as the dissociations yield of C#4-O halves to 7.2%. The C#3-O bond does not have such a significant reduction with the dissociation yield being 51.9% at 3000 K and 69% at 4000 K. This is likely due to the C#3-O bond being adjacent to the C=C electrophore, and the high stability of the C_2F_3O radical formed. Therefore outside of the O-H bond in the alcohol isomer of $C_4H_3F_7O$, the C#3-O bond is the most resistant to temperature found, and for that reason accounts for over half of all dissociations in PPVE at 3000 K.

The temperature dependence within the individual environments for both the C-C and C-O bonds is consistent such that at 4000 K the proportion of the bonds split between the different environments remains exactly the same, and very slightly shifts towards the more electrophore favoured environment at 3000 K. While the order of the bond environments of the C-F bonds is also maintained across the temperatures, the share of C-F dissociations attributed to the C#5-F environment doubles from 5000 K to 3000 K while the proportion of the C-F dissociations being C#3-F remains constant, which can be seen in Fig. 3.42. Interestingly, while the dissociation yield does decrease for the C#3-F at 4000 K, it takes up a larger proportion of the dissociated C-F bonds. This could be due to the fact that the lower number of C#3-O and C#2-C#3 dissociations allows for

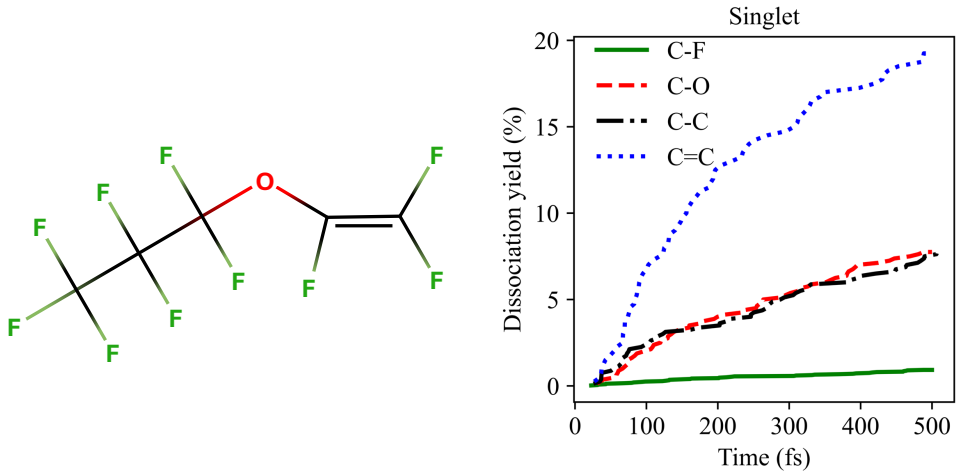

Figure 3.43: Dissociation kinetics of PPVE for each bond type over 400 singlet state trajectories at 5000 K. A dissociation event is defined as the first timestep at which a bond length exceeds 5 Bohr. Kinetics are normalised by the total number of bonds of each type present in the molecule.

more C#3-F dissociations (relative to the temperature) which could have been limiting what the dissociation yield of C#3-F would have been in a conceptual vacuum. At the lowest temperature of 3000 K, only the C#4-F and C#5-F have any significant dissociation yields. As these are the C-F environments bonded to the carbons involved in the C=C bond, this is further evidence that the double bond is acting as the dominant electrophore in the molecule which is consistent with prior findings that only C-F bonds around the electrophore dissociate at the lower temperature of 3000 K.

3.3.3.2 Comparison to singlet state dissociations

As expected the dissociation yields for the PPVE molecule in the singlet state in Fig. 3.43 are vastly lower than when compared to the triplet state. However in both states the C=C bond has the highest dissociation yield though only at 20% in the singlet state. The C-C and C-O dissociation yields are practically identical across the whole propagation, suggesting that there is no favouring of the C-

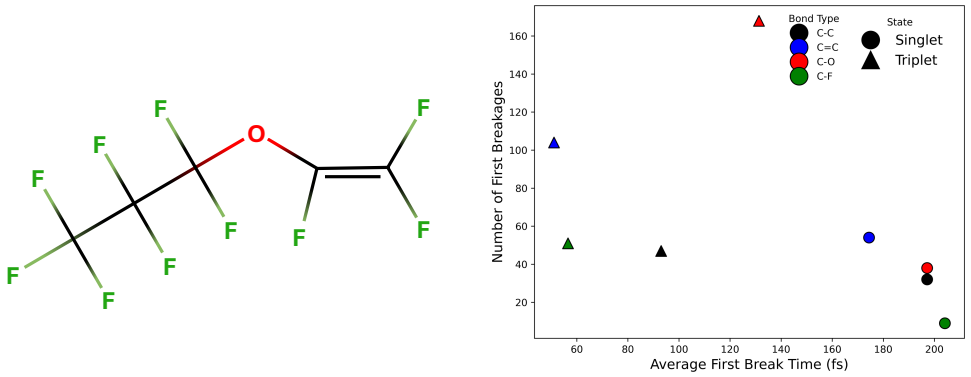

Figure 3.44: Count of each bond type breaking first in a trajectory against the average time of that first breakage in the PPVE molecule for both the singlet (circles) and triplet state (triangle) trajectories.

O bonds that is consistent with the localisation of dissociation caused by the presence of an electrophore in the triplet state. The dissociation yields of both bond types are also significantly lower than in the triplet state at only 7.8%. The C-F bonds almost never dissociate in the singlet state with a dissociation yield of only a single percentage. As with the $C_4H_3F_7O$ isomers, the trajectories break earlier in the triplet state than in the singlet state. However unlike the other molecules considered thus far, the PPVE molecule does not contain any hydrogens whose bonds normally break first in triplet state trajectories. This results in the most common first breakage in a trajectory being the C-O bonds though at a very late time on average of 131 fs. The first bond dissociations in the singlet state shown in Fig. 3.44 also occur very slightly later than the other molecules with all average times over 160 fs. As is common in the singlet state, not all trajectories dissociate, and in fact only 33% trajectories have any dissociation events and only 13.5% trajectories have more than one dissociation. In contrast, 100% of triplet state trajectories dissociate with 85% of them having more than one dissociation event. The second most common bond to be broken second is actually the most common to be broken first in the singlet state, C=C, though this only occurs in 13.5% of trajectories in the singlet state. In the triplet state, while the C=C bond is not the most common bond to dissociate

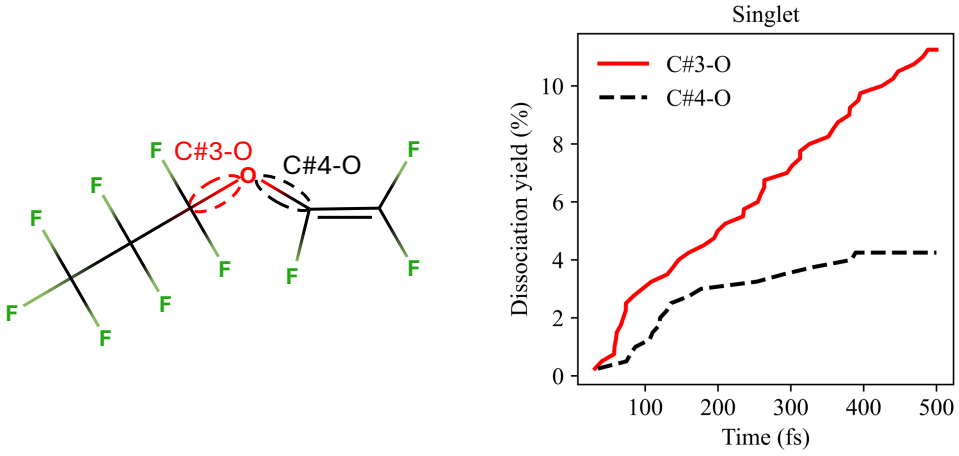

Figure 3.45: Dissociation kinetics of PPVE for each C-O bond environment over 400 singlet state trajectories at 5000 K. A dissociation event is defined as the first timestep at which a bond length exceeds 5 Bohr. Kinetics are normalised by the total number of bonds of each type present in the molecule.

first in a trajectory, when it is the first it happens almost immediately with an average of around 50 fs. This further suggests that the C=C bond is acting as the electrophore in the PPVE molecule, causing the noticeable differences in the dissociations observed between the singlet and triplet state trajectories.

Fig. 3.45 describes the dissociation yield of each C-O bond in PPVE on the singlet state. Unlike the singlet state trajectories for the ether isomers, the C-O bonds in the singlet state trajectories present with similar dissociation kinetics to those observed in the triplet state. The C#3-O bond is the dominant C-O bond in the triplet state, though the dissociation yield has decreased seven-fold to only 11%. The C#4-O bond similarly decreases five-fold to a very low dissociation yield of only 4%. A notable difference between the dissociation patterns in the singlet and triplet states is shown through the C-C bonds. In the triplet state the dissociation yield of the C-C bonds is determined by the proximity to the electrophore, and so the C#2-C#3 bond has a significantly higher dissociation yield than the C#1-C#2 bond. This is not true in the singlet state where both C-C bonds produce a dissociation yield of approximately 8%, and dissociate evenly

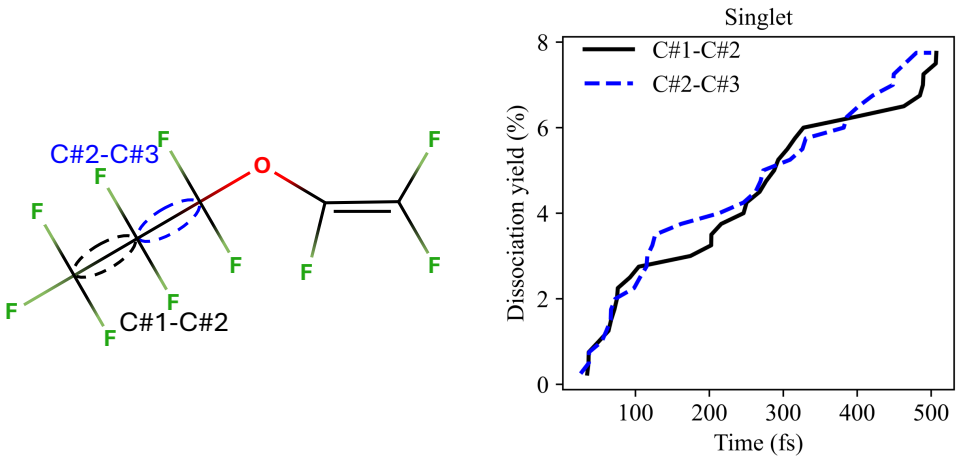

Figure 3.46: Dissociation kinetics of PPVE for each C-C bond environment over 400 singlet state trajectories at 5000 K. A dissociation event is defined as the first timestep at which a bond length exceeds 5 Bohr. Kinetics are normalised by the total number of bonds of each type present in the molecule.

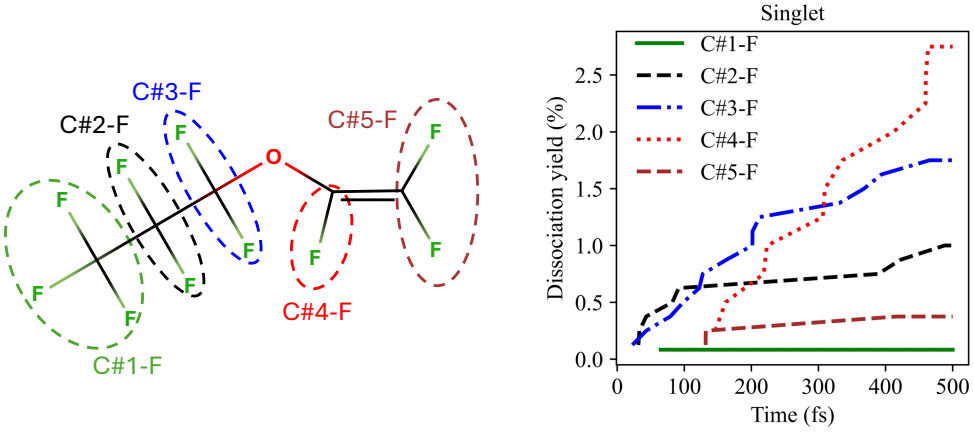

Figure 3.47: Dissociation kinetics of PPVE for each C-F bond environment over 400 singlet state trajectories at 5000 K. A dissociation event is defined as the first timestep at which a bond length exceeds 5 Bohr. Kinetics are normalised by the total number of bonds of each type present in the molecule.

throughout the whole propagation akin to more symmetrical C-C bonds, as there is no electrophore influencing the dissociation pathways in the singlet state. The order of the C-F bonds shown in Fig. 3.47 has a very low resolution due to the extremely low dissociation yields of the C-F environments; the C#1-F environment only has one dissociation across all 400 trajectories. While the C#4-F bond remains the environment with the highest dissociation yield, the other environment around the C=C bond (C#5-F) becomes one of the least broken with a dissociation yield of less than 0.5% as the C=C bond is no longer acting as an electrophore.

3.3.3.3 Comparison to experiment

PPVE was also considered in one of the experimental papers that compared n-$C_4H_3F_7O$ and i-$C_4H_3F_7O$ [**RN759**]. For better comparison, the experimental authors established a category for each type of fragment produced: atomic fluorine, small fluorocarbons (containing no more than one carbon) and large fluorocarbons (that contain more than one carbon). It was noted that the PPVE molecule produced more smaller than larger fluorocarbons. The MD simulations produced the same result, with the most common fragment being CF_2 outnumbering the number of atomic fluorines with respective counts of 382 to 202. Including only the small fluorocarbons that do not contain oxygen the number of fluorocarbons increases to 524, much more prevalent the 315 large fluorocarbons. It is fairly simple to see how PPVE produces such a significant number of CF_2 radicals. The most straightforward dissociation pathway is the dissociation of the C=C bond which results in a CF_2 and C_3F_7O radical. Another pathway that produces CF_2 is the dissociation of both the C#3-O and the C#2-C#3 bonds, which occurs in 24.5% of all the trajectories. As this requires dissociation of two bonds on the C#3 carbon, it is very unlikely that an additional C-F dissociation of the same carbon occurs, leaving the CF_2 radical.

3.3.4 Simulations at 1000 K

Three of the four molecules thus far considered were also run at lower temperatures with a simulated temperature of 1000 K. As the initial momentum of the trajectories is proportional to the temperature, the trajectories at 1000 K have very little kinetic energy, leading to few if any dissociations. To rectify this many initial conditions are generated, with only those with the highest energy used to perform MD. The lower energy trajectories were simply assumed to have no dissociation events.

The first molecule run in this fashion was PPVE, where the threshold of selecting a trajectory was given to be the 10% of the trajectories with the highest energy. Even under these conditions and after completing many such propagations, there were only 89 dissociation events across 876 trajectories, with only one trajectory containing two dissociations events, a 0.11% occurrence. Even with only the 10% highest energy trajectories, there are only 0.1 dissociations per trajectory. Of these dissociations shown in Fig. 3.48, only 4% are non C-O bonds and consist entirely of the dissociation of the C=C bond. 93% of the C-O bond dissociations are the C#3-O bond meaning that at 1000 K, it can be said that this is practically the only bond that dissociates within 500 fs.

Additional MD simulations were also performed for the ether isomers of $C_4H_3F_7O$, n-$C_4H_3F_7O$ and i-$C_4H_3F_7O$. In order to facilitate more dissociations the energy threshold for trajectory selection was increased to the highest 1% of energies. The increase in this threshold has a two-fold effect; not only is the average kinetic energy higher due to the stricter selection rule, but a larger number of initial conditions need to be generated in order for the 1% allowing for the highest 1% of trajectories to contain more extremes. For instance, for the 100 trajectories run for each of the ether isomers in this test case, it required creation of 10,000 initial conditions. With this in mind, the dissociations yields at 1000 K are very high, with the overall C-O yield reaching 35% for the i-isomer and all trajectories having a dissociation event. This suggests that this threshold is too high to give data on how often a bond breaks at this temperature but may provide insight into which bonds are the ones to dissociate. For example, in both molecules the

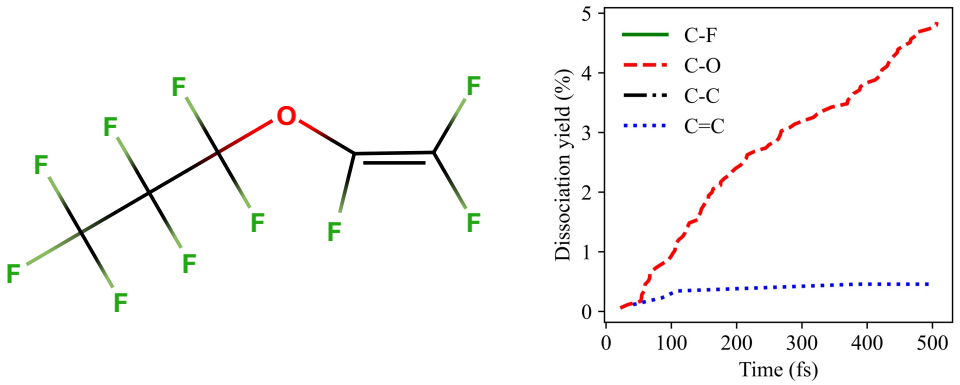

Figure 3.48: Dissociation kinetics of PPVE for each bond type over 876 triplet state trajectories at 1000 K. A dissociation event is defined as the first timestep at which a bond length exceeds 5 Bohr. Kinetics are normalised by the total number of bonds of each type present in the molecule.

C#4-O bond is by far the dominant C-O bond to dissociate, accounting for at least 80% of the C-O bond dissociations. This also suggests that the high temperature simulations provided data that were more comparable to experiments as the C#2-O and C#3-O bond were highlighted to be dissociative for the i-isomer and the n-isomer respectively. The fact that the high dissociation yields for both the C-O and C-H bonds arise practically entirely from the initial kinetic energy of the molecule, also suggesting that the energy selection threshold was too high.

As the threshold certainly needs to be lowered to achieve realistic data collection, a more rigorous approach would be to run a significantly large number of trajectories in descending energy order and plot the number of new dissociations per trajectory. When this has plateaued, it will be possible to say what energy threshold works for the given molecule and new initial conditions can be generated according to that discovery. As this requires a great computational effort just to develop reasonable initial conditions, it is possible to investigate other means of speeding up the propagation, namely the timestep. The timestep was originally kept small as the coupling and the AIMC amplitudes can change dramatically rather quickly. However with dynamics now being run on the lowest triplet state,

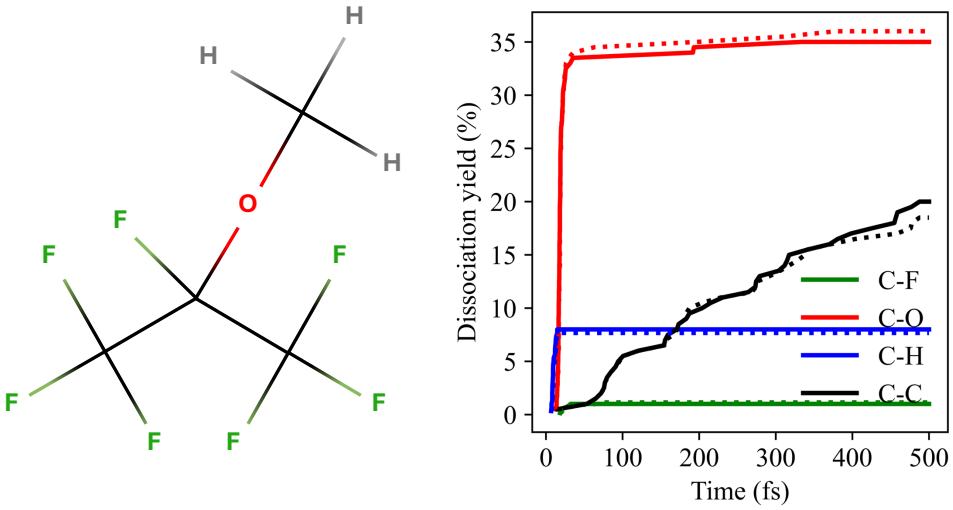

Figure 3.49: Dissociation kinetics of i-$C_4H_3F_7O$ for each bond type over 100 triplet state trajectories at 1000 K. The regular timestep of 10 atomic time units (solid line) is compared with a timestep of 30 atomic units (dotted line).

not only is the need for coupling calculations removed, the magnitude of a single amplitude when only one state is involved will always be 1. Therefore it may be possible to use a larger timestep at lower temperatures where the kinetic energy results in less distance travelled by the molecule. The same 100 trajectories that were run for both $C_4H_3F_7O$ isomers were run again with a timestep 3 times larger, effectively reducing the computational cost to a third. Figs. 3.49 & 3.50 show that for the molecules considered the increased timestep does not affect the propagation with only one additional C-F and C-O bond breaking in the n-isomer across 100 trajectories. The i-isomer also retains a similar level of accuracy with only the slightest disagreements being with the dissociation yields of the C-O and C-C bonds, where the different timesteps differ by a maximum of two additional dissociations. These findings suggest that at least when running standard MD on single triplet state, a dynamic timestep could be developed that significantly reduces the computational time by increasing the timestep when the molecule has low kinetic energy or a slow rate of change in the forces calculated.

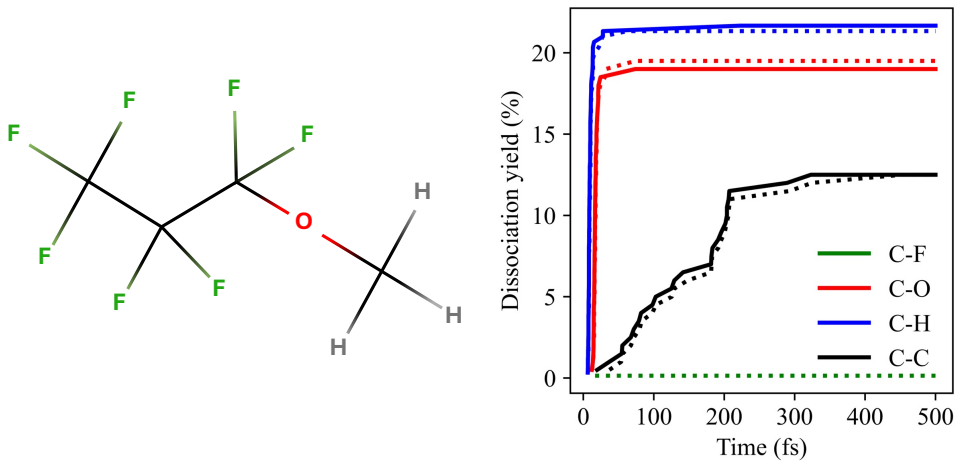

Figure 3.50: Dissociation kinetics of n-$C_4H_3F_7O$ for each bond type over 100 triplet state trajectories at 1000 K. The regular timestep of 10 atomic time units (solid line) is compared with a timestep of 30 atomic units (dotted line).

3.3.4.1 The inclusion of Spin-Flip DFT

Another simplification that requires testing is the removal of the Spin-Flip DFT when performing MD simulations on the lowest triplet state only. All results presented have been standard DFT without the inclusion of Spin-Flip, as it was introduced to manage the coupling between multiple excited states and the forces calculations required for each. In order to test that this simplification is valid for the purpose of trajectories propagated on only the lowest triplet state, the trajectories for the three $C_4H_3F_7O$ isomers along with PPVE were rerun with the same initial conditions employing Spin-Flip DFT. Comparison of the same trajectories with the different forms of DFT allows for investigation of which dissociations are affected more. The trajectories chosen to be rerun were those at 5000 K as the increased number of dissociations will better showcase the differences.

The comparison for the PPVE molecule in Fig. 3.51 shows that the difference between the two forms of DFT are negligible for almost all bond types across the whole range of propagation. Interestingly the trajectories using Spin-Flip DFT have very slightly more dissociations with the range of 1-3 more bonds broken.

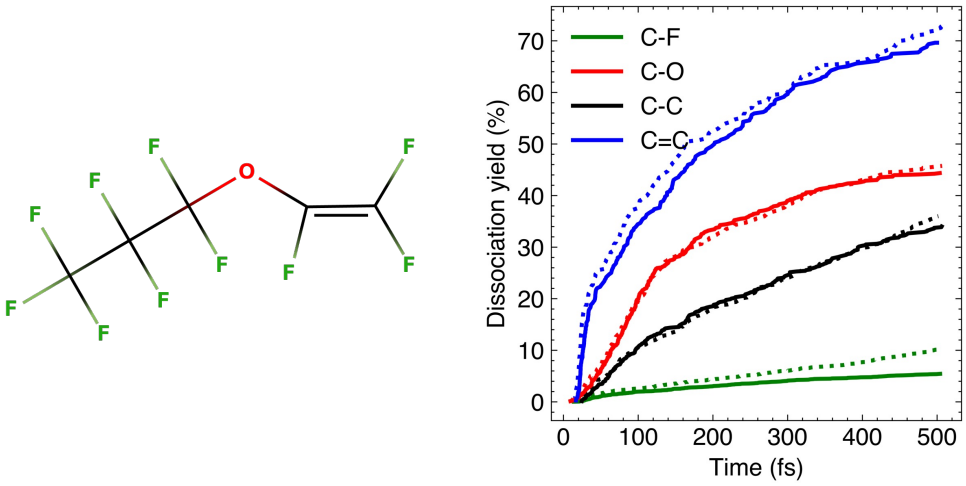

Figure 3.51: Dissociation kinetics of PPVE for each bond type over 372 triplet state trajectories at 5000 K. Spin-Flip DFT (dotted line) is compared with standard DFT (solid line).

The only exception to this is the C-F bonds for which the dissociation yield is approximately double in the trajectories using Spin-Flip DFT. Table. 3.2 shows how while no C-F bond is unaffected to the extent of the other bond types, there is still a wide range of impact between the individual C-F environments. The most dissociative C-F bond, C#4-F has the smallest difference, where 70.2% of the dissociations in the Spin-Flip trajectories also dissociate in the standard DFT trajectories. The lowest yield is the C#3-F environment at just 30.7%. This suggests that when the bond is incredibly dissociative like C#4-F more of the dissociations are preserved.

For the i-$C_4H_3F_7O$ and n-$C_4H_3F_7O$ isomers whose comparisons of the dissociations are shown in Figs. 3.52 and 3.53 respectively, the discrepancies between the Spin-Flip and standard DFT is larger for all bonds types, particularly for the i-isomer. For this molecule, the C-C bond has the largest difference between Spin-Flip and standard DFT, with the divergence occurring after the initial dissociations. The C-H bonds also have different dissociation kinetics and final dissociation yields where the Spin-Flip trajectories have a significant percentage

Bond	Standard DFT Yield (% of Spin-Flip)
C#1-F	48.0%
C#2-F	47.0%
C#3-F	30.7%
C#4-F	70.2%
C#5-F	40.7%

Table 3.2: Comparison of bond-breaking behaviour and yield between spin-flip and standard DFT methods.

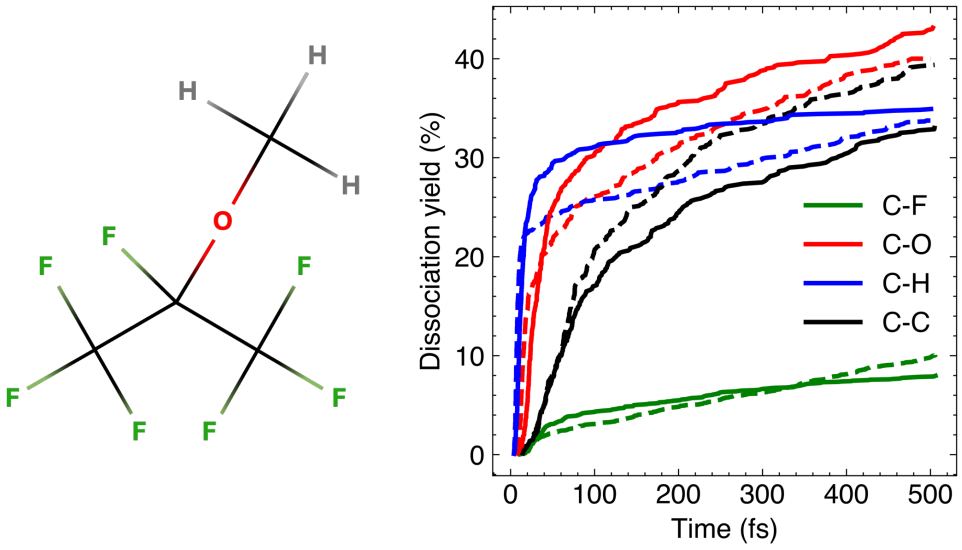

Figure 3.52: Dissociation kinetics of i-$C_4H_3F_7O$ for each bond type over 400 triplet state trajectories at 5000 K. Spin-Flip DFT (dotted line) is compared with standard DFT (solid line).

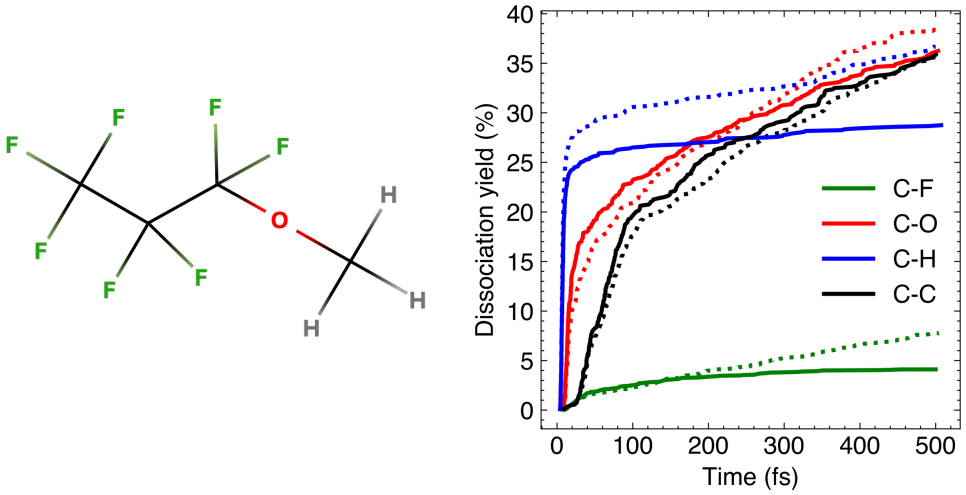

Figure 3.53: Dissociation kinetics of n-$C_4H_3F_7O$ for each bond type over 400 triplet state trajectories at 5000 K. Spin-Flip DFT (dotted line) is compared with standard DFT (solid line).

occurring after the initial spike in dissociations. In the n-isomer, the Spin-Flip calculations show that there is the same large gap for the C-F bonds. However, in this molecule the C-H bonds also have a large difference, especially in the initial part of the propagation where the majority of the dissociations take place. The C-C and C-O bonds have slight differences more akin to the ranges seen in the PPVE molecules.

The dissociation yield for the O-H bond in the $C_4H_2F_7OH$ molecule does not depend on the type of DFT chosen as shown in Fig. 3.54. The C-O and C-F bonds are present dissociation yields that appear indifferent to the choice of DFT, perhaps due to the very low dissociation yields. The only bond with any real disagreement is the C-H bond for which there are more late time dissociations when using Spin-Flip DFT, though the difference is not remarkably large. Overall, these four molecules show how the Spin-Flip trajectories are capable of simulating more bonds broken on the same atom, helping to gather more data on the dissociations pathways. The dissociation kinetics do not radically change for any bond type beyond an increase in dissociations during the later times of propaga-

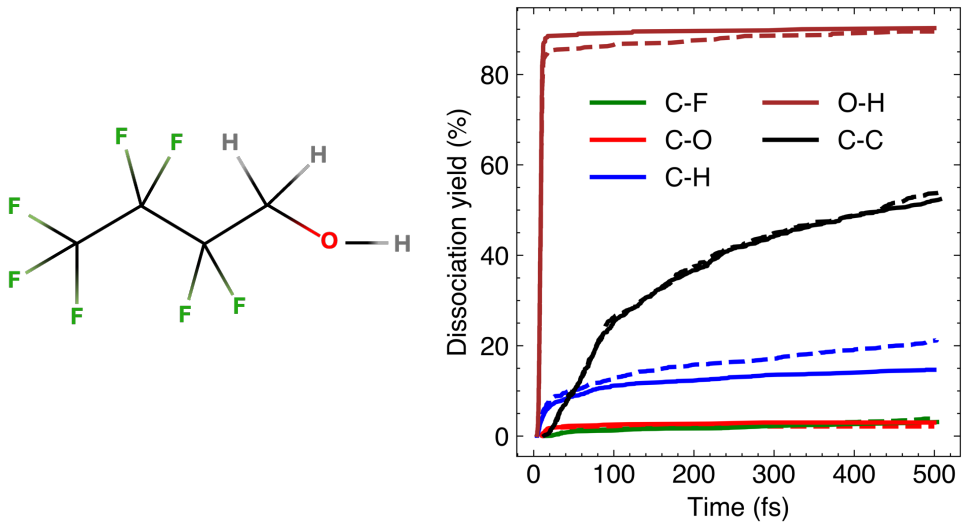

Figure 3.54: Dissociation kinetics of $C_4H_2F_7OH$ for each bond type over 400 triplet state trajectories at 5000 K. Spin-Flip DFT (dotted line) is compared with standard DFT (solid line).

tion. The C-F bonds in PPVE also show that the reduction in dissociation yields occurs mainly for bonds that are less dissociative. The cost of the inclusion of Spin-Flip is a roughly four times increase in computational cost, meaning that more standard DFT trajectories can be performed to analyse more dissociations while still being computationally cheaper which can offset the lower number of dissociation events. While this does somewhat limit the depth of the dissociation pathways by reducing the simulations ability to handle a high number of dissociation events, it is a justifiable trade-off due to the computational cost savings. For these reasons, all following MD simulations of different molecules will not incorporate Spin-Flip DFT unless NAMD is being employed for simulating multiple PES.

3.4 PIPVE

Perfluoro(isopropyl vinyl)ether (PIPVE) $C_5F_{10}O$ is an isomer that was compared to PPVE in terms of its plasma etching capabilities. PIPVE has the same func-

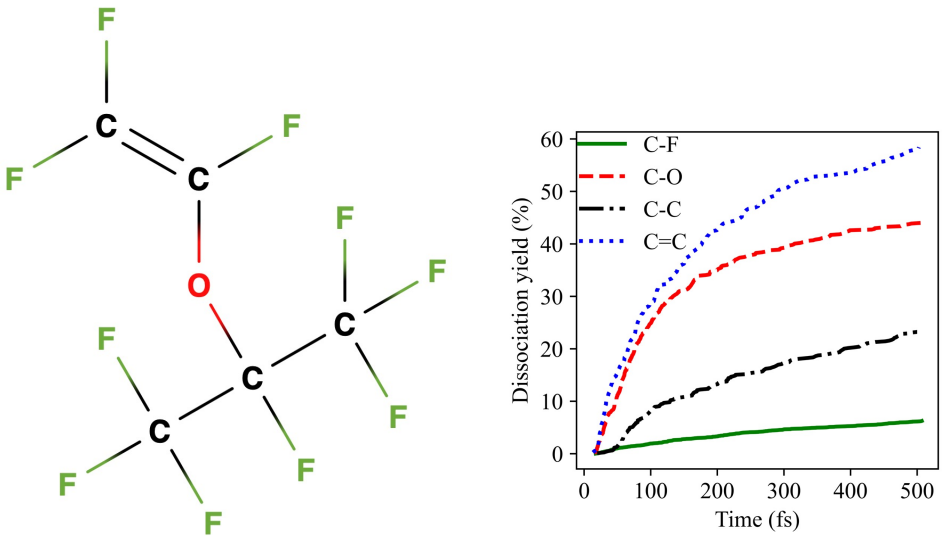

Figure 3.55: Dissociation kinetics of PIPVE for each bond type over 392 triplet state trajectories at 5000 K. A dissociation event is defined as the first timestep at which a bond length exceeds 5 Bohr. Kinetics are normalised by the total number of bonds of each type present in the molecule.

tional group but has a more centralised electrophore. The changes in dissociation yields and pathways can be predicted through the electrophore model and the precedent for isometric effects set by the n-$C_4H_3F_7O$ and i-$C_4H_3F_7O$ molecules. The symmetrical nature of the molecule suggests that both the C-C bonds and the CF_3 groups will present with symmetrical dissociations. The central electrophore means that there are a high number of C-F bonds surrounding the electrophore could suggest that there will be an increased average dissociation yield of the C-F bonds. However analysis of the PPVE dissociation pathways suggested that the C=C bond was the more dominant electrophore, and so the triplet state excitation was localised further away from the C-F environments than if the oxygen was acting as the sole electrophore.

The overall dissociation yields in Fig. 3.55 are roughly similar to PPVE in terms of order of most dissociated bond type. While still being the bond type with the highest dissociation yield, the C=C dissociation yield decreases significantly

by 12% to a final yield of 58%. The average C-O dissociation yield of 44% is slightly higher than the average dissociation yield of the PPVE, potentially due to the reduced number of C=C dissociations. As predicted by the electrophore model, the average dissociation yield of the C-F bonds is increased though only by 1%. However while this could be explained by the more centralised electrophore, it could also be due to the significantly lower average dissociation yield of the C-C bonds at 23.2%, a third lower than the PPVE isomer. It's possible that the low C-C dissociation yields are a product of the C=C bond playing the role of an electrophore as was suggested by the analysis of the dissociation pathways of the PPVE molecule. If the oxygen atom was playing the role of the electrophore then it could be expected to observe dissociation yields closer to those found in i-$C_4H_3F_7O$. Overall the average dissociation yield for all bonds in PIPVE is 16.8% compared to the overall average dissociation yield for all bonds of 17.8% in PPVE. While one would expect the molecule with a central electrophore to cause a higher number of dissociations, it is possible that the high temperature plays a role, in that dissociations across the whole molecule happen more readily and so the more compact molecule of PIPVE would have to break multiple bonds on the same carbon, something that is discouraged.

The distribution of the C-O dissociations in Fig. 3.56 are almost exactly the same between PIPVE and PPVE. The individual C-O bonds in PIPVE, C#2-O and C#4-O, have dissociation yields similar to the C#3-O and C#4-O bonds of the PPVE molecule respectively. This is due to the fact that the two molecules are positional isomers, meaning that the C=C-O functional group remains the same and so the C=C bond encouraging the dissociation of the opposite C-O bond is equal in both cases. For both molecules, the C#2-O (for PIPVE) and C#3-O (for PPVE) are the most common bond to be broken first within a trajectory, though this occurs slightly faster in the PIPVE molecule with an average dissociation time being the first bond broken of 107 fs vs 133 fs. Similar to the i-$C_4H_3F_7O$ molecule, the two C-C bonds are symmetrical and so present entirely symmetrical dissociation kinetics in Fig. 3.57, both achieving a final dissociation yield of 23%. Interestingly, despite the central electrophore affecting both C-C bonds, their

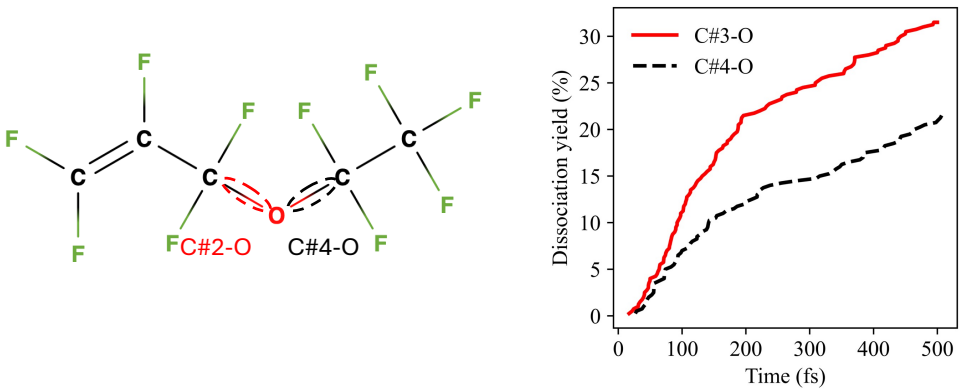

Figure 3.56: Dissociation kinetics of PIPVE for each C-O bond environment over 392 triplet state trajectories at 5000 K. A dissociation event is defined as the first timestep at which a bond length exceeds 5 Bohr. Kinetics are normalised by the total number of bonds of each type present in the molecule.

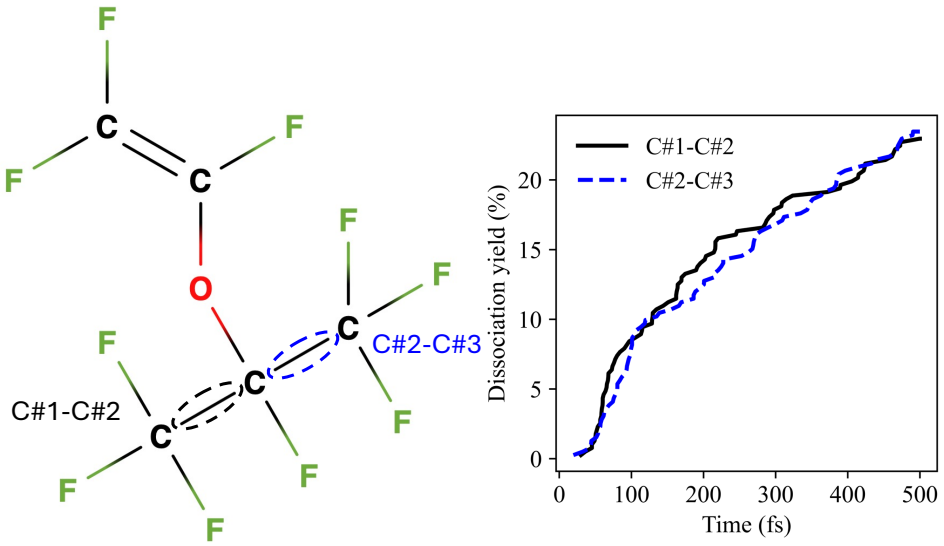

Figure 3.57: Dissociation kinetics of PIPVE for each C-C bond environment over 392 triplet state trajectories at 5000 K. A dissociation event is defined as the first timestep at which a bond length exceeds 5 Bohr. Kinetics are normalised by the total number of bonds of each type present in the molecule.

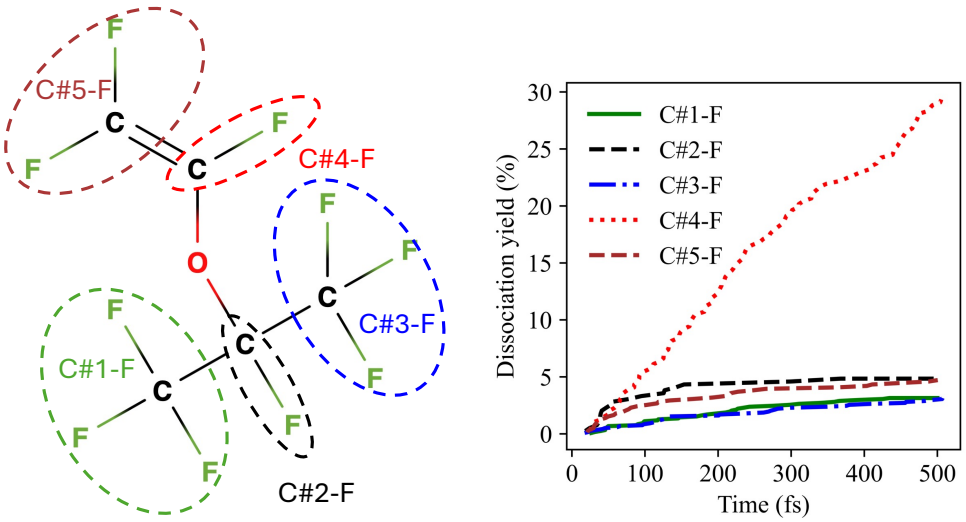

Figure 3.58: Dissociation kinetics of PIPVE for each C-F bond environment over 392 triplet state trajectories at 5000 K. A dissociation event is defined as the first timestep at which a bond length exceeds 5 Bohr. Kinetics are normalised by the total number of bonds of each type present in the molecule.

dissociation yield decreases significantly with the yield of the C-C bonds being below even the dissociation yield of C#1-C#2 in PPVE, the C-C bond furthest from the electrophore.

The dissociation yield of the C#4-F bond is 30%, equivalent to the C#4-F bond dissociation yield of PPVE, as the bond in both molecules is bonded to the double bonded carbon closest to the oxygen atom. The C#5-F bonds (which are also the same in both molecules) also have roughly equal dissociation yields, while the C#1-F and C#3-F have very low (exactly) equivalent yields due to being symmetrical environments. These lowest environments have a lower dissociation yield than the CF_3 groups in the i-$C_4H_3F_7O$ molecule (see Fig. 3.11) again suggesting that the C=C bond is acting as the dominant electrophore and therefore there is actually a larger distance between the electrophore and the CF_3 environments in PIPVE than i-$C_4H_3F_7O$. Unlike the PPVE molecule where the C#4-F and C#5-F environments were the only ones separated in terms of dissociation yield (Fig. 3.58), in PIPVE, the C#2-F bond has a higher dissociation

yield than the average dissociation yield of C#5-F, because of the lower number of C-C dissociations allowing for more C-F dissociations on an unperturbed carbon.

The isomeric differences between the PPVE and the PIPVE molecule have been discussed experimentally in recent years [262, 263]. However these two papers are not necessarily in agreement with each other. The earlier study states that PIPVE generates more CF_3+ ions due to the molecular structural differences between the two isomers. Other studies that have investigated the isomers more thoroughly with Quadrople Mass Spectrometry have found that in fact PPVE generates significantly more CF_3+ ions. The later study also presents bond energy analysis for both PIPVE and PPVE. For both molecules, the C-O bond away from the C=C bond that was observed to be weaker in the MD simulations was also the bond with the lowest bond energy, showing agreement with the experiment. However the bond dissociation energy between the different C-C bonds are in the range of 2 kcal/mol which is relatively small when compared to the almost 40 kcal/mol difference from the C-C bonds to the weak C-O bonds. Another fragment study also noted that PPVE formed CF_3+ as the dominant ion [264], which was also the conclusion of the experimental paper that compared PPVE with the $C_4H_3F_7O$ isomers [**RN759**]. The fragment analysis from our trajectories disagree with these findings and show that for both molecules the three most common fragments are the same in the same order, namely CF_2, F and C_3F_7. This is due to the C=C having a high dissociation yield, generating both the CF_2 and C_3F_7 radicals in a single dissociation event. The fourth most common radical for the PIPVE molecule is CF_3 with 144 counts, much higher than the CF_3 count of 85 for PPVE, due to the central electrophore in PIPVE being surrounded by CF_3 groups. It is worth mentioning that these fragments are ions and products of electron attachment and ionisation dissociation pathways and not the neutral fragments that are observed in simulations performed in this thesis. This difference is a key motivation behind MD simulations of neutral dissociation as neutral species are difficult to track and count in experiment. Future work on developing the electrophore model will have to include not only

extending and testing of the trends but also the investigation of which simulated initial conditions correspond best to the environment experienced by the molecule within the plasma reactor as it undergoes neutral dissociation.

3.5 C_4F_6

The isomers of C_4F_6 are interesting due to the different presentations of electron density. The two molecules considered in this section are hexafluoro-1,3-butadiene (1,3-C_4F_6) and hexafluorocyclobutene (c-C_4F_6). The different functional groups of these isomers allow for the investigation into how the structure of the molecule affects the dissociation patterns. While the hexafluoro-2-butyne (a C_4F_6 isomer with a triple bond) molecule would be interesting to study, the triple bond in the middle of the molecule causes the molecule to have a very linear structure which raises convergence issues with the DFT calculations. These issues are found in both the generation of the initial equilibrium geometry and the later force calculations of said geometry, and so no trajectories were capable of being completed for this molecule. It is worth noting that these convergent problems are heavily contingent upon the choice of basis set, though performing those MD simulations with a difference basis set would undermine the ability to compare the trajectories with the other molecules simulated and so analysis of the dissociation pathways for this molecule has been left as future work.

3.5.1 1,3-C_4F_6

1,3-C_4F_6 is a molecule that presents with two C=C bonds, meaning that there are two electrophores present in the molecule. However due to the fact that the molecule is symmetrical around the middle C-C bond, the triplet states that are populated by each electrophore should be degenerate. The high levels of symmetry in the molecule also mean that there are only 4 unique bonds, the C=C bonds, the C-C bond, the outer C-F bonds and the inner C-F bonds, the dissociation yields of which are presented in Fig. 3.59. Combining this with the fact that the molecule is small does not allow for a detailed application of the

electrophore model. As predicted, the C=C bonds have the highest bond type dissociation yield of the bond types at 22% which is consistent with prior studied molecules and the electrophore model with Fig. 3.60 showing that the C=C bonds dissociate equally. Interestingly however, 1,3-C_4F_6 is the first molecule considered thus far where the most common bond type to break first in a trajectory is the C-F bond, occurring in 63% of trajectories. The dissociative nature of the C-F bonds in this molecule is supported by the fact that 39.7% of trajectories contain only C-F dissociation events. Another uniqueness of the C-F bonds in the 1,3-C_4F_6 molecule is that their average dissociation yield of the C-F bonds is higher than the C-C bond at 11% vs 7.8% respectfully. The vast majority of the C-F dissociations are due to the C#2-F environment which has the individual highest dissociation yield in the molecule. The first bond breaking events in a trajectory also occur fairly late, with the C-F bonds having the earliest average time to be 70.7 fs. The electrophore C=C bond actually has the last average time for the first bond to break in a trajectory at 157.1 fs, though is a much more common occurrence than the C-C bond.

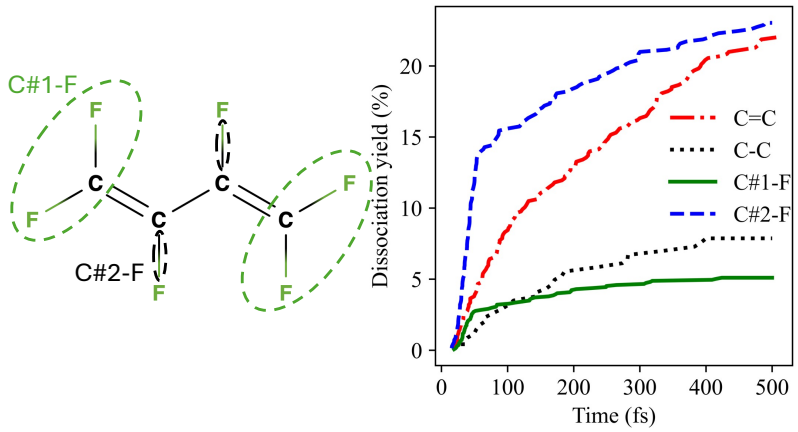

Figure 3.59: Dissociation kinetics of 1,3-C_4F_6 for each bond type over 382 triplet state trajectories at 5000 K. A dissociation event is defined as the first timestep at which a bond length exceeds 5 Bohr. Kinetics are normalised by the total number of bonds of each type present in the molecule.

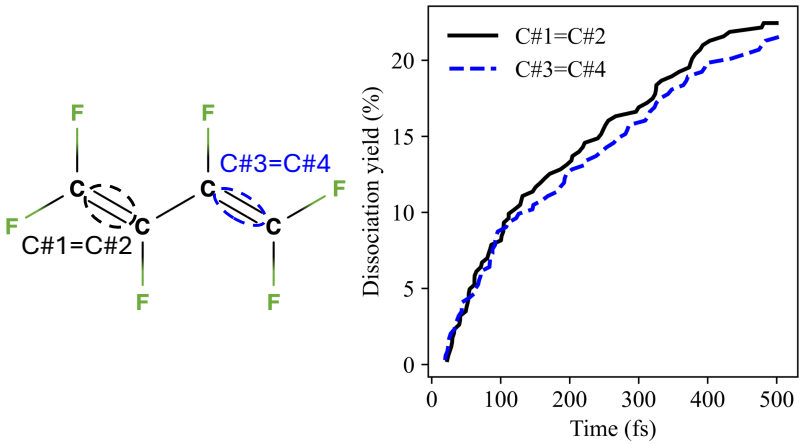

Figure 3.60: Dissociation kinetics of 1,3-C_4F_6 for each C-C bond environment over 382 triplet state trajectories at 5000 K. A dissociation event is defined as the first timestep at which a bond length exceeds 5 Bohr. Kinetics are normalised by the total number of bonds of each type present in the molecule.

3.5.2 c-C_4F_6

c-C_4F_6 is the C_4F_6 isomer with the most similarities to the c-C_4F_8 molecule commonly used as a plasma precursor due to their cyclic structure. In fact the only difference between the two molecules is the introduction of the C=C bond and the consequent change in the number of fluorines present.

The overall dissociation yields in Fig. 3.61 show a more typical electrophore behaviour with the C=C bonds not having the highest dissociation yield, but the highest number of initial dissociations. Despite the C-C bond being the most commonly broken first in a trajectory, when a C=C bond breaks first in a trajectory it occurs rapidly, with a an average time of 40.8 fs, suggesting that it is the site of the initial localisation. This is three times faster than when the C-C is the first bond to break in a trajectory with an average time of 127.8 fs. It is worth noting that while the C=C dissociation yield is not the highest in the c-C_4F_6 molecule, the dissociation yield of 19.9% is comparable to the C=C bond dissociation yield found in the 1,3-C_4F_6 molecule. The average C-C dissociation

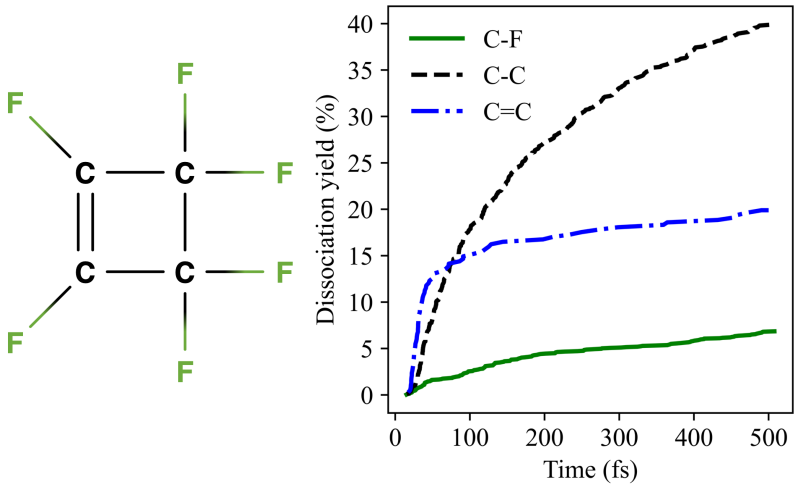

Figure 3.61: Dissociation kinetics of c-C_4F_6 for each bond type over 382 triplet state trajectories at 5000 K. A dissociation event is defined as the first timestep at which a bond length exceeds 5 Bohr. Kinetics are normalised by the total number of bonds of each type present in the molecule.

yield is, however, very different in the c-C_4F_6 molecule than the 1,3-C_4F_6 as the average yield is the highest in the molecule at 39.9%. The average C-F bond dissociation yield is 6.8%, only a percentage lower than in 1,3-C_4F_6 despite the significant increase in C-C dissociations. This suggests that the cyclic structure of the c-C_4F_6 molecule is more conductive to bond dissociation.

The dissociations of the C-C bonds early in the propagation are fairly identical with their dissociation yields (shown in Fig. 3.62) beginning to diverge. The final dissociation yields of the C#1-C#2 and C#3-C#4 are practically identical at approximately 35% which can be expected by the symmetry of the environments. The other C-C bond that is opposite of the C=C bond has the highest dissociation yield of any bond in the c-C_4F_6 molecule at 49.5%. The fact that this separation occurs at a later point of the trajectory could be explained by the fact that the C=C bond dissociates and therefore discourages the C#1-C#2 and the C#3-C#4 bond from dissociating. The C-F bonds (shown in Fig. 3.63) however have a higher average dissociation yield for the C-F bonds bonded to the carbons

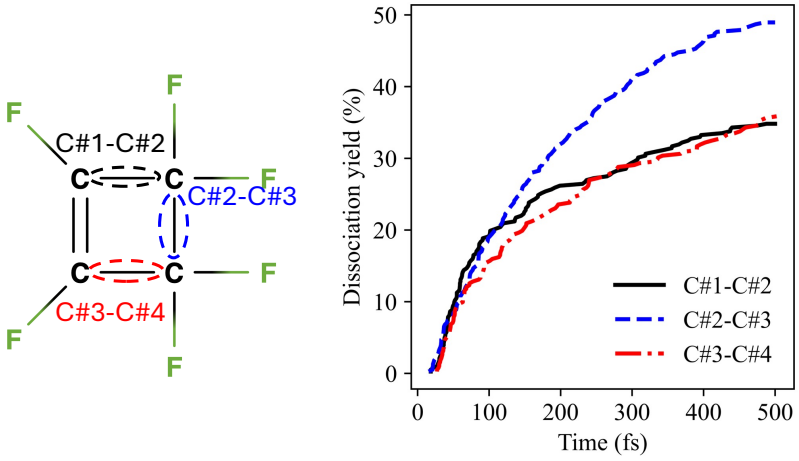

Figure 3.62: Dissociation kinetics of c-C_4F_6 for each C-C bond environment over 382 triplet state trajectories at 5000 K. A dissociation event is defined as the first timestep at which a bond length exceeds 5 Bohr. Kinetics are normalised by the total number of bonds of each type present in the molecule.

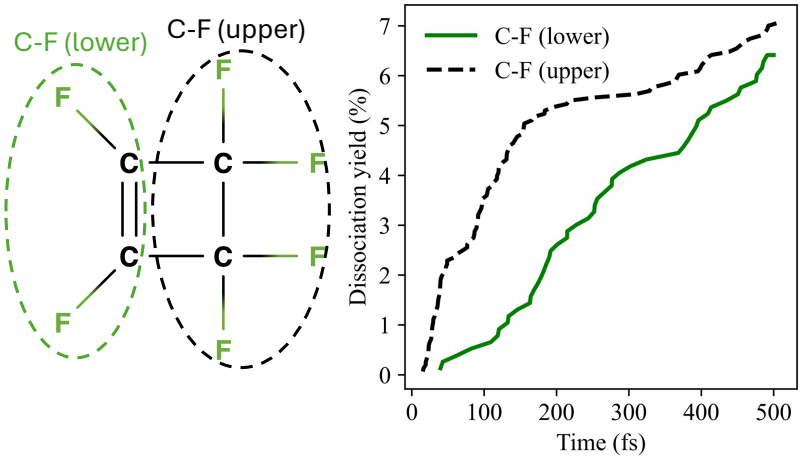

Figure 3.63: Dissociation kinetics of c-C_4F_6 for each C-F bond environment over 382 triplet state trajectories at 5000 K. A dissociation event is defined as the first timestep at which a bond length exceeds 5 Bohr. Kinetics are normalised by the total number of bonds of each type present in the molecule.

involved in only the C-C bonds (upper C-F bonds) than the C-F bonds bonded to the carbons involved in the C=C bond (lower C-F bonds). This statement is even stronger in terms of pure number of dissociations as the environments away from the C=C bond have a higher number of fluorines. The upper C-F bonds also have a higher number of initial dissociations and of the 20% of the trajectories that begin with a C-F dissociation, 90% of those trajectories begins with a dissociation of the upper C-F bonds. This behaviour is fairly typical within the context of the electrophore model where a C=C bond causes a greater increase in the dissociation yields of adjacent C-X bonds rather than the C-X bonds involving the carbons involved in the C=C electrophore itself. However neither of the C-F environments of the c-C_4F_6 present with the extensive number of dissociations observed for the inner C-F environment of 1,3-C_4F_6, as the cyclic molecule experiences many more C-C bond dissociations which does not occur readily in the more linear 1,3-C_4F_6 molecule. The final comparison between the C_4F_6 isomers is the total number of dissociations, with an overall average dissociation yield for 1,3-C_4F_6 of 13.2% and 18% for c-C_4F_6. This suggests that the singular electrophore combined with a more compacted space due to the cyclic structure greatly increases the molecule's readiness to dissociate, particularly in this case through the C-C bonds.

3.5.3 Basis set dependency

As 1,3-C_4F_6 is a molecule of great industrial interest, it was chosen to be a test of the simulations dependence on the choice of basis sets. The standard basis used throughout this thesis is the 6-31+G* basis set which was chosen to as a balance between basis set size (and therefore accuracy) and the computational cost. The basis set also contains diffuse functions which are necessary to properly describe the multiple bond dissociations events that the MD trajectories experience. In order to properly present the electrophore model and MD simulations as a useful tool to industry, it requires to be shown that the electrophore effects do not only appear for a singular basis.

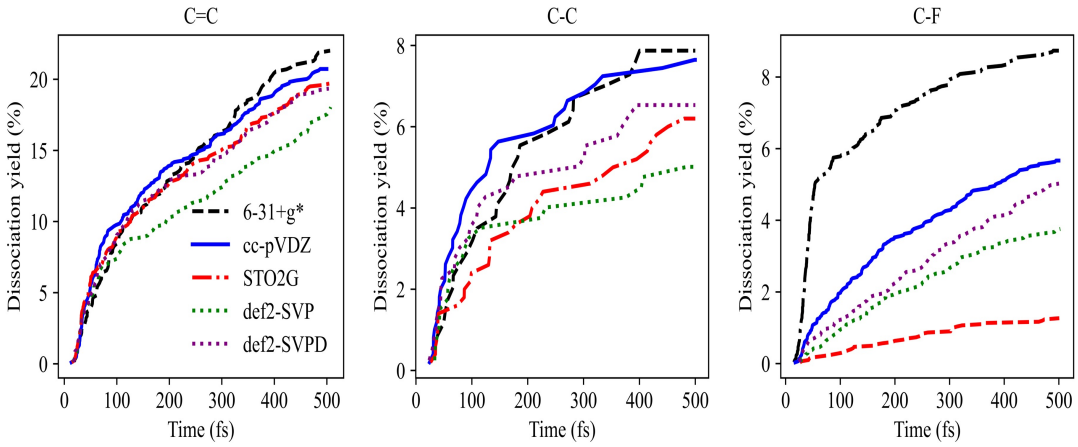

Figure 3.64: Dissociation kinetics for 1,3-C_4F_6 at 5000 K, comparing the 6-31+G*, cc-pVDZ, STO-2G, def2-SVP and def2-SVP basis sets.

Surprisingly almost all basis sets, including the smallest STO-2G, approximately matches the dissociation kinetics of the electrophore C=C bond when compared with the standard basis set 6-31+G* as shown in Fig. 3.64. The only large exception to this is the def2-SVP basis set which upon the addition of the diffuse functions forming the def2-SVPD basis set, produces a result closer to the standard. However for the rest of the bond types, the smaller basis sets generally produce much lower dissociation yields, with the C-F bonds seeing an almost five times reduction from the 6-31+G* basis set to the minimal STO-2G. This suggests that the smallest basis set works rather well in predicting the initial localisation of the triplet state where C=C bonds are acting as an electrophore. The spread of the dissociative character into the surrounding anti-bonding orbitals of adjacent bonds is less well captured. Across all bond types it is worth noting that the inclusion of diffuse functions in the def2-SVPD basis set results in a higher dissociation yield. This is because the diffuse functions of are capable of capturing the bond dissociation events for the stronger bonds in the molecule, such as the C-F in the propagation after the dissociation of another bond, the diffuse functions are capable of capturing more bond dissociation events.

There are also discrepancies not only in the dissociation yields of the bond environments, but in the dissociation pathways. With the 6-31+G* basis set, the C-F bond is the most common bond to dissociate first occurring in 60% of trajectories. This is underestimated by all other basis sets by a significant amount, with the minimal basis set reporting the lowest at only 9% and the other basis sets often report approximately 30% of trajectories. In these cases, the bond most commonly broken first is the electrophore, the C=C bond, again suggesting that the other basis sets are still capable of capturing the initial localisation of the excitation. There is also a comparison to be made in terms of the number of dissociations for each basis set. While the graphs shown in Fig. 3.64 are sufficient enough to conclude that the 6-31+G* basis set trajectories have the most dissociations, it is not shown that 19.3% of these trajectories do not contain any bond dissociation events. This percentage is less than half of that reported by other basis sets, with the minimal basis set having 60% of its trajectories not contain any dissociation events. Once again comparing the def2-SVP and def2-SVPD basis sets shows that the diffuse basis set lends itself more to bond dissociation as they have 52.4% and 46.6% of trajectories not dissociating respectively. Therefore further investigations into the basis set dependency should focus the choice of basis sets to diffuse basis sets only. Studying a larger diffuse basis set would also be interesting to discover the efficacy and accuracy of the commonly used 6-31+G* basis set. It is also important to expand further basis set tests to molecules containing the oxygen atom acting as an electrophore in order to gather a sample set that covers the a wider range of molecules whose dissociation can be predicted via the electrophore model.

3.6 Conclusions

The combined MD simulations of multiple different molecules are capable of developing concepts in terms of trends and patterns. It has also shown that, as expected, the triplet state trajectories contain a much higher number of dissociations when compared to the singlet state trajectories of the same molecule,

with the largest change being in the C-H bonds which are very dissociative in the triplet state. There is also a consistent increase of initial bonds breaking particularly in the C=C and oxygen containing bonds which have been identified to be electrophores.

Via comparing these dissociation pathways of the different molecules that have been identified in other works as industrially relevant, it is possible to formulate preliminary trends of triplet state driven neutral dissociation after excitation via electron impact:

Rule 1: C=C bonds and oxygen atoms can act as an electrophore, localising the excitation (and therefore bond dissociations) when a molecule is excited to the triplet state via electron impact.

All molecules considered in this chapter exhibited dissociation pathways consistent with the electrophore model. The localisation of the triplet state excitation causes bonds containing the electrophore to dissociate earlier in the propagation. The distance between the electrophore and the atoms within the different bonds in the molecule is a key predictor for which bonds will dissociate the most.

Rule 2: The dissociation of hydrogen containing bonds is consistent across different molecules: occurring rapidly. These dissociations can have consequences on the subsequent dissociation pathways of the molecule.

Across the three hydrogen containing molecules within this chapter, the hydrogen containing bonds had a large number of initial dissociations. This consistent behaviour is exacerbated by the high temperature of the simulations, causing the C-H bond to occasionally dissociate with a frequency approximate to the most dissociative bonds in the molecule. As multiple bonds from a single centre are discouraged from dissociating within the same trajectory, the hydrogen containing bonds can limit the dissociations of the other bonds of the atom bonded to

the hydrogen. They can also be used as a stopgap between the C-F bonds in a molecule and the electrophore that localises the dissociations. It is worth noting that the hydrogen atoms have always been adjacent to the electrophore and so the observed dissociation yields may not always be consistently as high.

Rule 3: The functional group of the oxygen atom does not impact its ability to act as an electrophore, it can have a strong effect on the dissociation pathways.

This rule can be seen as a specific subset of rule 2, where substituting the ether functional group of the oxygen to an alcohol causes excessive breaking of the O-H bond, as the weak hydrogen containing bond is bonded to the electrophore. This consequently significantly reduces the dissociation yield of the C-O bonds as the oxygen atom has already experienced one dissociation.

Rule 4: Due to its nature as an electrophore the C=C bond can dissociate more frequently than the single C-C bond, at least initially.

In both isomers of $C_5F_{10}O$ (PPVE and PPVE) the C=C bond has the highest dissociation yield within the molecule. For the C_4F_6 isomers, the C=C bond is either has one of the highest dissociation yields (as in 1,3-C_4F_6) or has the largest number of the initial dissociations (as in c-C_4F_6). This is due to the C=C bond acting as an electrophore, meaning that the triplet state dissociative character is initially localised around this bond, causing the initial and/or prominent dissociations.

Rule 5: The presence of multiple electrophores within a molecule can have a cumulative effect on nearby bonds, greatly increasing the number of dissociations.

While only one electrophore will localise the triplet state excitation to a given

part of the molecule, the effect of multiple adjacent electrophores is cumulative resulting in much higher dissociation yields of bonds that experience proximity to both. The best evidence for this rule is the C#4-F bond environments in the PPVE and PIPVE molecule, where the singular bond accounts for over half of the C-F bonds dissociated in each molecule.

These trends can be used, at least to an extent, in order to accurately predict the dissociation of these PFAS molecules. The order of the dissociation yields for the bond types present within a given molecule can also be qualitatively predicted. The resulting general dissociation bond yields for the molecule can be vaguely determined from the strength of the bond in the triplet state. The hydrogen containing bonds are fairly weak and so dissociate fairly rapidly, and in certain molecules up to a single C-H bond is broken from each possible carbon in every trajectory. The C-C bonds often dissociate with high dissociation yields that sometimes rival those of the C-H bonds, whereas the C-F bonds are consistently the least dissociated when averaged across the molecule. Within the individual bond types, the dissociation yields can be generally ordered in terms of their distance to the electrophore; the closer the particular bond to the electrophore, the higher its dissociation yield. There are exceptions to this general rule, with the most present example being that rapid dissociation of C-H bonds near the electrophore can decrease the dissociation yield of the C-C or C-F bonds that are also near the electrophore.

It is important to note that while these 5 trends are capable of determining the order of the dissociation yields for the molecules considered in this chapter, these molecules can only be taken as a small sample and not perfectly representative, especially in terms of functional groups. In order to expand these preliminary trends into a more concrete overview, more molecules containing different arrangements of functional groups need to be considered, at a range of different temperatures. Further simulations can also reveal in more detail how the dissociation pathways of the triplet state differ from the dissociation pathways of the singlet state usually considered. NAMD simulations will also provide insights into

how multiple electrophores interact, particularly which electrophore is the most dominant and will therefore localise the excitation to the lowest triplet state.

Chapter 4

Testing of triplet state dissociation trends

The development of a theoretical framework for studying processes such as neutral dissociation on the triplet state allows for a level of flexibility that is not present in experiment. Once the workflow of the simulations has been designed, the limit of simulation is essentially equivalent to the computational power available. With access to high powered computing, it is possible to test multiple molecules with a just small change to an input file. Therefore it is possible to easily test theories through test molecules as opposed to focusing on molecules that are potential candidates for plasma precursors. This allows for the direct testing of the electrophore trends of triplet dissociation found established in Chapter 3.

The simulation of these PFAS industrially relevant molecules that have been previously identified by other works and studies has revealed the presence of electrophores and their effect on the dissociation pathways undertaken after excitation via electron impact. These trends appear fairly consistent, leading to the 5 general triplet state driven neutral dissociation trends presented in the conclusion of the previous chapter. There are, however, several questions that remain when considering these dissociation processes, whether the trends are currently incomplete (which functional groups can act as an electrophore) or based on insufficient data (does the alcohol always affect dissociation pathways by limiting the C-O dissociation?). The advantage of the development of theoretical methods is their ease of transfer of use. Studying a new molecule not does require a re-design and preparation of experiment but rather a simple resubmission of input files. This then presents essentially a sandbox where the electrophore trends developed for triplet state driven neutral dissociation may be tested and refined.

4.1 Computational Details

The molecular dynamics simulations presented in this chapter were performed using the same electronic structure methods, initial condition generation, and propagation algorithms as described in detail in Section 3.X. In brief, electronic structure calculations were carried out using density functional theory as implemented in QChem, with triplet excited states described using standard DFT or

spin-flip TDDFT as appropriate with the 6-31g+* basis set and the B3LYP exchange functional. Nuclear dynamics were propagated using the Ehrenfest-based algorithm described in Chapter 3, with identical time-stepping, force evaluation, and dissociation criteria.

Unless otherwise stated, all simulation parameters, including time step, basis set, functional choice, temperature treatment, and post-processing procedures, were identical to those employed in Chapter 3. Any deviations from this protocol are explicitly stated in the relevant sections of this chapter. The exception of note is that chapter 4.4 contains the only calculations that employ trajectories on multiple PES. For these molecules, a set of trajectories begin on each PES involved in propagation. The plotting of the populations of these states as a function of timesteps allows to see how long lived is the excited PES. The investigation of the excited triplet PES allows for the testing of the assumption that only the lowest excited state by discerning the difference in dissociation kinetic profiles from the trajectories starting on each PES.

4.2 The impact of the oxygen functional group

Of the four molecules considered thus far that contain oxygen, three of them are ethers with the remaining molecule being an alcohol. There are then natural questions that arise that the molecules considered thus far have lacked sufficient range and variety to provide answers. Is the rapid dissociation of the O-H bond a feature of all alcohols, or a feature of $C_4H_2F_7OH$? Are there certain features of an alcohol that could limit the O-H breaking, or increase the rate of dissociation of the C-O bond? What are the factors that determine which of the C-O bonds are favoured to dissociate in the ethers?

In order to provide insight to these questions, it is possible to select certain molecules to be studied. To begin answering questions about the different molecules, it is natural to first investigate the simplest alcohols, such as methanol and propanol.

While the low number of 100 trajectories is too low for perfect quantitative

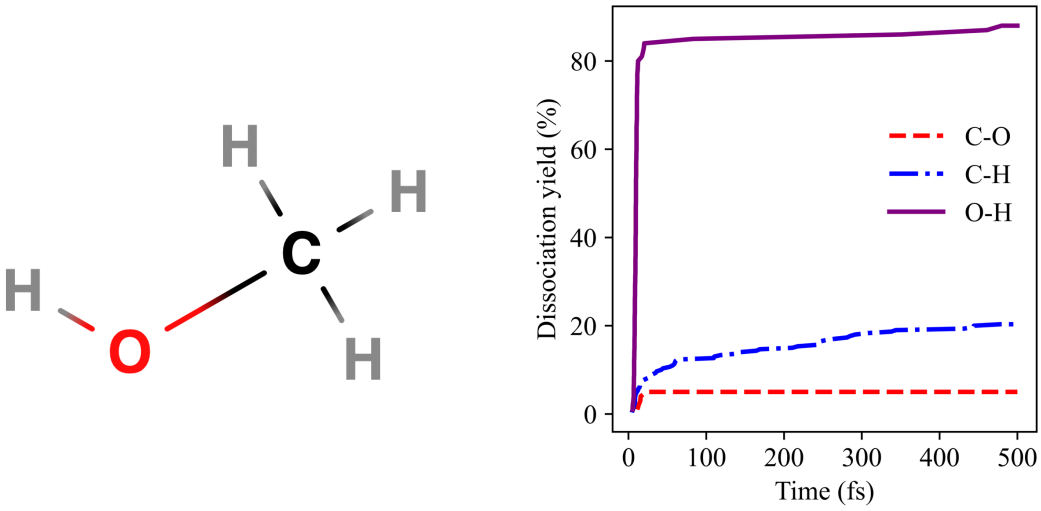

Figure 4.1: Dissociation kinetics of methanol for each bond type, obtained from 100 independent trajectories propagated on the lowest triplet potential energy surface at 5000 K. A dissociation event is defined as the first timestep at which a bond length exceeds 5 Bohr. Kinetics are normalised by the total number of bonds of each type present in the molecule.

accuracy, it is still sufficient to conclude that general pattens in the dissociation pathway, in this case that methanol follows the same general trends as the $C_4H_3F_7O$ alcohol. Fig. 4.1 shows that the O-H bond is rapid to dissociate and clearly the most dissociative bond in the molecule, with an average dissociation time of 21.9 fs. However after removing the 3 outlier dissociations that occur late in the propagation, the average dissociation time reduces to just 7.8 fs. Interestingly, the dissociation yield of the O-H bond is also approximately equal to that seen in $C_4H_2F_7OH$. The dissociation yield can also be found to be consistent for larger alcohols as 400 MD simulations have also been run for propanol shown in Fig. 4.2. Not only is the difference between methanol and propanol in terms of the O-H bonds is negligible, the average dissociation yield of the C-H bond is also fairly similar. Investigation within in the individual C-H environments for propanol (shown in Fig. 4.3) also show the alcohol functional group acting as the electrophore as the C#1-H bonds have the highest dissociation yields at 25%. The other environments do fall into the expected order hypothesised by the electrophore model, though this is partly due to the differing number of hydrogens in the C#2-H and C#3-H bond. The analysis of both of these molecules confirms that the alcohol effect seen in the dissociation pathways of the $C_4H_2F_7OH$ is consistent across alcohols and not a feature of that specific molecule.

4.3 The hydrogen buffer

4.3.1 The secondary effect of C-H bond dissociations

While the C-H dissociation kinetics remain relatively similar (i.e rapid initial dissociations before tailing off for the rest of propagation) throughout each molecule, the inclusion of hydrogen containing bonds can in fact have a secondary effect on the other bonds present within a molecule as stated in trend 2 of the triplet state driven neutral dissociation trends posited in the conclusion of the previous chapter. For example, in both n-$C_4H_3F_7O$ and i-$C_4H_3F_7O$, the C-O bond containing the carbon bonded to hydrogens has different behaviour where a very large number of initial dissociations is followed by a similar tapering of

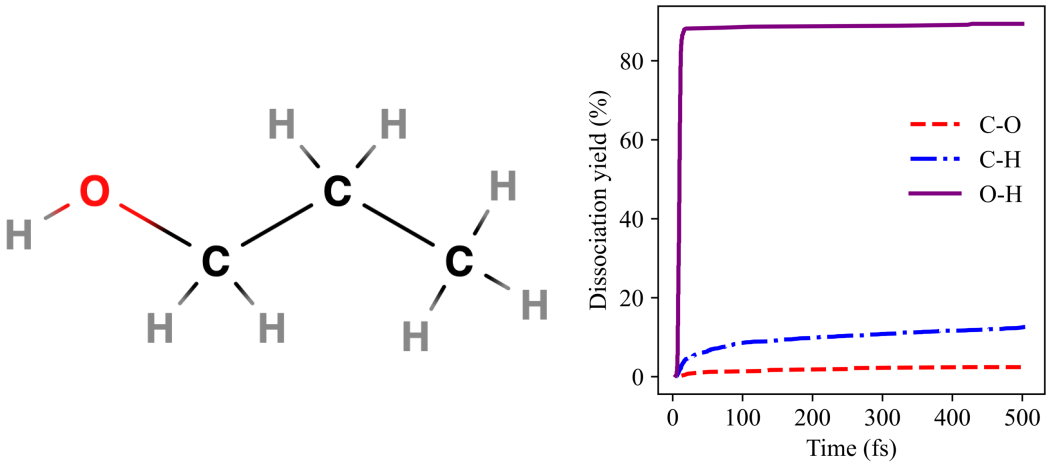

Figure 4.2: Dissociation kinetics of propanol for each bond type over 400 lowest triplet state trajectories at 5000 K. A dissociation event is defined as the first timestep at which a bond length exceeds 5 Bohr. Kinetics are normalised by the total number of bonds of each type present in the molecule.

the C-H bonds. It can therefore be suggested that as the hydrogen containing bonds are very weak at the high temperatures considered in the MD simulations, their near immediate dissociation can discourage the dissociation of bonds on the same carbon, essentially dampening the number of dissociations of the other bonds. This effect can also be seen in the C-O bond of the alcohol isomer of $C_4H_3F_70$. To show this effect in its most simplest form, two molecules are considered. The first molecule trifluoromethyl methyl ether ($C_2F_3OH_3$) shows how the dissociation kinetics found for the C-O bonds in the $C_4H_3F_7O$ isomers is a result from the influence of the methyl group.

The overall dissociation of the molecule in Fig. 4.4 appears standard with that expected from the dissociation of previous molecules in terms of the bond type order. The C-H bonds break with the largest dissociation yield of approximately 35%, meaning that, not unusually, on average 1 C-H bond is broken per trajectory, as the removal of one hydrogen atom heavily discourages another. This mirrors both the kinetics and the final dissociation yields found for the C-H bonds in the i-

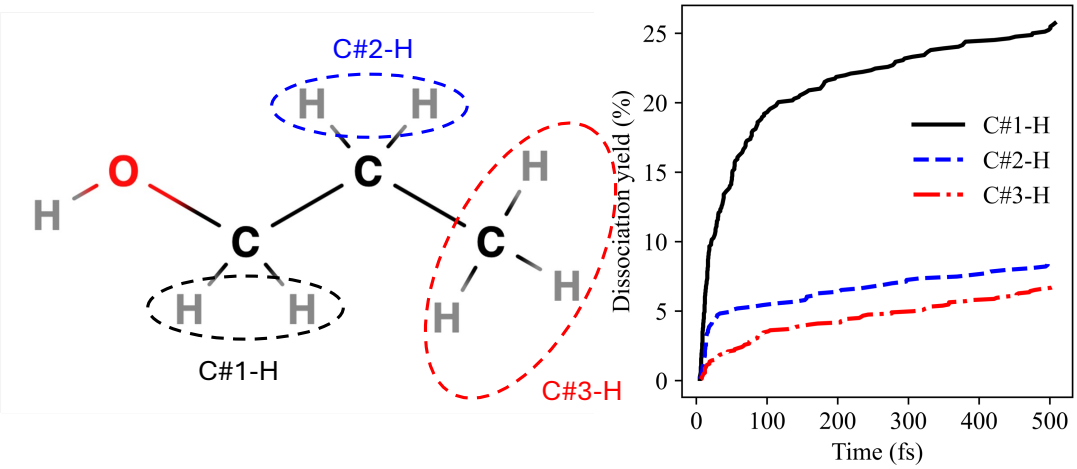

Figure 4.3: Dissociation kinetics of propanol for each C-H bond environment over 400 lowest triplet state trajectories at 5000 K. A dissociation event is defined as the first timestep at which a bond length exceeds 5 Bohr. Kinetics are normalised by the total number of bonds of each type present in the molecule.

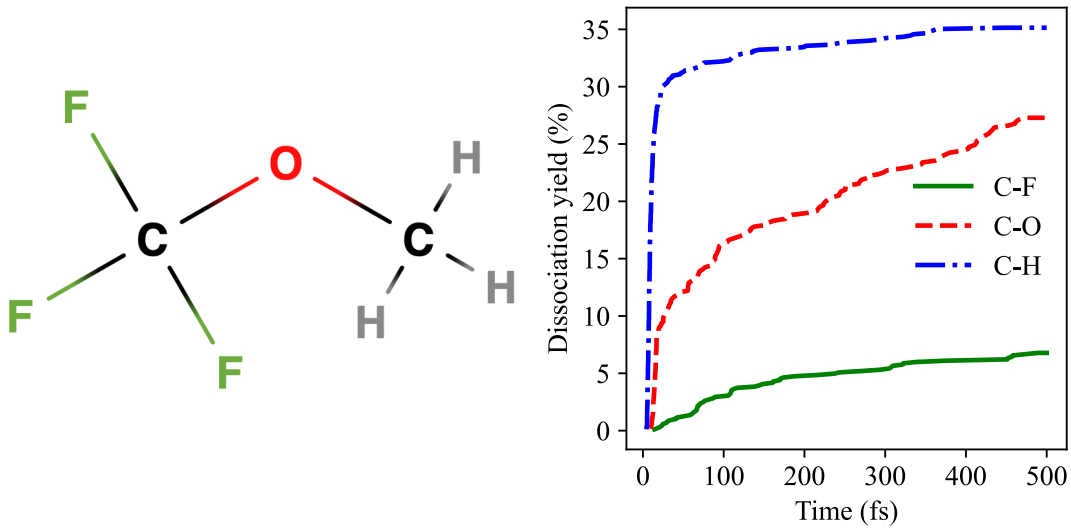

Figure 4.4: Dissociation kinetics of $C_2OF_3H_3$ for each bond type over 250 lowest triplet state trajectories at 5000 K. A dissociation event is defined as the first timestep at which a bond length exceeds 5 Bohr. Kinetics are normalised by the total number of bonds of each type present in the molecule.

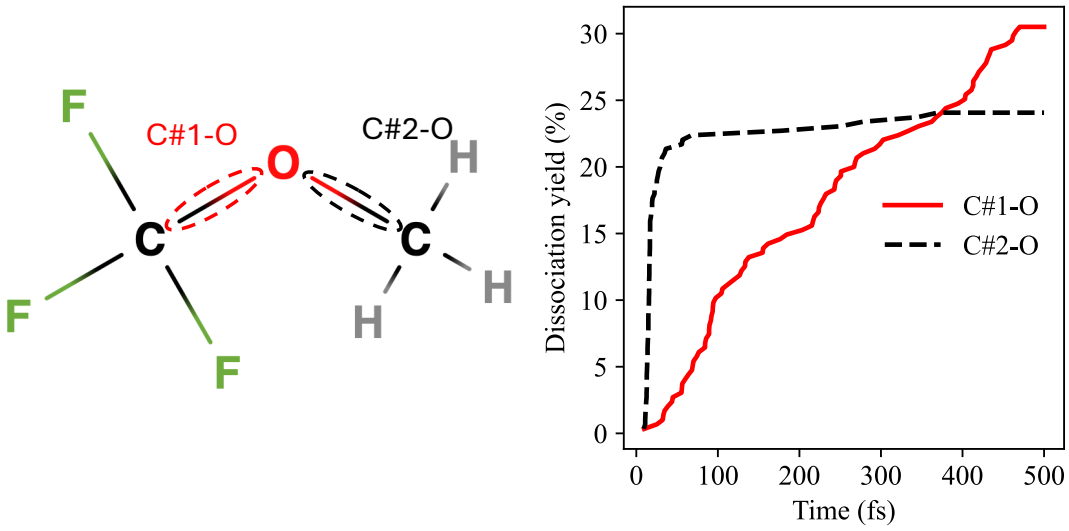

Figure 4.5: Dissociation kinetics of $C_2OF_3H_3$ for each C-O bond environment over 250 lowest triplet state trajectories at 5000 K. A dissociation event is defined as the first timestep at which a bond length exceeds 5 Bohr. Kinetics are normalised by the total number of bonds of each type present in the molecule.

$C_4H_3F_7O$ molecule. The C-O and the C-F bonds similarly have usual dissociation kinetics where the strong C-F bonds have a relatively low average dissociation yield and the C-O bonds not only have a high dissociation yield but also the number of initial dissociations signifying it's role as an electrophore.

Investigating the individual C-O bonds in Fig. 4.5 within the molecules reveals that their behaviours are rather different. The C#1-O bond containing the carbon bonded to fluorines has a rather linear dissociation yield, however the C#2-O bond has a dissociation profile that more closely resembles that of the C#4-O shown in the n-$C_4H_3F_7O$ molecule. This is due to the dissociation of hydrogens discouraging the later dissociations in both molecules. However the interesting fact is not only that the dissociation of the hydrogens appear to stop late-time dissociations of the C#2-O bond but that it appears to be encouraging early dissociations. In 81% of the trajectories ran for this molecule, the fist bond

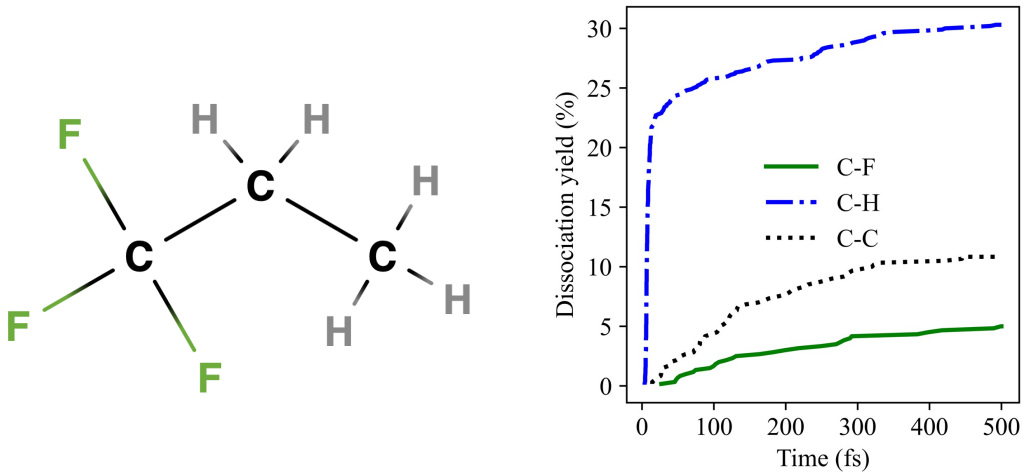

Figure 4.6: Dissociation kinetics of $C_3H_5F_3$ for each bond type over 200 lowest triplet state trajectories at 5000 K. A dissociation event is defined as the first timestep at which a bond length exceeds 5 Bohr. Kinetics are normalised by the total number of bonds of each type present in the molecule.

dissociated is the C-H bond, which can be expected due to the rapid dissociation time frame, occurring at an average of 9 fs. However in the 18% of trajectories where the C-O bond broke first, it was almost exclusively the C#2-O bond that dissociated (98% of the time). These initial dissociations also account for 72% of all C#2-O dissociations. In contrast, the C#1-O bond only breaks initially once, and therefore breaks after a C-H bond in all other instances. As this high number of early dissociations of the C#2-O bond also occurs with the C#4-O bond of the n-$C_4H_3F_7O$ suggest that the methyl group has the effect of directing the movement of the triplet state excitation localised by the electrophore, which then causes a competition of dissociations between the C-O and C-H bonds. This effect is not however observed in the i-$C_4H_3F_7O$, potentially due to the increased stability of the isofluoropropyl radical formed.

The next molecule is another small and simple molecule, 1,1,1-trifluoropropane ($C_3H_5F_3$), whose overall dissociation yields are shown in Fig. 4.6 which shows

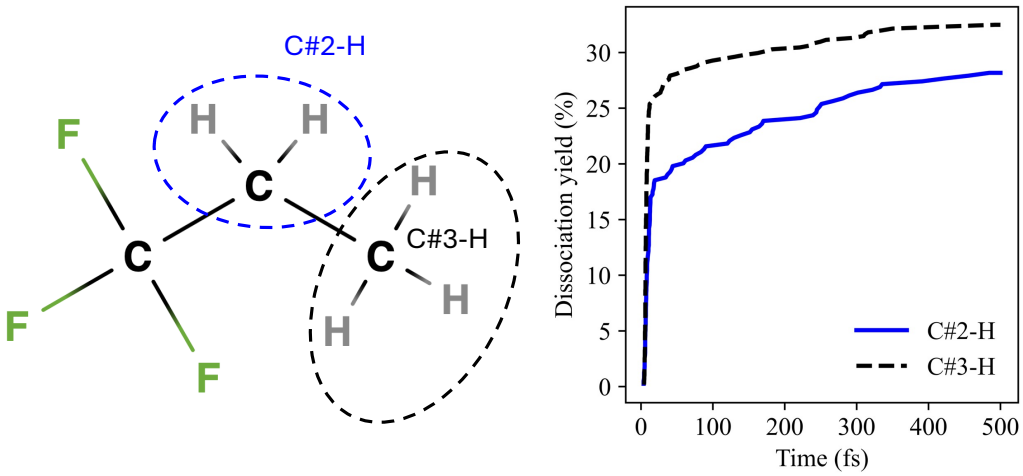

Figure 4.7: Dissociation kinetics of $C_3H_5F_3$ for each C-H bond environment over 200 lowest triplet state trajectories at 5000 K. A dissociation event is defined as the first timestep at which a bond length exceeds 5 Bohr. Kinetics are normalised by the total number of bonds of each type present in the molecule.

how the presence of hydrogen containing bonds can affect more than just C-O bonds. As expected when both molecules contain a single CF_3 group as their only C-F bonds, the C-F dissociation kinetics are not too different between the $C_3H_5F_3$ and $C_2OF_3H_3$ molecules, though the dissociation yield is slightly higher in the molecule containing an electrophore. However due to the increased number of hydrogens in the molecule, the average dissociation yield across all C-H bonds lowers (though only slightly) with an average dissociation yield of 31%. Further inspection of the two individual C-H bond environments in Fig. 4.7 shows that the CH_3 group (C#3-H) that was also present in $C_2OF_3H_3$ has an almost identical dissociation yield, and the average dissociation yield reduction seen is from the C-H bonds on the middle CH_2 group (C#2-H) having a lower dissociation yield of 27%. The main feature of this molecule that should be highlighted is the difference in both yields and kinetics of the two C-C bonds.

The individual C-C bond environments are considered in Fig. 4.8. The C#1-

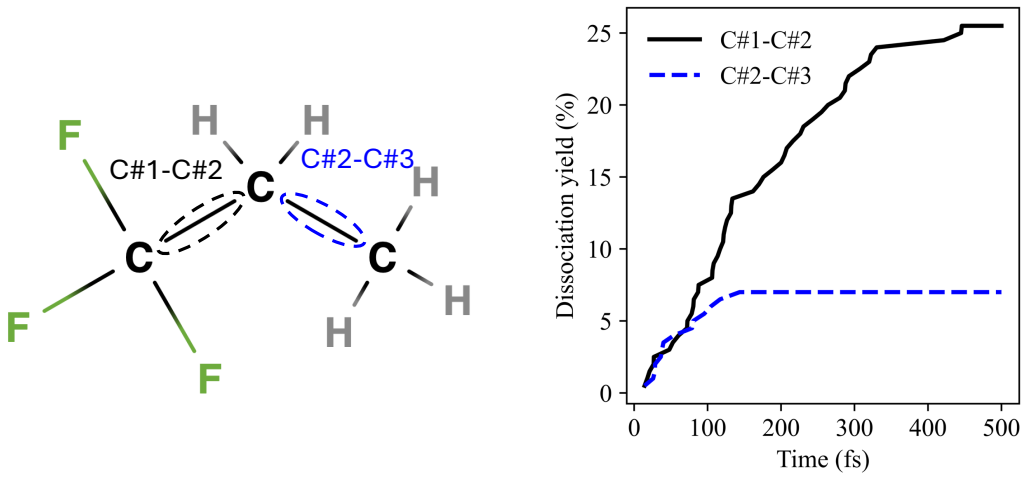

Figure 4.8: Dissociation kinetics of $C_3H_5F_3$ for each C-C bond environment over 200 lowest triplet state trajectories at 5000 K. A dissociation event is defined as the first timestep at which a bond length exceeds 5 Bohr. Kinetics are normalised by the total number of bonds of each type present in the molecule.

C#2 bond has what could be described as typical C-C bond kinetics, a fairly linear increase in number of dissociations with a final dissociation yield of 25%. While the C#2-C#3 bond has the same initial number of dissociations as the other C-C bond, the dissociation yields begin to differ around and after 150 fs, where there are not many dissociations of the C#2-C#3 bond. This significant difference in the two C-C bonds is a direct consequence of the C-H bonds present in the molecule. In 99% of trajectories, a C-H bond is the first to break meaning that almost all of the bond dissociation events (including even some C-H bonds) are occurring in a radical created after the dissociation of a C-H bond, with the C#3-H group being the first to dissociate 70.5% of the time. As the C-F bonds are bonded to a carbon with no C-H bonds, the dissociation yield of the C-F bonds is largely unaffected by the near immediate dissociation of the C-H bonds. However, the C-C bonds are indeed affected. Regardless of which C-H bond dissociates, the C#2-C#3 bond is discouraged from dissociating as either carbon (or both) has already participated in a bond breaking event. The C#1-C#2 bond is only discouraged by the dissociation of the C#2-H bonds or the dissociation of the C-F bonds, which occurs much less rapidly and on a slower time frame. The effect is strengthened by the fact the C-H environment that only limits the dissociation of the C#2-C#3 bond is the C#3-H group that has the highest average dissociation yield (despite the increased number of C-H bonds).

A more quantitive effect can be seen when investigating the actual dissociation pathways undertaken by both molecules. The most common outcome for a trajectory in both molecules is a single dissociation of a C-H bond from the methyl group, with this occurring in 42% of trajectories in $C_2OF_3H_3$ and 27% of trajectories for $C_3H_5F_3$. While a trajectory containing only this specific dissociation does appear to be a lot more frequent in the oxygen containing molecule, it is important to note that there is another C-H environment in $C_3H_5F_3$. When searching for trajectories in which there are only C-H bonds broken, but including any number of dissociations and from any environment, this accounts for 45.1% of trajectories in $C_2OF_3H_3$ and 63.5% of trajectories for $C_3H_5F_3$. The second most common dissociation pathway for $C_2OF_3H_3$ is a C-H dissociation followed by the

dissociation of the C#1-O bond, occurring in 29.5% of dissociations. Similarly a common pathway that is observed in $C_3H_5F_3$ is a dissociation of the C#3-H environment followed by the dissociation of the C#1-C#2 bond which occurs 15.5% of all the trajectories and accounts for 42.5% of all trajectories that don't contain only C-H dissociations. This effect that hydrogens can have on bonds is something to consider when performing simulations at high temperatures, as C-H bonds dissociate incredibly rapidly at 5000 K, but rarely at lower temperatures such as 2000 K. While this reduction of C-H dissociations could be potentially argued to not greatly affect the C-C bonds as they tend to dissociate after the time frame of C-H bonds, it could definitively have a notable effect on the C-O bonds which when acting as an electrophore localising the triplet state excitation can dissociate very rapidly themselves.

4.3.2 $C_4H_3F_7O$ alcohol isomers

The low number of C-F dissociations occurring in the $C_4H_2F_7OH$ alcohol isomer when compared to the other $C_4H_3F_7O$ isomers can be accounted for by the hydrogens acting as a stop gap between the electrophoric oxygen and the fluorine atoms. As there exist many positional isomers of this alcohol molecule, it is possible to test the effect of moving the hydrogen atoms to other carbons.

4.3.2.1 An issue with inventing isomers

The first two isomers chosen to test this were 1,2,3,3,4,4,4-Heptafluoro-1-butanol and 1,1,3,3,4,4,4-Heptafluoro-1-butanol as it would provide results for a swapping one hydrogen with fluorine and swapping both. The hypothesis being that replacing only one hydrogen will not have a dramatic effect in increasing the C-F dissociation yield as the C-H bond on the carbon closest to the oxygen will still dissociate first, limiting the potential dissociations of the fluorine bonded to the same carbon. The advantage of a computational method is that the testing of isomer molecules is trivial as it often only requires the change of input files, with no need to redesign and perform an experiment. The reality is not always so simple though as the first two isomers selected were found to not be stable after a single

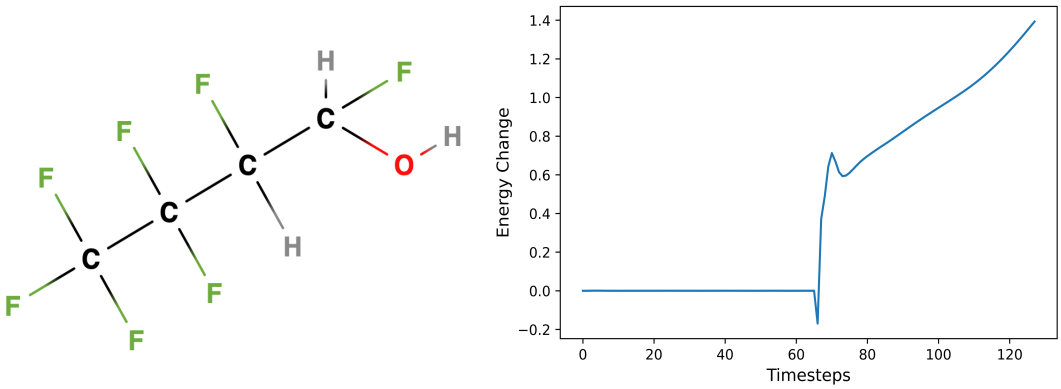

Figure 4.9: Change from initial energy for a triplet state trajectory of 1,2,3,3,4,4,4-Heptafluoro-1-butanol at 5000 K. The removal of the atom from the propagation occurs at timestep 64.

removal of an atom from propagation, which occurs readily with the O-H and C-H bond, as shown by the change in energy plotted for both molecules in Figs. 4.9 and 4.10 where the conservation of energy is lost after the removal of an atom from the propagation. This removal is done to reduce the computational cost as an atom that is sufficiently separated from the rest of the molecule will have negligible forces and a negligible effect on the forces of the rest of the molecule, and so the atom can be removed in order to speed up calculations. If the choice is made not to remove the atom then the energy is conserved for longer but eventually the same issues reappear, meaning that the molecules cannot run under the current conditions used for other molecules. The changing of these conditions, i.e. the basis set choice or temperature would not allow for faithful comparisons between molecules and so other isomers must be more carefully selected.

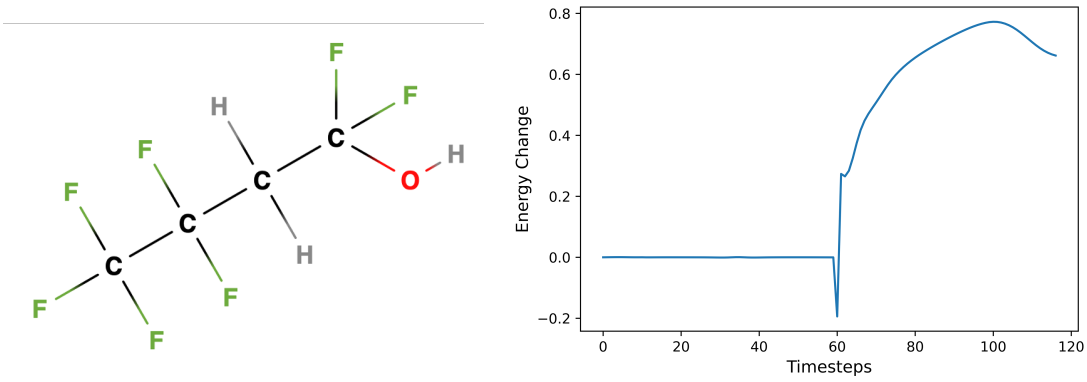

Figure 4.10: Change from initial energy for a triplet state trajectory of 1,1,3,3,4,4,4-Heptafluoro-1-butanol at 5000 K. The removal of the atom from the propagation occurs at timestep 60.

4.3.2.2 Functional $C_4H_3F_7O$ alcohol isomers

The second set of $C_4H_3F_7O$ alcohol isomers were then taken to be molecules that have a pre-existing record, being sourced in this thesis from PubChem [265] suggesting that the molecules are stable and capable of being studied. The first is 1,1,1,3,4,4,4-heptafluorobutan-2-ol ($C_4H_2F_7$-2-OH), which has the alcohol group on the third carbon of the chain as opposed to the the terminal carbon as in the original $C_4H_2F_7$-2-OH isomer; the second is fluoromethyl hexafluoroisopropanol (iso-$C_4H_2F_7OH$), where the electrophore is at the centre of a propane chain opposite a fluoromethyl group. In both molecules the distance between the electrophore and the C-F environments is shorter than in the original $C_4H_3F_7O$ molecule. This suggests that the dissociation yields of the C-F bonds should be higher. Due to the central electrophore, it is possible that all bonds in the molecule will be dissociative leading to overall higher dissociation yields and changing of the dissociation pathways.

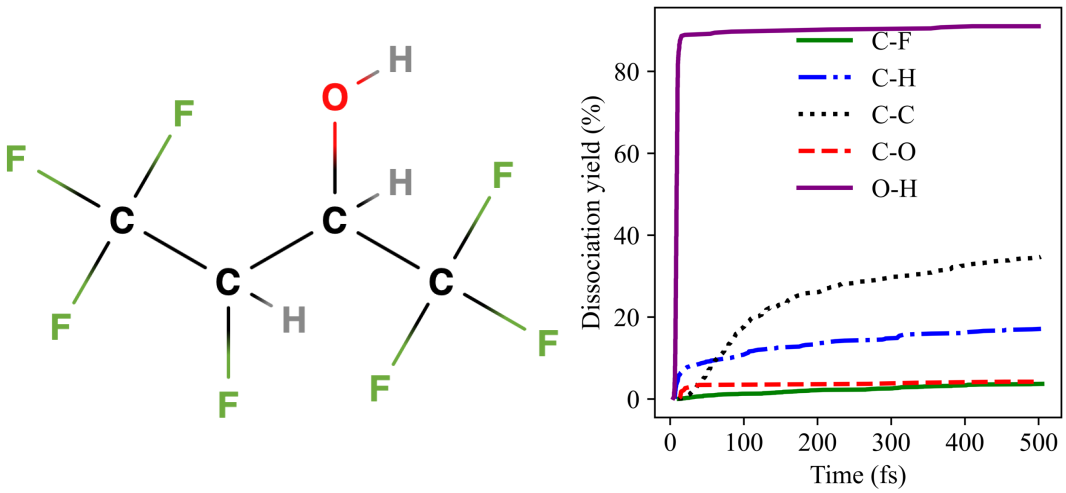

Figure 4.11: Dissociation kinetics of $C_4H_2F_7$-2-OH for each bond type over 400 triple state trajectories at 5000 K. A dissociation event is defined as the first timestep at which a bond length exceeds 5 Bohr. Kinetics are normalised by the total number of bonds of each type present in the molecule.

The overall dissociation yields for the two molecules are compared through Figs. 4.11 and 4.12. Unsurprisingly, both molecules have a very high dissociation yield for the O-H bond, which is consistent with the alcohol functional group. There are however differences in the rest of the bond types. The C-C bonds for example have a higher average dissociation yield of 41% in iso-$C_4H_2F_7OH$ compared to 35% in $C_4H_2F_7$-2-OH. This is due to the central electrophore being bonded to the carbon involved in all three C-C bonds in the molecule. The C-O bond dissociation is also much higher in the iso-$C_4H_2F_7OH$ molecule at a yield of 11.7% compared to 4.2%, as the C-O bond in the latter molecule has to compete with the O-H bond and with the dissociation of the C#3-H bond leading to a lower dissociation yield. As is common with the alcohol functional group, over two-thirds of the C-O bonds occur as the first bond broken in a trajectory. The higher dissociation yield of C-H bonds in the $C_4H_2F_7$-2-OH molecule can be explained by the fact that the two hydrogens are bonded to different carbons

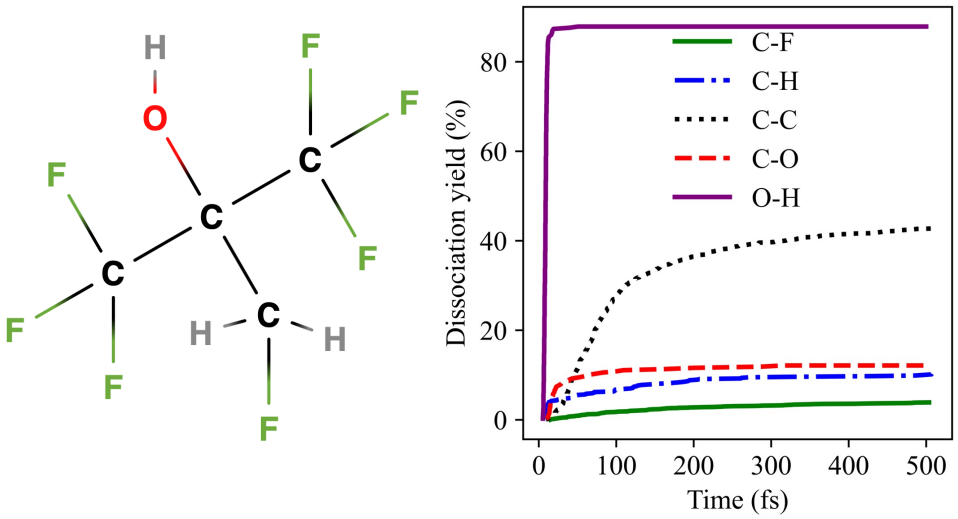

Figure 4.12: Dissociation kinetics of iso-$C_4H_2F_7OH$ for each bond type over 400 triple state trajectories at 5000 K. A dissociation event is defined as the first timestep at which a bond length exceeds 5 Bohr. Kinetics are normalised by the total number of bonds of each type present in the molecule.

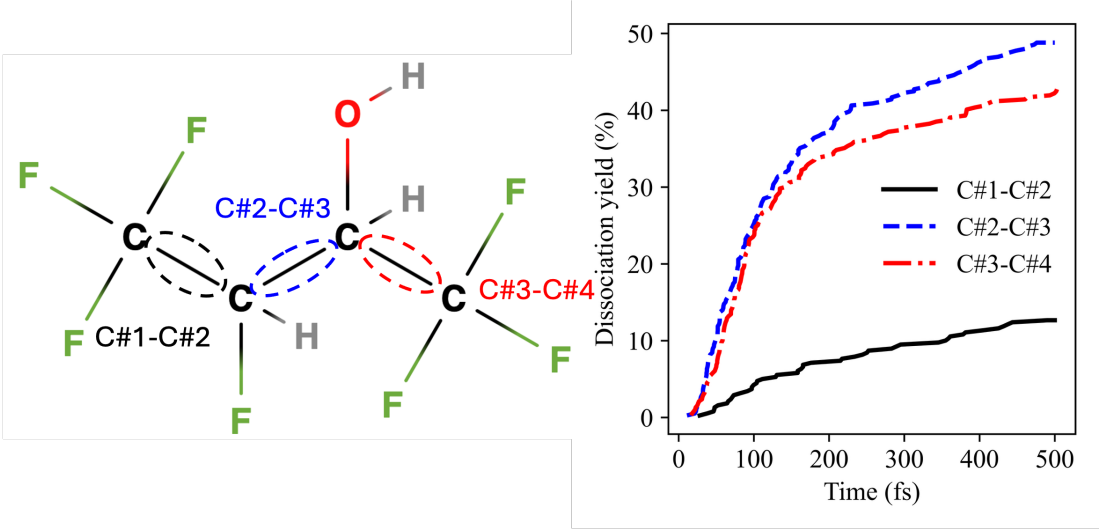

Figure 4.13: Dissociation kinetics of $C_4H_2F_7$-2-OH for each C-C bond environment over 400 triple state trajectories at 5000 K. A dissociation event is defined as the first timestep at which a bond length exceeds 5 Bohr. Kinetics are normalised by the total number of bonds of each type present in the molecule.

and so both hydrogens involved in C-H bonds can dissociate without directly discouraging the other.

The different C-C bonds in $C_4H_2F_7$-2-OH (shown in Fig. 4.13) show that the C-C bond that is the only one in the molecule to not contain the carbon bonded to the electrophore oxygen, C#1-C#2, is the one most separated from the other two in terms of dissociation yield, with almost no initial dissociation events and a final dissociation yield of 12.8%. The other two bonds, C#2-C#3 and C#3-C#4 have a very high number of dissociations due to the proximity to the electrophore, with very similar initial kinetics. At 100 fs, the kinetics begin to diverge slightly, with C#2-C#3 having the higher final dissociation yield of 49.4% compared to the yield of 43.3% for the C#3-C#4 bond, which is slightly surprising due to the C#2-C#4 bond competing with the C-H dissociations. This might be due to differences in the radical stability formed after the dissociations of the different C-C bonds. The two most common dissociation pathways also

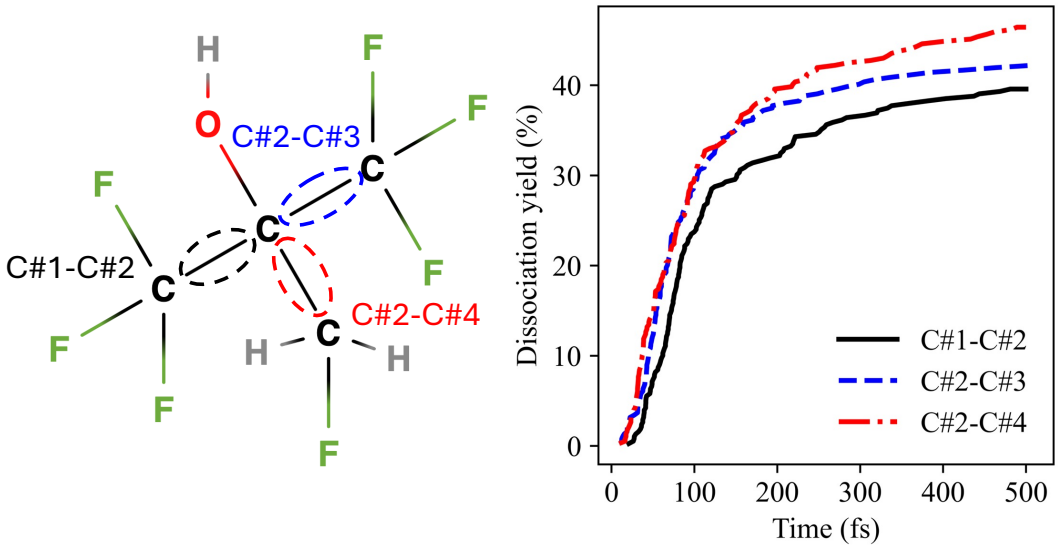

Figure 4.14: Dissociation kinetics of iso-$C_4H_2F_7OH$ for each C-C bond environment over 400 triple state trajectories at 5000 K. A dissociation event is defined as the first timestep at which a bond length exceeds 5 Bohr. Kinetics are normalised by the total number of bonds of each type present in the molecule.

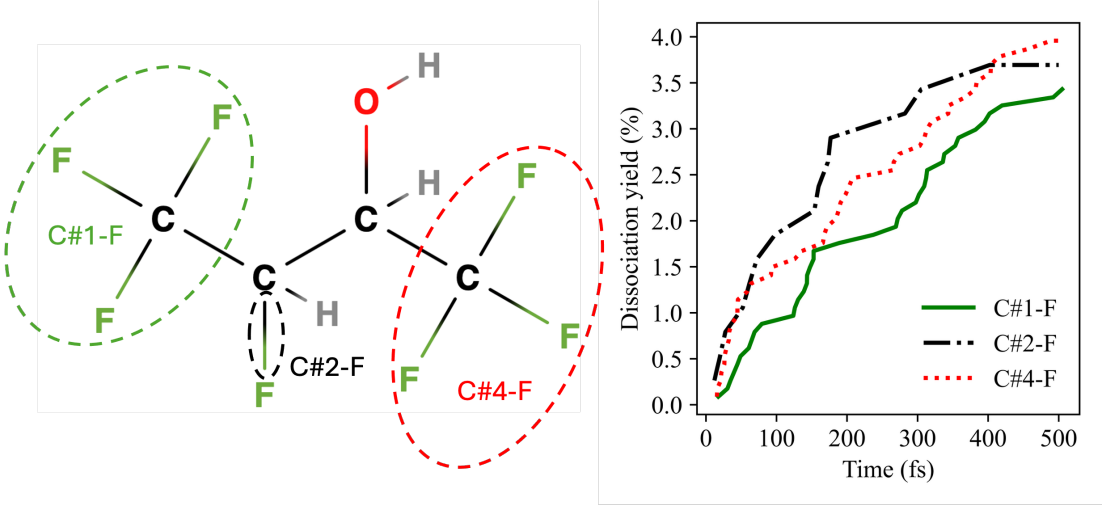

Figure 4.15: Dissociation kinetics of $C_4H_2F_7$-2-OH for each C-F bond environment over 400 triple state trajectories at 5000 K. A dissociation event is defined as the first timestep at which a bond length exceeds 5 Bohr. Kinetics are normalised by the total number of bonds of each type present in the molecule.

favour the C#2-C#3 bond over the C#3-C#4. 27.2% of all trajectories contain only the dissociation of the O-H bond followed by the C#2-C#3 bond compared to the 21.4% of the trajectories that contain only the O-H dissociation before the dissociation of C#3-C#4 bond.

In the case of the iso-$C_4H_2F_7OH$ in Fig. 4.14, the C-C bonds have much closer dissociation yields due to the whole molecule being more compacted around the electrophore. The seemingly symmetrical C-C environments of C#1-C#2 and C#2-C#3 have slightly different dissociation profiles where both of the general behaviours seem relatively identical but the dissociation yield of the C#1-C#2 is consistently lower than that of the C#2-C#3 bond, with the difference growing larger over the propagation. This could be due to the steric effects similar to the i-$C_4H_3F_7O$ where the hydrogen that forms part of the alcohol functional group is closer to the C#2-C#3 group influencing the dissociation pathways.

The dissociation of the C-F bonds for which these molecules were investigated show different behaviours. The $C_4H_2F_7$-2-OH molecule does not have a clear

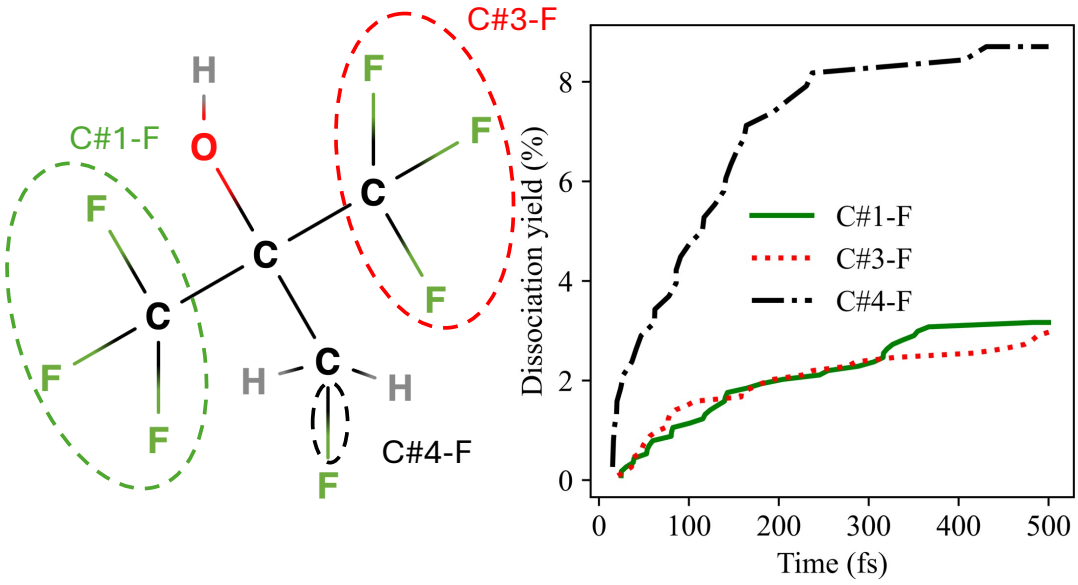

Figure 4.16: Dissociation kinetics of iso-$C_4H_2F_7OH$ for each C-F bond environment over 400 triple state trajectories at 5000 K. A dissociation event is defined as the first timestep at which a bond length exceeds 5 Bohr. Kinetics are normalised by the total number of bonds of each type present in the molecule.

pattern in Fig. 4.15. The two environments that have slightly higher dissociation yields are the environments that are closer to the electrophore, though the dissociation yields are very close across all the environments. However the C-F dissociations often occur late into the propagation, namely after the dissociation of other bonds. Due to the lack of the C-O dissociations in alcohol molecules, in a lot of trajectories the C-C bonds around the C-O bond dissociate, sometimes both within a single trajectory, heavily discouraging the dissociation of the C-F bonds around the electrophore. The C#2-F environment also has to contest with the dissociation the C#2-H bond whose dissociation occurs rapidly in trajectory. Therefore, as a C-F bond only dissociates once as the first bond in a trajectory, it is important to view these events as at least a secondary event. Therefore while the dissociation yields do not differ greatly, the C-F environments can still be said to be more dissociative as they still occur more often with less opportunities to do so.

The C-F dissociations in the iso-$C_4H_2F_7OH$ shown in Fig. 4.16 are more straightforward. The two CF_3 groups of C#1-F and C#2-F are predictably similar particularly in the context of the low number of dissociations, they are taken to be identical due to symmetry. The C#4-F bond is the bond that has the highest dissociation yield though the lowest total number of dissociations. This is due to competing with the C#2-C#4 bond that dissociates slightly more than the other C-C bonds as well as the C-H bonds that are bonded to the C#4 carbon, meaning that the bond is still rather efficient.

When comparing the C-F dissociations between the three $C_4H_3F_7O$ alcohol molecules as in Fig. 4.17, the original $C_4H_3F_7O$ alcohol has the lowest yield, which coincides with the fact that there is separation between the C-F bonds and the electrophore that localises the dissociative triplet character. In the other molecules, the triplet state excitation is localised closer to the C-F bonds producing a higher dissociation yield, though not by a truly significant amount. The small differences observed show that even when an alcohol containing molecule has a structure more conductive to C-F dissociations still does not produce dissociation yields similar to the other functional group isomer of $C_4H_3F_7O$. This

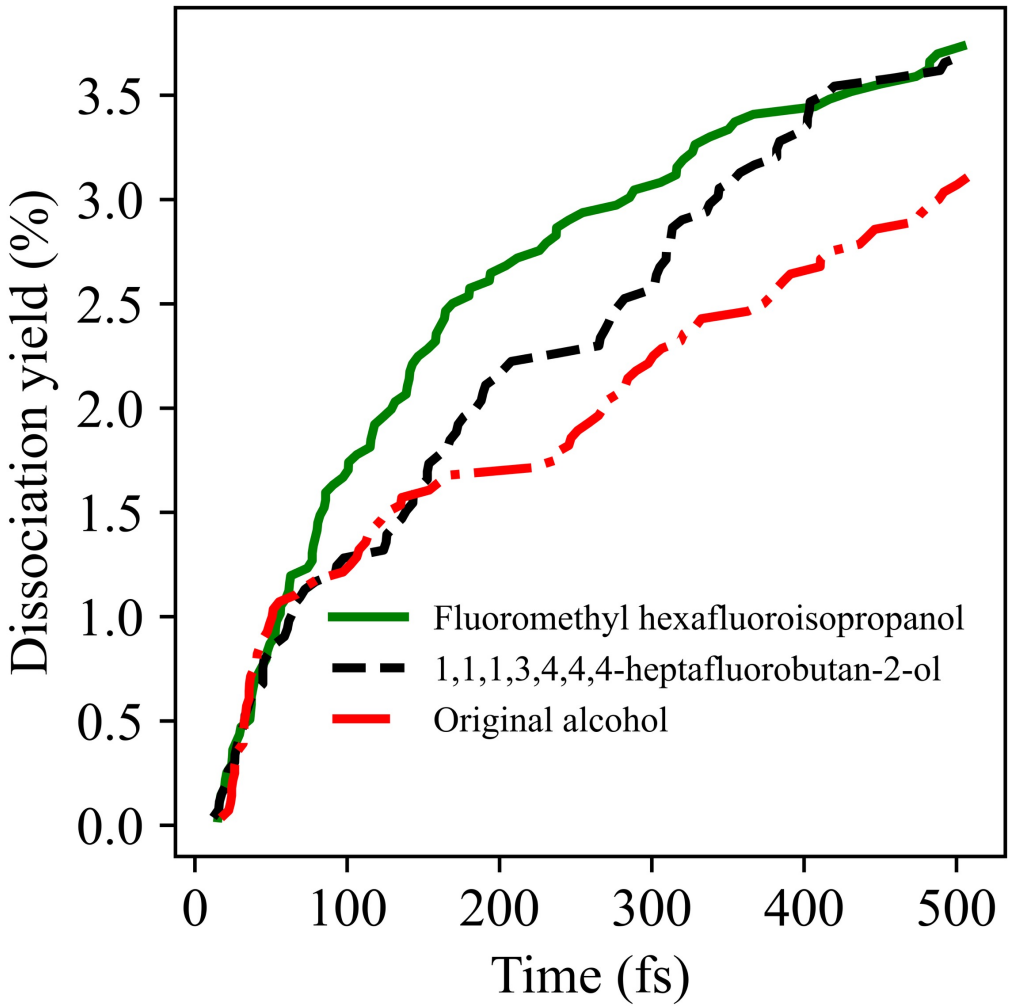

Figure 4.17: The comparison of the average C-F dissociation yields for three different molecules, $C_4H_2F_7$-2-OH, iso-$C_4H_2F_7OH$ and the original $C_4H_2F_7OH$ isomer studied in section 3.2.

result is a cascading consequence of the alcohol functional group itself. The weak nature of the O-H bond in the triplet state combined with being bonded to the active electrophore causes the O-H dissociation yield to be incredibly high and the dissociation events occurring on a incredibly rapid time-frame causing the C-O bond to inversely not dissociate often. The lack of dissociation yields of the C-O bond (which can be said to be dominant in the other oxygen electrophore containing molecules) further encourages the dissociation of the C-C bonds, particularly those involving the carbon bonded to the oxygen, leading to a higher dissociation yield. This in turn therefore consequently reduces the number of the C-F dissociations. The observation that there are fewer C-F dissociations is therefore not a direct comment on the dissociative nature of the bond in a vacuum but a secondary consequence of the C-F bond having a slower dissociation time frame. This also signifies that while certain molecular structures can increase the C-F dissociation yield seen in alcohol electrophore molecules, the lower than average dissociation yield found in these molecules is a consequence of the functional group.

4.4 CH_2F - A potential new electrophore?

4.4.1 1,1,2,2,3,3,4-Heptafluoro-1-butanol

The final $C_4H_3F_7O$ alcohol isomer that was tested to investigate the 'hydrogen buffer' stop gap effect between the electrophore and the C-F bonds was 1,1,2,2,3,3,4-Heptafluoro-1-butanol. This molecule was chosen due to having a more linear structure closer resembling the original $C_4H_2F_7OH$ isomer and also having record in the PubChem database, meaning that the molecule has been studied before in some context. The fact that both hydrogens being bonded to the same carbon should reduce the number of dual dissociations. The C-H bonds are also on the opposite side of the molecule to the electrophore limiting the number of C-H dissociations, potentially stabilising the molecule with respect to the DFT calculations.

It was originally hypothesised that reducing the space between the fluorines

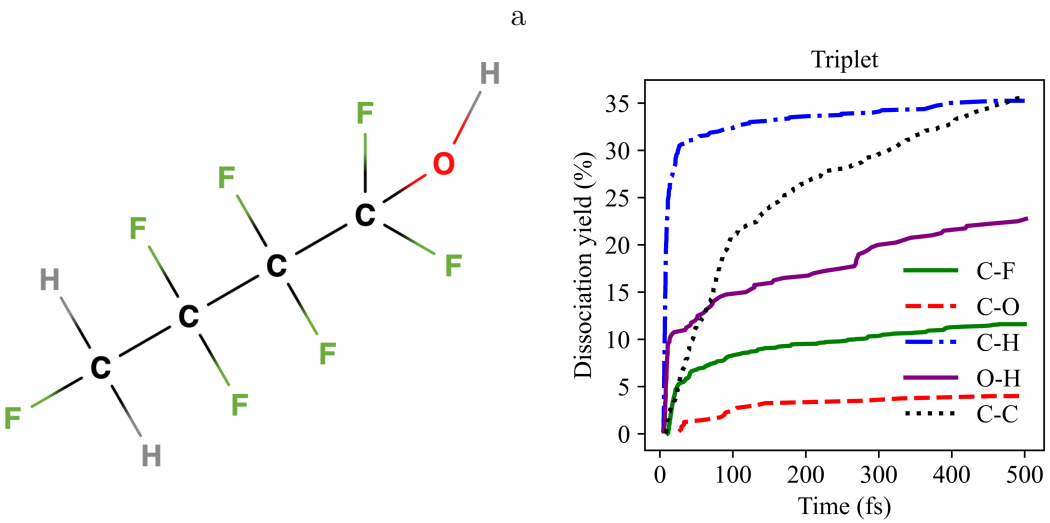

Figure 4.18: Dissociation kinetics of 1,1,2,2,3,3,4-Heptafluoro-1-butanol for each bond type over 200 lowest triplet state trajectories at 5000 K. A dissociation event is defined as the first timestep at which a bond length exceeds 5 Bohr. Kinetics are normalised by the total number of bonds of each type present in the molecule.

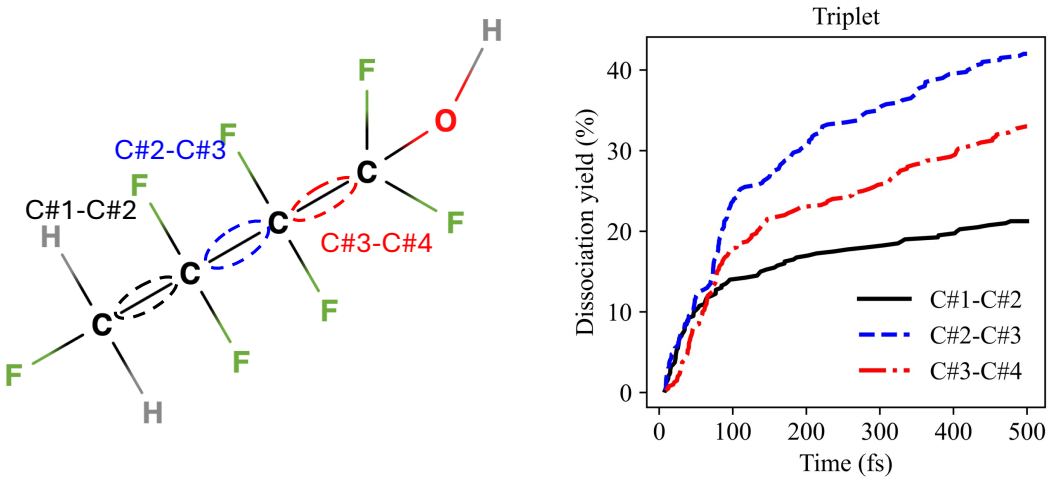

Figure 4.19: Dissociation kinetics of 1,1,2,2,3,3,4-Heptafluoro-1-butanol for each C-C bond environment over 200 lowest triplet state trajectories at 5000 K. A dissociation event is defined as the first timestep at which a bond length exceeds 5 Bohr. Kinetics are normalised by the total number of bonds of each type present in the molecule.

and the electrophore would result in a larger number of C-F dissociations. While the average dissociation yield (shown in Fig. 4.18) for the C-F bonds is in fact higher than the original $C_4H_2F_7OH$ alcohol isomer tested, the results were not as predicted. The average dissociation yields for the C-H and the C-C bonds were fairly similar to the original molecule, with dissociation yields of 35% each. However the dissociation of the O-H bond, a defining feature of the alcohol molecules has a very different behaviour more similar to the molecules containing multiple electrophores (see the next section 4.4), with a final dissociation yield of 25%. This suggests that perhaps the oxygen atom is not acting as the electrophore in this molecule.

Investigation of the individual C-C and C-F environments also lends evidence to this claim shown in Figs. 4.19 and 4.20 respectively. As the C-H bonds dissociate rapidly and usually only once a trajectory (50.3% of trajectories begin

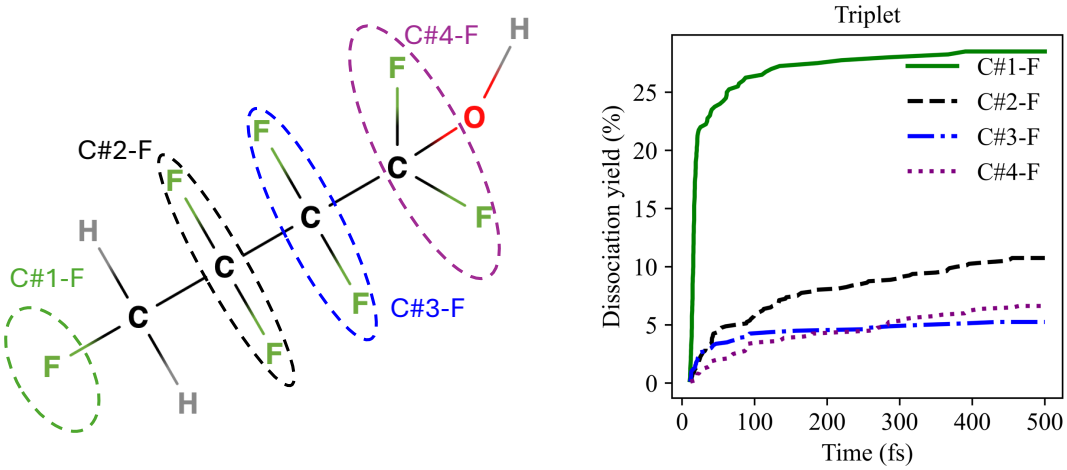

Figure 4.20: Dissociation kinetics of 1,1,2,2,3,3,4-Heptafluoro-1-butanol for each C-F bond environment over 200 lowest triplet state trajectories at 5000 K. A dissociation event is defined as the first timestep at which a bond length exceeds 5 Bohr. Kinetics are normalised by the total number of bonds of each type present in the molecule.

with a C-H dissociation), the dissociation of the C#1-C#2 bond is discouraged, but still dissociates more than the C#3-C#4 bond, which is the opposite of what would be expected if the oxygen is acting as an electrophore. The C-F environments show that not only does the C#1-F environment have an incredibly high (for a C-F bond) dissociation yield of 25%, but it also breaks incredibly rapidly, with kinetics that are more normally attributed to C-H bonds. 20.6% of trajectories begin with the dissociation of the C#1-F bond. This evidence suggests that in fact that the -CH_2F group is acting as an electrophore. The rest of the C-F environments also have an order that would be expected if the electrophore was near the C#1 carbon. The amount of spin on each atom in the equilibrium geometry taken to start the trajectory is given when performing the first force calculation. While it can be expected for there to be spin around the oxygen atom if it is indeed localising the triplet state, table. 4.1 shows that the magnitude of the spin of the oxygen atom is almost negligible. The atom with the highest spin is C#1 followed by C#2 and C#1-F.

Atom	**Spin**
C#1	1.165741
C#2	0.346054
C#3	-0.032949
C#4	0.126403
C#1-F	0.180327
C#2-F (avg.)	0.027829
C#3-F (avg.)	0.0164885
C#4-F (avg.)	0.005575
O	-0.007364

Table 4.1: Spin populations on atoms and bonds for the ground state equilibrium geometry for the molecule 1,1,2,2,3,3,4-Heptafluoro-1-butanol.

While originally the fluorine atoms were discounted from being able to act as an electrophore due to their extremely high electronegativity placing the LUMO much higher in energy than say for an oxygen atom, the specific arrangement

of the -CH_2F group may present an exception. Due to there only being one fluorine atom bonded to the carbon there is no opportunity for excessive fluorine crowding which allows access to lower electronic states combined with the hyper-conjugation provided by the hydrogen bonds causing some electron density to remain on the carbon and preserve "orbital accessibility" causing the triplet state excitation to localise around the carbon in -CH_2F.

4.4.2 1,1,2,2,2-pentafluoroethanol

Given the dissociation pathways observed for the 1,1,2,2,3,3,4-Heptafluoro-1-butanol molecule, it is possible to question whether it is in fact the -CH_2F group acting as an electrophore or that in this particular molecule alone, the oxygen is not acting as an electrophore. This functional group is also present in the iso-$C_4H_2F_7OH$ molecule whose dissociation pathways are determined by the oxygen atom acting as an electrophore, not the -CH_2F group. This shows that the -CH_2F at the very least is not consistently a more dominant electrophore than the oxygen atom. The main difference between the other alcohol molecules studied thus far and 1,1,2,2,3,3,4-Heptafluoro-1-butanol is that the alcohol functional group is of the form -CF_2OH which could potentially prevent the oxygen as acting as an electrophore. To test this hypothesis, the neutral dissociation of 1,1,2,2,2-pentafluoroethanol (C_2F_5OH) was also simulated, a simple alcohol that contains no other hydrogen apart from the one bonded to the oxygen in the alcohol functional group.

Despite the very low number of trajectories, the overall dissociation yields in Fig. 4.21 are sufficient to qualitatively state that the hydrogens are not required for the oxygen atom in an alcohol to act as an electrophore. This can be seen with the O-H dissociation yield of 96%, and the dissociation events happening very rapidly in the propagation. The C-C dissociation yield is also incredibly high at 76% which while not exactly evidence of an electrophore as there is only one C-C bond, is higher than the C-C bond dissociation yields found in other molecules and could be due to proximity to an electrophore combined with no discouraging from the C-O bond nor C-H bonds found in other molecules. The

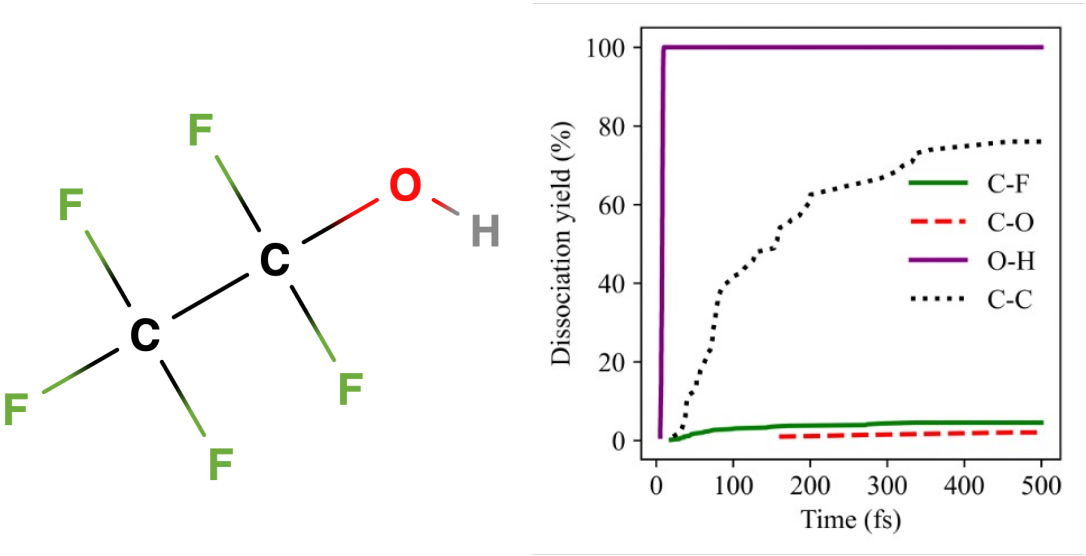

Figure 4.21: Dissociation kinetics of C_2F_5OH for each bond type over 100 lowest triplet state trajectories at 5000 K. A dissociation event is defined as the first timestep at which a bond length exceeds 5 Bohr. Kinetics are normalised by the total number of bonds of each type present in the molecule.

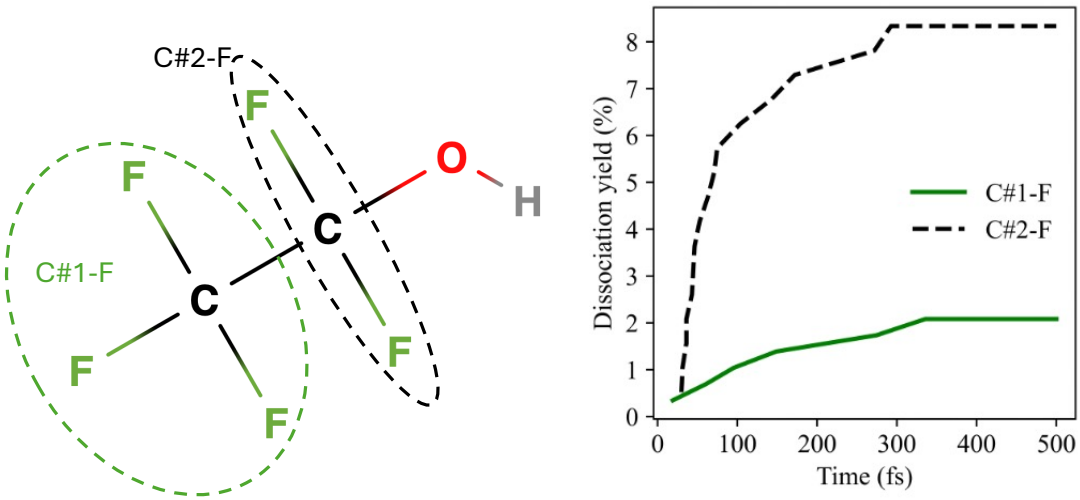

Figure 4.22: Dissociation kinetics of C_2F_5OH for each C-F bond environment over 100 lowest triplet state trajectories at 5000 K. A dissociation event is defined as the first timestep at which a bond length exceeds 5 Bohr. Kinetics are normalised by the total number of bonds of each type present in the molecule.

C-F environments in Fig. 4.22 do show direct evidence of the oxygen acting as an electrophore as the C#2-F environment has a higher dissociation yield than the C#3-F environment as well as a higher number of initial dissociations. This evidence suggests that the functional group -COF_2 is capable of acting as an electrophore. Therefore the reason that the oxygen does not act as an electrophore in 1,1,2,2,3,3,4-Heptafluoro-1-butanol on the lowest triplet state considered in the standard MD performed is because there is another more dominant electrophore that localises the excitation to the lowest triplet state, namely the -CH_2F group. More evidence could be gathered via running non-adiabatic multiple state Ehrenfest dynamics with the trajectories starting on each state and comparing the dissociation yields found, similar to the process covered in the next section detailing the interaction of the multiple electrophores.

4.4.3 1-Fluoropropane

To investigate whether this -CH_2F group acting as an electrophore is consistent, several other molecules are investigated, namely 1-Fluoropropane (1-C_3H_7F), 1,1,3-Trifluoropropane (1,1,3-$C_3H_5F_3$), 1,1,4-trifluorobutane (1,1,4-$C_4H_7F_3$) and 1,1,2,2,3,3,4-heptafluorobutane ($C_4H_3F_7$). The general dissociation yields of 1-C_3H_7F shown in Fig. 4.23 are surprising, as the C-F dissociation yield is higher than the average dissociation yield of the C-C bonds, with a final dissociation yield of 20.5%.

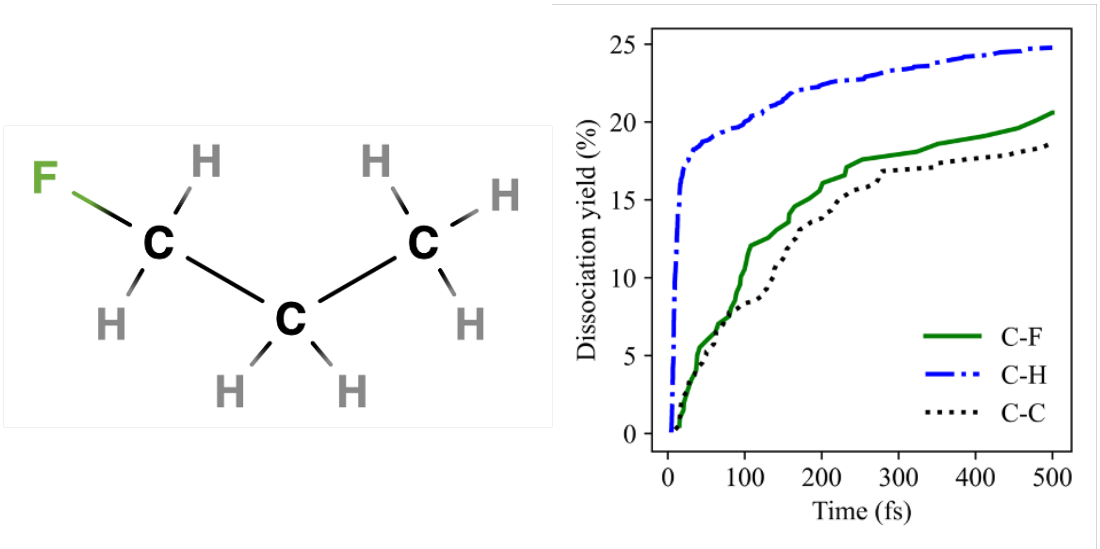

Figure 4.23: Dissociation kinetics of 1-C_3H_7F for each bond type over 200 lowest triplet state trajectories at 5000 K. A dissociation event is defined as the first timestep at which a bond length exceeds 5 Bohr. Kinetics are normalised by the total number of bonds of each type present in the molecule.

The C-H dissociation yield of 20% is averaged across the three different C-H environments. Comparing those against each other as in Fig. 4.24 shows that there is a clear order of dissociation yields, with the C#1-H environment having a dissociation yield of 40% being the highest, followed by the C#2-H environment with a dissociation yield 28% and finally the C#3-H environment with the smallest yield of only 13%. While the C#3-H environment does have more hydrogens than the other environments and so is averaged by a greater amount, the overall number of C-H bonds dissociated also follows the same trend, suggesting that again the -CH_2F group is acting as an electrophore, similar to the 1,1,2,2,3,3,4-Heptafluoro-1-butanol molecule studied earlier. In Fig. 4.25, the C-C bond that is closest to this potential electrophore does not have the highest dissociation yield but it is possible that the high number of initial dissociations around the C#1 carbon discourage the dissociation of the C#1-C#2 bond as unusually due to the very fast C-F bond dissociation, the C-C bond is the slowest

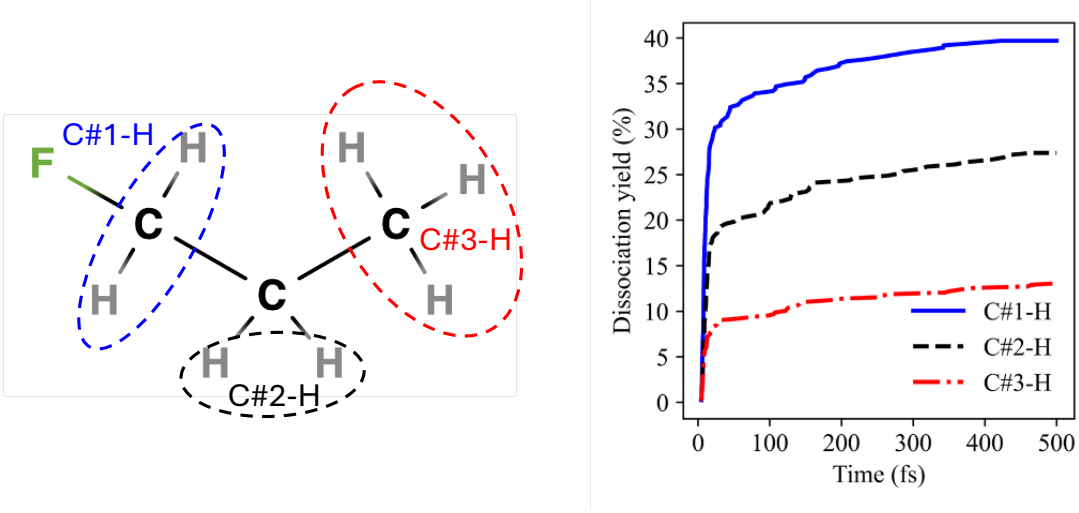

Figure 4.24: Dissociation kinetics of 1-C_3H_7F for each C-H bond environment over 200 lowest triplet state trajectories at 5000 K. A dissociation event is defined as the first timestep at which a bond length exceeds 5 Bohr. Kinetics are normalised by the total number of bonds of each type present in the molecule.

bond dissociation time frame present in the molecule.

As is perhaps unsurprising in a molecule with several C-H bonds, 49.7% of the trajectories contained only C-H dissociations, with 22.8% trajectories containing only a single C-H dissociation throughout the whole trajectory. The hydrogens that are bonded to the potential electrophore are most commonly dissociated first in a trajectory with the C#1-H bonds dissociating first in 52.8% of trajectories. The most common dissociation pathway, occurring in 10.9% of trajectories is the dissociation of the C#1-H bond followed by a dissociation of the C#2-C#3 bond, producing atomic hydrogen, a CH_3 radical and a C_2H_3F radical. Likewise the most common dissociation pathway involving the dissociation of the C#1-C#2 bond is another two step process where the dissociation of a C#3-H bond is followed by the C#1-C#2 bond. This is further evidence that the increased number of dissociations around the C#1 bond is the reason that the C#1-C#2 bond has the lower C-C dissociation yield, meaning that this subversion of expectation does

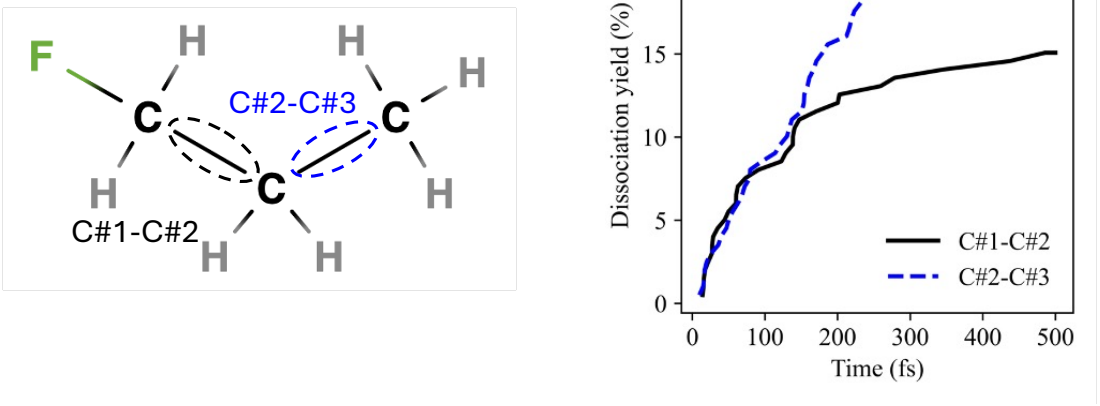

Figure 4.25: Dissociation kinetics of 1-C_3H_7F for each C-C bond environment over 200 lowest triplet state trajectories at 5000 K. A dissociation event is defined as the first timestep at which a bond length exceeds 5 Bohr. Kinetics are normalised by the total number of bonds of each type present in the molecule.

not serve as evidence against the -CH_2F group acting as an electrophore.

4.4.4 1,1,3-Trifluoropropane

In order to test that it is only -CH_2F that can act as an electrophore and not any other combination of hydrogen and fluorine, MD simulations were also run for 1,1,3-$C_3H_5F_3$. The addition of the CHF_2 group on the opposite side of the molecule allows for insight into which group, if any, acts as an electrophore in this molecule. This molecule is also an isomer of the $C_3H_5F_3$ molecule presented in section 3.1. The presence of the -CH_2F group acting that is hypothesised to act as an electrophore should increase the number of dissociations when compared to the CF_3 group found on the other molecule. However when analysing the dissociation yields, the difference in overall dissociations is almost negligible. Looking at the dissociation yields in Fig. 4.26 show that this is a result of a lowered C-H dissociation yield combined with a significant increase in C-C and C-F dissociations. Despite the 1,1,3-$C_3H_5F_3$ molecule having the hydrogen atoms bonded to a higher number of carbons, the dissociation yield is 24.9%, which is 82% of the yield in the 1,1,1-$C_3H_5F_3$ molecule. This reduction in C-H dissociations can also be seen in the dissociation pathways undertaken by the trajectories, with only 43.7% of trajectories containing only C-H dissociations.

The individual bond environments once again show that the -CH_2F group is acting as an electrophore. The C-C bonds in Fig. 4.8 show that the dissociation yield is higher for the C-C bond further away from the -CH_2F electrophore (C#2-C#3), the kinetics appear standard in the fact that the C#1-C#2 bond has higher initial dissociation kinetics before plateauing. This behaviour has been seen in the other molecule containing the -CH_2F group, 1-C_3H_7F, and other molecules containing C=C electrophores, and so can be said to still be aligned with the electrophore model. While this distribution of C-C bonds does look similar to the 1,1,1-$C_3H_5F_3$ isomer, the initial peak of dissociations of the C#1-C#2 bond is sharper in the isomer containing an electrophore. The presence of an electrophore also has a subsequent effect of increasing the dissociation yield of the C#2-C#3 bond, up to 35%. This is due to a combination of lower C-H yields limiting the

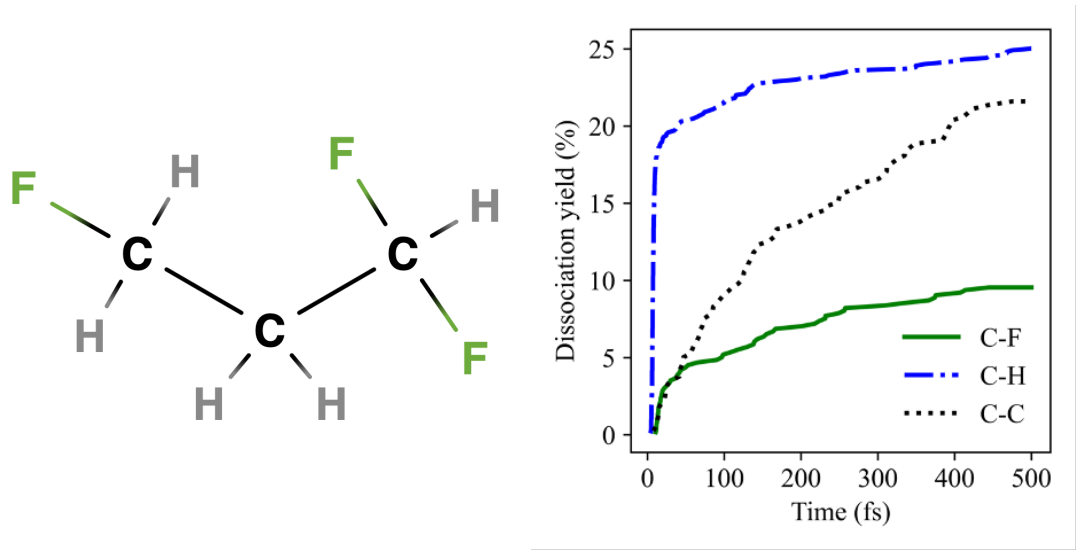

Figure 4.26: Dissociation kinetics of 1,1,3-$C_3H_5F_3$ for each bond type over 200 lowest triplet state trajectories at 5000 K. A dissociation event is defined as the first timestep at which a bond length exceeds 5 Bohr. Kinetics are normalised by the total number of bonds of each type present in the molecule.

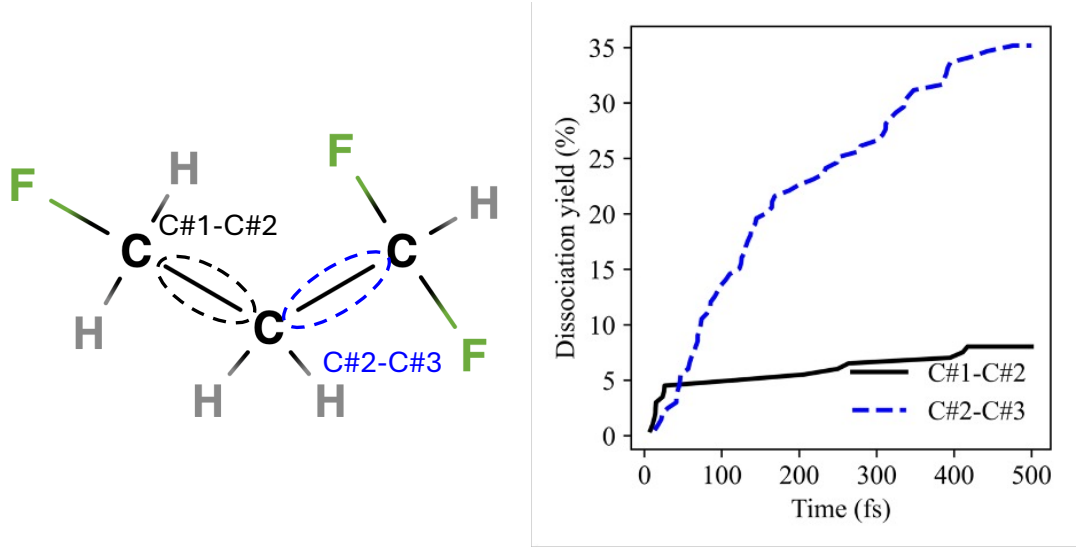

Figure 4.27: Dissociation kinetics of 1,1,3-$C_3H_5F_3$ for each C-C bond environment over 200 lowest triplet state trajectories at 5000 K. A dissociation event is defined as the first timestep at which a bond length exceeds 5 Bohr. Kinetics are normalised by the total number of bonds of each type present in the molecule.

discouragement of dissociation and the localisation of the triplet state dissociative character resulting in a higher number of C#2-C#3 dissociations. 24.5% of all trajectories begin with (or consist entirely of) with the dissociation of the C#1-H bond followed by the C#2-C#3 bond.

The C-F bonds and the C-H bonds similarly also show the environments closest to the -CH_2F electrophore have dramatically higher dissociation yields. Fig. 4.28 shows the dissociation yield of the C#1-F bond which is part of the electrophore group has a dissociation yield of 20%, which is high for a C-F bond. Approximately half of these dissociations occur rapidly, within 25 fs, which is also unusual for a C-F bond suggesting the initial localisation of the triplet state excitation caused by an electrophore. This is not the case for the C#3-F environment as the earliest dissociation is at 30 fs, with the dissociation yield being 4.5%, approximately 4 times smaller than the C#1-F environment. This means that the total number of dissociations is significantly higher in the C#1-F environment as

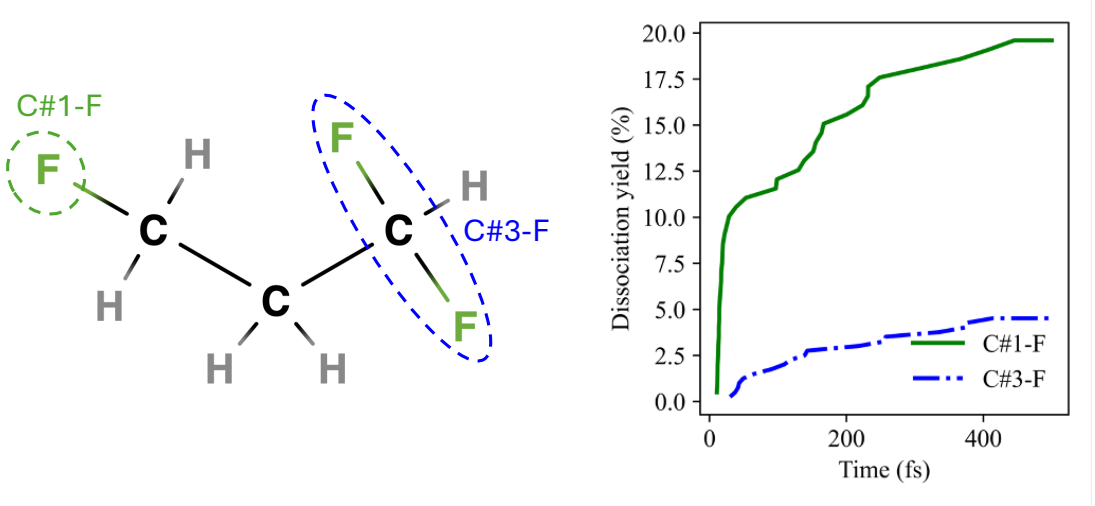

Figure 4.28: Dissociation kinetics of 1,1,3-$C_3H_5F_3$ for each C-F bond environment over 200 lowest triplet state trajectories at 5000 K. A dissociation event is defined as the first timestep at which a bond length exceeds 5 Bohr. Kinetics are normalised by the total number of bonds of each type present in the molecule.

the single C-F bond outcompetes the dissociation of both C-F bonds present in the C#3-F environment.

The gap in dissociations between the C#1-F and the C#3-F environments is even more significant when dissociation pathways are taken into account as 23% of C#1-F dissociations occur after the dissociation of at least one C#1-H. Similarly to the C-F environments, Fig. 4.29 shows that the C#1-H environment (which constitutes part of the -CH_2F electrophore) also produces a much higher dissociation yield when compared to the other two C-H environments present in the molecule. The other two environments, C#2-H and C#3-H, appear to present identical dissociation yields across the entire propagation. These yields are lower than observed in the 1,1,1-$C_3H_5F_3$ isomer as the dissociations are localised more around the C#1 carbon due to the localising of the triplet state excitation by the -CH_2F electrophore. While the dissociation yields are identical for both environments, the number of dissociations are not due the difference in number of C-H bonds present in each environment. While the data are presen-

ted in terms of dissociation yield, it sometimes obscures the difference between environments with different number of bonds as the each of the C-H bonds in the C#2-H environment dissociate as often as the lone C#3-H bond, producing an average that matches almost exactly. However, the number of dissociations of the C#2-H bonds is twice as high as the C#3-H bond, and as a bond breaking on a carbon discourages more bonds on the same carbon from breaking, there are more trajectories containing a C#2-H dissociation than a C#3-H dissociation.

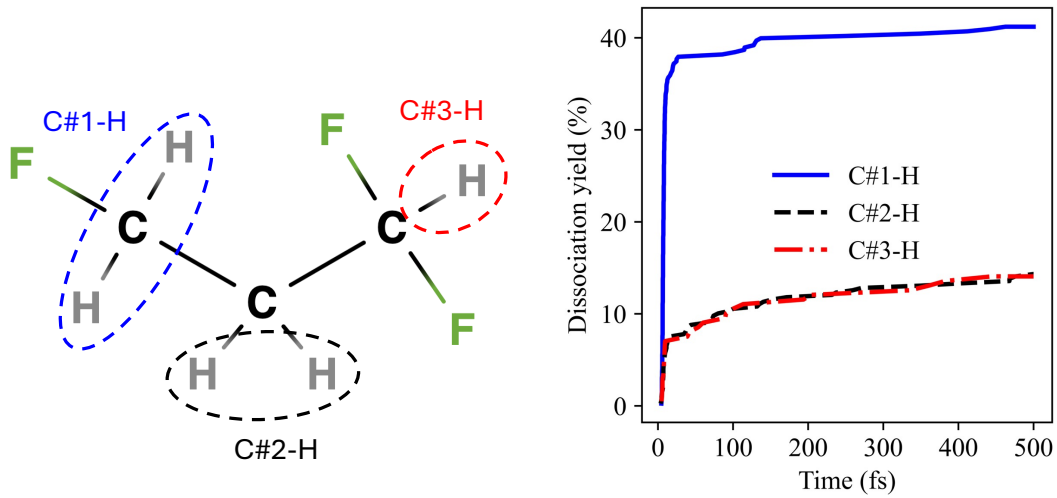

Figure 4.29: Dissociation kinetics of 1,1,3-$C_3H_5F_3$ for each C-H bond environment over 200 lowest triplet state trajectories at 5000 K. A dissociation event is defined as the first timestep at which a bond length exceeds 5 Bohr. Kinetics are normalised by the total number of bonds of each type present in the molecule.

4.4.5 1,1,4-trifluorobutane

Another interesting molecule studied is 1,1,4-$C_4H_7F_3$ which has the same features as 1,1,3-$C_3H_5F_3$ but with an additional CH_2 group extending the carbon chain, allowing for a more detailed insight into the ordering of bond breaking with respect to the electrophore. As a result of the small changes between the two molecules, the overall dissociation yields are almost identical for all bond types considered

when factoring in the increased number of carbons and hydrogens with Fig 4.30 presenting a very similar overview of dissociation yields. The increased number of bonds does however have the effect of complicating the potential dissociation pathways as now only 33.7% of trajectories contain solely C-H dissociations, with the percentage of trajectories containing an C-C bond increasing from 43.2% to 55.6%.

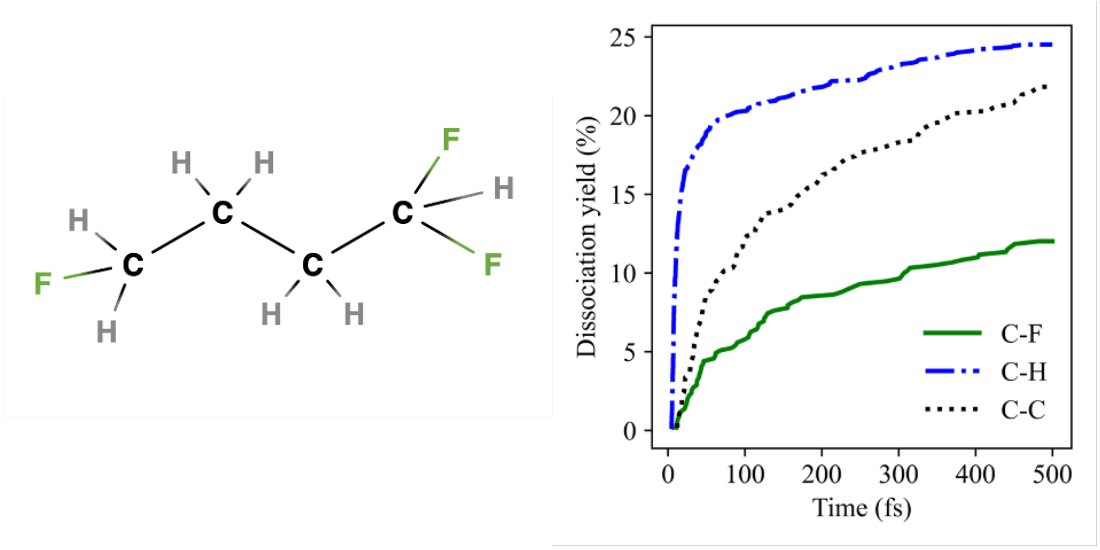

Figure 4.30: Dissociation kinetics of 1,1,4-$C_4H_7F_3$ for each bond type over 200 lowest triplet state trajectories at 5000 K. A dissociation event is defined as the first timestep at which a bond length exceeds 5 Bohr. Kinetics are normalised by the total number of bonds of each type present in the molecule.

The individual C-C environments in Fig. 4.31 present a usual case (for the -CH_2F electrophore) of the C-C bond closest to the electrophore (C#1-C#2) having the highest initial dissociations before the rate of the dissociations severely flattens. The C-C bond with the highest dissociation yield is the C#2-C#3 bond, which is the closest C-C bond not involving the electrophore carbon. The C-F and C-H bond environments in Fig. 4.32 and Fig. 4.33 respectively are more complicated. After observing this trend across multiple molecules, it can be safely concluded that this is the expected behaviour of the -CH_2F, where the high

number of dissociations around the electrophore carbon reduces the dissociation yield of it's corresponding C-C bond but increases the dissociation yield of the most adjacent C-C bond.

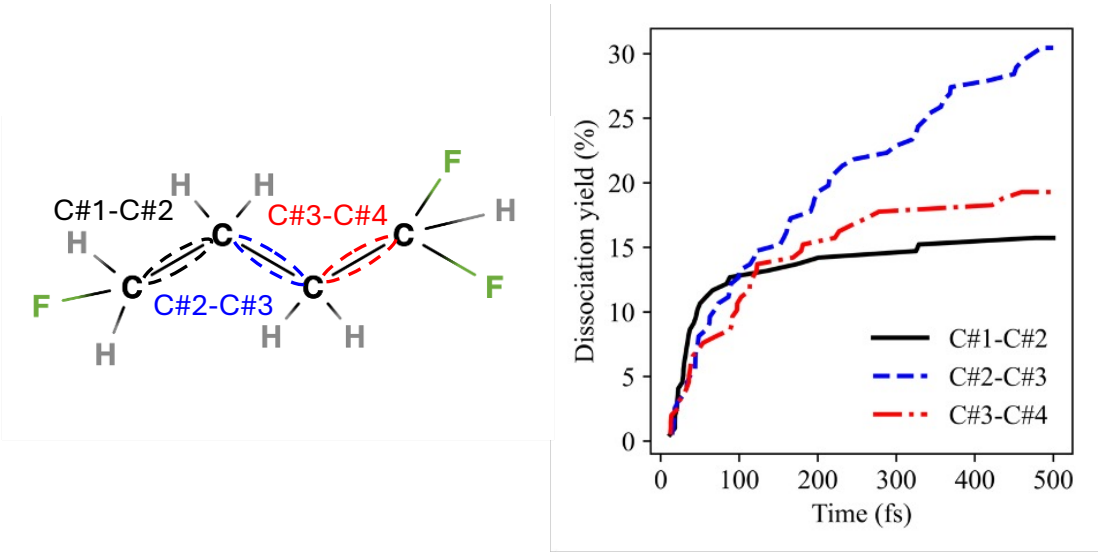

Figure 4.31: Dissociation kinetics of 1,1,4-$C_4H_7F_3$ for each C-C bond environment over 200 lowest triplet state trajectories at 5000 K. A dissociation event is defined as the first timestep at which a bond length exceeds 5 Bohr. Kinetics are normalised by the total number of bonds of each type present in the molecule.

In terms of dissociation yields, the C#1-F dissociations outcompete the C#4-F dissociations, but only due to the C#4-F environment containing double the C-F bonds. As C-F bonds are generally slow and difficult to break and so despite having two bonds, it is unlikely for both of those bonds to break in a single trajectory. When the dissociation yields are not averaged by number of bonds, the two environments present practically identically. However it is also important to note the context in which these bonds dissociate. The C-H dissociations favour heavily the C#1-H environment as both C-H bonds break to the extent that their average is higher than the lone C#4-H bond. As the C-H bond breaks rapidly and in 91.3% of trajectories is the first bond to break, the molecule is more often in a

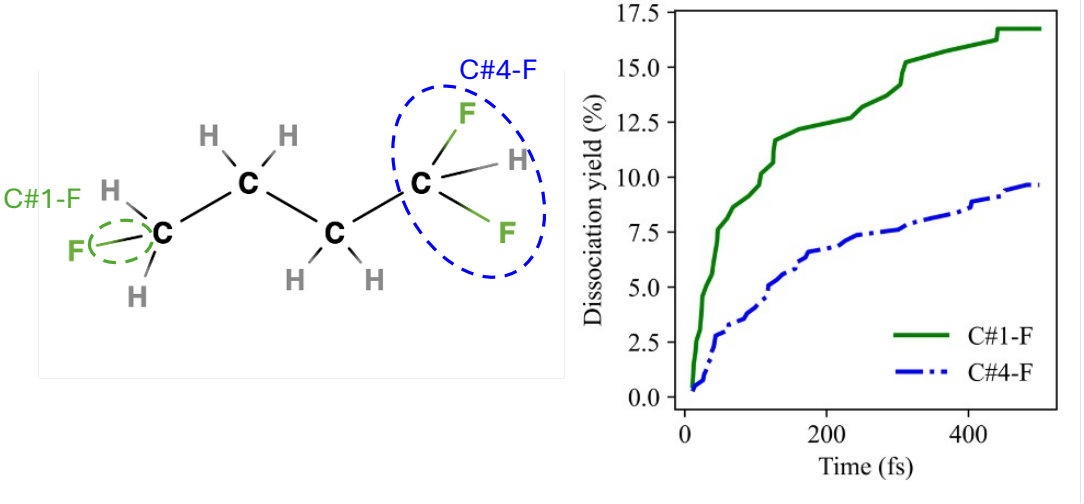

Figure 4.32: Dissociation kinetics of 1,1,4-$C_4H_7F_3$ for each C-F bond environment over 200 lowest triplet state trajectories at 5000 K. A dissociation event is defined as the first timestep at which a bond length exceeds 5 Bohr. Kinetics are normalised by the total number of bonds of each type present in the molecule.

state where the C#1-F bond is discouraged to break, rather than the C#4-F bond being discouraged. The C#1-H bond environment specifically is also the most common environment to dissociate first, with the two most common dissociation pathways beginning with this dissociation and the C#1 carbon being involved in 44.4% of the first bonds dissociation across all trajectories. This is much higher than the 11.7% of trajectories that begin with a bond containing the C#4 carbon. This suggests that the -CH_2F group still acts as an electrophore. The C-H bond dissociation order does also show an order that is expected of the -CH_2F electrophore, as while the C#4-H dissociation yield is higher than the C#3-H environment, this is only due to averaging, as the C#4-H contains half as many C-H bonds, essentially doubling its comparative yield. If only the pure number of C-H dissociations per environment is considered, there is a perfect order of shorter the distance to the electrophore -CH_2F group, the higher the number of C-H dissociations.

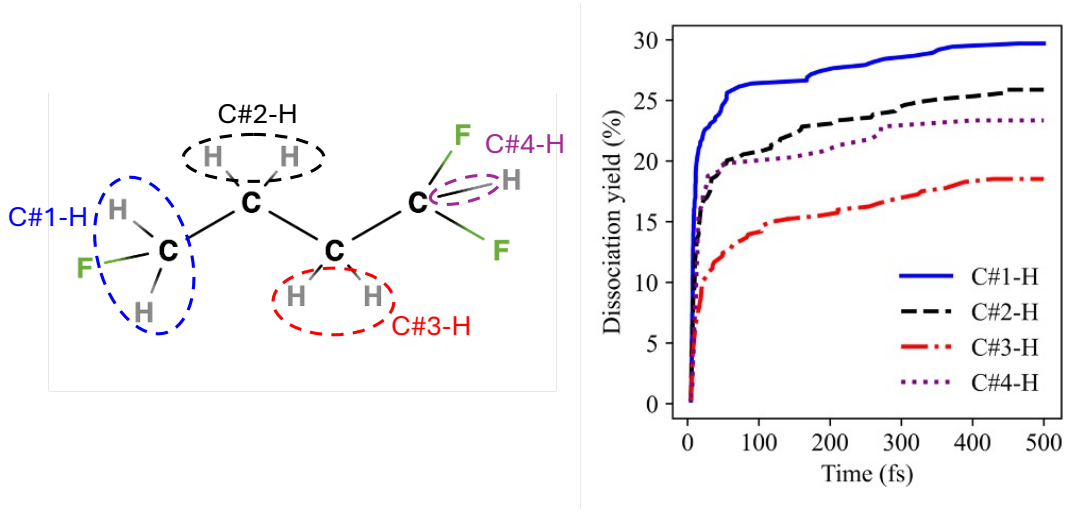

Figure 4.33: Dissociation kinetics of 1,1,4-$C_4H_7F_3$ for each C-H bond environment over 200 lowest triplet state trajectories at 5000 K. A dissociation event is defined as the first timestep at which a bond length exceeds 5 Bohr. Kinetics are normalised by the total number of bonds of each type present in the molecule.

Additional MD simulations were run for the same 1,1,4-$C_4H_7F_3$ molecule at a lower temperature of 3000 K in order to investigate the effect of the potential electrophore when the molecule has overall less kinetic energy and so less prone to breaking bonds, potentially making the effect of an electrophore more pronounced. While the overall bond type dissociation order is preserved (presented in Fig. 4.34, all bonds have an expected lower dissociation yield, with the average yields of the C-H bonds decreasing from 25% to 16%, the average yield of the C-C bonds decreases from 21.5% to almost a third at just 7.6%. The C-F bonds had the largest relative decrease from 11.8% to 3.5%, a 70% decrease.

Due to the lower initial kinetic energy, 68.5% of all trajectories contain only C-H dissociations. In fact, the 4 most common dissociation pathways observed in the trajectories at 3000 K are single dissociations corresponding to a dissociation of each C-H environment. The initial dissociations are still however located around the C#1 carbon, with the C#1-H dissociating first in 32% of trajectories and the C#1-C#2 bond being the most common C-C bond to dissociate first in a trajectory. The next most common in terms of first dissociations is the C#2-H environment, the closest C-H environment to the electrophore that does not form part of the -CH_2F electrophore group.

While Fig. 4.37 shows that the C#4-H bond has the highest dissociation yield this is because the C#4-H environment is the only environment to contain a single C-H bond, and as the lower temperature further discourages multiple bond breaking events for the same centre, the other environments report a lower dissociation yield. If only the pure number of dissociations is taken into account, the C#4-H dissociations look similar to the C#3-H environment, which presents with the lowest dissociation yield, explainable as they are the environment furthest away from the proposed electrophore. The C-F bonds in Fig. 4.36 are simple to explain as the environments present a similar behaviour to the higher temperature though to a greater extent, where the lone C#1-F bond now dissociates more than both C#4-F bonds together. This revelation exhibits why additional lower temperature simulations are useful, and provides further evidence of the electrophore. The C-C bonds in Fig. 4.31 are not straightforward, as

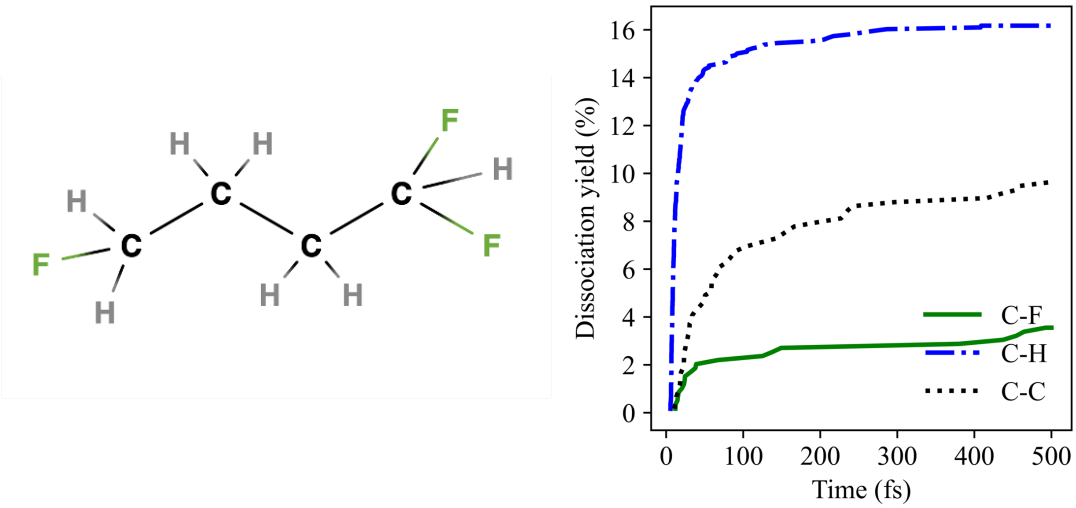

Figure 4.34: Dissociation kinetics of 1,1,4-$C_4H_7F_3$ for each bond type over 200 lowest triplet state trajectories at 3000 K. A dissociation event is defined as the first timestep at which a bond length exceeds 5 Bohr. Kinetics are normalised by the total number of bonds of each type present in the molecule.

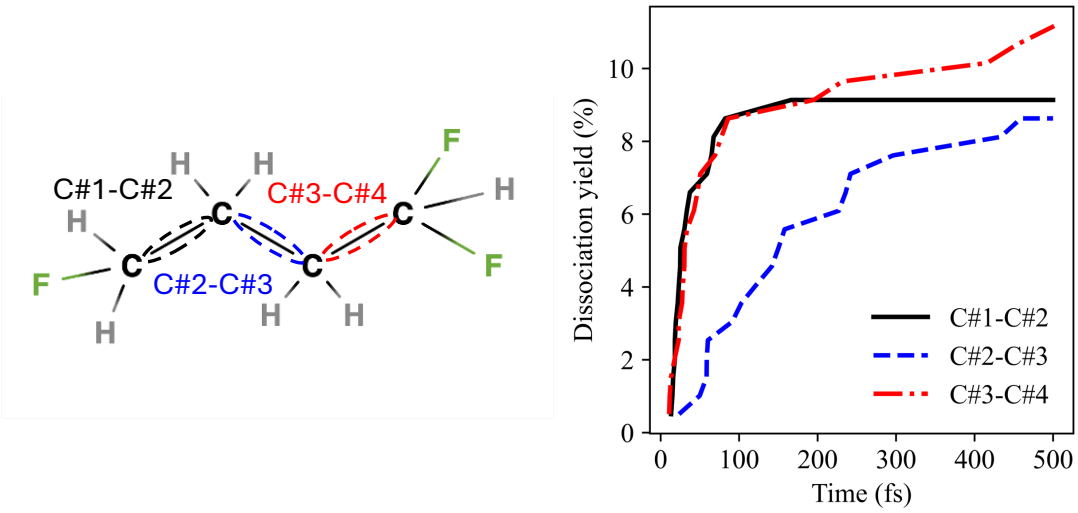

Figure 4.35: Dissociation kinetics of 1,1,4-$C_4H_7F_3$ for each C-C bond environment over 200 lowest triplet state trajectories at 3000 K. A dissociation event is defined as the first timestep at which a bond length exceeds 5 Bohr. Kinetics are normalised by the total number of bonds of each type present in the molecule.

while the C#1-C#2 bond has a high number of initial dissociations so does the C#3-C#4 bond. While the C#1-C#2 bond plateaus similar to the behaviour observed at 5000 K, the C#3-C#4 bond has additional late time dissociations causing it to be the C-C bond with the highest dissociation yield at 3000 K while the C#2-C#3 bond now has the lowest. This could be explained by the fact that at lower temperatures all bonds are more difficult to dissociate, reducing the number of dissociations surrounding the C#1 carbon which in turn allows for the initial localisation to cause dissociations of the C#1-C#2 bond instead of the C#2-C#3 bond.

4.4.6 1,1,2,2,3,3,4-heptafluorobutane

The final molecule to be investigated to find evidence of the -CH_2F electrophore is the $C_4H_3F_7$ molecule. Having hydrogens bonded to every carbon in the carbon

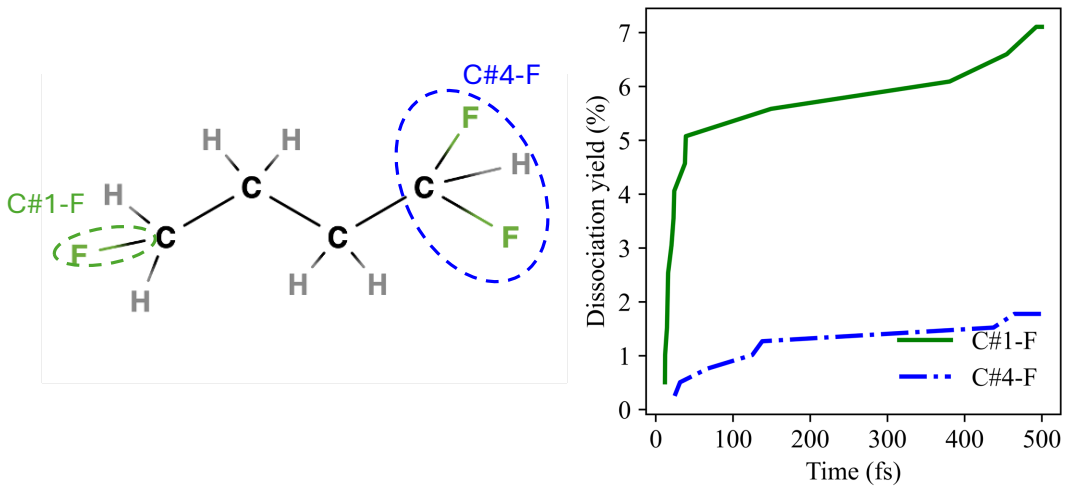

Figure 4.36: Dissociation kinetics of 1,1,4-$C_4H_7F_3$ for each C-F bond environment over 200 lowest triplet state trajectories at 3000 K. A dissociation event is defined as the first timestep at which a bond length exceeds 5 Bohr. Kinetics are normalised by the total number of bonds of each type present in the molecule.

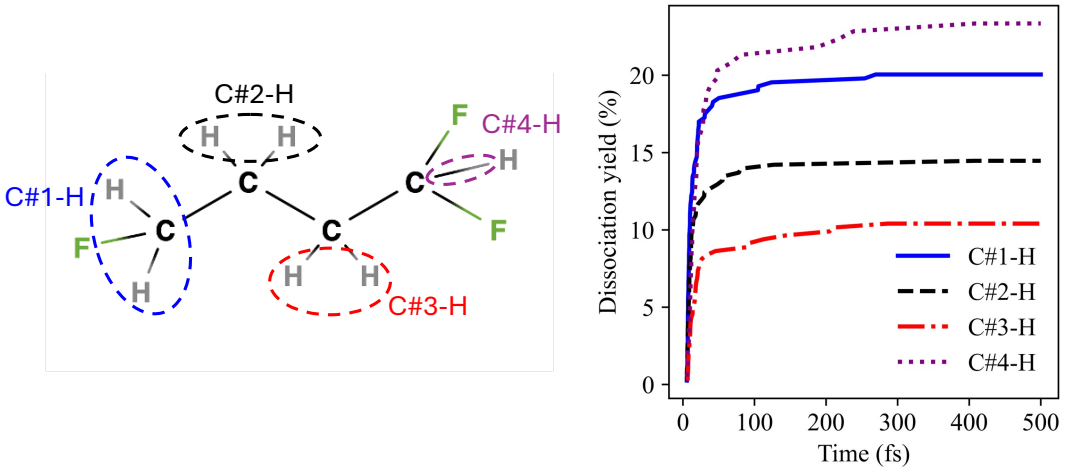

Figure 4.37: Dissociation kinetics of 1,1,4-$C_4H_7F_3$ for each C-H bond environment over 200 lowest triplet state trajectories at 3000 K. A dissociation event is defined as the first timestep at which a bond length exceeds 5 Bohr. Kinetics are normalised by the total number of bonds of each type present in the molecule.

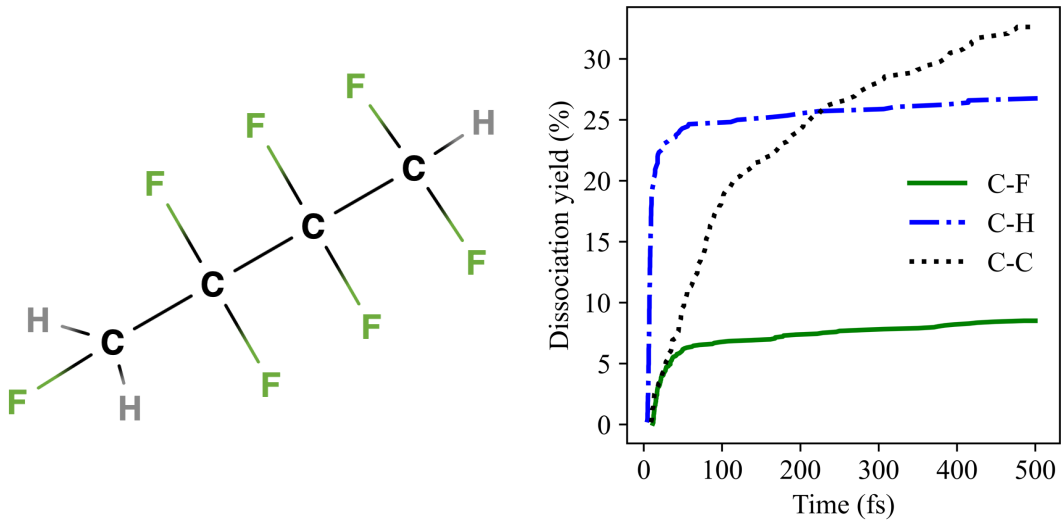

Figure 4.38: Dissociation kinetics of $C_4H_3F_7$ for each bond type over 200 lowest triplet state trajectories at 5000 K. A dissociation event is defined as the first timestep at which a bond length exceeds 5 Bohr. Kinetics are normalised by the total number of bonds of each type present in the molecule.

chain of a molecule as with the 1,1,3-$C_3H_5F_3$ and 1,1,4-$C_4H_7F_3$ molecules can have an effect of neutering certain dissociation pathways. This is due to trend 2 established in Chapter 3 that states the rapid dissociation of multiple C-H bonds from several carbon centres dominates the dissociations and discourages further bonds from breaking. To gather evidence in spite of this fact, the 1,1,4-$C_4H_7F_3$ molecule was run at lower temperatures, namely 3000 K, in order to limit the number of C-H dissociations. Another way to tackle this issue is to replace the hydrogens with fluorines, as their tendency to break slower than other bonds removes the limiting effect of the C-H bond, though this does result in an increase of computational cost due to the much higher number of electrons in the molecule. While the electronegativity of the fluorine atoms will also indeed affect the molecules features and therefore its dissociation pathways, a collection of these molecules can be used to make an argument for the -CH_2F electrophore.

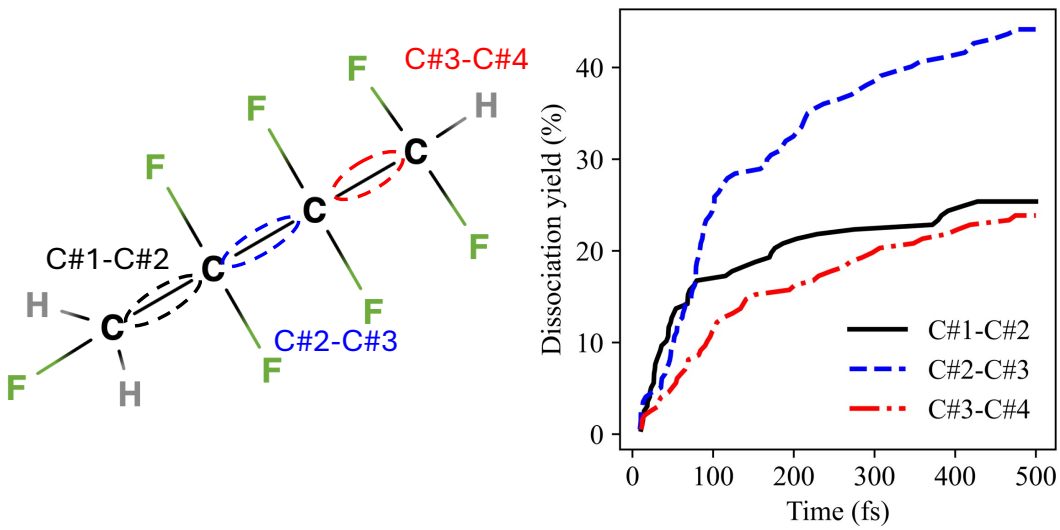

Figure 4.39: Dissociation kinetics of $C_4H_3F_7$ for each C-C bond environment over 200 lowest triplet state trajectories at 5000 K. A dissociation event is defined as the first timestep at which a bond length exceeds 5 Bohr. Kinetics are normalised by the total number of bonds of each type present in the molecule.

The overall dissociation yields in Fig. 4.38 are different compared to the $C_4H_3F_7$ molecule due to the replacement of the hydrogens with fluorine. The C-C bonds is the bond type with the highest dissociation yield present in the molecule. The C-C bond type also has a higher average dissociation yield than most individual C-C bond dissociation yields in the -CH_2F containing molecules considered in this section. The only other molecule in this section to have a higher average C-C dissociation yield is the 1,1,2,2,3,3,4-Heptafluoro-1-butanol molecule to which $C_4H_3F_7$ bares the most resemblance as the hydrogen on the C#4 carbon is substituted with the alcohol functional group. The C-H dissociation yield is 26.3% and the C-F dissociation yield is 8.4% which is again lower than the dissociation yield of the 1,1,2,2,3,3,4-Heptafluoro-1-butanol molecule of 12.4%, suggesting that the inclusion of the oxygen atom induces a higher number of dissociations even when not acting as an electrophore.

The individual C-C bonds in Fig. 4.39 do indeed show the same trends as the other molecules containing the -CH_2F electrophore, where the C#1-C#2 bond dissociates the most for the initial part of the propagation before the other C-C bonds overtake in dissociation yield and the order of the bonds finalises as C#2-C#3, C#1-C#2, C#3-C#4. The C#2-C#3 bond has a dissociation yield of 45.5% which is very slightly higher than the C#2-C#3 dissociation yield of the 1,1,2,2,3,3,4-Heptafluoro-1-butanol at 43.8%. The main difference between the C-C dissociation yields of the two molecules is in the C#3-C#4 bond which dissociates more than the C#1-C#2 bond in 1,1,2,2,3,3,4-Heptafluoro-1-butanol, due to the electron withdrawing nature of the oxygen atom weakening the C#3-C#4 bond. The absence of the oxygen atom in the $C_4H_3F_7$ means that there is not an extra encouragement of the C#3-C#4 bond to break resulting in it being the least broken C-C bond. The second and third most common dissociation pathways are both two step processes with the C#2-C#3 bond broken second. The difference between these two pathways is the first dissociation, which is either the breaking C#1-H or the C#1-F bond, meaning that as with the previously considered -CH_2F containing molecules the localisation of the triplet state excitation and therefore dissociative character is centralised around the C#1 carbon causing a bond breaking event on that carbon followed by the dissociation of a bond on the adjacent carbon.

Further evidence of the -CH_2F electrophore can be seen in the C-H bond dissociations. The most common dissociation pathway for the $C_4H_3F_7$ molecule is a single dissociation of particularly one of the C#1-H bonds. Fig. 4.40 shows that the two C-H environments have very different dissociation yields, with the C#1-H yield being over double that of the singular C#4-H bond. This is also within the context of the C#1-H bond containing two C-H bonds compared to the one bond present in the C#4-H environment, meaning that the total number of C-H dissociations is approximately 4 times higher on the side of the electrophore. The C-F bonds in Fig. 4.41 also show a very similar trend with the single C#1-F having a dissociation yield of 21% which is similar to the C#1-F yield seen in the 1,1,3-$C_3H_5F_3$. Other, though lesser, similarities also exist with 1-C_3H_7F (where

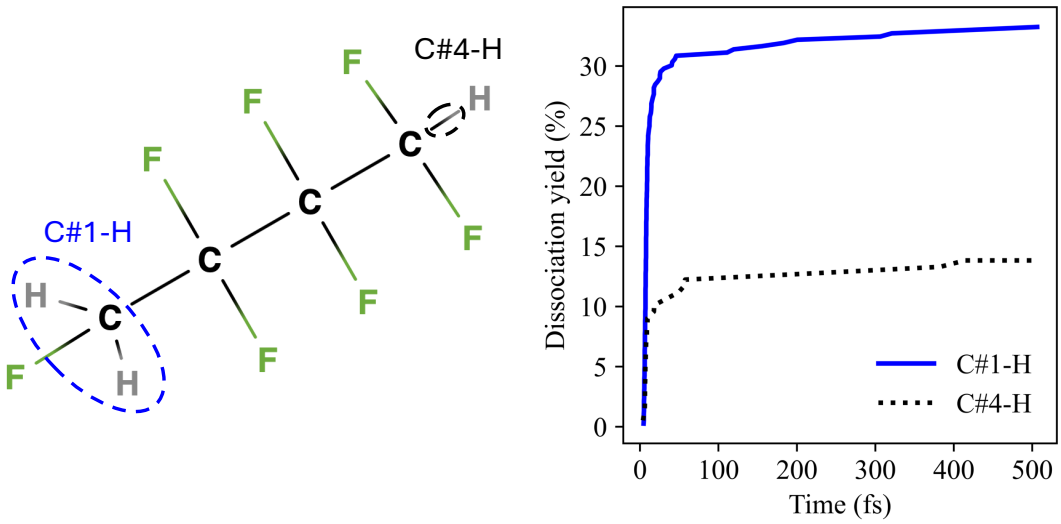

Figure 4.40: Dissociation kinetics of $C_4H_3F_7$ for each C-H bond environment over 200 lowest triplet state trajectories at 5000 K. A dissociation event is defined as the first timestep at which a bond length exceeds 5 Bohr. Kinetics are normalised by the total number of bonds of each type present in the molecule.

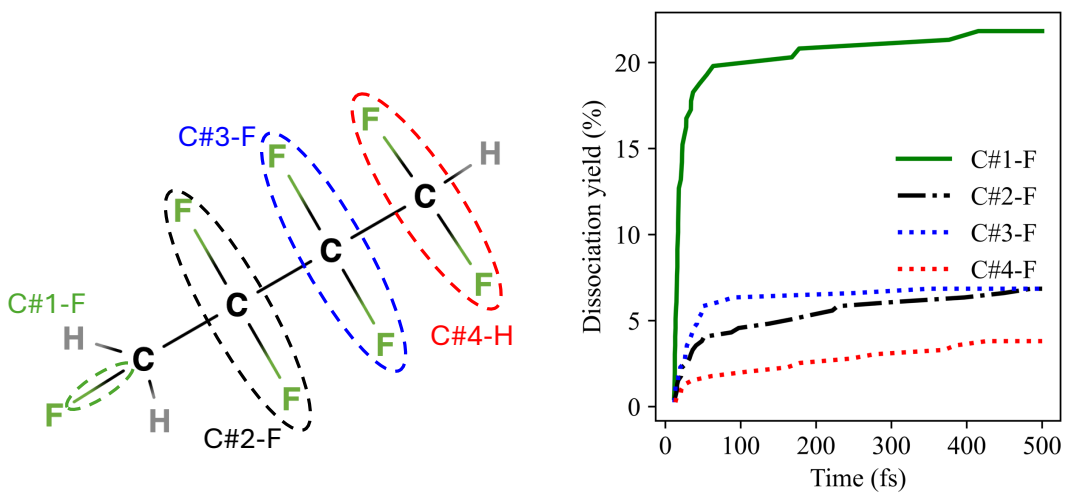

Figure 4.41: Dissociation kinetics of $C_4H_3F_7$ for each C-F bond environment over 200 lowest triplet state trajectories at 5000 K. A dissociation event is defined as the first timestep at which a bond length exceeds 5 Bohr. Kinetics are normalised by the total number of bonds of each type present in the molecule.

the final yield is similar but the kinetics are different) and other molecules where the initial rapid kinetics are observed but result in different final dissociation yields, suggesting that the effect of the -CH_2F electrophore on its own C-F bond is fairly consistent.

4.5 Interactions of multiple electrophores

Investigations of the molecules in Section 2.7, as well as analysis of the dissociation pathways of the $C_5F_{10}O$ molecules considered in the previous chapter showed that the C=C bond can also play the role of an electrophore. If a single electrophore is responsible for determining the dissociation pathways of a molecule, it is natural to question the effect that multiple electrophores could have. Is one type of electrophore favoured over the other? Does the preferred electrophore depend on the position of each electrophore? If two electrophores are present, does the involvement of non-adiabatic coupling elements in MD become necessary?

4.5.1 Propen-1-ol

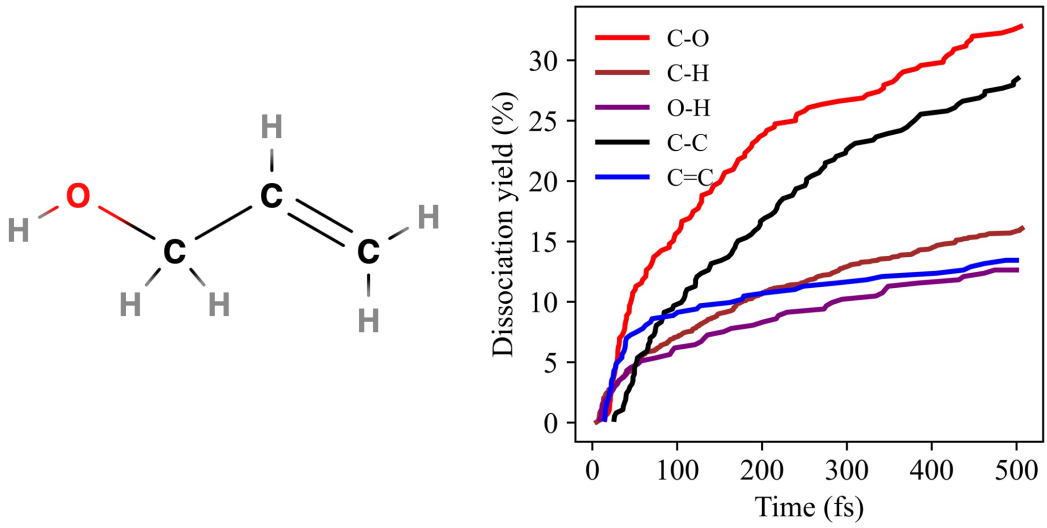

Figure 4.42: Dissociation kinetics of propen-1-ol for each bond type over 414 lowest triplet state trajectories at 5000 K. A dissociation event is defined as the first timestep at which a bond length exceeds 5 Bohr. Kinetics are normalised by the total number of bonds of each type present in the molecule.

Introducing a C=C bond to the propanol molecule (studied in Section 4.1) to from propen-1-ol dramatically shifts the dissociation pathways as the dissociation kinetics (shown in Fig. 4.42) of the O-H bond are completely different to that seen not only in propenol but alcohol molecules as a whole. The only exception to this trend was found in the 1,1,2,2,3,3,4-Heptafluoro-1-butanol due to the presence of the -CH_2F electrophore, suggesting that this electrophore is more dominant than the oxygen atom. Conversely, the dissociation of the C-O bond increases from practically non-existent to 30% of the C-O bonds dissociating in 500 fs at 5000 K. This suggests that the double bond is the most favoured electrophore. The C-C bond dissociates more often than the C=C bond, but this can not be said to be definitive evidence that the oxygen atom is no longer acting as an electrophore, as

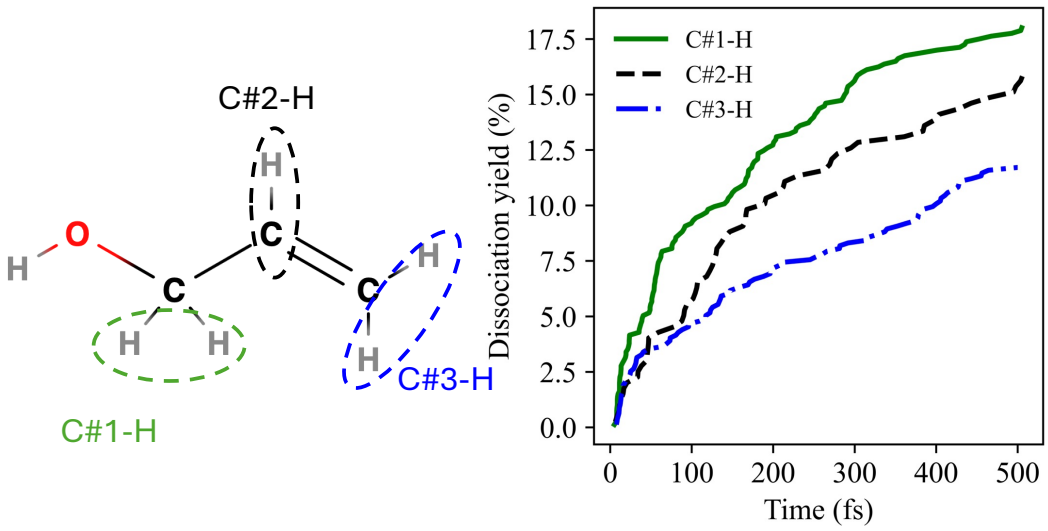

Figure 4.43: Dissociation kinetics of propen-1-ol for each C-H bond environment over 414 lowest triplet state trajectories at 5000 K. A dissociation event is defined as the first timestep at which a bond length exceeds 5 Bohr. Kinetics are normalised by the total number of bonds of each type present in the molecule.

the single C-C bond is in between the C=C bond and the oxygen atom. Similarly, due to the small size of the molecule the distribution of the dissociated C-H bonds in Fig. 4.43 does not provide any extra information as to whether the oxygen is acting as an electrophore as the C-H bonds adjacent to the oxygen atom are also adjacent to the C=C bond.

This molecule is therefore a perfect example to showcase where the assumption that MD simulations can be performed only on the lowest triplet state fails. In order to achieve an explanation of the role of the two electrophores in this molecule, NAMD are required. 400 trajectories were run via multiple trajectory Ehrenfest dynamics with the propenol molecule starting on the lowest and second lowest triplet state. The population dynamics shown in Fig. 4.44 were found to be similar to the non-adiabatic simulations run for the $C_3H_2F_6$ molecule in Section 2.7. When the trajectory begins with full population in state 1, there is an initial

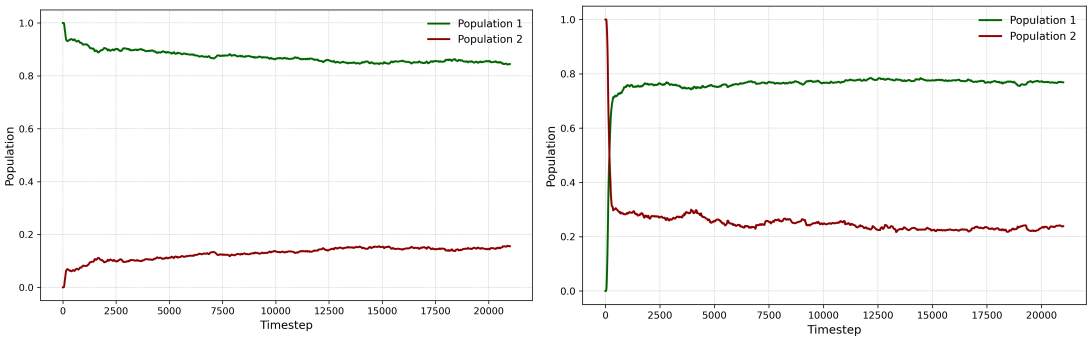

Figure 4.44: Average populations of 400 triplet state multiple trajectory Ehrenfest trajectories for propen-1-ol at 5000 K starting at state 1 (left) and state 2 (right).

population transfer to state 2 though this rate slows rather quickly and through all of the propagation the population stagnates at around 0.8 for state 1 and 0.2 for state 2. Interestingly, when a trajectory starts in state 2, by the end of the propagation the populations have the same ratio, with very rapid population transfer within the first 250 timesteps.

However even though for the majority of the propagation the populations of the two states are relatively equal regardless of the starting state, the resulting dynamics differ greatly. When the trajectories start in state 1, the dissociation yields in Fig. **??** unsurprisingly resemble the yields found when performing MD on only the lowest triplet state. The O-H bond has the lowest dissociation yield, lower than even the simulations on only the lowest state, and the C-O bond has the highest dissociation yield paired with the C-C bond. The C=C bond also has a large number of initial dissociations with a final dissociation yield of 16.5%. When the trajectories begin populating the second state, the dissociation yields in Fig. 4.46 return to resembling the usual expectations of an alcohol molecule with the O-H bond having by far the highest dissociation yield of 80%. The C=C bond that before had a spike of initial dissociations now has almost none with a final dissociation yield of only 5.3%. The C-O bond also dissociates much less often as is common in alcohols, though the dissociation yield of 13% is rather high perhaps due to the presence of two electrophores in the molecule allowing for

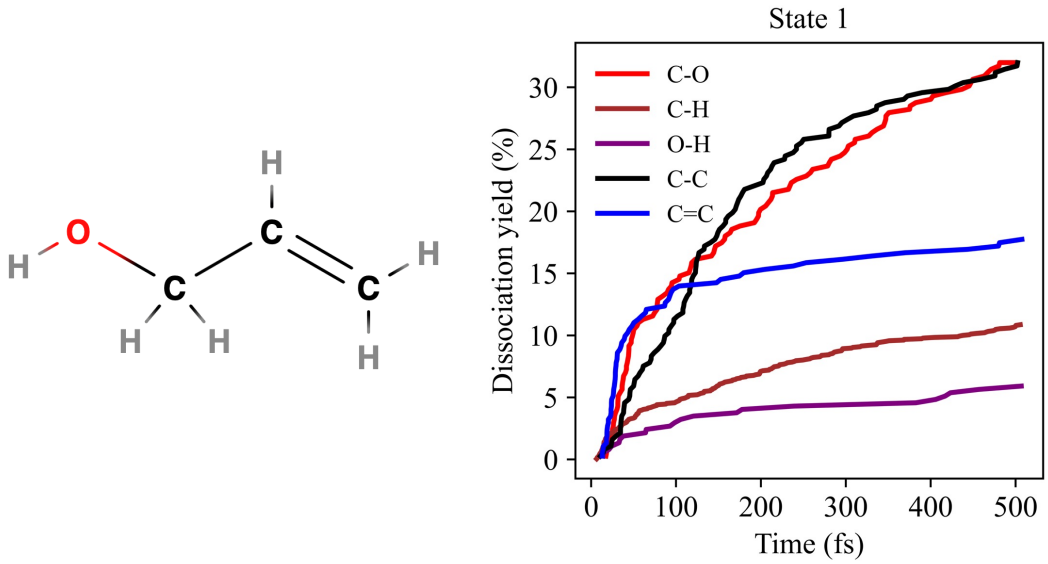

Figure 4.45: Dissociation kinetics of propen-1-ol for each bond type over 414 triplet state multiple trajectory Ehrenfest trajectories at 5000 K with the population beginning in state 1.

more dissociations. However only over a quarter of the C-O dissociations occur after the dissociation of the O-H bond as is usual. These results suggest that the triplet excited states of a molecule containing multiple separate electrophores can be mapped to the electrophores with each of the electrophores localising a triplet state.

4.5.2 Allyl mehtyl ether

It is possible to argue the alcohol functional group is a 'fast' electrophore, due to the rapid and excessive O-H breaking caused by its localisation. This allows for greater clarity from just observing the dissociation yields where the triplet state localisation is localised. In fact it is true that when using a molecule with a 'slower' electrophore, such as a methoxy functional group, the differences in the dissociation yields for allyl methyl ether are less differential.

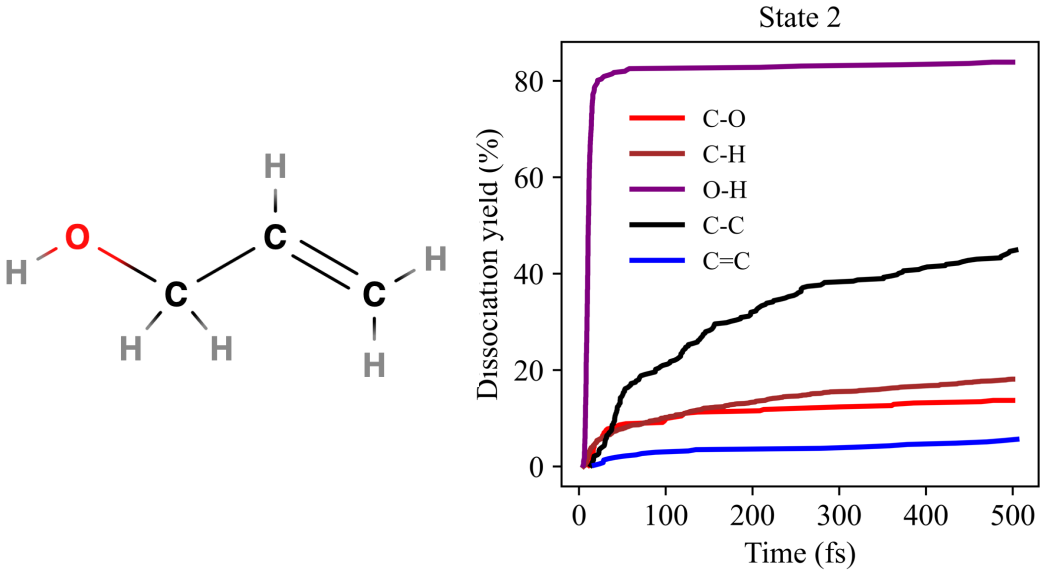

Figure 4.46: Dissociation kinetics of propen-1-ol for each bond type over 400 triplet state multiple trajectory Ehrenfest trajectories at 5000 K with the population beginning in state 2.

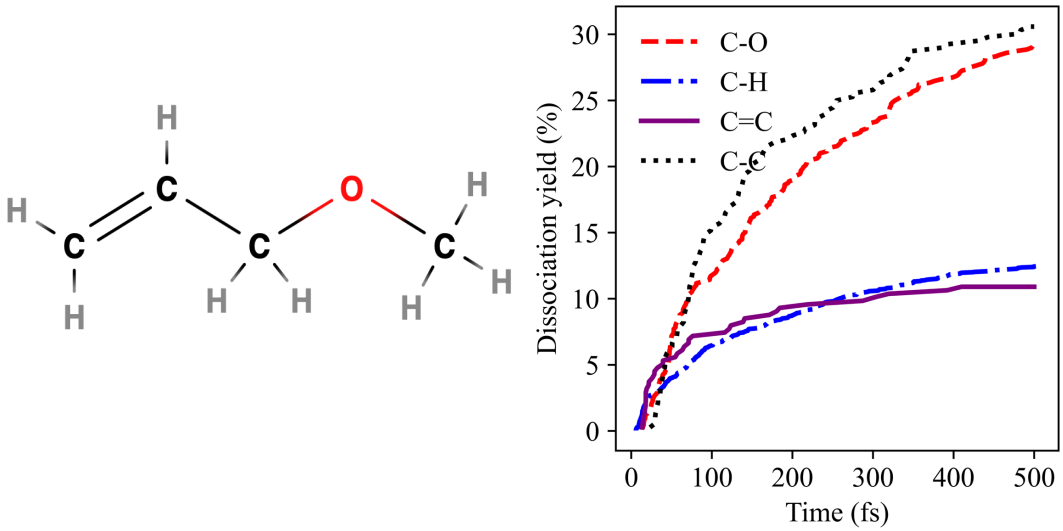

Figure 4.47: Dissociation kinetics of allyl methyl ether for each bond type over 376 lowest triplet state trajectories at 5000 K. A dissociation event is defined as the first timestep at which a bond length exceeds 5 Bohr. Kinetics are normalised by the total number of bonds of each type present in the molecule.

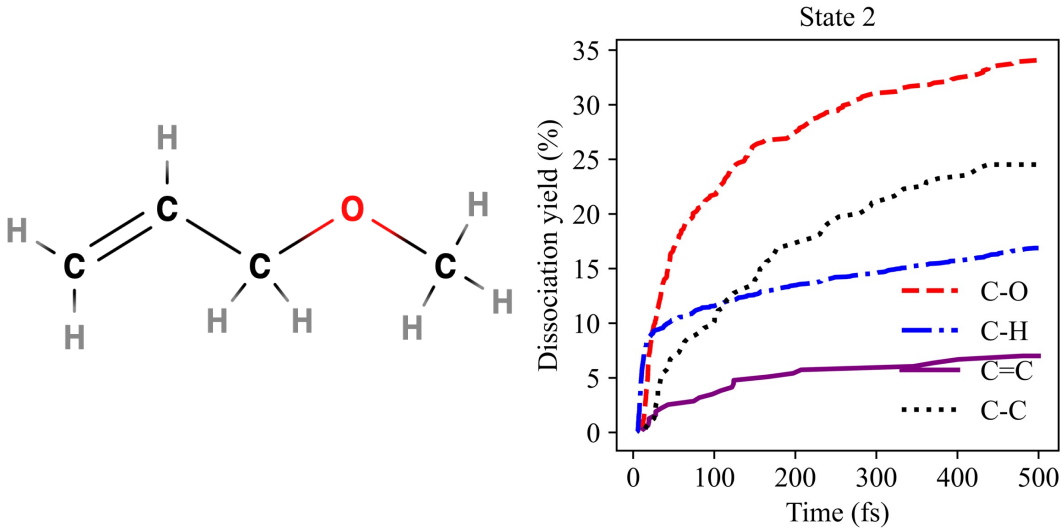

Figure 4.48: Dissociation kinetics of allyl methyl ether for each bond type over 314 multiple state Ehrenfest triplet state trajectories at 5000 K with the population beginning in state 2.

Trajectories were performed using standard MD on the lowest triplet state only and the average dissociation yields are shown in Fig. 4.47. The C-C bond and C-O bond have the highest dissociation yields, with 30.5% and 29.3% respectively. Interestingly, despite being hypothesised to localise the excitation for the lowest triplet state, the C=C bond dissociation yield is lower at 10.9%, more in line with the dissociation of the C-H bonds at 12.4%. However, this dissociation yield is within the range of other molecules without the C=C electrophore being adjacent to the oxygen atom. It is also important to note that during the initial propagation, the C=C bond has the highest number of dissociations suggesting that it is still acting as an electrophore.

If as before the non-adiabatic dynamics are reintroduced considering two triplet states and the trajectories start on the highest state as in Fig. 4.48, the average C-O dissociation yield increases to a dissociation yield of 34% while the C=C bond decreases to a yield of 7%, with fewer initial dissociations. This suggests that once again the C=C bond acts as the dominant electrophore, with the second lowest triplet state being localised by the other electrophore in the molecule, in this case the methoxy group.

While the average dissociation yield of the C-H bonds is not radically different whether the trajectories are performed with standard DFT on the lowest state (as in Fig. 4.49) or with multiple trajectory Ehrenfest trajectories with population starting on the highest state (as in Fig. 4.50), the individual C-H environments do experience a change. The C#3-H bond is the between both electrophores, being adjacent to the C=C bond while bonded to the oxygen atom, and so reports the highest dissociation yield of all C-H environments for both forms of trajectories. However when the trajectories are propagated on only the lowest triplet state using standard MD, the order of the rest of the C-H bonds in terms of dissociation yield are as follows: C#2-H, C#1-H, C#4-H. This is proof that the localisation continues to be around the C=C bond as the C#1-H and the C#2-H bond are bonded to the carbons involved in the double bond. The least dissociative C-H environment, C#4-H is on the opposite side of the molecule to the C=C electrophore, and so has a very low dissociation yield of 7.8%. When the multiple

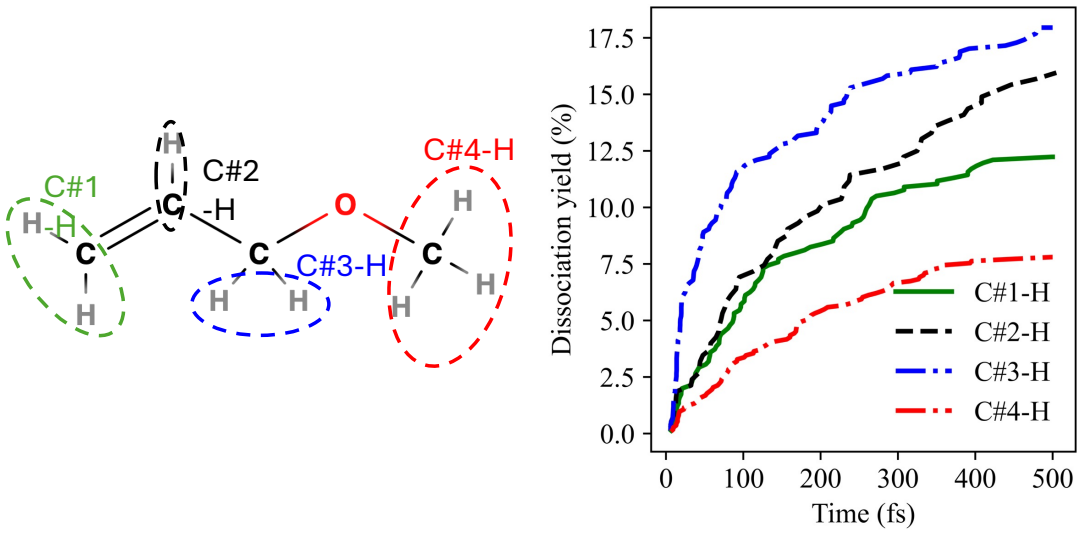

Figure 4.49: Dissociation kinetics of allyl methyl ether for each C-H bond environment over 376 lowest triplet state trajectories at 5000 K. A dissociation event is defined as the first timestep at which a bond length exceeds 5 Bohr. Kinetics are normalised by the total number of bonds of each type present in the molecule.

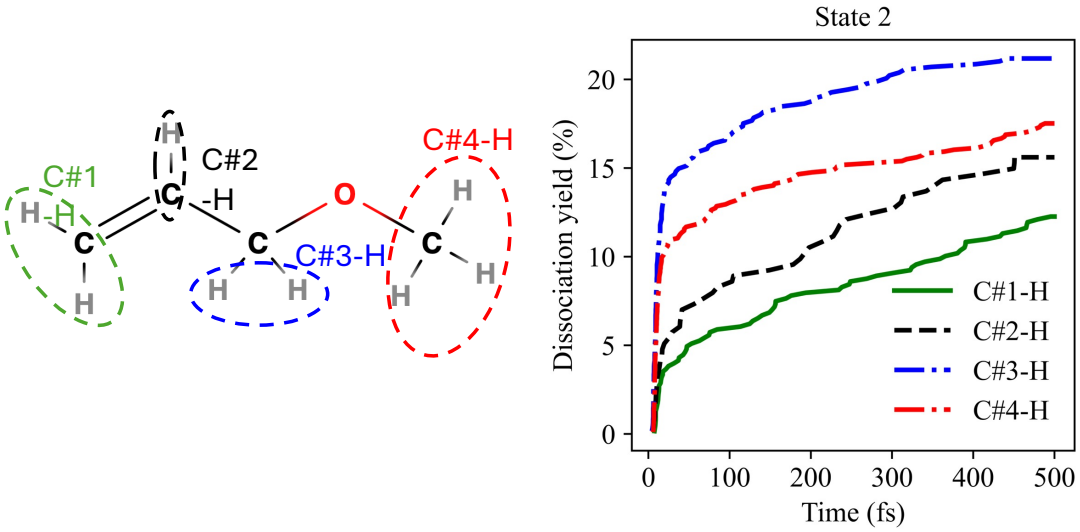

Figure 4.50: Dissociation kinetics of allyl methyl ether for each C-H bond environment over 314 multiple state Ehrenfest triplet state trajectories at 5000 K with the population beginning in state 2.

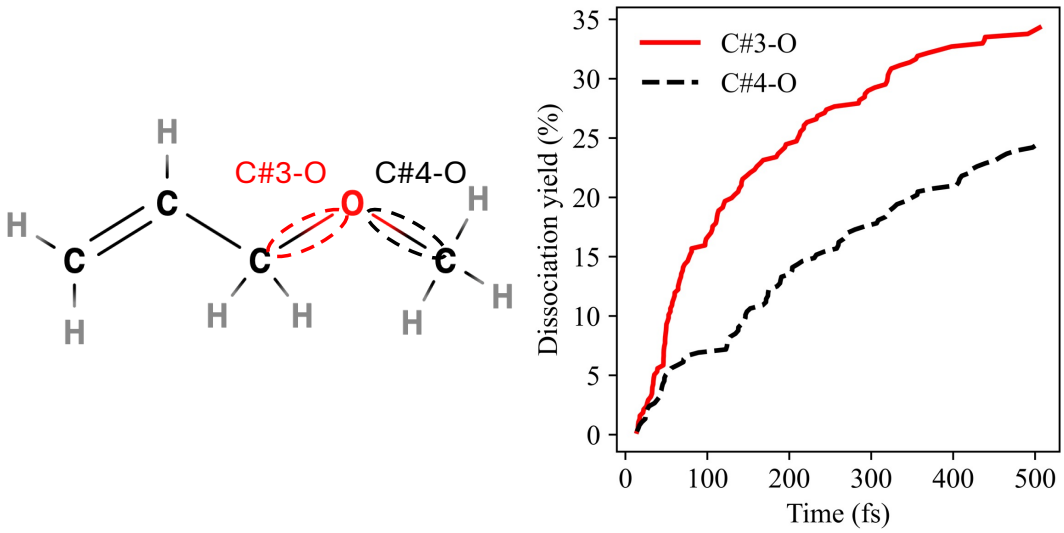

Figure 4.51: Dissociation kinetics of allyl methyl ether for each C-O bond environment over 376 lowest triplet state trajectories at 5000 K. A dissociation event is defined as the first timestep at which a bond length exceeds 5 Bohr. Kinetics are normalised by the total number of bonds of each type present in the molecule.

trajectory Ehrenfest trajectories are performed with the population starting on the highest triplet state, the order of the C-H environments changes entirely with the aforementioned exception of the C#3-H bond. Now the second most dissociative C-H bond environment is C#4-H, which is adjacent to the oxygen atom electrophore, again suggesting that the second highest triplet state is localised by the oxygen and there exists the same hierarchy of electrophores. Again the lowest environment are the C-H bonds furthest away from the currently active electrophore, in this case the C#1-H environment.

The order of the C-O environments do not change between standard DFT trajectories (as in Fig. 4.51) and multiple trajectory Ehrenfest trajectories starting in state 2 (as in 4.52), and in fact the proportion between the 2 environments with the C#3-O bond accounting for 59% of all C-O dissociations for dynamics on a single triplet state, and account for 61% of all dissociations in the multiple

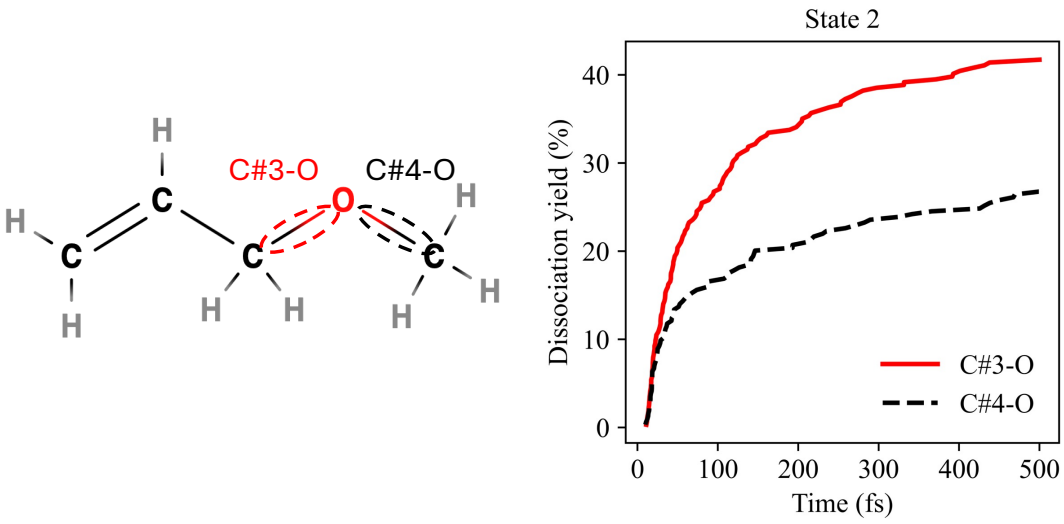

Figure 4.52: Dissociation kinetics of allyl methyl ether for each C-O bond environment over 314 multiple state Ehrenfest triplet state trajectories at 5000 K, with the populations beginning in state 2.

trajectory Ehrenfest trajectories. The dissociation yields for both C-O bonds increase in the multiple trajectory Ehrenfest trajectories, only slightly for the C#4-O bond from 24.5% to 26.8%, though the effect of the oxygen being the active electrophore is more notable in the C#3-O bond where the dissociation yield increases from 34.3% to 41.7%. The dissociation kinetics also differ between the different type of trajectories, with the C-O bonds having a more vertical peak in initial dissociations as the triplet state excitation is localised around the C-O bonds as the oxygen is the active electrophore in the second lowest triplet state. While the kinetics do change between states, the dissociation yields and the proportions suggest that the direction that the C-O bonds dissociate is determined by the stability of the radical products.

4.5.3 PPVE isomer

A more impactful molecule to study within the theme of multiple electrophores would be a PFAS molecule considering their application to the plasma etching processes. It is possible to imagine an isomer where the electrophores of the PPVE and PIPVE molecules are separated and the C=C bond is instead on the terminal C#1 carbon. Simple MD trajectories on a single triplet state have been run for this molecule and can now be compared to PPVE and PIPVE to confirm that the C=C bond still acts as the dominant electrophore when the molecule is fluorinated instead of consisting of C-H bonds. As the electrophores are separated, the dissociation yield of all bond types are lower than that observed in PPVE and PIPVE as while the triplet state is still localised around the double bond acting as the active electrophore in the lowest triplet state, the oxygen can still act as an electron withdrawing group, allowing for an increased number of dissociations. This results in the C=C dissociation yield being half of the yield in PPVE at 35.8% in Fig. 4.53. Unlike the other $C_5F_{10}O$ isomers, the C-C bonds have a higher average dissociation yield than the C-O bonds, due to the active electrophore being the C=C bond which is now further removed from the C-O bonds. The C-F bonds also report a lower dissociation yield of 5.5% as while there still remain C-F bonds close to the electrophore, there is still a reduction of general dissociative character after the separation of the electrophores.

Surprisingly the C-C bonds in Fig. 4.54 have almost completely symmetrical dissociation yields and while the C#1-C#2 bond dissociates quicker initially and maintains a higher number of dissociations across all trajectories, there is not clear evidence that the dissociation yield of one C-C bond is affected more due to the electrophore. Likewise with the C-O bonds in Fig. 4.55, while the closest C-O bond to the electrophore has a significantly higher dissociation yield, it does not differ to PPVE as the double bond adjacent to the oxygen atom causes the opposite C-O bond to dissociate more often. The C-F bonds in Fig. 4.56, however, do clearly show the effect of the electrophore as the two C-F environments on the C=C bond constitute the two C-F environments with the highest dissociation yields, which are cleanly separated from the rest. The next most dissociative

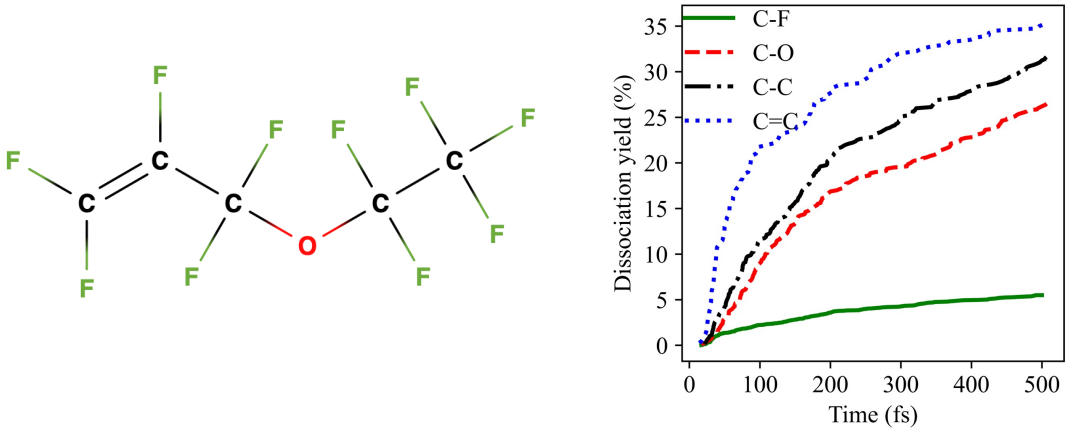

Figure 4.53: Dissociation kinetics of the PPVE isomer for each bond type over 314 lowest triplet state trajectories at 5000 K. A dissociation event is defined as the first timestep at which a bond length exceeds 5 Bohr. Kinetics are normalised by the total number of bonds of each type present in the molecule.

C-F environment is the C#3-F bond which is the adjacent carbon to the active electrophore, the C=C bond. The C-F environment that is furthest from the active electrophore, C#5-F, has the lowest dissociation yield of just 2.1% almost four times lower than those bonded to the active electrophore. The fact that the furthest C-F or C-H environment from the active electrophore consistently has the lowest dissociation yield despite being adjacent to an oxygen atom that could potentially serve as an electrophore on another triplet state shows that the localisation is entirely based on a single electrophore for each triplet state. It is predicted that NAMD trajectories with the populations staring on state 2 would present with dissociation yields suggesting that the oxygen is acting as the dominant electrophore. However due to the size of the molecule and the number of fluorines present the computational cost of running these trajectories is prohibitive and is left as future work.

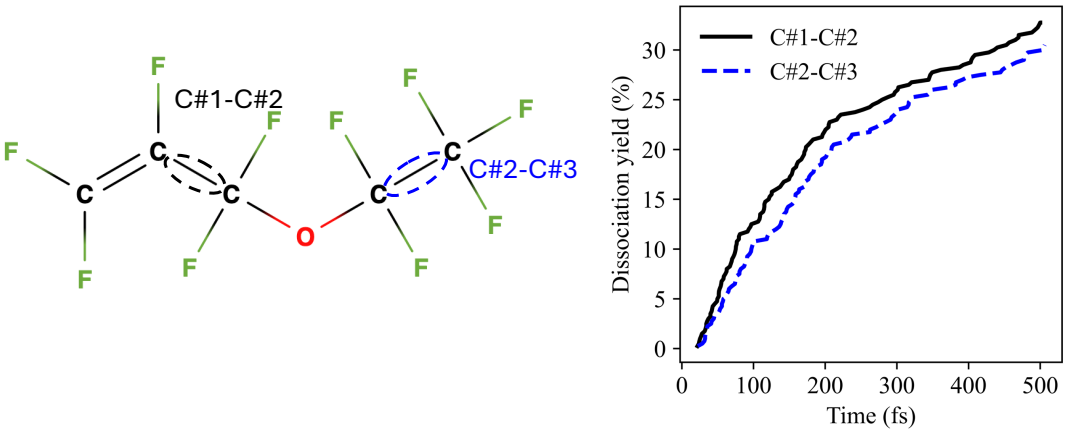

Figure 4.54: Dissociation kinetics of PPVE isomer for each C-C bond environment over 314 lowest triplet state trajectories at 5000 K. A dissociation event is defined as the first timestep at which a bond length exceeds 5 Bohr. Kinetics are normalised by the total number of bonds of each type present in the molecule.

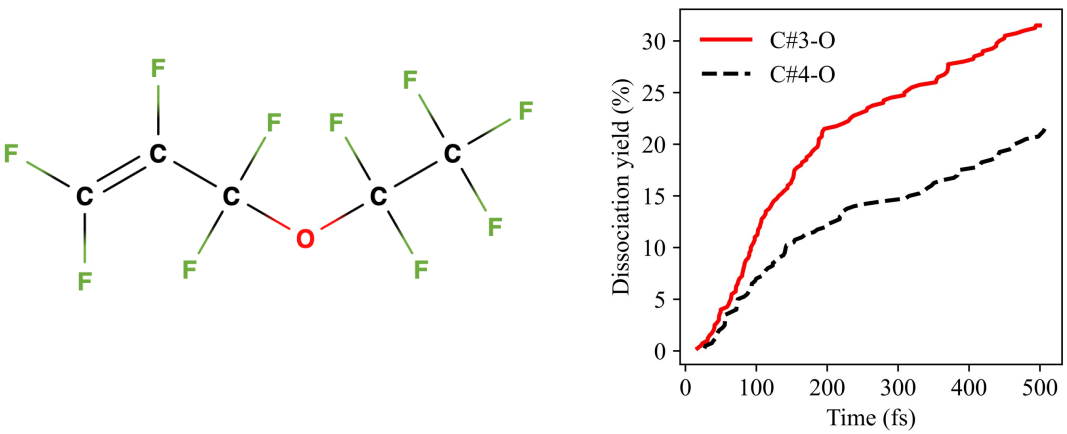

Figure 4.55: Dissociation kinetics of PPVE isomer for each C-O bond environment over 314 lowest triplet state trajectories at 5000 K. A dissociation event is defined as the first timestep at which a bond length exceeds 5 Bohr. Kinetics are normalised by the total number of bonds of each type present in the molecule.

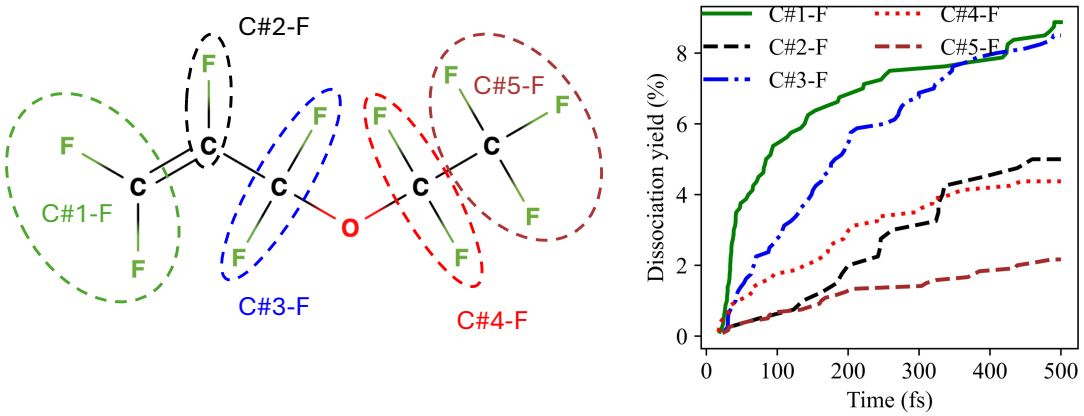

Figure 4.56: Dissociation kinetics of PPVE isomer for each C-F bond environment over 314 lowest triplet state trajectories at 5000 K. A dissociation event is defined as the first timestep at which a bond length exceeds 5 Bohr. Kinetics are normalised by the total number of bonds of each type present in the molecule.

4.6 Conclusions

The analysis of the neutral dissociation pathways after excitation via electron impact for these molecules has provided further evidence for the five trends laid out in Chapter 3. The simple alcohol molecules chosen in Section 3.1 shows that the alcohol functional group having a incredibly high O-H bond dissociation yield and consequent lowering of the C-O dissociation yield is consistent, initially outlined in trend 3. The C_2F_5OH molecule in section 3.4 shows that the -CH_2OH group acts as an electrophore in the same way as the -CF_2OH group. Simple molecules in section 4.2 are selected such that the effects observed can only be due to the secondary effect of the hydrogen containing bonds hypothesised in trend 2. The rapid and frequent C-H dissociations can dictate the kinetics and the dissociation yield of C-O and C-C bonds. The C-C bonds will still be discouraged as the temperature of the trajectories are decreased as the C-C and C-H bonds will both dissociate less due to the reduction in kinetic energy. However this is not necessarily the case for the C-O bond as the oxygen atom has the capability to act

as a electrophore and so may at lower temperatures dissociate more rapidly than the hydrogen-containing bonds which could result in very different dissociation kinetics. These intricacies stress the need for a MD method that can simulate the lower temperatures and conditions that are accurate to real processes undergone by molecules without having prohibitive computational costs.

The -CH_2F group has been identified as another group capable of acting as an electrophore. Multiple molecules containing this electrophore have exhibited high dissociation yields and rapid dissociation events of the bonds that surround the carbon of the -CH_2F group, including a unusually high dissociation yield for a C-F bond. This trend is also shown to be true across multiple temperatures and even is the more dominant electrophore when compared to the oxygen atom in some molecules. The nature of this discovery being accidental and found simply by analysing isomers highlights the fact that even the trend set detailed at the end of Chapter 3 even including all of the detail provided this chapter is still not sufficient as further effort must be undertaken in order to identify potential electrophores and place these electrophores within the hierarchy in order to accurately predict the neutral dissociation pathways of a molecule without performing MD simulations. Section

Finally, Section 4.4 outlines the interactions of multiple electrophores and posits that there exists a hierarchy of electrophores. A molecule containing many separated electrophores will have a lowest triplet state localised around each electrophore. It is shown that when comparing multiple molecules that contain multiple electrophores, namely the C=C bond and the oxygen atom, the C=C bond electrophore consistently localises the lowest triplet state, which can be observed both through the higher number of initial dissociations of this bond along with the increased dissociation yield of bonds surrounding this electrophore comparative to other bonds of the same type further away from the electrophore. NAMD of these molecules with separated electrophores reveals consistently that if a trajectory begins on the second lowest triplet state then the dynamics revolve around the second electrophore with (in the cases considered) the oxygen-containing bonds have a much higher rate of initial dissociations and the bonds closer to the oxygen

electrophore having a higher relative dissociation yield for that bond type. Therefore it can be said that for as many separated electrophores exist in a molecule, there will be a triplet state whose dissociation pathways are determined by its localisation to that state's active electrophore. Further, it can be said that certain electrophores are more dominant than others in that they localise excitation to a lower lying triplet states than others. In that sense, the C=C electrophore has been found to be more dominant than the oxygen atom electrophore for all molecules considered. Therefore while trend 5 of the set presented in the conclusion of chapter 3 remains correct for PPVE and PIPVE, separated electrophores require the creation of a hierarchy of electrophores. The updated trend 5 would be:

Trend 5: When multiple potential electrophores exist within a molecule, the lowest triplet states will correspond to localisation around each electrophore. When the electrophores are separated, a hierarchy can be formed of which electrophore will be dominant (and therefore will localise the lowest triplet state). For all molecules considered the C=C bond is a more dominant electrophore than the O atom.

Applying this perspective in retrospect, there are now two possibilities for the PPVE and PIPVE molecules considered in section 3.3 and section 3.5 respectively. One is that the adjacent electrophores both play a role in the localisation of the lowest triplet state and that the excitation causes some resonance structure across both electrophores. The other is that the C=C bond remains the most dominant and the oxygen atom, while not acting as an electrophore, still has electron withdrawing effects that weaken adjacent bonds. Further simulations of varied and more complicated molecules are required in order to properly distinguish both cases. Future work requires a more detailed analysis and comparison into molecules containing multiple separated electrophores. For example, the iso-$C_4H_2F_7OH$ molecule showed the -CH_2F functional group doesn't always outcompete the oxygen atom as an electrophore. What features of the electrophore

determines whether a given functional group is more dominant in localising the excitation to the triplet state along with a more complete list of which functional groups can serve an electrophore is vital to the prediction of the dissociation pathways of molecules with multiple separated electrophores.

Chapter 5

Introduction of Cloning to MCEv1

5. INTRODUCTION OF CLONING TO MCEV1

The majority of the molecules considered in this thesis were simulated under the assumption that only the lowest triplet state was relevant for analysis of its dissociations and therefore did not require the use of NAMD, instead opting for cheaper standard MD propagating only on the lowest triplet state. However, as the complexity of the molecule and need for more quantitative data increases, there is no definitive proof that this assumption will always hold, meaning it therefore will be necessary to reintroduce multiple electronic states, and with that NAMD. MCEv1 is a method developed by the group of Shalashilin. While the lack of configurational amplitudes makes the integration of MCEv1 method with electronic structure codes difficult, the extension of similarly constructed methods to Ab Initio versions [266] presents a framework for a similar extension of MCEv1. As MCEv1 offers good computational cost scaling with respect to the degrees of freedom, it should be aptly suited to efficient simulations of the plasma relevant molecules.

MCEv1 already is capable of converging a wide range of regimes, often tested in the Spin Boson model [68, 74]. In order to present it as a valid alternative to other methods such as MCTDH, it is necessary to expand the method to be able to simulate the cases which it currently struggles to converge to the correct result. Due to the success of the implementation of the cloning procedure in MCEv2, it is believed that cloning will be a useful tool in expanding the range and increasing the efficiency of MCEv1. Not only was cloning important in the development of the Ab Initio extension of MCE, AIMC, but it was also in fact necessary for MCEv2 to simulate cases of the Spin Boson model with the same accuracy as MCEv1, which has been show to tackle various more cases without the use of sampling techniques. As cloning expanded the range of cases able to be tackled by MCEv2, it is reasonable to assume that the cloning procedure would have the same effect on MCEv1, allowing the method to tackle the edge cases of the Spin Boson model that were previously inaccessible, such as the zero temperature regime.

5.1 Computational details

Throughout this chapter, each case of the Spin Boson model is discussed via labelling of the parameters of the Hamiltonian (as shown in 2.74) and the exponential cut-off (as shown in 2.76). The bath of the Spin Boson model is constructed as outlined in chapter 2.5.1. For all cases, the maximum frequency used in the construction of the bath modes was taken to be 5 times the characteristic frequency ($\omega_{max} = 5\omega_c$). In order for each case to be identified, characteristic frequency (ω_c) and the coupling strength (α_k) has been given in each figure caption as well as the discussion of the results.

As all cases considered are of PES wells with no energy shifting (i.e. $\epsilon = 0$), the simulation can be initialized with the population entirely contained within either well. The well with the starting population was designated as the primary well with the population difference observable being defined as the population of the primary well minus the population of the secondary well. For each case, the timestep was increased until numerical instability was shown through either failure during the initialisation of the bath modes or the propagation equations producing unphysical changes in the population difference observable. The remaining parameters, namely the basis set size and number of bath modes, were converged by systematic increase until no further change in the population difference observable was observed.

5.2 Development of the cloning procedure

Conceptually the idea of cloning in MCE can be and should be seen as the analogous process to the spawning procedure present in AIMS [62]. Unlike AIMS, where each PES is assigned a set of basis functions that are guided by a classical trajectory, MCE employs an Ehrenfest approach where a pseudo PES is constructed as a quantum average of all present PES. The Ehrenfest dynamics that utilise this pseudo PES affords MCE its fast dynamics and is accurate as long as the pseudo PES remains a faithful representation of the system. Unfortunately this assumption is not always true, particularly in the context of non-adiabatic

processes. When the energy of two electronic states converges, the geometric conceptualisation can be represented by the two PES moving closer before the curves intersect. As the curves move closer to this intersection, the rate of population transfer between the PES increases resulting in an increase in non-adiabatic effects. The challenge for the model of the pseudo quantum averaged PES is accurately representing the wavefunction after multiple PESs have intersected and now diverge. It is possible for the wavefunction to follow any of these intersected PES or bifurcate and follow many. However an averaged PES such as that employed by MCE could theoretically continue relatively unchanged as multiple diverging PESs could still produce the same average, meaning that the Ehrenfest PES is no longer an accurate reduction of the system. To rectify this, it is possible to allow the basis set to bifurcate in a similar way to the wavefunction with the resulting dynamics therefore more accurately simulating the true dynamics of the system. The cloning implemented in MCEv2 bifurcates the basis set by identifying basis functions that have their amplitudes straddled between multiple PES and replace it with two new child basis functions, where the general equation for cloning for a system with two electronic states can be given as,

$$(a_k^{(1)}|1\rangle + a_k^{(2)}|2\rangle)|z_k(t)\rangle = (0|1\rangle + a_k^{(2)}|2\rangle)|z_k(t)\rangle + (a_k^{(1)}|1\rangle + 0|2\rangle)|z_k(t)\rangle \quad (5.1)$$

It is important to note that the amplitudes are split among the two clones such that their sum gives the original basis function and as such at the timestep of cloning, the wavefunction is unaltered. The larger, more flexible basis set now involves the cloned basis functions propagating on different PES which is capable of producing. The different ensuing dynamics of MC-MCEv2 which has been shown to be more accurate than standard MCEv2 in modelling the dynamics of model systems [74] and has been used in the simulation of various real molecules [173]. While the amplitudes are different in each clone, the Gaussian CS that constitute the nuclear part are identical to the original basis function meaning, albeit only initially, the two clones occupy the exact same phase space. This sharing of phase space is the issue that prevents straightforward implementation of cloning into MCEv1.

Within the ansatz for MCEv1, both the inter- and intra-basis function couplings are contained within the quantum amplitudes of the Ehrenfest configuration, due to the lack of the configurational $D_n(t)$ amplitude present in the MCEv2 ansatz. This combination of coupling allows for the MCEv1 trajectories to "push" one another along in phase space aiding with the propagation and reducing computational cost. It also has the advantage of the basis functions "pushing" each other so that they stay coupled for longer in relevant areas of phase space, a natural weakness of trajectory based methods. However the disadvantage of this form of construction is the numerical singularity that arises from having two CS occupying the same phase space, which Eqn. 5.1 shows is a requirement for cloning in MCEv2. Therefore a more laborious and computationally expensive version of cloning is required for MCEv1, where instead of cloning an individual basis function that is straddled between multiple PESs, the entire basis function is cloned,

$$|\Psi(t)\rangle = \sum_{n=1}^{N} \left(a_{n1}|1\rangle + a_{n0}|0\rangle|z_n(t)\rangle\right) = \sum_{n=1}^{N} \Big(a_{n1}|1\rangle + 0|0\rangle|z_n^{(0)}(t)\rangle\Big) + \sum_{n=1}^{N} \Big(0|1\rangle + a_{n0}|0\rangle|z_n^{(1)}(t)\rangle\Big) \quad (5.2)$$

While $|z_n^{(0)}(t)\rangle$ and $|z_n^{(1)}(t)\rangle$ in Eqn. 5.2 are still equal Gaussian CS as in the cloning procedure in MC-MCEv2, they now represent the Gaussian CS for an entire basis set as opposed to the Gaussians CS attached to a single basis function. These two basis sets are now also seen as two separate objects which can be propagated individually, according to the usual MCEv1 propagation equations. In a similar fashion to the cloning procedure in MC-MCEv2, the two clone basis sets sum to reproduce the the original basis set, and as basis functions and basis sets in MCEv1 do not need to have a norm of 1 via construction, the norm of the two cloned basis sets will be the populations of the states whose corresponding PES they have the amplitudes for at the timestep of cloning. While this full basis set cloning is more expensive than its single basis function counterpart, it is still economical when compared to the doubling of a basis set. As the cost of

propagation of the basis set scales with the size of the basis set cubed, the cost of propagating two basis sets of size $\frac{n}{2}$ is approximately 4 times cheaper than propagating a basis set of size n. This combined with the fact that cloning is only required for the fringe cases that MCEv1 cannot converge, MCEv1 may still be an economical choice of method for a wide range of systems.

As the condition of cloning is that the generated clones sum to the original basis set at the time of cloning, another construction of clones is possible. Instead of assigning all of the population of a state to a given clone, it is possible to instead scale the amplitudes as follows,

$$|\Psi(t)\rangle = \sum_{n=1}^{N} (a_{n1}|1\rangle + a_{n0}|0\rangle|z_n(t)\rangle) = \sum_{n=1}^{N} \Big(cos^2(\theta)a_{n1}|1\rangle + sin^2(\theta)a_{n0}|0\rangle|z_n^{(0)}(t)\rangle\Big) + \sum_{n=1}^{N} \Big(sin^2(\theta)a_{n1}|1\rangle + cos^2(\theta)a_{n0}|0\rangle|z_n^{(1)}(t)\rangle\Big) \quad (5.3)$$

where θ is a randomly generated angle, relying on the trigonometric identity such that the clones still sum to the original basis set at the time of cloning. This angular form of cloning maintains at least some of the population of each state within each clone. While the cloning procedure was originally developed to rectify straddled basis functions, in the case of cloning the entire basis set it may be advantageous to maintain the momentum of population transfer of the propagation as the more standard form of Full Cloning in Eqn. 5.2 generates two clones that have no population of a state on any basis functions within that clone, similar to the beginning of a propagation. The generation of the angle θ on each repeat of the propagation also allows for a wide sampling of clones. Forcing θ to be 0 reduces angular Full Cloning back to the standard form of Full Cloning originally presented.

5.2.1 Cross-terms and first applications

The first test case for these new cloning equations was a simple Spin Boson case that was in fact the first case presented in MCEv1's first presentation of results [68]. While a more detailed description of the Spin Boson Hamiltonian

was given in section 2.4, a brief overview will be given of the parameters needed to summarise a given case within the model. Δ is the tunnelling parameter to which all other parameters are often scaled; ω_c is the characteristic frequency of the bath, defining at which point the relationship between frequency and spectral density is no longer linear; α_k, describes the strength of the system-bath coupling; ϵ is the difference in the minimum energy between two different wells; and finally β is the inverse temperature parameter, given by 1/kT. For all cases of the Spin Boson model considered in this thesis, the spectral density is taken to be Ohmic and the cut-off function to be employed to determine the behaviour after the characteristic frequency of the bath was exponential. This first case contains weak coupling between the system and the bath at high temperatures. In its original paper, MCEv1 was shown to be capable of converging this case with a basis set size of 50 basis functions and 50 degrees of freedom. While this was an easy case for MCEv1 to produce results that agree with the benchmark and therefore does not necessarily require the cloning procedure, it may be possible to decrease the number of basis functions required for convergence, while the small basis set required for convergence also provides a great economical test case.

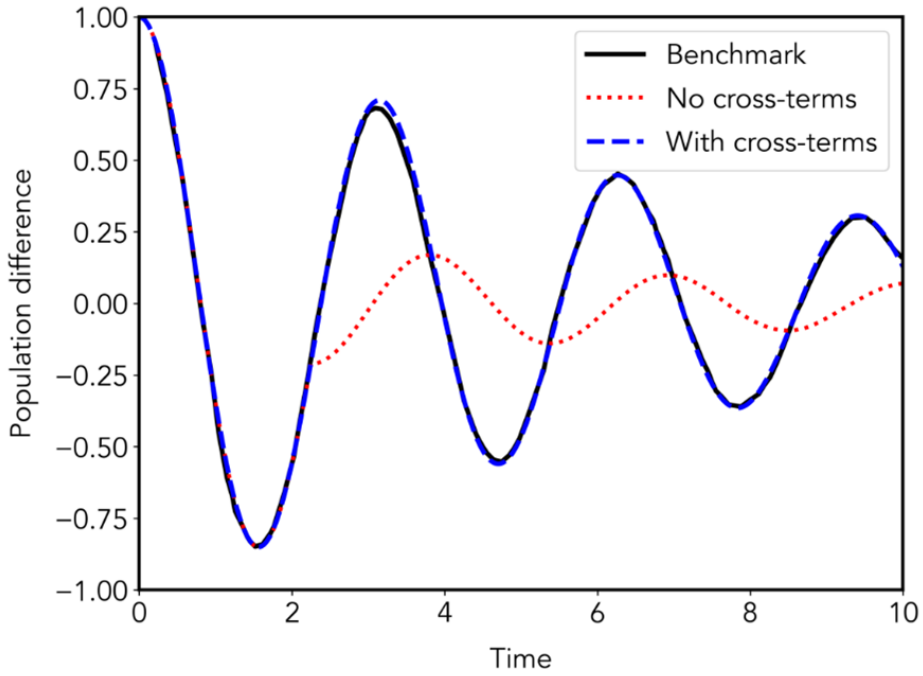

Figure 5.1: Spin Boson case with parameters, $\epsilon = 0$, $\omega_c = 2.5$, $\beta = 5$, and $\alpha_k = 0.09$. Comparison of MCEv1 cloned propagations with (dashed) and without (dotted) the inclusion of cross terms to the MCTDH benchmark (solid line). Both MCEv1 propagations performed with $N_{bf} = 50$ basis functions and M = 50 bath modes and converged with 64 repeats.

The first application of cloning showed that when the cloning procedure occurred just after 2 atomic time units (a.t.u.), the propagation and resulting population difference changes radically, as shown in Fig. 5.1. The oscillations immediately dampen compared to the benchmark and are shifted out of phase. Interestingly the oscillations do still revolve around an equal population difference. This change in behaviour can be explained by viewing the generated cloned basis sets as individual propagations of the system beginning with the population being localised entirely to opposite states (with that ”entire” population within the clone being a portion of the original total population). As this system has two symmetrical wells, the resulting dynamics do differ but only in that they are opposite but equal. Therefore if cloning is performed when the population difference

is exactly 0, the two cloned basis sets will propagate in this equal and opposite way, resulting in the summation of these basis sets cancelling out. Therefore the oscillations observed in Fig. 5.1 are a result of the cloning procedure occurring when the populations of the two states are not exactly equal and so the resulting cloned basis sets have different weightings, meaning that their sums do not perfectly cancel out giving the muted yet present oscillations. Another key difference between the clone basis sets and the original basis that began propagation is the overlap of the nuclear basis functions. When the original basis set is constructed, swarm sampling is used in order to generate a basis with both sufficient norm and coupling through CS overlap. When the cloning procedure is performed after the basis set has propagated, the nuclear basis functions will have dispersed slightly leading to the 'reset' of the propagation being with a nuclear basis set with less coupling which could have effects on the later propagation.

This dramatic derailing of the propagation can be rectified by the introduction of cross-terms that embody the movement of population between the different cloned basis sets. The equations for these cross-terms after a single cloning event are given by,

$$CT_i^{\langle c,d\rangle} = \sum_k \sum_j a_{ik}^{c*} a_{ij}^{d} \langle z_k^c | z_j^d \rangle \tag{5.4}$$

and,

$$CT^{\langle c,d\rangle} = \sum_i CT_i^{\langle c,d\rangle} \tag{5.5}$$

where the superscript determines which clone the amplitude or CS belongs to. The populations of the whole basis set including both clones and their cross terms can then be calculated as,

$$P_{1,tot} = \frac{P_1^c + P_1^d + CT_1^{\langle c|d\rangle}}{P_1^c + P_1^d + P_2^c + P_2^d + CT^{\langle c|d\rangle}} \tag{5.6}$$

$$P_{2,tot} = \frac{P_2^c + P_2^d + CT_2^{\langle c|d\rangle}}{P_1^c + P_1^d + P_2^c + P_2^d + CT^{\langle c|d\rangle}} \tag{5.7}$$

The full basis cloning procedure is flexible in the way that, as with multiple cloning in MCEv2, a cloned basis set may be cloned again creating additional basis sets. Each of the cloned basis sets require the calculation of cross-terms between all others and so the number of cross terms required for calculation can be given as $\binom{k}{2}$ where k is the number of clones. Cloning in MCEv1 including the cross terms in the calculations of populations results in Full Cloning MCEv1 (FC-MCEv1).

Applying FC-MCEv1 to the same trivial Spin Boson test case shows that the inclusion of the cross-terms radically changes the subsequent dynamics after the cloning procedure. The potential efficiency of FC-MCEv1 was also shown as a basis set with only one initial basis function was able to be produce results that were close to the benchmark after only several cloning events. As is common with Gaussian trajectory based methods, even with the smallest possible number of Ehrenfest configurations the propagation still remains accurate at short times before overestimating greatly the first oscillation. With the introduction of only three cloning events, the agreement with the benchmark can be extended to later times, even when all cloning events are confined within the first 0.6 atomic units of propagation as in Fig 5.2. While this case has been repeatedly declared a trivial one and so does not represent a new additional case now solvable by MCEv1, the capability to converge to the correct result with a small basis set is still an achievement. The computational time of simulation should also be taken into account as propagating the 8 cloned basis sets present for most of the propagation results in a time of only 1.75 s per repeat, a significant reduction of the time needed to propagate a full basis set of 50 Ehrenfest configurations. Increasing the number of cloning events to 9 (with the additional cloning events occurring at 0.8, 3.7, 4.5, 5.5, 8, and 9 a.t.u.) greatly increases both the number of clones from 8 to 256 and the number of cross-terms from 28 to 130,816, with the average time per repeat now 36.6 s. While this computational cost of propagating this large number of cross-terms is still cheaper than the average time per repeat

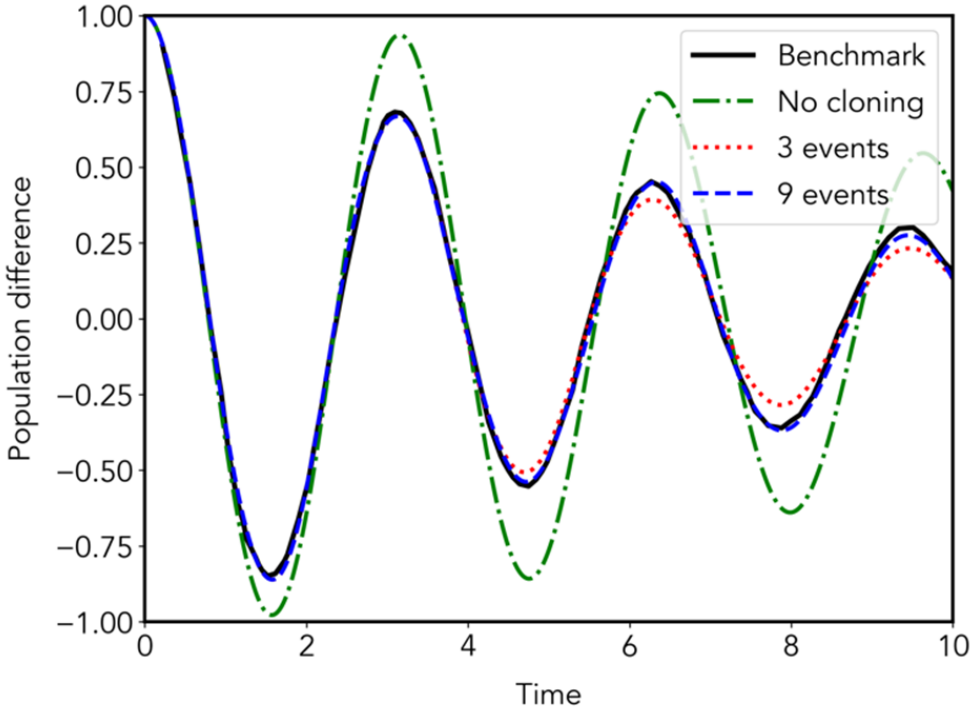

Figure 5.2: Symmetrical well Spin Boson case with $\omega_c = 2.5$, $\beta = 5$, and $\alpha_k = 0.09$. Comparison of MCEv1 cloned propagations with three cloning events (dotted), nine cloning events (dashed) and without (dotted-dashed) cloning to the MCTDH benchmark (solid line). All MCEv1 propagations were performed with $N_{bf} = 1$ basis function and M = 50 bath modes and converged with 64 repeated randomly selected "bits."

of the benchmark basis of 50 basis functions, it also shows how the repeated application of the cloning procedure in the FC-MCEv1 method will require a balance between number of cloning events and size of the initial basis set, as continuous cloning causes excessive scaling issues.

5.3 MCEv1 vs MCEv2 in the zero temperature Spin Boson Model

The zero temperature regime of the Spin Boson regime is one that is dominated by quantum effects, and is therefore often used as a model for quantum systems such as quantum dots, qubits or the study of decoherence theory [267, 268]. This regime has been used as a difficult testing ground, where methods such as the non-interacting blip approximation (NIBA) [269, 270] were compared to the exact benchmark MCTDH and was found to have difficultly converging to the exact result. The zero temperature regime has also presented a challenge for other methods such as HEOM where extensions were developed to simulate the sub-ohmic zero temperature cases [228]. The MCEv1 method converges easier those cases where the characteristic frequency and coupling strength are low. MCEv1 is in fact capable of converging several different cases without the introduction of the Full Cloning procedure.

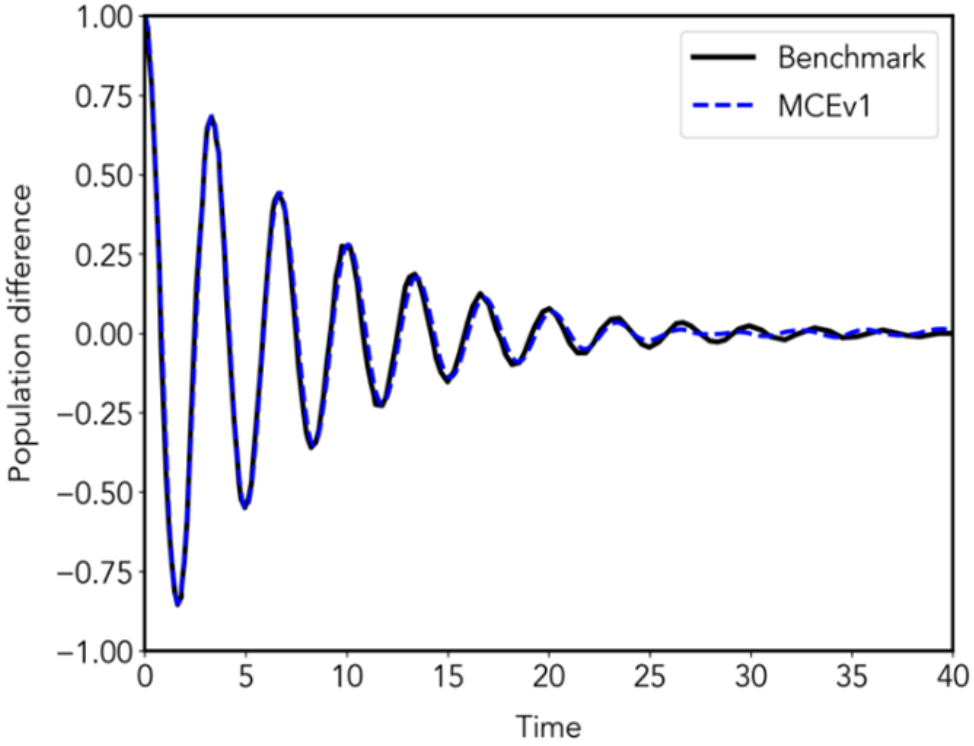

Figure 5.3: Symmetrical well Spin Boson case with $\omega_c = 10$, $\beta = 5000$ (as an estimation of infinity), and $\alpha_k = 0.05$. The MCEv1 propagation was performed with $N_{bf} = 200$ basis function and M = 200 bath modes and converged with 64 repeated randomly selected "bits."

Fig. 5.3 shows that for a weak coupling case with a relatively low characteristic frequency, MCEv1 can converge to the MCTDH benchmark for the whole propagation without the need for Full Cloning nor an overly large basis set. Due to the high number of oscillations present, the timestep does have to be kept small in order to properly capture the changes in the rate of population transfer and MCEv1 converges to this result with an average time of 0.795 CPU hours per repeat. The fact that MCEv1 converges to the benchmark is due to the unique construction of the MCEv1 ansatz as performing the simulation with the same basis set size but with MCEv2 produces the results in Fig. 5.4. With MCEv2, the overall oscillatory character is preserved but the magnitudes of the oscillations

are overestimated and after a couple of cycles shift out of phase. The cost of this MCEv2 propagation is also slightly higher than that of its MCEv1 counterpart with an average repeat time of 0.888 hours while employing the exact same basis set size and timestep parameters. While standard MCEv2 cannot converge to the benchmark, this case still provides a perfect example of the strengths of the cloning procedure as the MC-MCEv2 propagation is capable of matching the benchmark for a much longer period of time. These four cloning events also begin from a smaller initial basis set of 100 basis functions, leveraging the strength of the MCE method that even a small basis set is accurate for short times. The mismatch between the MC-MCEv2 propagation and the benchmark could theoretically be moved further back via the introduction of more cloning events. However this is rather prohibited computationally as the current 4 cloning events per basis function results in a final basis set size of 1600 basis functions, meaning that another doubling would be too costly. The computational cost of including the cloning processes and propagating the expanding basis increases the average time per repeat from 0.888 to 47.29 CPU hours per repeat. A large reason for this increase in cost is despite starting from a smaller initial basis than the MCEv2 propagation without cloning, on the first timestep of the propagation, all repeats experienced a cloning event of between 87 and 95 basis functions out of the 100 initially generated.

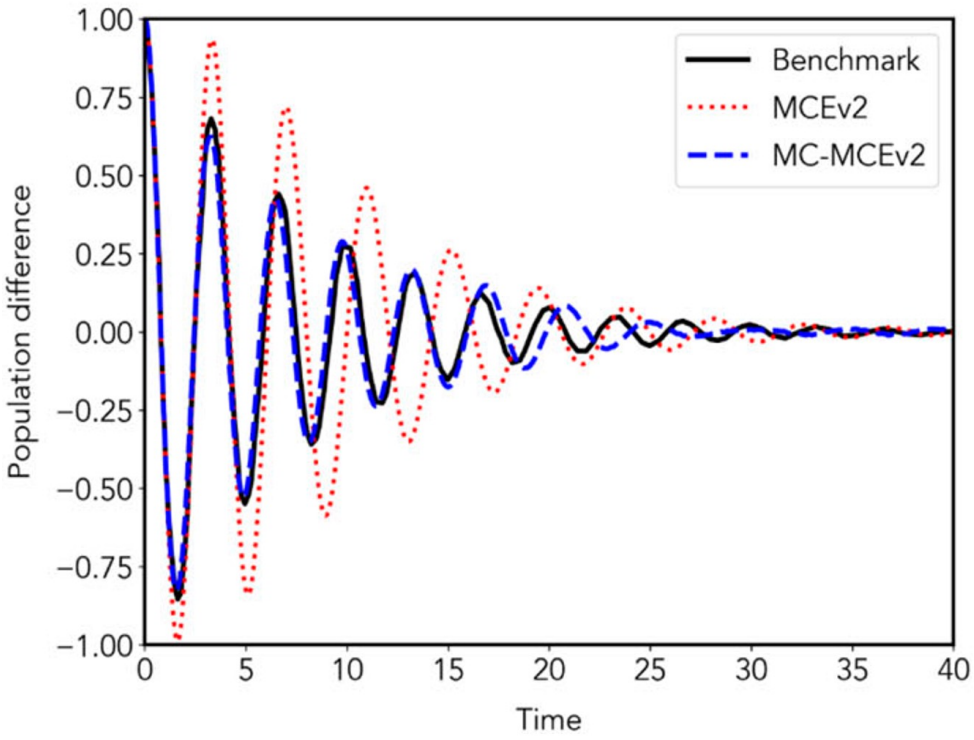

Figure 5.4: Symmetrical well Spin Boson case with $\omega_c = 10$, $\beta = 5000$ (as an estimation of infinity), and $\alpha_k = 0.1$. The MCEv2 propagations were performed with $N_{bf} = 200$ basis function and M = 200 bath modes and the MC-MCEv2 propagation had an initial basis set size of $N_{bf} = 200$ basis function and M = 200 bath modes and allowed for 4 cloning events. All propagations were converged with 64 repeated randomly selected "bits."

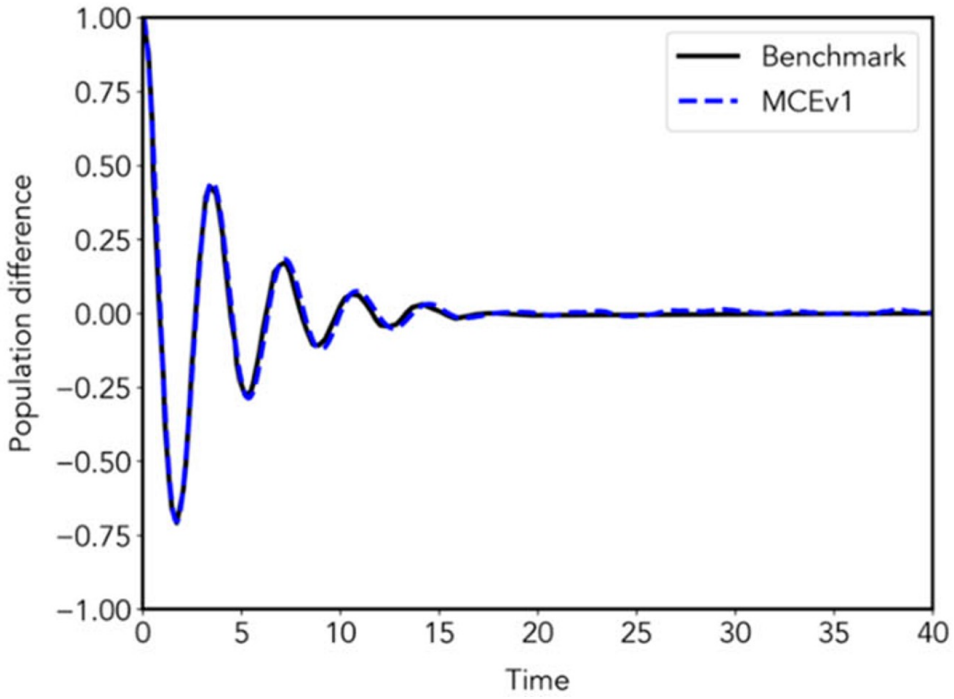

Figure 5.5: Symmetrical well Spin Boson case with $\omega_c = 10$, $\beta = 5000$ (as an estimation of infinity), and $\alpha_k = 0.1$. The MCEv1 propagation was performed with $N_{bf} = 200$ basis function and M = 200 bath modes and converged with 64 repeated randomly selected "bits."

Just a slight increase in coupling between the system and the bath (via the kondo parameter) is enough to significantly reduce the accuracy of the MCEv2 method as shown in Fig. 5.8. A α_k of 0.1 is still considered to be within the weak coupling regime and oscillations of the population difference are still observed, albeit a fewer number and with less amplitude. The initial part of the propagation is similar to the case before where MCEv2 still matches the propagation for very short time before overestimating the magnitude of the oscillation. Later in the propagation not only is the phase of the oscillations misguided but the character of the oscillations themselves is disturbed with the population difference not returning to favour the original donor state, with the propagation only returning to match the benchmark when the equilibrium population has been reached and there is no more population transfer. While reintroducing four cloning events and

performing the simulation with MC-MCEv2 does greatly improve the result and regain the normal oscillation behaviour, it is not perfect when compared to the benchmark. All oscillations are slightly underestimated, including even the first where MC-MCEv2 moves away from the benchmark at roughly the same time as the MCEv2 propagation. The full final basis set is again 1600 basis functions after the four cloning events and the computational cost increases from an average time of 0.788 to 46.2 CPU hours. Despite the propagation having a rather large timescale, all four of the cloning events for each repetition occurred within the first 10% of the propagation, showing that even with cloning, these cases are difficult to converge with MC-MCEv2. MCEv1 in Fig. 5.5, however, is still capable of converging exactly to the benchmark while employing the same basis set size of 200 basis functions and 200 bath modes, resulting in a average time per repeat of 0.775 CPU hours approximately equal to the MCEv2 propagation without any cloning events.

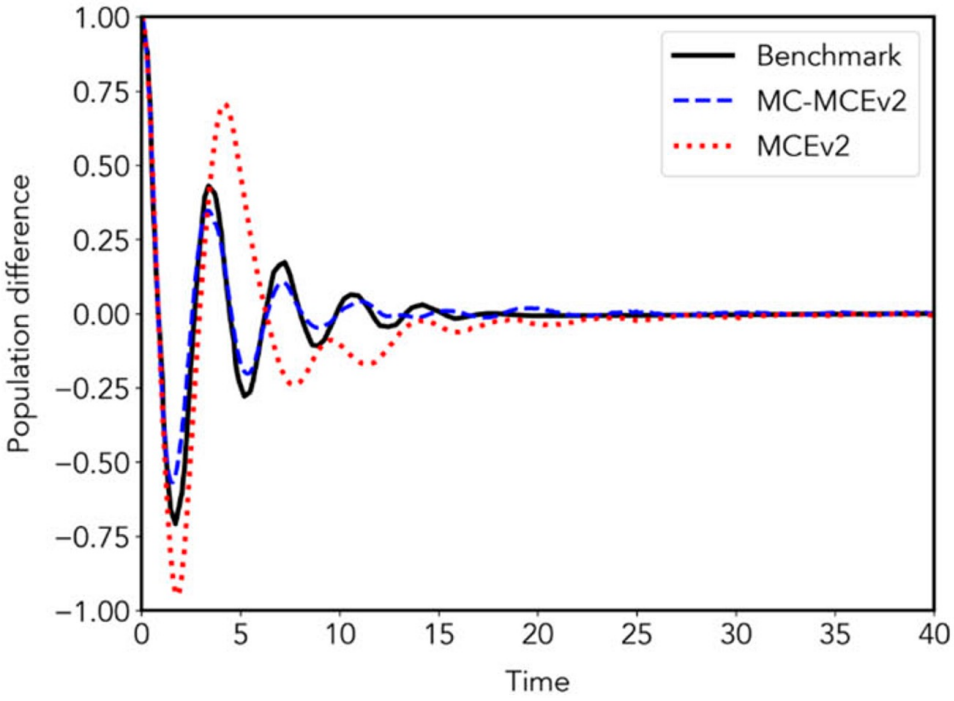

Figure 5.6: Symmetrical well Spin Boson case with $\omega_c = 10$, $\beta = 5000$ (as an estimation of infinity), and $\alpha_k = 0.1$. The MCEv2 propagations were performed with $N_{bf} = 200$ basis function and M = 200 bath modes and the MC-MCEv2 propagation had an initial basis set size of $N_{bf} = 200$ basis function and M = 200 bath modes and allowed for 4 cloning events. All propagations were converged with 64 repeated randomly selected "bits."

Further increasing the condo parameter such that the case can now be considered to have a moderate coupling presents the limit of the MC-MCEv2 method. With $\alpha_k = 0.4$, the benchmark shows that rapid population transfer to the acceptor state causes the population difference to present with the sharp initial drop with the oscillations of the weaker coupled cases being replaced with a relaxation of the negative population difference to the equilibrium populations. The regular MCEv2 propagation for this case is not capable of reproducing any part of the nature of the case, with the population trapped in the original donor state causing rapid oscillations of the population difference never lowering past 0.8. While the MC-MCEv2 propagation is still not perfectly matched to the benchmark, it

is significantly more accurate, reproducing the behaviour completely. While the lack of oscillations present in this case might suggest that a larger timestep could be justified, it is not indeed possible in the MC-MCEV2 propagation due to the need for the train sampling technique. Similar to the previous cases considered with MC-MCEv2, there is a significant number of cloning events occurring on the first timestep. However unlike the previous cases, it is not common for a repeat to have all four cloning events with the largest final basis set sizes within the range of 1400-1550 basis functions, usually reaching this size around half way through the propagation. For this reason the computational cost of the MC-MCEv2 propagation was an average time per repeat of 10.7 CPU hours, much lower than the previous cases that involved propagating a full basis set of 1600 basis set for a longer portion of the propagation.

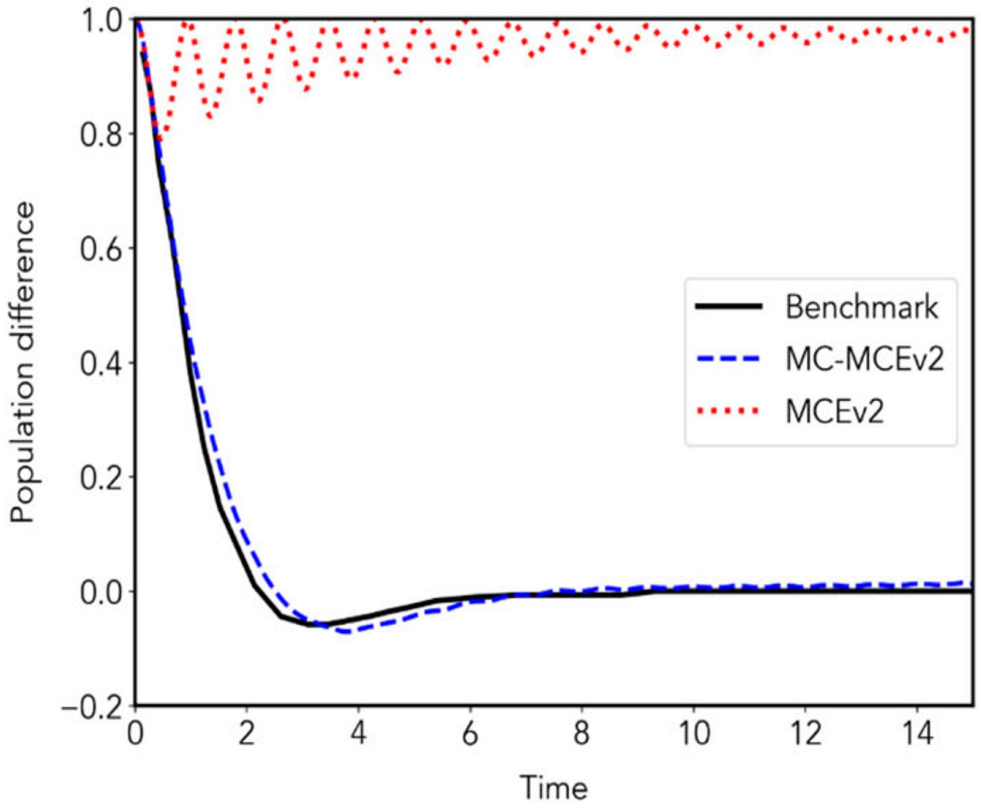

Figure 5.7: Symmetrical well Spin Boson case with $\omega_c = 10$, $\beta = 5000$ (as an estimation of infinity), and $\alpha_k = 0.4$. The MCEv2 propagations were performed with $N_{bf} = 200$ basis function and M = 200 bath modes and the MC-MCEv2 propagation had an initial basis set size of $N_{bf} = 200$ basis function and M = 200 bath modes and allowed for 4 cloning events. All propagations were converged with 64 repeated randomly selected "bits."

The case where α_k is increased further to 0.55, the trapped oscillations have a higher frequency and even smaller amplitudes. MC-MCEv2 maintains an improvement to the basic MCEv2 method, which is no longer capable of matching the benchmark even at short times. The general behaviour is produced where the population transfers fairly rapidly before relaxing to a final temperature. In the MC-MCEv2 propagation, the relaxation is present but happens slower than the benchmark and results in a final population difference of approximately 0.2 instead 0, and so for this case MC-MCEv2 can be said to be at most semi-

quantitively correct. This inaccuracy is, perhaps surprisingly, however not due to the limited number of cloning events as with previous cases as each repeat only has a maximum of one cloning event. This means that due to the smaller initial basis set size, the computational cost is not large at only 0.643 CPU hours. This is also taking into account that as the coupling is increased, a smaller timestep of 0.012 is required for the proper formation of the trains. The standard MCEv2 propagation that provided no information regarding the system and utilising the larger timestep of 0.02 had a larger computational cost with an average time per repeat of 0.911 CPU hours, exemplifying the advantage of beginning with a smaller basis set.

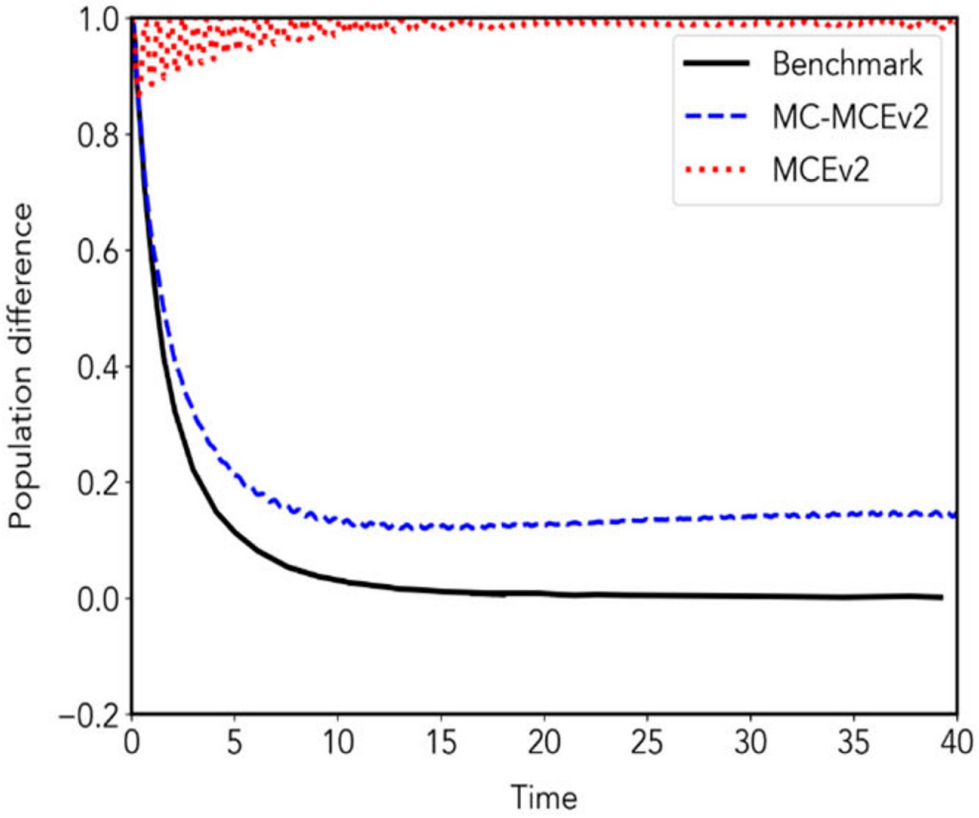

Figure 5.8: Symmetrical well Spin Boson case with $\omega_c = 10$, $\beta = 5000$ (as an estimation of infinity), and $\alpha_k = 0.5$. The MCEv2 propagations were performed with $N_{bf} = 200$ basis function and M = 200 bath modes and the MC-MCEv2 propagation had an initial basis set size of $N_{bf} = 200$ basis function and M = 200 bath modes and allowed for 4 cloning events. All propagations were converged with 64 repeated randomly selected "bits."

5.3.1 FC-MCEv1 in the zero temperature regime

As the coupling strength increases to the moderate coupling regime that was found to be a limit for MCEv2, MCEv1 results also begin to become less accurate and incapable of converging perfectly with the small basis sets. For the case with $\alpha_k = 0.4$, MCEv1 is still almost entirely accurate, with the initial population descent being accurate with the disagreement from the benchmark being introduced as the MCEv1 propagation slightly moves away from the stationary

equilibrium population difference. FC-MCEv1, however, with performing only a single angular Full Cloning event causes the population difference to remain steady for much longer, agreeing almost exactly with the benchmark in Fig. 5.9. The cloning event is called when the population difference of the repeat is 0 for the second time, meaning that the majority of the population has already transferred to state 2 and is now returning to the equilibrium. In most repeats this cloning event occurred at approximately a third of the way through the propagation. Due to the lack of oscillations and no need to construct trains for the basis set in MCEv1, a much larger timestep can be used of 0.05. This combined with a smaller basis set of 200 basis functions and 100 bath modes results in a computational cost of an average time of 7.88 CPU minutes per repeat for FC-MCEv1 compared to an average time of 4.62 CPU minutes for the standard MCEv1 propagation.

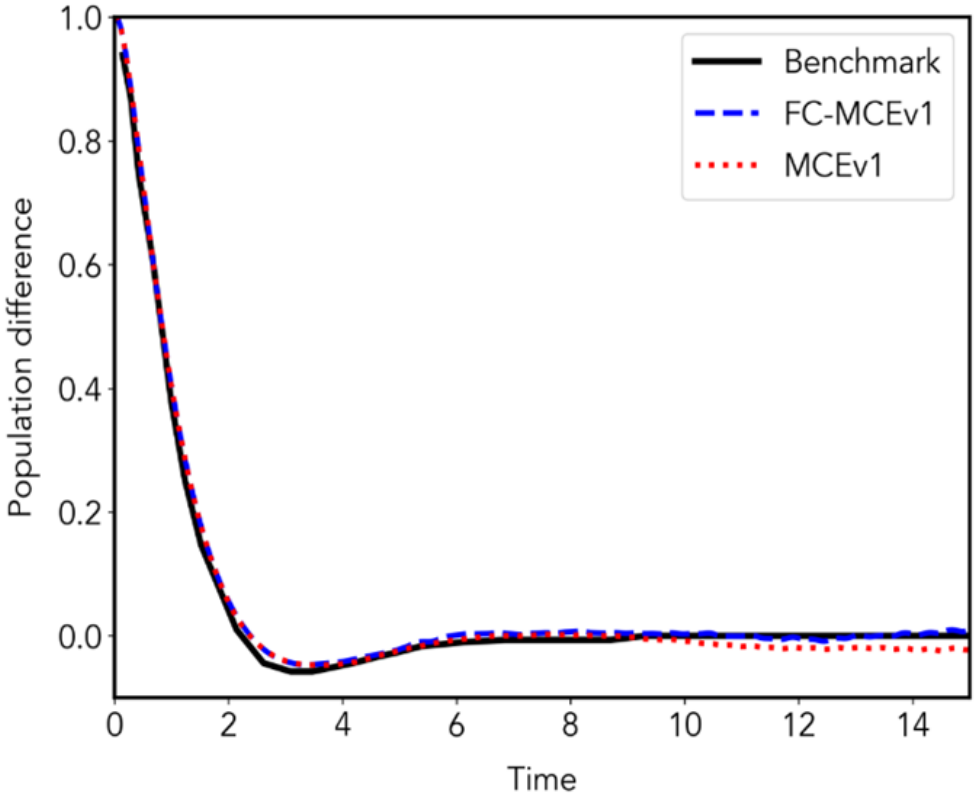

Figure 5.9: Symmetrical well Spin Boson case with $\omega_c = 10$, β =5000 (as an estimation of infinity), $\alpha_k = 0.4$. MCEv1 (dotted), FC-MCEv1 (dashed) were compared to the MCTDH benchmark (full line). MCEv1 had parameters: N_{bf} = 200 basis functions and M = 200 bath modes. FC-MCEv1 had parameters: N_{bf} = 200 basis functions and M = 100 bath modes. All runs converged with 64 repeats or randomly selected "bits".

When $\alpha_k = 0.55$, as was the case with MCEv2, the disagreements between MCEv1 and the MCTDH benchmark become more clear. The decay to the equilibrium population difference is still accurately captured even with a basis set as small as 50 basis functions and 200 bath modes, though where benchmark shows the true population transfer of the system then stabilises after reaching a population difference of 0, the population transfer of MCEv1 continues to a final population difference of -0.1. Similar to the previous case, only a single (standard)

Full Cloning event is required for the FC-MCEv1 propagation to perfectly match the benchmark for the length of the whole propagation in Fig. 5.10. These cloning events occur at the most varied timesteps of any case considered, with almost all cloning times within the range of 7 to 22.5 a.t.u.. However the latest cloning time is after 96% of the propagation at 38.5 a.t.u.. This large variation is one of the key reasons why multiple repeats of MCEv1 are necessary as while individual repeats may not appear at all representative of the benchmark, the average of the 64 repeats converge to match it exactly. Due to only a single cloning event (that can potentially happen rather late into the propagation) and the small basis set, the increase in computational cost is negligible with the average time of a repeat for MCEv1 being 2.28 CPU minutes and the average time of a repeat for FC-MCEv1 being only 2.69 CPU minutes. This average is also helped by the fact that in the FC-MCEv1 propagations, 10 of the 64 repeats contained no cloning event meaning that in this context, at no point throughout the whole propagation of said repeats the population difference reached zero.

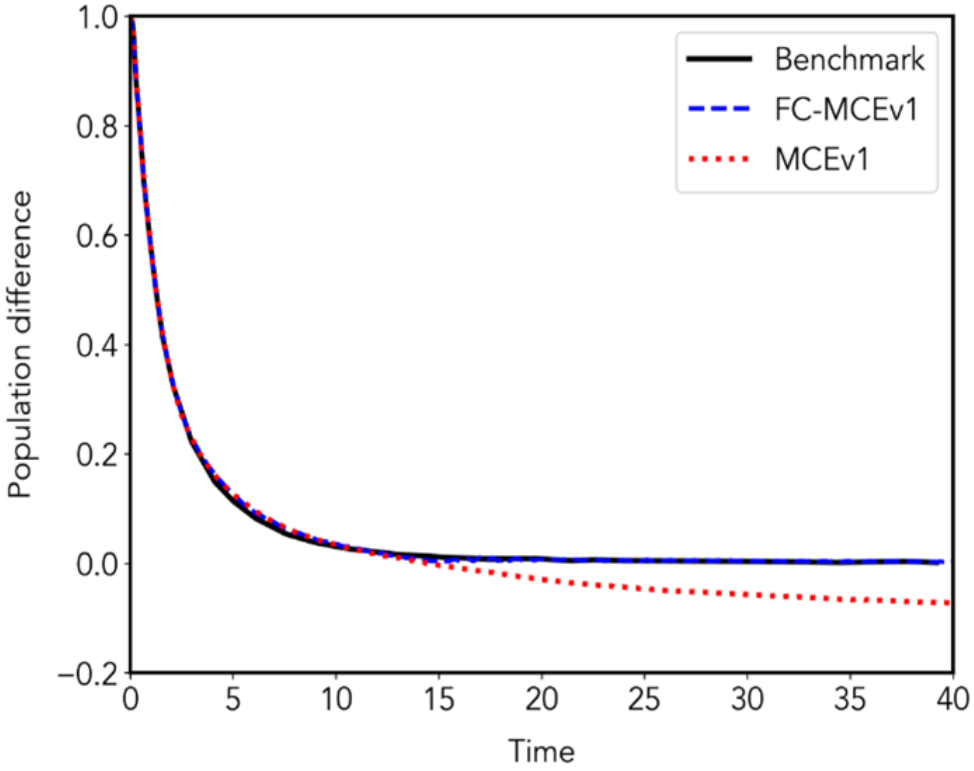

Figure 5.10: Symmetrical well Spin Boson case with $\omega_c = 10$, β =5000 (as an estimation of infinity), $\alpha_k = 0.55$. MCEv1 (dotted), FC-MCEv1 (dashed) were compared to the MCTDH benchmark (full line). MCEv1 had parameters: N_{bf} = 200 basis functions and M = 200 bath modes. FC-MCEv1 had parameters: N_{bf} = 200 basis functions and M = 100 bath modes. All runs converged with 64 repeats or randomly selected "bits".

When the characteristic frequency is increased to $\omega_c = 20$, MCEv1 is still capable of converging to the MCTDH benchmark with the standard basis of 200 basis functions the difference zero temperature Spin Boson cases within the weak coupling regime. MCEv1 returns to struggling to converge the moderate cases with $\alpha_k = 0.4$ and $\alpha_k = 0.55$. With the higher characteristic frequency the population transfer that creates the small overshoot of negative population difference is even less pronounced. The standard MCEv1 propagation remains capable of perfectly matching the initial population transfer from the donor state

to the acceptor state, but greatly overestimates the negative population difference before over correcting and passing through the equilibrium population to a final population difference of 0.1. FC-MCEv1 however is capable of converging to the benchmark with the inclusion of two standard Full Cloning events. Both cloning events have the condition of occurring when the population difference reaches 0. The first Full Cloning event helps to correct for the population difference overshoot, which can be seen in Fig. 5.11 when FC-MCEv1 undergoes only 1 cloning event. The propagation is accurate for longer times and does correctly produce the first pass through the equilibrium population before beginning to deviate away the benchmark via population transferring back to the donor state. Interestingly the last quarter of the FC-MCEv1 with a singular standard Full Cloning events returns to producing results that match the standard MCEv1 propagation. With both cloning events, FC-MCEv1 is capable of matching the benchmark completely apart from some minor oscillations around the equilibrium population. Unlike other cases, the timings of the cloning events were relatively consistent with the first event having a time range of 3.7 and 4.2 a.t.u. and the second a range of 8.4 and 10.2 a.t.u.. Despite the Full Cloning event causing a doubling of the number of basis sets required, the computational cost of the propagation from MCEv1 to FC-MCEv1 does not even double with the average time per repeat increasing from from 0.244 to 0.394 CPU hours. However the second cloning event does have a significant impact on the computational cost with the average time per repeat at 0.84 CPU hours due to every repeat now containing 4 cloned basis sets and a large number of cross-terms.

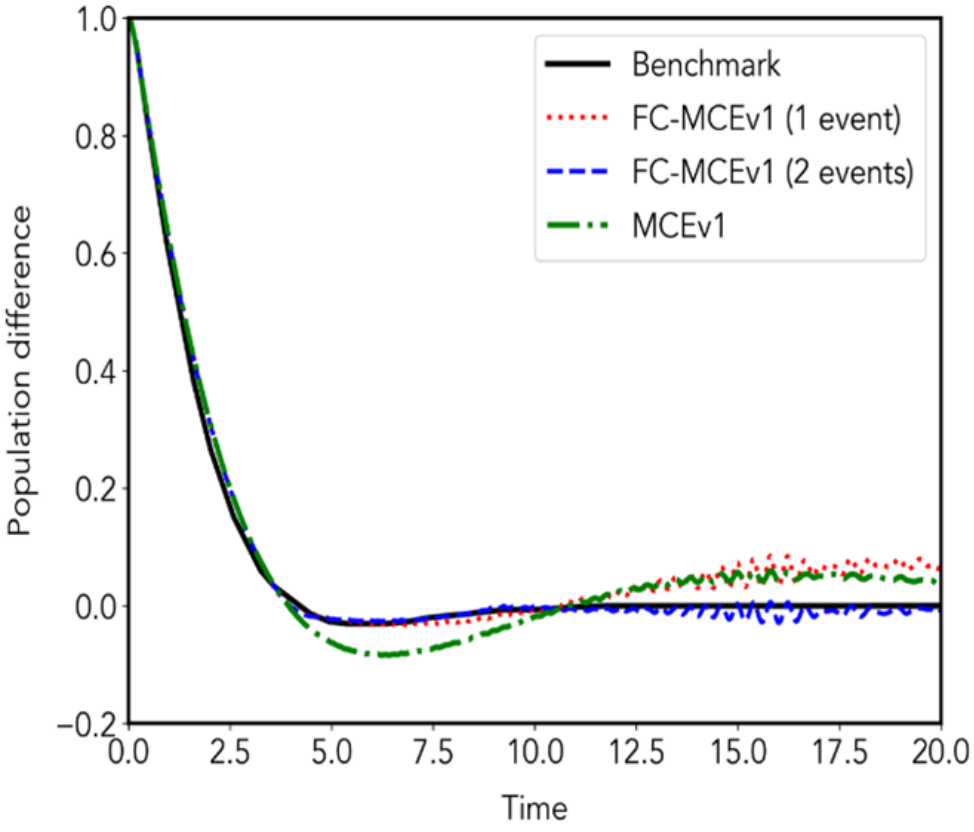

Figure 5.11: Symmetrical well Spin Boson case with $\omega_c = 20$, β =5000 (as an estimation of infinity), $\alpha_k = 0.4$. MCEv1 (dotted), FC-MCEv1 (dashed) were compared to the MCTDH benchmark (full line). MCEv1 had parameters: N_{bf} = 200 basis functions and M = 200 bath modes. FC-MCEv1 had parameters: N_{bf} = 200 basis functions and M = 100 bath modes. All runs converged with 64 repeats or randomly selected "bits".

With the case of $\omega_c = 20$ and $\alpha_k = 0.5$, FC-MCEv1 is needed for MCEv1 to converge to the MCTDH benchmark as the MCEv1 propagation without cloning once again does not stop the population transfer when the equilibrium population is reached. FC-MCEv1 is however capable of matching to MCTDH benchmark almost exactly after two cloning events (in Fig. 5.12, the first of the angular form of Eqn. 5.3 and the second the standard form of Eqn. 5.2. The angular Full Cloning event occurs when the population difference reaches 0.1 followed by a

second standard form of Full Cloning when the population difference is 0 helping to keep the propagation centred around the equilibrium population. Despite the two Full Cloning events, the computational cost of FC-MCEv1 is not double when compared to MCEv1 as the average time per repeat only increases to 4.81 CPU minutes from the 2.81 minutes. This small cost for FC-MCEv1 can be explained that while two Full Cloning events were allowed to happen, only 86 of the 128 clones generated after the initial cloning event went on to clone again. The timings of both Full Cloning events are also significantly varied, with the angular Full Cloning event generally occurring between 6 and 11 a.t.u. (although an outlier was called as late as 17.5) with times of the standard Full Cloning event as early as 6.5 atomic times units and the latest as at 17.5. There also existed a small number of trajectories for which the first cloning event was never called meaning there were several MCEv1 propagations that were not close to approaching the equilibrium temperature. Further work into the application of the FC-MCEv1 will have to devise a balance between the choice in size of initial basis set in order to create a baseline and the number of cloning events.

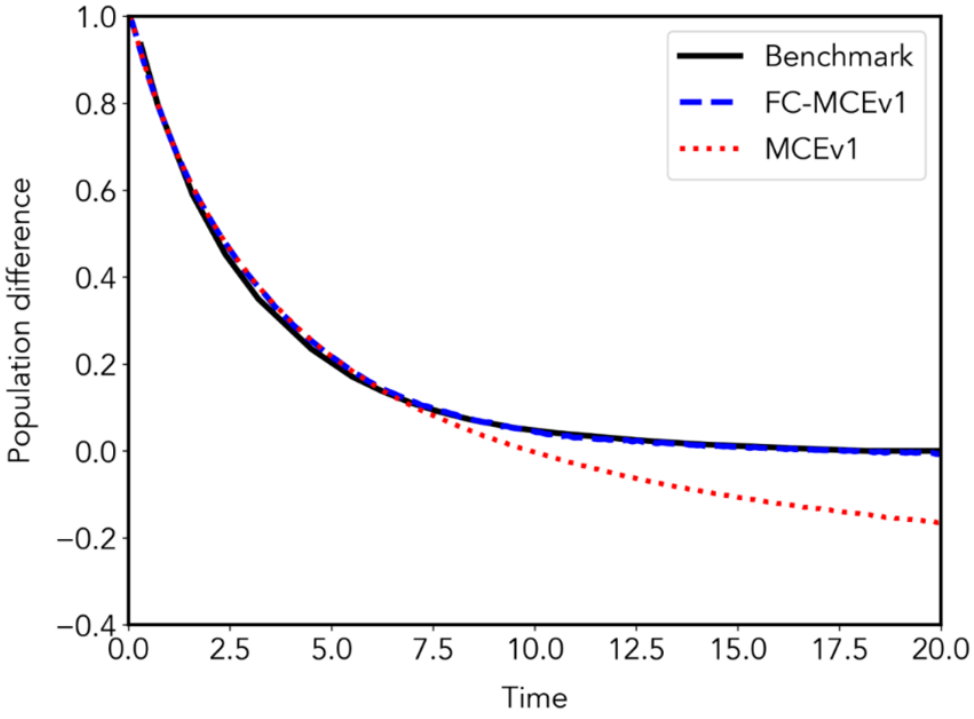

Figure 5.12: Symmetrical well Spin Boson case with ω_c = 20, β =5000 (as an estimation of infinity), α_k = 0.5. MCEv1 (dotted), FC-MCEv1 (dashed) were compared to the MCTDH benchmark (full line). MCEv1 had parameters: N_{bf} = 200 basis functions and M = 200 bath modes. FC-MCEv1 had parameters: N_{bf} = 200 basis functions and M = 100 bath modes. All runs converged with 64 repeats or randomly selected "bits".

5.4 Potential conditions for cloning in FC-MCEv1

The last case considered in the previous section is evidence that the condition used for the cases prior, simply when the population difference reaches 0, is not sufficient for all cases. The evidence for this is made stronger when considering cases where the coupling strength between the system and the bath and/or the characteristic frequency increases to the extent where the population difference does not approach 0 across the whole time frame considered or even cases that MCEv1 struggles to converge to the point where disagreement from the

benchmark begins very early in propagation before approaching the equilibrium population. The existence of the MCTDH benchmark has been vital in knowing where cloning has been beneficial to the propagation. For FC-MCEv1 to be truly useful in a range of contexts, an automatic yet general condition needs to be found that not only selects the correct timestep for cloning but also the optimal form (whether to use the standard or angular form of Full Cloning). The optimal cloning timestep also will change with respect to basis set size as is demonstrated by Fig. 5.13 where increasing the basis set size in terms of both number of basis functions and number of modes produces a less accurate result. This is because the increase of one of the features can in fact require a more than equal increase in the other meaning that simply tripling the basis set size, while significantly increasing the computational cost, does not necessarily increase the accuracy for a basis set that hasn't fully converged.

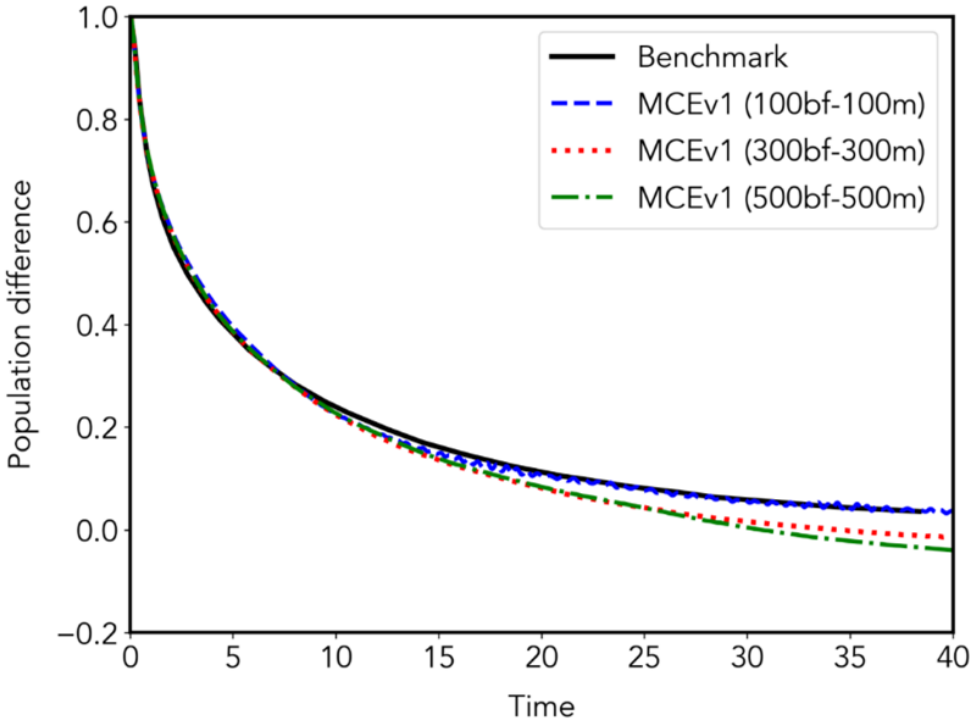

Figure 5.13: Symmetrical well Spin Boson case with $\omega_c = 10$, β =5000 (as an estimation of infinity), $\alpha_k = 0.7$. MCEv1 shows propagation without cloning for different basis set sizes, compared to the MCTDH benchmark (full line). All runs converged with 64 repeats or randomly selected "bits".

Due to the construction of the Full Cloning procedure, it is impossible to directly mimic the cloning condition that is utilised in MC-MCEv2 and AIMC as it impossible to clone only the problematic basis functions. Needing to clone the entire basis set greatly reduces the specificity of the condition as the problematic effects must be widespread enough to warrant a Full Cloning procedure. To this end, it is possible to generalise the MC-MCEv2 cloning condition in two very similar ways, namely to track the average breaking force across all of the basis functions or to track the percentage of Ehrenfest configurations that are over the set breaking force threshold. It is possible that the second condition becomes more feasible as the basis set grows large as the percentage will be changed less radically by the value of a single basis function and the average of the other

condition will become more skewed by the larger number of basis functions that have very little breaking force. However while both conditions appear similar to the MC-MCEv2 condition, the latter has an additional degree of freedom in their parameter selection. After choosing the threshold for the breaking force it is then necessary to choose the percentage of Ehrenfest configurations over the breaking force that triggers the cloning procedure.

To gather more insights into both conditions, a zero temperature Spin Boson case was chosen that within the time frame of the MCTDH benchmark the population difference never reaches zero. It was also important that the characteristic frequency and coupling are not too high to the extent that the case is inaccessible with a relative small basis set which would hinder testing. For these reasons, the case chosen has the following parameters: $\epsilon = 0$, $\omega_c = 20$, $\alpha_c = 0.7$ and $\beta = 5000$. First, a reasonable number of modes is found for a testing basis set via running multiple propagations with 50 basis functions and increasing the number of modes until there is no loss of stability (seen through introduced oscillations or severe deviation from the smooth decline of population difference). As can be observed in Fig. 5.14, any basis set with less than 150 modes is not sufficiently stable and the propagation begins to distort with the population difference dropping significantly. As the number of modes increases, the propagation continues coherently for longer times. It should be noted that the initial prorogation for all three basis functions considered Fig. 5.14 are practically identical and the disagreements between all three basis sets only grow to be significant at the point where the propagation breaks down.

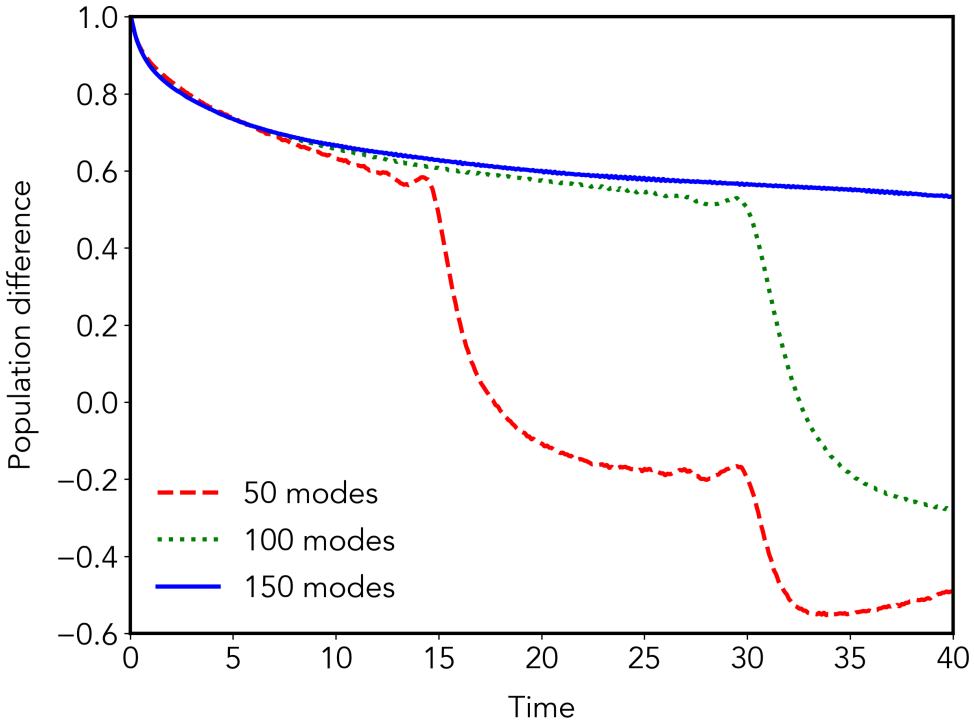

Figure 5.14: Symmetrical well Spin Boson case with $\omega_c = 20$, β =5000 (as an estimation of infinity), $\alpha_k = 0.7$. MCEv1 propagation without cloning is shown for basis sets with $N_{bf} = 50$ and differing number of bath modes, compared to the MCTDH benchmark (full line). All runs converged with 64 repeats or randomly selected "bits".

With the chosen number of bath modes at 150, multiple propagations can be run with an increasing number of basis functions as in Fig. 5.15. When compared to the benchmark, the small basis set with 50 basis functions deviates very early in the propagation with the final population difference not being particularly close to the benchmark. The results of the larger basis sets are significantly closer to the MCTDH benchmark. However, the same phenomenon occurs as in Fig. 5.13 where a larger basis set does not guarantee closer convergence, as the basis set with 150 basis functions has a better result than the larger basis set with 250 basis functions. Interestingly while the basis sets are much larger than the initial 50 basis functions, they do not stay exact to the benchmark for much longer with

both larger basis functions beginning to diverge around 5 atomic units, where the population difference falls lower than it should and the error remains for the rest of the propagation.

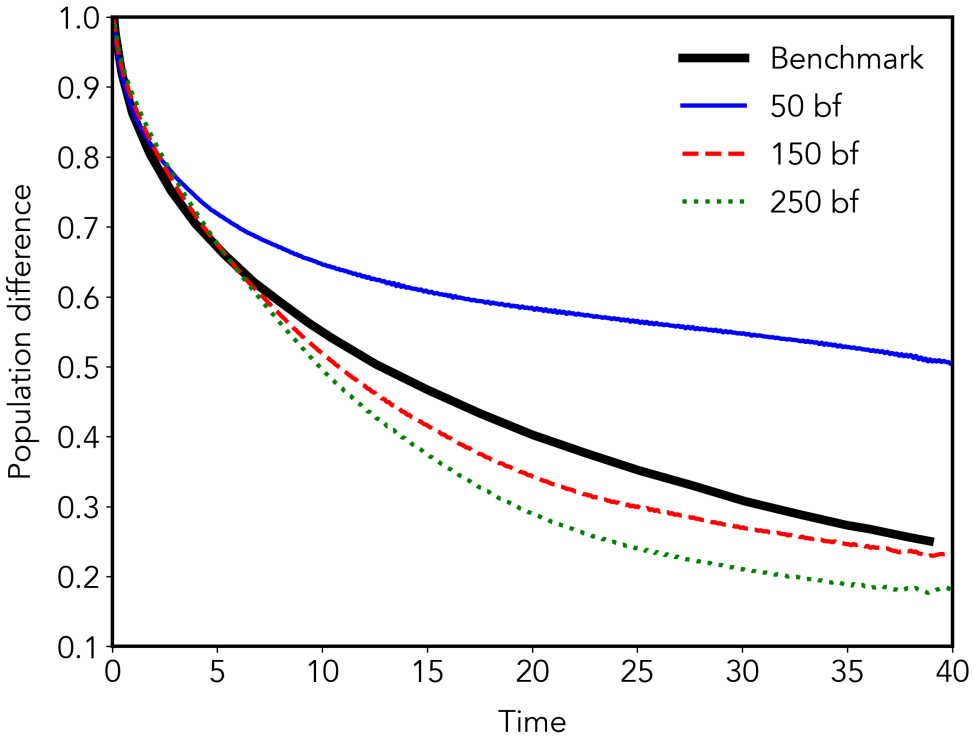

Figure 5.15: Symmetrical well Spin Boson case with $\omega_c = 20$, β =5000 (as an estimation of infinity), $\alpha_k = 0.7$. Propagation without cloning for basis sets with 50 (blue), 150 (red) and 250 (green) basis functions and 150 bath modes, compared to the MCTDH benchmark (black). All runs converged with 64 repeats or randomly selected "bits".

Fig. 5.16 compares the different cloning conditions for the basis set that produced the result closest to the MCTDH benchmark with 150 basis functions and 150 bath modes. For the cloning condition based around using a percentage of Ehrenfest configurations that exceed a certain breaking force value, the threshold was taken to be 0.149. As expected the two conditions are relatively similar and only really differ in magnitude. The maximum value across the repeats for each

condition show that there are no significant outliers across the trajectory as the maximum values are fairly consistent in their difference from the average. While Fig. 5.16 only compares data from one basis set size for one case of the Spin Boson model, almost identical graphs are produced for different basis set sizes, with the only major difference being the magnitude of the observables. This can be seen in Fig. 5.17 which compares the percentage of Ehrenfest configurations that have a breaking force over 0.149 for different sized basis sets. This threshold has been used in MC-MCEv2 cases in the past as the standard threshold has been shown to be not reached in zero-temperature cases [74]. This choice of threshold seems to be reasonable as even for the smallest basis set considered with only 50 basis functions, the average across all repeats has a percentage of only 30%. The smallest basis set also has a small resurgence of breaking force that is not present in the larger basis set, with the two larger basis sets presenting almost identically with regards to the condition. However for both conditions considered across all three basis set sizes, the condition peaks immediately at the beginning of the propagation before reducing to negligible values for the rest of the time frame. This suggests either that the MCEv1 propagation requires cloning almost instantly or the peak of the condition is not a suitable measure for where the propagation appears to begin diverging from the benchmark and 'true' value of the system.

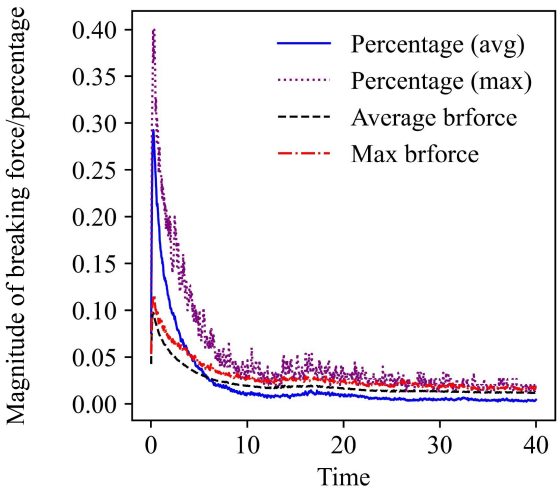

Figure 5.16: A comparison of different observables of the breaking force for the case with parameters $\omega_c = 20$, β =5000 (as an estimation of infinity), $\alpha_k = 0.7$. The MCEv1 propagation was performed with $N_{bf} = 150$ and 150 bath modes and 64 'bit-by-bit' repeats.

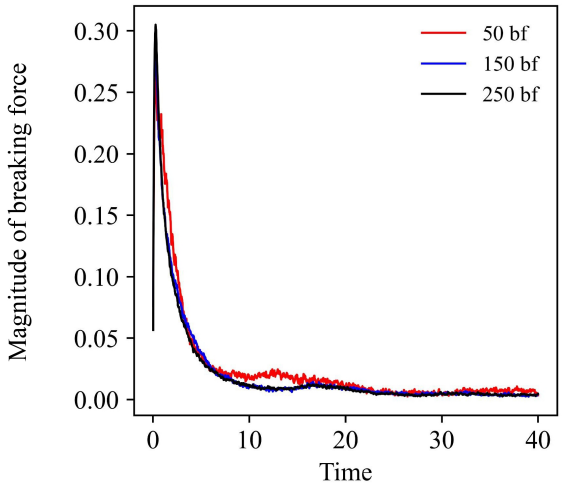

Figure 5.17: A comparison of different breaking forces for the case with parameters $\omega_c = 20$, β =5000 (as an estimation of infinity), $\alpha_k = 0.7$. The MCEv1 propagation was performed with $N_{bf} = 50$, 150 and 250 basis functions, 150 bath modes and 64 'bit-by-bit' repeats.

Fig. 5.18 shows both forms of FC-MCEv1, using standard and angular Full Cloning equations, applied to the Spin Boson case study. The percentage condition applied for both types of cloning was the first timestep where a quarter of the basis functions have a breaking force of over 0.149. This happens incredibly fast within the propagation with the majority of cloning events happening before 10 timesteps have occurred. However both FC-MCEv1 propagations are no closer to the MCTDH benchmark than the original MCEv1 propagation. The standard FC-MCEv1 standard propagation appears to diverge from the benchmark slightly earlier but begins to match the original MCEv1 propagation with both methods producing a practically identical final population difference that is a slight underestimation when compared to the benchmark. The angular FC-MCEv1 has a more highly visible effect on the propagation but actually caused the population difference to decrease at a significantly higher rate. Despite using the same condition for both types of cloning events the angular cloning propagation diverges more rapidly and while the rate of population transfer does stabilise within the

time frame of the propagation it's significantly far from the benchmark. While this is evidence that angular Full Cloning is less applicable than the standard version, it is possible that the angular form of cloning requires a much larger number of repetitions than the 64 that is used as a standard for MCE propagations used throughout this thesis in order to sufficiently sample a variety of angles necessary to average to an improvement on the standard MCEv1 without cloning.

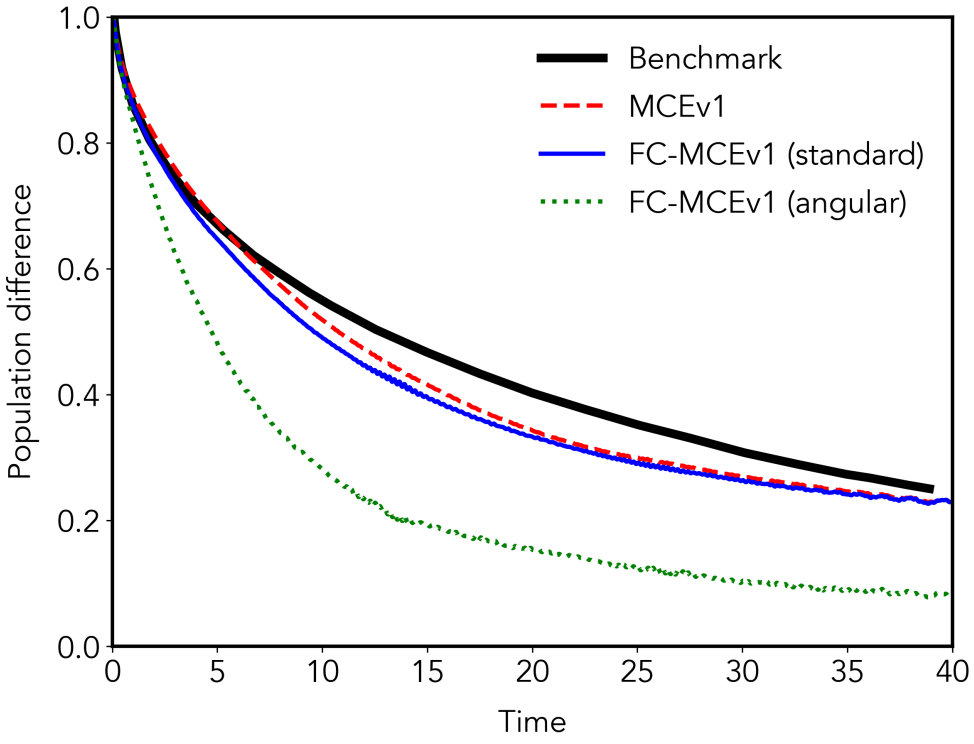

Figure 5.18: Symmetrical well Spin Boson case with ω_c = 20, β =5000 (as an estimation of infinity), α_k = 0.7. MCEv1 and FC-MCEv1 had parameters: N_{bf} = 150 basis functions and M = 150 bath modes. Both the angular and standard form of FC-MCEv1 cloned when 25% of basis functions had a breaking force over 0.149.

Comparing the standard MCEv1 to the MCTDH benchmark as in Fig. 5.15, shows that both of the larger basis set sizes considered begin to diverge at approximately the same time, around 5 a.t.u.. While not providing insight into

an optimal cloning condition, it is possible to orchestrate a cloning event at this time, to show if cloning is capable of rectifying the propagation at this point. This idea is implemented in Fig. 5.19 where both forms of cloning are applied at 5 atomic times units. For both forms of cloning, having a Full Cloning event later into the propagation but while the rate of population exchange is still high causes a discontinuity in the basis sets that can be seen by a sudden jump in population difference immediately after the Full Cloning event. While the introduction of the cross-terms does solve this discontinuity for some cases, it is not a universal fix, which limits the range in which the Full Cloning procedure can actually be applied without disrupting the propagation. There appears to be a loss of the 'true momentum' for the population transfer that is incurred by the complete changing of the coupling as the amplitude of every single basis function is separated to a particular PES, essentially 'resetting' the propagation from the perspective of the cloned basis set. This was the main motivation for the development of the angular form of cloning, that rotating the amplitudes instead of producing binary cloned basis sets would assist in preserving some of the coupling and prevent any jumps in the population difference when the cross-terms alone are not sufficient. This does not appear to be the case however as while the drop in population difference is slightly smaller for the angular form the following propagation matches very closely to the original MCEv1 propagation. The standard FC-MCEv1 propagation does also contain the disconnect and does not match exactly to the benchmark but does arrive at the correct final population difference. It is possible that Full Cloning may be beneficial for converging this case, though without an accurate condition, the only remaining option is trail and error of cloning before the divergence from the benchmark which is computationally expensive and limits the method to only cases that have already been solved exactly.

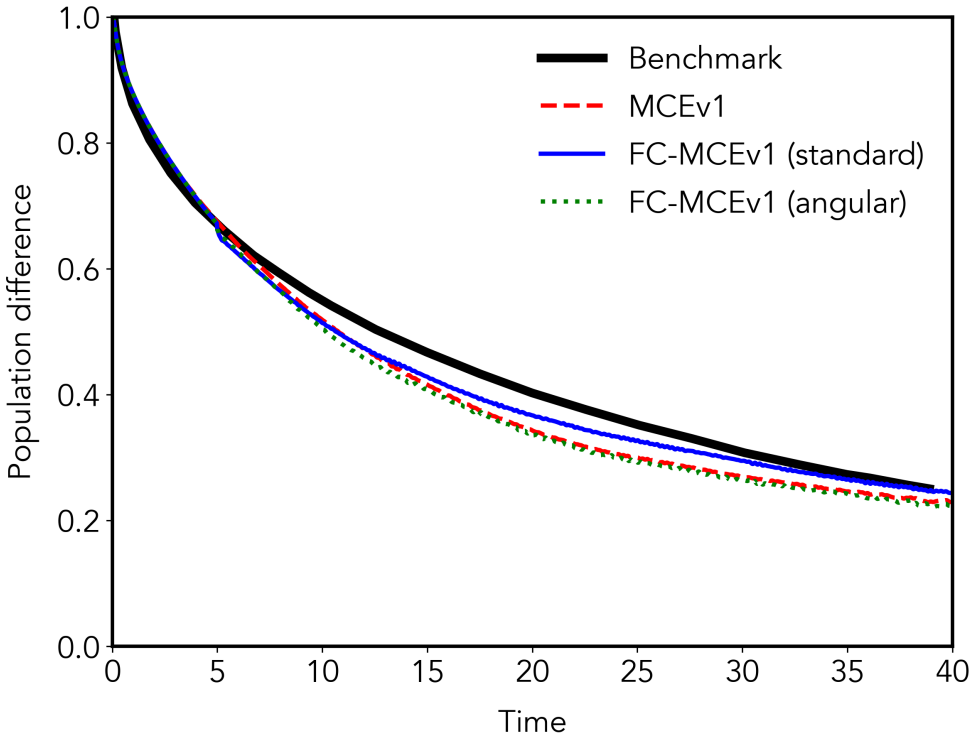

Figure 5.19: Symmetrical well Spin Boson case with $\omega_c = 20$, β =5000 (as an estimation of infinity), $\alpha_k = 0.7$. Both the angular and standard form of FC-MCEv1 had the Full Cloning event at 5 a.t.u..

It may also be possible to establish a variable that can dictate the separation of the MCEv1 method from the true wavefunction. Previous work [271] has laid the foundation for the establishment of an upper bound of the error between the 'true' Hamiltonian and the so-called 'hard-disk' Hamiltonian that is stored within the hardware. As this error bound can be applied to any method that employs an approximate unitary time operator, including both versions of MCE, it can be calculated throughout propagation. Improving this error bound and collecting data of how this error evolves through both cases that MCEv1 is known to converge completely as well as cases that still remain unsolvable for MCEv1 could equip the method with a database from which a boundary could be constructed for when MCEv1 gives incorrect results. The fact that the conditions originally developed for MCEv2 treat the wavefunction on the scale of basis functions

prevents their straightforward assimilation into FC-MCEv1 as it is a resolution inaccessible to Full Cloning events. This upper bounded error threshold could perhaps be a better suited condition for FC-MCEv1 as the error is computed on the basis set as a whole.

5.5 Conclusions

The initial formalisation for Full Cloning has been laid out with two forms of clones that can be generated. The standard form produces clones that completely separate the two PES of the Spin Boson model at the time of cloning. The second uses trigonometric identities to create two cloned basis sets that still sum to the original basis set while scaling the amplitudes for each PES. The application to several zero temperature cases shows the potential impact that FC-MCEv1 could have in terms of allowing the MCE method to converge to results that match the exact MCTDH benchmark with relatively small basis set sizes.

The single largest current limitation of FC-MCEv1 that should be addressed in any future work is that of an automatic cloning condition. Without this, there exists no justification for Full Cloning apart from trial and error when compared against an exact benchmark. An absence of an exact benchmark therefore prohibits the application of the FC-MCEv1 method as it is currently formulated to any novel system. Two generalised versions of the MC-MCEv2 cloning condition were tested in order to find a suitable automatic condition for FC-MCEv1. Unfortunately due to the construction of the basis set, both generalised conditions do not highlight areas where cloning is necessary. The conditions also do not clearly demonstrate where cloning is not needed as the propagation is already converging to the correct result which is problematic due to the heavy computational cost enacted by the cloning of an entire basis set, particularly if the cloning is allowed to occur multiple times in a single propagation. When the population difference is approaching zero, it appears that cloning often has the desired effect of preventing an MCEv1 propagation from overshooting. Interestingly when the exact result does contain a brief overshoot multiple Full Cloning events are

capable of reproducing the overshoot correctly as well as the return to the equilibrium population. An important concept to have in mind for any future work involving the Full Cloning procedure is the weakness that is shared by all coupled trajectory methods, namely that the method is only viable on the timescale that its trajectories remain coupled. It is possible that for a case that requires a long propagation (particularly with a smaller basis set) that any Full Cloning event should be accompanied by some sort of resampling that enhances the cloned basis sets in terms of maintaining the coupling present between the two PES.

FC-MCEv1 was shown to be capable of converging cases that were inaccessible to MC-MCEv2. While historically MCEv2 has been harder to converge for model systems like the Spin Boson model, it is important to note that MCEv1 still converges certain cases easier even when including the sampling tricks used to enhance MC-MCEv2: swarms, trains and cloning. Within recent years, most attention within the group of Shalashilin, who originated the method, has been focused on NAMD simulations through the use of AIMC, which is based upon the ansatz of MCEv2. This is because the MCEv2 ansatz allows for easier, fairly straightforward implementation of the electronic structure as each configuration can be run separately. The additional configurational amplitude unique to MCEv2 allows for all of the equations between configurations to be treated as post-processing. Not only does this simplify greatly the electronic structure but it also allows for trajectories to be run at separate times and later coupled together to form a large basis set, reducing the need to have access to a large amount of computational resources at the same time. Unfortunately MCEv1 does not have such a capability as it requires by necessity that all of the trajectories are run together as information from each configuration is needed for propagation. While these are the reasons that MCEv1 does not currently have an Ab Initio extension, there have recently been attempts to develop Ab Initio extensions for other methods that have similarly restrained construction, namely the variational Multiconfigurational Gaussian method [266]. If such an extension is developed for MCEv1 then its efficient nature combined with the potential additional flexibility of FC-MCEv1 will allow for its application not only to other regimes of the

Spin Boson that it has yet to converge [197, 224, 230] but also to NAMD such as the simulation of the triplet state driven neutral dissociation of plasma relevant molecules that have been the main subject of this thesis.

Chapter 6

Conclusions and outlook

6. CONCLUSIONS AND OUTLOOK

This thesis presents a novel application for well established MD methods as well as a conceptual advancement of MCEv1 via the introduction of Full Cloning. Chapter 5 details the adjustments needed to apply the cloning procedure originally designed for MCEv2 into MCEv1. The main contribution of this thesis is the development of the electrophore model through the simulation of neutral dissociation, a topic of great interest to the academic and industrial plasma communities. The techniques that have been traditionally applied to the field of photochemistry can be transferred practically without edit to the study of neutral dissociation after electron impact. The continued application of NAMD methods to this area of study by the community would greatly assist the plasma industry due to the nature of neutral radicals rendering them invisible to experiment. As such industry has been wanting for a tool to accurately and affordably investigate neutral dissociation of a vast array of potential molecules. Advancement of understanding with regards to these dissociation pathways can lead to more environmentally friendly and more selective semiconductors that enable practically every piece of technology designed over the past few centuries. The largest change between these two processes is which excited state is populated, which is more of a change of input to the electronic structure than a required change to the dynamics. There is also a potentially large subset of molecules that require dynamics only of the lowest triplet state meaning that the calculations for the dynamics are readily accessible and can in fact be accurately performed with standard MD operating on a Verlet algorithm.

The electrophore model provides a lens through which to understand the localisation of the excitation to the triplet state after electron impact and therefore as a direct consequence can be used to predict the neutral dissociation pathways of molecules in that context. For a molecule containing an electrophore, the relatively weak and strong bonds can be immediately identified. Chapter 3 employs standard MD on a single PES to simulate multiple molecules that have been investigated experimentally as potential replacements of industry standard molecules. The first set of molecules considered all contain oxygen and show that the oxygen acts as an electrophore, causing the bonds closest to the oxygen atom

to have the highest dissociation yields. Combining this fact with the isometric effects observed across the molecules allowed for the proposing of preliminary rules that guide the neutral dissociation pathways on the lowest triplet state based on the triplet state. Chapter 4 continues with MD simulations but with molecules selected not for industrial relevance but in order to test and expand the rule set of Chapter 3. Simple and small molecules were simulated to limit the possible causes of any trend observed. The dissociations of MD trajectories for a molecule selected to test the hydrogen buffer effect in the original $C_4H_22F_7OH$ isomer lead to the discovery of the -CH_2F group acting as an electrophore that caused the lowest triplet state to be localised away from the oxygen atom. The interaction between multiple separated electrophores in a single molecule was then studied, with NAMD trajectories showing that the second lowest triplet state will be localised by the non-dominant electrophore in the lowest triplet state. The current molecules considered suggest that the C=C bond is consistently the more dominant electrophore when compared with the oxygen atom, corroborated by both MD simulations and the fact that molecules containing the C=C bond tend to have electronic excitation cross-sections found at lower energy. As the range of molecules simulated increases, it may be possible to expand the electrophore model to include a hierarchy of electrophores that can predict which part of a molecule will localise the excitation to a specific triplet state.

While this thesis presents two previously unidentified electrophores, it is by no means a complete list and a search needs to be conducted for a fuller understanding of both how many possible electrophores exist and their interactions. The more comprehensive the model of electrophores can be made, the less reliance is needed on performing the MD simulations. A more comprehensive understanding of how dissociation events take place in the triplet state would also help more clearly establish the differences between dissociation pathways known for the more commonly studied singlet state. Initial trajectories of four molecules have shown that triplet state trajectories have an increased number of dissociations due to being an excited state, with the electrophores having frequent initial dissociations, some on average over 100 fs faster.

As investigation into this hierarchy of electrophores and more complex plasma molecules continues, the inclusion of NAMD becomes increasingly necessary. There is also the potential that more than two states will need to be considered, adding a significant level of complexity. In such regimes, an accurate description of the dissociation pathways of the molecule will require the ability to dynamically refine the basis representation of the nuclear wavefunction in regions where wavepacket branching occurs. This represents a potential future application for the FC-MCEv1 method developed in this thesis, as this issue was the motiviation for the development of the cloning method in AIMC. The FC-MCEv1 method has been applied to the zero-temperature regime of the Spin Boson model where it was shown capable of reproducing results matching the MCTDH benchmark that were previously unattainable to both MCEv1 and MCEv2. While previously MCEv1 has been shown to be solve cases more efficiently than MCEv2, and to scale more favourably into the solving of systems with a large number of dimensions compared to both HEOM and mDa2 [226], its difficulty to be extended to Ab Initio calculations combined with its lack of basis set expansion has prevented it from presenting applications to on the fly molecular dynamics. The introduction of Full Cloning into MCEv1 has begun to rectify one of these issues. The largest current limitation of FC-MCEv1 is that the automatic cloning condition employed by MCEv2 and AIMC is not directly transferable, meaning the method is restricted in its current range of applications. Future work on the development of this cloning condition would be a further argument to develop a Ab Initio extension for MCEv1 and take advantage of its scaling potential to efficiently simulate practical high-dimensional molecules.

Neutral dissociation, while important and thus far understudied, is only one process via which a molecule excited via electron impact can return to the ground state. At sufficiently high energies, a molecule can undergo both ionisation and electron attachment dissociation. How the energy of the impacting electron affects the likelihood of each dissociation process is an important concept to understand, and so insights into neutral dissociation does not provide the entire picture. However sufficiently accurate branching ratios can be derived via the

dissociation yields found in efficient and accurate MD simulations if the probability of the excitation is known (via electronic excitation cross-sections) as well as the quantum yield of neutral dissociation. These neutral dissociation branching ratios can then be used to populate a plasma-centred reaction database such as Quantemol's database [272]. Once there is a sufficiently complete neutral dissociation database, these branching ratios can be included in total plasma reactor simulation, for instance HPEM [273] (developed by the group of Professor Mark Kusher) for which Quantemol's database has direct integration through another product of Quantemol, Q-VT. This would directly connect the results produced by MD simulations to a much more complete idea of interacting plasma process, useful to both academia and industry.

Appendix A

Programming and algorithms for simulations of Plasma Dissociation

A.1 Program Overview

The program developed for this thesis focuses on the simulation of dissociation of certain molecules. To achieve this, the code is capable of generating initial conditions for the molecule according to inputs, propagating the molecule through time and finally analysing all trajectories to collect and present the total dissociation kinetics and pathways of all bonds and bond types. While the equations of propagation (whether standard molecular dynamics or AIMC) as well as an interface to electronic structure is not novel, the code was designed with several key concepts in mind:

1. The code must be accurate, particularly when compared to pre-existing codes.

2. The code must be efficient and not contain redundancies where possible.

3. The code must offer flexibility in terms of molecule selection, electronic structure and propagation parameters.

4. The code must be accessible and is designed for a potential audience who may not be familiar with molecular dynamics or high powered computing.

The code for performing plasma dissociation simulations was designed with flexibility, accuracy, and ease of extension in mind. To achieve these outcomes, the code is written with a very modular design, with the different modules being partitioned into files. The standard equations of motion for AIMC are employed with an interface constructed for the electronic structure software. The code is entirely written in Python, which provides flexible file handling while also leveraging C-based packages for efficient computation of certain propagation equations (such as the exponentiation of the Hamiltonian). Python also has the advantage of dependencies being provided though a conda environment which can be initialised through a simple YAML file supplied to users. To this end, the code has been designed to require minimal setup on a high powered computing system, minimal inputs from the user, and allow ease of extension or adaptation.

For all dynamics calculations, the choice of electronic structure software must be a deliberate one. For non-adiabatic dynamics, the requirement of Spin Flip TDDFT means that the code was originally developed for use with QChem. QChem also has the advantage of being highly accurate and efficient. However licenced code is always a drawback and so where possible the use of the electronic structure has been made possible with an open-source electronic structure package, namely PySCF. PySCF is an open-source package, meaning that the code is accessible to anyone, as well as the GPU extension package GPU4PySCF, which is also open source allowing porting of the costly electronic structure calculations to GPUs, resulting in great cost reductions. PySCF is not a full replacement however due to the current lack of Spin Flip functionality limiting the number of states that can be involved in the propagation.

A.2 Folder and File Structure

The plasma dissociation program can be taken as having two key folder structures, the folders containing the code and the folders containing these results. While it is definitely possible to design a programme that is all contained within one directory, this separation is derived from the architecture of the high powered computing environment for which it was designed. The first section concerns itself with the code and the input files (referred to henceforth as the main section) while the second is the result framework that will be generated for each run (referred to as the result section).

The main section of the programme primarily consists of the code directory used to propagate the main steps of the programme. Each file within the code directory can be thought of as modules. These files are as follows:

1. main module - controls the flow of the program, calling other modules.

2. globar_vars module - Reads in inputs and establishes multiple global variables.

3. init module - This module provides initialisation of the molecule objects and related functionalities.

4. prop module - contains all propagation equations for the simulations.

5. QChem module - Contains the functions that interface with QChem, including the creation of input files, running of QChem and reading in of data.

6. pyscf module - Contains the functions that interface with PySCF, including the creation of input files, running of PySCF and reading in of data.

7. output module - Contains all the functions that involve the writing data to the file.

8. setup module - A separate file to the rest of the main program flow, contains the setup functions that prepare the optimised geometries and momentum to begin propagation.

9. results module - contains functions called at the end of propagation, involves finding dissociation events and sorting to generate result files.

10. Graph module - creates results graphs after each repetition finishes.

11. specifics module - expands on the results and generates more detailed statistics.

A.3 Program Flow

The program is designed to be as simple as possible and as such the overall flow can be simplified to the flowchart in Fig. A.1.

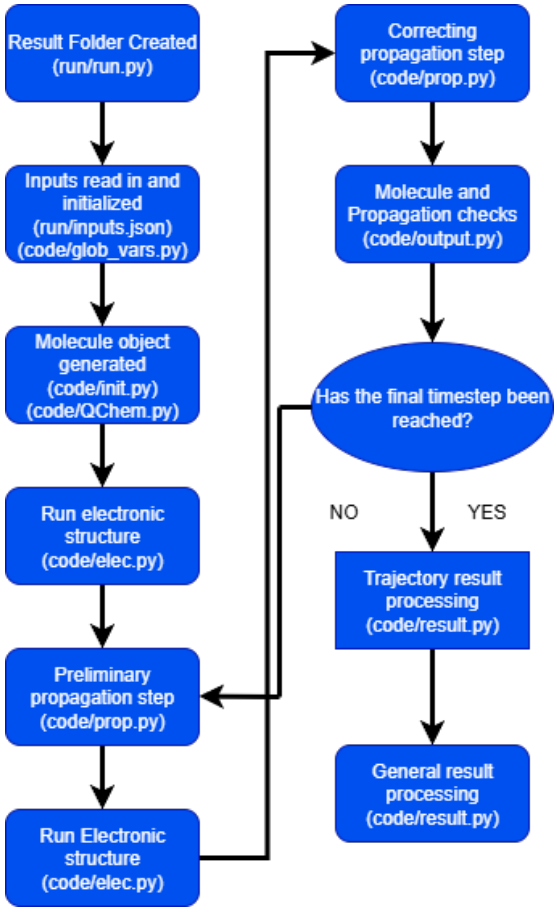

Figure A.1: Flowchart of the generalised steps for the Plasma dissociation code. The most relevant file for each step is contained within brackets.

The key main sections of the code are as follows: inputs, propagation, electronic structure, outputs and results. Each of these sections will be discussed and detailed in further sections highlighting the processes or equations that govern them.

A.4 Preparation of input

The inputs required for propagation are separated into 2 sources, a inputs.json file that is constant for all repetitions, and geometry files that contain initial geometry and momenta for each atom. The inputs.json file itself is separated

into four sections. The first labelled 'HPC' which is concerned primarily with computational resources and overview:

"HPC"

1. "Runfolder": The name of the runfolder that is created where all of the code and data is held.
2. "repeats": The number of repetitions that are performed
3. "cores": The number of CPU cores used for each repetition.
4. "initre": - HPC specific input, submits restart commands in advance for when the task surpasses the set time-limit.
5. "hours": - The number of hours requested from the HPC.

The second, Molecule_data, which outlines the choice of molecule, the features of the molecule and the source of the geometry inputs:

"Molecule_Data"

1. "Geom_flg": Whether to create geometry inputs or read from a file. This can take one of three options, "Initial" where the code reads in a guess of geometry which is then optimised and used to generate accompanying momentum, "Full" where both the geometry and momentum of each trajectory is read in for each trajectory and "PubChem" which uses the PubChem API to source a geometry which can be used to generate the inputs.
2. "Molecule": The format of this input depends on the "Geom_flg". If the molecule is to be read in from a user geometry, then this input should take the name of the file within the initial geometry folder. If the entire inputs of the trajectories are to be read in, then this input should be the name of the folder that contains the full input file. Finally, if the PubChem option is chosen, then this input should take the form of the name or code of the molecule that can be used by the PubChem API to source the molecule.
3. "States": The number of potential energy states considered for the molecule.

4. "Multiplicity": The initial multiplicity of the molecule in the propagation.

5. "Start_State": The state for which the molecule begins (amplitudes for that state will be set to 1 and amplitudes for all other states to 0.)

6. "Temp": The temperature of the simulation in Kelvin.

7. "Cutoff": Percentage of the created geometries that are run. This input is not commonly used and is often commented out from the setup code but is useful for creating high energy momentum inputs when creating inputs at low temperature.

8. "Geom_file_start": If Geom_flg is selected to be "Full", this number denotes the number of the first geometry file that is read in, the files are assumed to be of the form Geometry.x, where x is an integer.

The third is the inputs surrounding electronic structure, including the basis set choice and functional.

Elec_Structure

1. "package": The choice of electronic structure package. Currently accepted inputs are "QChem" and "PySCF".

2. "Spin_flip": If 1 Spin Flip is included in the force and coupling calculations, 0 results in standard DFT calculations.

3. "Basis": This input relates to the basis set used by the force and coupling calculations.

4. "GPU": If this input is 1 then GPU acceleration is utilised for the electronic structure calculations.

The final section is the inputs surrounding the choices relating to the propagation of the molecule.

Propagation

1. "Timestep": The increment of each timestep of the propagation.

2. "Tot_timesteps": The number of timesteps to be performed in the propagation.

3. "Checks": This input determines whether or not checks of the propagation are performed. If this input is set to "0", no checks are performed. If this input is set to "1", then at each timestep, the force magnitudes for each atom, the displacement of each atom and the overall energy of the molecule. If this input is set to "2", then corresponding graphs are also created each timestep.

4. "Remove_atoms": If this input is set to 1 then an atom is removed from the propagation once its force magnitude falls below a certain threshold.

The rest of the inputs required for propagation are stored within a geometry file containing both the initial geometry in terms of coordinates and momentum for each atom as outlined in Section 3.1. The lines drawn between these sections of the inputs are rather arbitrary, as the choice to use GPU accelerated calculations could be argued to belong to the "HPC" group detailing computational details. These sections are designed only to declutter the inputs and maintain clarity, not to adhere to any clear boundaries.

These inputs are then taken by a run file to create the bash script necessary to interact with the high powered computing framework. This abstraction of the bash script allows for the use of the code by only having to change the input file and then run the python run code.

A.5 Electronic Structure

The interface for the electronic structure is designed to be entirely hands-off and flexible only in the areas of basis set and the number of electronic states for which the calculations are run. The code has been designed to interact primarily with the QChem package and all inputs detailed in this section will be within that context. While the basis set is a choice for the user, examples in this section will be presented with the basis set of 6-31+G* which has become standard for these

calculations. The largest choice to be made in terms of electronic structure is the inclusion of Spin Flip TDDFT.

The first set of electronic structure calculations is the initialisation of the molecular inputs which begins with a geometry optimisation of the molecule in the singlet state:

```
$molecule
0 1
INITIAL MOLECULE GEOMETRY GUESS
$end
$rem
jobtype opt
exchange bhhlyp !50% hf +  50% becke88 exchange
basis 6-31+g*
thresh 14
scf_convergence 8
scf_algorithm diis
max_scf_cycles 500
gui 2
set_iter 30
RPA False
mem_total 2000
mem_static 64
n_frozen_virtual 0
mom_start False
scf_guess_mix False
skip_scfman False
unrestricted True
symmetry True
sym_ignore True
sym_tol 5
geom_opt_dmax 300
```

```
geom_opt_update -1
geom_opt_linear_angle 165
geom_opt_coords -1
geom_opt_tol_gradient 300
geom_opt_tol_displacement 1200
geom_opt_tol_energy 100
geom_opt_max_cycles 50
input_bohr true
$end
```

This is immediately followed by a calculation to find the vibrational modes of the optimised molecule.

```
$Molecule
0 1
OPTIMISED MOLECULAR GEOMETRY
$end
$rem
jobtype freq
exchange bhhlyp
basis 6-31+g*
thresh 14
scf_convergence 8
scf_algorithm diis
max_scf_cycles 50
gui 2
set_iter 30
RPA False
mem_total 2000
mem_static 64
n_frozen_virtual 0
mom_start False
```

```
scf_guess_mix False
skip_scfman False
symmetry True
sym_ignore False
sym_tol 5
input_bohr true
$end
```

The molecular inputs are then generated through the equations for momentum laid out in Section 3.1. The only other electronic structure calculations that are necessary for the propagation of the molecule is the calculations for the forces and coupling for each geometry. These inputs are also relatively simple with the skeleton of the forces calculation being

```
$molecule
0 CURRENT MOLECULE MULTIPLICITY + 2
CURRENT MOLECULE GEOMETRY
$end
$rem
jobtype force
exchange bhhlyp
basis 6-31+g*
thresh 14
scf_convergence 8
scf_algorithm diis
max_scf_cycles 500
gui 2
set_iter 30
RPA False
mem_total 2000
mem_static 64
n_frozen_virtual 0
```

```
mom_start False
scf_guess_mix False
skip_scfman False
unrestricted True
cis_convergence 6
cis_n_roots NUMBER OF STATES CONSIDERED
cis_singlets False
cis_triplets False
cis_ampl_anal False
loc_cis_ov_separate False
er_cis_numstate 0
boys_cis_numstate 0
max_cis_cycles 30
cis_state_deriv CURRENT STATE FOR CALCULATION
symmetry True
sym_ignore True
sym_tol 5
input_bohr true
spin_flip true
set_iter 500
$end
```

and the input for the calculation of the coupling being

```
$molecule
0 5
CURRENT MOLECULE GEOMETRY
$end
$rem
jobtype sp
exchange bhhlyp
basis 6-31+g*
```

```
thresh 14
scf_convergence 8
scf_algorithm diis
SCF_GUESS           Read
max_scf_cycles 500
gui 0
set_iter 30
RPA False
mem_total 2000
mem_static 64
n_frozen_virtual 0
mom_start False
scf_guess_mix False
skip_scfman False
unrestricted True
cis_convergence 6
cis_n_roots TOTAL NUMBER OF THE STATES
cis_singlets False
cis_triplets False
cis_ampl_anal False
loc_cis_ov_separate False
er_cis_numstate 0
boys_cis_numstate 0
max_cis_cycles 30
symmetry True
sym_ignore True
sym_tol 5
input_bohr true
spin_flip true
set_iter 500
calc_nac true
```

```
cis_der_numstate TOTAL NUMBER OF STATES
$end


$derivative_coupling
comment
NUMBERS OF THE STATES INVOLVED IN THE COUPLING
$end
```

While the inclusion of Spin Flip changes significantly the computational cost of the propagation, the input differs by the simple addition or removal of the 'spin_flip true' line. As Spin Flip is normally removed when performing the calculations on a single PES, the additional lines 'cis_state_deriv' and 'cis_n_roots' would also be no longer needed in this case.

Within the current implementation, the electronic structure jobs that are related to the generation of the molecular inputs, namely the geometry optimisation and the frequency calculations, are written in the QChem.py file and called via the setup.py file that is run before the main.py is called for each trajectory. The electronic structure jobs that occur within a timestep are called after the preliminary propagation step and loop through all selected PESs and coupling permutations. These jobs are designed to first use the SCF algorithm 'DIIS'. If for any reason the electronic structure calculation was not capable of finishing correctly, a second job is performed with a more robust SCF algorithm 'DIIS_GDM. If this job also fails, the program is halted and an error is raised containing all available outputs of the final failed job.

A.6 Processing of output

Each trajectory is contained within its own folder. Within the outputs of the trajectory folder, several files detail the propagation:

Output files

1. xyz.all - The coordinates of each atom at each timestep.

2. momentum.all - The momenta of each atom at each timestep.

3. forces.all - The forces and coupling of each atom, the multiplicity and energy of the molecule at each time step.

4. time.all - The timings of each timestep, and the total time of the propagation to reach each timestep.

5. molecule.json - The data of the molecule at the last timestep.

6. dissociation.out - A record of which bond broke at which timestep.

7. fragments.out - A record of which fragments are present at the end of the propagation.

These outputs for a single trajectory can also be separated into two separate categories. First, the files that end in .all and .json are updated at every timestep with the .all files contain the data for each timestep. The final two files "dissociation.out" and "fragments.out" are created when the trajectory has finished.

A.7 Checks

The 'Check' directory within each directory is only populated if the checks input in the 'inputs.json' file is a '1' or a '2'. In this case, there will be several sub directories, 'energy', 'forces' and 'displacement'. Within the first directory, the total energy of the system is calculated at each timestep and plotted (if '2' is the given input). This directory will also contain a text file noting the timestep at which any atom is removed from the propagation as this will result in a sharp energy change. The second directory contains the force magnitude calculated for each atom and a final total force magnitude across the whole molecule. The final directory contains the displacement for each atom at every timestep.

Result folder files

1. Bonds folder - contains multiple files of 3 types: the ”allbond.out” which contains the timestep of any bond dissociation event, the ”element1-element2.out” which contains the timestep of any dissociation event concerning a specific bond type, e.g. ”C-H.out”, ”C-C.out” and ”atom1-atom2.out” which contains the timestep of any dissociation event containing a specific bond, e.g. ”1-2.out”, ”2-3.out” where the numbers correspond to the atom as presented in the geometry file.

2. Graphs folder - contains automatically created graphs for all bond types and each individual bond within a bond type.

3. Specifics folder - contains five files with specific details of trajectories. ”Firstbond.out” details which bond breaks first most often. ”Secondbond.out” details which bond breaks second most often. ”Nextbonds.out” details how likely a given dissociation is to directly follow another given dissociation. ”Subsequent_bonds_any.out” how likely a given dissociation is to follow another given dissociation even if it’s not the next dissociation in the trajectory. Finally, ”pathways.out” tallies and details the numerous dissociation pathways undertaken by the trajectories.

4. bondarr.txt - this file contains the bonds of the molecule in the form of ”1-2:C-H” where the numbers correspond to the atoms in the geometry file, and the letters correspond to type of bond.

5. collated_diss.txt - contains the information from each dissociation.out within a finished trajectory folder.

6. completed_trajectories.txt - contains the number of finished trajectories.

7. fragments.out - contains a sum total of all final fragments from each finished trajectory.

8. graphs_config.out - contains the descriptions of each graph of a form that graph.py in the code section ca use to create the automatic graphs.

When a trajectory is finished, the files ”dissociation.out” and ”fragments.out” that are created in the trajectory file have their information copied into the ”collated_diss.txt” and ”fragments.out” contained in the results folder. These files are then used by the results.py and specifics.py to create the files in the bonds, graphs and specifics folder. As these files are updated whenever a trajectory finishes, these files (namely the graphs) can be checked to view updates of the trajectories.

Another subdirectory within the runfolder generated is the 'Setup' folder which contains the electronic structure output for the optimisation and vibrational frequency jobs in the files 'optimisation.out' and 'modes.out' respectively. The final file is 'momentum_checks.out' which compares the kinetic energy of each trajectory against the expected kinetic energy for that molecule.

A.8 An example to run

The running of the code after the setup of both the electronic structure and the conda environment is incredibly simple. The first step would be to supply the data necessary to the inputs.json file to properly describe the trajectory, as is shown in Fig. A.2. Many of these inputs that generated the results of this thesis are unedited between all molecules, with the only changes required for this example was the changing of the runfolder name, the number of repeats and the molecule name. The inputs as they stand in this example will produce 200 repeats of the '1,1,4-trifluorobutane' molecule as it is recorded in the PubChem database propagated only on the lowest triplet state at temperature of 5000 K. The electronic structure will be performed with the 6-31+G* basis set over 2100 timesteps with a timestep moving forward the propagation by 10 atomic time units. At each timestep the checks will be performed and plotted with atoms being removed from the propagation when they do not sufficiently affect the force calculations. Once the inputs have been set, the only other step required for the running the programme is to run the run.py file.

```
{
    "HPC":{
        "Runfolder":"114-trifluorobutane",
        "repeats":200,
        "cores":8,
        "initre":0,
        "hours": 40
    },

    "Molecule_data":{
        "Geom_flg": "PubChem",
        "Molecule":"1,1,4-trifluorobutane",
        "States":1,
        "Multiplicity":3,
        "Start_State": 1,
        "Temp":5000,
        "Cutoff": 100,
        "Geom_file_start":1
    },

    "Elec_structure":{
        "method": "QChem",
        "Spin_flip":0,
        "Basis":"6-31+G*",
        "GPU": 0
    },

    "Propagation":{
        "Timestep":10,
        "Tot_timesteps":2100,
        "Checks": 2,
        "Remove_atoms": 1
    }

}
```

Figure A.2: A screen grab of the inputs.json file used for the 1,1,4-trifluorobutane molecule presented in section 4.3.5

Bibliography

[1] G Frenking. *Theoretical Chemistry Accounts*, **103**, pp. 177–179, (2000)

[2] JH Cai, XZ Zhu, PY Guo, P Rose, XT Liu, X Liu and YZ Zhu. *Frontiers In Chemistry*, **11**, p. 1114970, (2023)

[3] PP Guan, M Davies, DJ Taylor, SZ Wan, HM McSparron, SL Hemsley, C Toseland, MJ Blythe, PD Taylor, V Walshe, CK Hattotuwagama, IA Doytchinova, PV Coveney, P Borrow and DR Flower. *Current Computer-Aided Drug Design*, **1**, pp. 377–395, (2005)

[4] U Gupta and D Paliwal. *Letters In Drug Design & Discovery*, **20**, pp. 2–15, (2023)

[5] S Rösel and PR Schreiner. *Isreal Journal Of Chemistry*, **62**, e202200002, (2022)

[6] P Prieto, A de la Hoz, A Díaz-Ortiz and AM Rodríguez. *Chemical Society Reviews*, **46**, pp. 431–451, (2017)

[7] V Graves, B Cooper and J Tennyson. *Journal Of Physics B - Atomic Molecular And Optical Physics*, **54**, p. 235203, (2021)

[8] CL Wang, B Cooper and J Tennyson. *Physica Scripta*, **98**, p. 065401, (2023)

[9] KN Houk and F Liu. *Accounts of Chemical Research*, **50**, pp. 539–543, (2017)

[10] F Zeller, CM Hsieh, W Dononelli and T Neudecker. *Wiley Interdisciplinary Reviews - Computational Molecular Science*, **14**, e1708, (2024)

[11] GE Moore. *Proceedings Of The IEEE*, **86**, pp. 82–85, (1998)

[12] KL Brown, WJ Munro and VM Kendon. *Entropy*, **12**, pp. 2268–2307, (2010)

[13] L Nützel, A Gresch, L Hehn, L Marti, R Freund, A Steiner, CD Marciniak, T Eckstein, N Stockinger, S Wolf, T Monz, M Kühn and MJ Hartmann. *Quantum Science And Technology*, **10**, p. 015066, (2025)

[14] I Kassal, JD Whitfield, A Perdomo-Ortiz, MH Yung and A Aspuru-Guzik. *Annual Review of Physical Chemistry*, **62**, pp. 185–207, (2011)

[15] A Bhattacharya, K Dasgupta and B Paine. *Journal Of Chemical Education*, **101**, pp. 1599–1609, (2024)

[16] WF van Gunsteren and C Oostenbrink. *Journal Of Chemical Information And Modeling*, **64**, pp. 6281–6304, (2024)

[17] S Plimpton. *Computational Materials Science*, **4**, pp. 361–364, (1995)

[18] M Pandey, M Fernandez, F Gentile, O Isayev, A Tropsha, AC Stern and A Cherkasov. *Nature Machine Intelligence*, **4**, pp. 211–221, (2022)

[19] GB Goh, NO Hodas and A Vishnu. *Journal Of Computational Chemistry*, **38**, pp. 1291–1307, (2017)

[20] AI Osman, YB Zhang, ZY Lai, AK Rashwan, M Farghali, AA Ahmed, YF Liu, BB Fang, ZH Chen, A Al-Fatesh, DW Rooney, CL Yiin and PS Yap. *Environmental Chemistry Letters*, **21**, pp. 3159–3244, (2023)

[21] MF Guest, AM Elena and ABG Chalk. *Molecular Simulation*, **47**, pp. 194–227, (2021)

[22] Br Brooks, Re Bruccoleri, Bd Olafson, Dj States, S Swaminathan and M Karplus. *Journal Of Computational Chemistry*, **4**, pp. 187–217, (1983)

[23] S Pronk, S Páll, R Schulz, P Larsson, P Bjelkmar, R Apostolov, MR Shirts, JC Smith, PM Kasson, D van der Spoel, B Hess and E Lindahl. *Bioinformatics*, **29**, pp. 845–854, (2013)

[24] H Buragohain and K Talukdar. *Resonance - Journal Of Science Education*, **29**, pp. 1095–1110, (2024)

[25] KA Ball, K He and HP Hendrickson. *International Journal Of Quantum Chemistry*, **120**, 120:e26341, (2020)

[26] LI Bendavid. *Journal Of Chemical Education*, **100**, pp. 389–394, (2023)

[27] BJ Esselman and NJ Hill. *Journal Of Chemical Education*, **93**, pp. 932–936, (2016)

[28] D Lafuente, B Cohen, G Fiorini, AA García, M Bringas, E Morzan and D Onna. *Journal Of Chemical Education*, **98**, pp. 2892–2898, (2021)

[29] I Tuvi-Arad. *Isreal Journal Of Chemistry*, **62**, e202100042, (2022)

[30] B Pölloth. *Journal Of Chemical Education*, **102**, pp. 1367–1379, (2025)

[31] SA Hollingsworth and RO Dror. *Neuron*, **99**, pp. 1129–1143, (2018)

[32] BFE Curchod and TJ Martínez. *Chemical Reviews*, **118**, pp. 3305–3336, (2018)

[33] T Sperger, IA Sanhueza and F Schoenebeck. *Accounts of Chemical Research*, **49**, pp. 1311–1319, (2016)

[34] LS Cederbaum. *Journal of Chemical Physics*, **128**, p. 124101, (2008)

[35] LP Wang and CC Song. *Journal of Chemical Physics*, **144**, p. 019901, (2016)

[36] CL Brooks, DA Case, S Plimpton, B Roux, D van der Spoel and E Tajkhorshid. *Journal of Chemical Physics*, **154**, p. 100401, (2021)

[37] Q Mao, MY Feng, XZ Jiang, YH Ren, KH Luo and ACT van Duin. *Progress In Energy And Combustion Science*, **97**, (2023)

[38] SB Kylasa, HM Aktulga and AY Grama. *Journal Of Computational Physics*, **272**, pp. 343–359, (2014)

[39] TP Senftle, S Hong, MM Islam, SB Kylasa, YX Zheng, YK Shin, C Junkermeier, R Engel-Herbert, MJ Janik, HM Aktulga, T Verstraelen, A Grama and ACT van Duin. *NPJ Computational Materials*, **2**, p. 15011, (2016)

[40] N Mardirossian and M Head-Gordon. *Molecular Physics*, **115**, pp. 2315–2372, (2017)

[41] PJ Ollitrault, A Miessen and I Tavernelli. *Accounts of Chemical Research*, **54**, pp. 4229–4238, (2021)

[42] M. Ceotto, G. F. Tantardini and A. Aspuru-Guzik. *Journal of Chemical Physics*, **135**, p. 214108, (2011)

[43] W. H. Miller. *Journal of Chemical Physics*, **53**, pp. 3578–&, (1970)

[44] KG Kay. *Annual Review of Physical Chemistry*, **56**, pp. 255–+, (2005)

[45] W. H. Miller. *Journal Of Physical Chemistry A*, **105**, pp. 2942–2955, (2001)

[46] N. K. Naseri, E. A. Sundararajan, M. Ayob and A. Jula. *Symmetry-Basel*, **12**, (2020)

[47] B. Balzer, S. Dilthey, G. Stock and M. Thoss. *Journal of Chemical Physics*, **119**, pp. 5795–5804, (2003)

[48] G. Cohen, E. Gull, D. R. Reichman and A. J. Millis. *Physical Review Letters*, **115**, p. 266802, (2015)

[49] S. Malpathak and N. Ananth. *Journal of Chemical Physics*, **158**, p. 104106, (2023)

[50] S. Malpathak, M. S. Church and N. Ananth. *Journal Of Physical Chemistry A*, **126**, pp. 6359–6375, (2022)

[51] Shouryya Ray, Paula Ostmann, Lena Simon, Frank Grossmann and Walter T Strunz. *Journal of Physics A: Mathematical and Theoretical*, **49**, p. 165303, (2016)

[52] V. S. Batista, M. T. Zanni, B. J. Greenblatt, D. M. Neumark and W. H. Miller. *Journal of Chemical Physics*, **110**, pp. 3736–3747, (1999)

[53] W. H. Miller. *Journal Of Physical Chemistry A*, **103**, pp. 9384–9387, (1999)

[54] D. E. Skinner and W. H. Miller. *Chemical Physics Letters*, **300**, pp. 20–26, (1999)

[55] X. Sun, H. B. Wang and W. H. Miller. *Journal of Chemical Physics*, **109**, pp. 7064–7074, (1998)

[56] H. D. Meyer, U. Manthe and L. S. Cederbaum. *Chemical Physics Letters*, **165**, pp. 73–78, (1990)

[57] H. B. Wang and M. Thoss. *Journal of Chemical Physics*, **119**, pp. 1289–1299, (2003)

[58] JC Tully. *Journal of Chemical Physics*, **93**, pp. 1061–1071, (1990)

[59] M Dutra, S Wickramasinghe and S Garashchuk. *Journal Of Chemical Theory And Computation*, **16**, pp. 18–34, (2020)

[60] M. D. Hack, A. M. Wensmann, D. G. Truhlar, M. Ben-Nun and T. J. Martinez. *Journal of Chemical Physics*, **115**, pp. 1172–1186, (2001)

[61] M. Ben-Nun and T. J. Martinez. *Journal of Chemical Physics*, **112**, pp. 6113–6121, (2000)

[62] M. Ben-Nun, J. Quenneville and T. J. Martinez. *Journal Of Physical Chemistry A*, **104**, pp. 5161–5175, (2000)

[63] M. Ronto and D. V. Shalashilin. *Journal Of Physical Chemistry A*, **117**, pp. 6948–6959, (2013)

[64] M Vacher, MJ Bearpark and MA Robb. *Theoretical Chemistry Accounts*, **135**, (2016)

[65] Y Zhao. *The Journal of Chemical Physics*, **158**, p. 080901, (2023)

[66] Y Zhao, KW Sun, LP Chen and M Gelin. *The Journal of Chemical Physics*, **12**, (2022)

[67] D. V. Shalashilin. *Journal of Chemical Physics*, **132**, p. 244111, (2010)

[68] D. V. Shalashilin. *Journal of Chemical Physics*, **130**, p. 244101, (2009)

[69] D. V. Shalashilin and M. S. Child. *Journal of Chemical Physics*, **113**, pp. 10028–10036, (2000)

[70] D. V. Shalashilin and M. S. Child. *Journal of Chemical Physics*, **115**, pp. 5367–5375, (2001)

[71] D. V. Shalashilin and M. S. Child. *Journal of Chemical Physics*, **119**, pp. 1961–1969, (2003)

[72] A Kirrander and DV Shalashilin. *Physical Review A*, **84**, p. 033406, (2011)

[73] M Eidi, M Vafaee, AR Niknam and N Morshedian. *Chemical Physics Letters*, **653**, pp. 60–66, (2016)

[74] C. Symonds, J. A. Kattirtzi and D. V. Shalashilin. *Journal of Chemical Physics*, **148**, p. 184113, (2018)

[75] D. V. Makhov, W. J. Glover, T. J. Martinez and D. V. Shalashilin. *Journal of Chemical Physics*, **141**, p. 054110, (2014)

[76] V. M. Freixas, S. Fernandez-Alberti, D. V. Makhov, S. Tretiak and D. Shalashilin. *Physical Chemistry Chemical Physics*, **20**, pp. 17762–17772, (2018)

[77] D. V. Makhov, K. Saita, T. J. Martinez and D. V. Shalashilin. *Physical Chemistry Chemical Physics*, **17**, pp. 3316–3325, (2015)

[78] J. A. Green, D. V. Makhov, N. C. Cole-Filipiak, C. Symonds, V. G. Stavros and D. V. Shalashilin. *Physical Chemistry Chemical Physics*, **21**, pp. 3832–3841, (2019)

[79] D. V. Makhov, T. J. Martinez and D. V. Shalashilin. *Faraday Discussions*, **194**, pp. 81–94, (2016)

[80] S Mathew, A Yella, P Gao, R Humphry-Baker, BFE Curchod, N Ashari-Astani, I Tavernelli, U Rothlisberger, MK Nazeeruddin and M Grätzel. *Nature Chemistry*, **6**, pp. 242–247, (2014)

[81] M Grätzel. *Accounts of Chemical Research*, **42**, pp. 1788–1798, (2009)

[82] DM Schultz and TP Yoon. *Science*, **343**, pp. 985–+, (2014)

[83] M Grätzel. *Nature*, **414**, pp. 338–344, (2001)

[84] AY Chan, IB Perry, NB Bissonnette, BF Buksh, GA Edwards, L Frye, OL Garry, MN Lavagnino, BX Li, YF Liang, E Mao, A Millet, J Oakley, NL Reed, HA Sakai, CP Seath and DWC MacMillan. *Chemical Reviews*, **122**, pp. 1485–1542, (2022)

[85] CK Prier, DA Rankic and DWC MacMillan. *Chemical Reviews*, **113**, pp. 5322–5363, (2013)

[86] HH Zhang, H Chen, CJ Zhu and SY Yu. *Science China - Chemistry*, **63**, pp. 637–647, (2020)

[87] WJ Zhou, YX Jiang, L Chen, KX Liu and DG Yu. *Chinese Journal Of Organic Chemistry*, **40**, pp. 3697–3713, (2020)

[88] DV Makhov, L Hutton, A Kirrander and DV Shalashilin. *Journal of Chemical Physics*, **160**, p. 164310, (2024)

[89] O Bennett, A Freibert, KE Spinlove and GA Worth. *Journal of Chemical Physics*, **160**, p. 174305, (2024)

[90] AMS Daria, J Hernández-Rodríguez, LM Ibele and S Gómez. *Journal of Chemical Physics*, **160**, (2024)

[91] J Eng, CD Rankine and TJ Penfold. *Journal of Chemical Physics*, **160**, p. 154301, (2024)

[92] L Hutton, AM Carrascosa, AW Prentice, M Simmermacher, JE Runeson, MJ Paterson and A Kirrander. *Journal of Chemical Physics*, **160**, p. 204307, (2024)

[93] J Janos, JPF Nunes, D Hollas, P Slavicek and BFE Curchod. *Journal of Chemical Physics*, **160**, p. 144305, (2024)

[94] JE Lawrence, IM Ansari, JR Mannouch, MA Manae, K Asnaashari, A Kelly and JO Richardson. *Journal of Chemical Physics*, **160**, (2024)

[95] XC Miao, K Diemer and R Mitric. *Journal of Chemical Physics*, **160**, (2024)

[96] ER Miller, SJ Hoehn, A Kumar, DH Jiang and SM Parker. *Journal of Chemical Physics*, **161**, (2024)

[97] S Mukherjee, RS Mattos, JM Toldo, H Lischka and M Barbatti. *Journal of Chemical Physics*, **160**, (2024)

[98] J Suchan, F Liang, AS Durden and BG Levine. *Journal of Chemical Physics*, **160**, (2024)

[99] AE Green, Y Liu, F Allum, M Grassl, P Lenzen, MNR Ashfold, S Bhattacharyya, X Cheng, M Centurion, SW Crane, R Forbes, NA Goff, L Huang, B Kaufman, MF Kling, PL Kramer, HVS Lam, KA Larsen, R Lemons, MF Lin, AJ Orr-Ewing, D Rolles, A Rudenko, SK Saha, J Searles, X Shen, S Weathersby, PM Weber, H Zhao and TJA Wolf. *Journal of Chemical Physics*, **162**, (2025)

[100] D Hait, D Lahana, OJ Fajen, ASP Paz, PA Unzueta, B Rana, LX Lu, YH Wang, EF Kjonstad, H Koch and TJ Martínez. *Journal of Chemical Physics*, **160**, (2024)

[101] JW Peng, H Liu and ZG Lan. *Journal of Chemical Physics*, **160**, (2024)

[102] VK Jaiswal, F Montorsi, F Aleotti, F Segatta, D Keefer, S Mukamel, A Nenov, I Conti and M Garavelli. *Journal of Chemical Physics*, **160**, (2024)

[103] Dominik Metzler, Robert L. Bruce, Sebastian Engelmann, Eric A. Joseph and Gottlieb S. Oehrlein. *Journal of Vacuum Science & Technology A: Vacuum, Surfaces, and Films*, **32**, p. 020603, (2014)

[104] Kang-Yi Lin, Chen Li, Sebastian Engelmann, Robert L. Bruce, Eric A. Joseph, Dominik Metzler and Gottlieb S. Oehrlein. *Journal of Vacuum Science & Technology A*, **36**, p. 040601, (2018)

[105] S You, EJ Sun, Y Hwang and CK Kim. *Korean Journal Of Chemical Engineering*, **41**, pp. 1307–1310, (2024)

[106] Y. Kim, H. Kang, C. Kim and H. Chae. *Acs Sustainable Chemistry & Engineering*, **11**, pp. 6136–6142, (2023)

[107] Jong Kyu Kim, Sung Il Cho, Sung Ho Lee, Chan Kyu Kim, Kyung Suk Min and Geun Young Yeom. *Journal of Vacuum Science & Technology A*, **31**, p. 061302, (2013)

[108] GS Oehrlein, SM Brandstadter, RL Bruce, JP Chang, JC Demott, VM Donnelly, R Dussart, A Fischer, RA Gottscho, S Hamaguchi, M Honda, M Hori, K Ishikawa, SG Jaloviar, KJ Kanarik, K Karahashi, AKTR Ko, H Kothari, N Kuboi, MJ Kushner, T Lill, PS Luan, A Mesbah, E Miller,

S Nath, Y Ohya, M Omura, C Park, J Poulose, S Rauf, M Sekine, TG Smith, N Stafford, T Standaert and PLG Ventzek. *Journal of Vacuum Science & Technology B*, **42**, p. 041501, (2024)

[109] H Omori, A Kikuchi, A Yao, I Mori and IEEE. "Evaluation of etching property in $C_3H_X > F_{(6-X)}plasma$". *2016 IEEE 16th International Conference On Nanotechnology (IEEE-NANO)*, pp. 127–130.

[110] T Ichikawa, T Takase and N Tamaoki. "Modeling of deposition during C¡sub¿5¡/sub¿F¡sub¿8¡/sub¿/CO/O¡sub¿2¡/sub¿/Ar plasma etching using topography and composition simulation". *SISPAD 2007: SIMULATION OF SEMICONDUCTOR PROCESSES AND DEVICES 2007*, pp. 425–+.

[111] HJ Lee, HW Tak, SB Kim, SK Kim, TH Park, JY Kim, D Sung, WS Lee, SB Lee, K Kim, BO Cho, YL Kim, KC Lee, DW Kim and GY Yeom. *Applied Surface Science*, **639**, p. 158190, (2023)

[112] MF Cuddy and ER Fisher. *Applied Materials & Interfaces*, **4**, pp. 1733–1741, (2012)

[113] K Takahashi, A Itoh, T Nakamura and K Tachibana. *Thin Solid Films*, **374**, pp. 303–310, (2000)

[114] K Goswami, AK Arora, A Bharadvaja and KL Baluja. *European Physical Journal D*, **75**, (2021)

[115] K Goswami, M Luthra, AK Arora, A Bharadvaja and KL Baluja. *European Physical Journal D*, **76**, (2022)

[116] M Ziólkowski, A Vikár, ML Mayes, A Bencsura, G Lendvay and GC Schatz. *Journal of Chemical Physics*, **137**, (2012)

[117] Y Kumar and M Kumar. *Chemical Physics Letters*, **740**, p. 137071, (2020)

[118] D. V. Makhov, G. Armstrong, H. H. Chuang, H. Ambalampitiya, K. Lemishko, S. Mohr, A. Nelson, J. Tennyson and D. Shalashilin. *Journal Of Physical Chemistry Letters*, **15**, pp. 3404–3411, (2024)

[119] B. Bagchi, R. Ghosh and A. Khare. *International Journal of Modern Physics A*, **35**, p. 2030011, (2020)

[120] E Schrödinger. *Physical Review*, **28**, pp. 1049–1070, (1926)

[121] RJ Glauber. *Physical Review*, **130**, pp. 2529–&, (1963)

[122] RJ Glauber. *Physical Review Letters*, **10**, pp. 84–+, (1963)

[123] RJ Glauber. *Physical Review*, **131**, pp. 2766–+, (1963)

[124] E Munguía-González, S Rego and JK Freericks. *American Journal Of Physics*, **89**, pp. 885–896, (2021)

[125] TQ Song and HY Fan. *Journal of Physics A - Mathematical and General*, **35**, pp. 1071–1077, (2002)

[126] AS Pereira and AS Lemos. *Physics Letters A*, **405**, p. 127428, (2021)

[127] M Bohloul, A Dehghani and H Fakhri. *Physica Scripta*, **99**, (2024)

[128] ZY Wang, ZJ Shi, YJ Shen, Q Liu and X Fu. *ACS Photonics*, **11**, pp. 4407–4413, (2024)

[129] Y Lai, Ha Haus and Y Yamamoto. *Optics Letters*, **16**, pp. 1517–1519, (1991)

[130] GJ Milburn and SL Braunstein. *Physical Review A*, **60**, pp. 937–942, (1999)

[131] G Mouloudakis and P Lambropoulos. *Photonics*, **8**, p. 72, (2021)

[132] L Barsotti, J Harms and R Schnabel. *Reports On Progress In Physics*, **82**, p. 016905, (2019)

[133] MV Satyanarayana. *Physical Review D*, **32**, pp. 400–404, (1985)

[134] SM Almas and G Najarbashi. *International Journal Of Geometric Methods In Modern Physics*, **8**, (2024)

[135] R Dey and K Ghosh. *Symmetry Integrability And Geometry - Methods And Applications*, **18**, (2022)

[136] A Motamedinasab and A Anbaraki. *Chinese Journal Of Physics*, **65**, pp. 139–145, (2020)

[137] M Assanioussi. *Physical Review D*, **101**, p. 124022, (2020)

[138] DJ Fernández and DI Martínez-Moreno. *European Physical Journal Plus*, **135**, (2020)

[139] M Combescure and D Robert. *Journal of Physics A - Mathematical and Theoretical*, **45**, p. 244005, (2012)

[140] A Dehghani, B Mojaveri and RJ Bahrbeig. *Reports On Mathematical Physics*, **87**, pp. 111–127, (2021)

[141] M. A. M. de Aguiar, S. A. Vitiello and A. Grigolo. *Chemical Physics*, **370**, pp. 42–50, (2010)

[142] E. J. Heller. *Journal of Chemical Physics*, **75**, pp. 2923–2931, (1981)

[143] Herbert Shore and L Sander. *Physical Review*, **7**, (1973)

[144] Jiří Vaníček and Tomislav Begušić. "Ab Initio Semiclassical Evaluation of Vibrationally Resolved Electronic Spectra With Thawed Gaussians". *Molecular Spectroscopy and Quantum Dynamics*. Elsevier, 2021, pp. 199–229.

[145] T Begusic, M Cordova and J Vanícek. *Journal of Chemical Physics*, **150**, (2019)

[146] MS Child, P Sherratt and YK Sturdy. *Journal Of Physical Chemistry A*, **108**, pp. 8860–8865, (2004)

[147] E Pollak and S Miret-Artés. *Journal of Physics A - Mathematical and General*, **37**, pp. 9669–9676, (2004)

[148] YP Pang. *Proteins-Structure Function And Bioinformatics*, **84**, pp. 1490–1516, (2016)

[149] DJ Huggins. *Journal Of Chemical Theory And Computation*, **18**, pp. 2616–2630, (2022)

[150] Shichen Lin, Daoling Peng, Weitao Yang, Feng Long Gu and Zhenggang Lan. *The Journal of Chemical Physics*, **155**, p. 214105, (2021)

[151] WL Jia, H Wang, MH Chen, DH Lu, L Lin, R Car, E Weinan, LF Zhang and IEEE. "Pushing the Limit of Molecular Dynamics with Ab Initio Accuracy to 100 Million Atoms with Machine Learning". *Proceedings Of SC20: The International Conference For High Performance Computing, Networking, Storage And Analysis (SC20)*.

[152] V Briganti and A Lunghi. *Machine Learning - Science And Technology*, **4**, p. 035005, (2023)

[153] ACT van Duin, S Dasgupta, F Lorant and WA III Goddard. *Journal Of Physical Chemistry A*, **105**, pp. 9396–9409, (2001)

[154] C Hartmann, R Banisch, M Sarich, T Badowski and C Schütte. *Entropy*, **16**, pp. 350–376, (2014)

[155] SS Iyengar, HB Schlegel, I Sumner and JJ Li. *Journal Of Physical Chemistry A*, **128**, p. 5386, (2024)

[156] N Aho, G Groenhof and P Buslaev. *Journal Of Chemical Theory And Computation*, **20**, pp. 6674–6686, (2024)

[157] Y Mitsuta and T Asada. *Journal Of Chemical Theory And Computation*, **20**, pp. 6531–6548, (2024)

[158] RJ Shannon, S Amabilino, M O'Connor, DV Shalishilin and DR Glowacki. *Journal Of Chemical Theory And Computation*, **14**, pp. 4541–4552, (2018)

[159] B Ensing, A Laio, M Parrinello and ML Klein. *Journal Of Physical Chemistry B*, **109**, pp. 6676–6687, (2005)

[160] L Maragliano and E Vanden-Eijnden. *Chemical Physics Letters*, **426**, pp. 168–175, (2006)

[161] S Park and K Schulten. *Journal of Chemical Physics*, **120**, pp. 5946–5961, (2004)

[162] P Brault. *Reviews Of Modern Plasma Physics*, **8**, (2024)

[163] D Jones, JE Allen, Y Yang, WFD Bennett, M Gokhale, N Moshiri and TS Rosing. *Journal Of Chemical Theory And Computation*, p. 4047, (2022)

[164] Si Sawada, R Heather, B Jackson and H Metiu. *Journal of Chemical Physics*, **83**, pp. 3009–3027, (1985)

[165] S Sawada and H Metiu. *Journal of Chemical Physics*, **84**, pp. 227–238, (1986)

[166] DV Shalashilin and B Jackson. *Chemical Physics Letters*, **318**, pp. 305–313, (2000)

[167] D. V. Shalashilin and M. S. Child. *Journal of Chemical Physics*, **128**, p. 244111, (2008)

[168] D. V. Shalashilin and M. S. Child. *Chemical Physics*, **304**, pp. 103–120, (2004)

[169] P. A. J. Sherratt, D. V. Shalashillin and M. S. Child. *Chemical Physics*, **322**, pp. 127–134, (2006)

[170] D. V. Shalashilin and M. S. Child. *Journal of Chemical Physics*, **122**, p. 224108, (2005)

[171] D. V. Shalashilin and M. S. Child. *Journal of Chemical Physics*, **121**, pp. 3563–3568, (2004)

[172] D. V. Shalashilin and I. Burghardt. *Journal of Chemical Physics*, **129**, p. 084104, (2008)

[173] H. J. Song, V. M. Freixas, S. Fernandez-Alberti, A. J. White, Y. Zhang, S. Mukamel, N. Govind and S. Tretiak. *Journal Of Chemical Theory And Computation*, **17**, pp. 3629–3643, (2021)

[174] D. V. Makhov, S. Adeyemi, M. Cowperthwaite and D. V. Shalashilin. *Journal of Physics Communications*, **6**, p. 025001, (2022)

[175] D. V. Makhov and D. V. Shalashilin. *Journal of Chemical Physics*, **154**, p. 104119, (2021)

[176] V. M. Freixas, W. Malone, X. Y. Li, H. J. Song, H. Negrin-Yuvero, R. Pérez-Castillo, A. White, T. R. Gibson, D. V. Makhov, D. V. Shalashilin, Y. Zhang, N. Fedik, M. Kulichenko, R. Messerly, L. N. Mohanam, S. Sharifzadeh, A. Bastida, S. Mukamel, S. Fernandez-Alberti and S. Tretiak. *Journal Of Chemical Theory And Computation*, **19**, pp. 5356–5368, (2023)

[177] T. Stauber and F. Guinea. *Physical Review A*, **73**, p. 042110, (2006)

[178] Leggett A.J., Chakravarty S. Dorsey A.T., Matthew P. A. Fisher and Anupam Zwerger W. Garg. *Dynamics of the dissipative two-state system.* Generic. 1987.

[179] A. Suarez and R. Silbey. *Journal of Chemical Physics*, **95**, pp. 9115–9121, (1991)

[180] U. Weiss, H. Grabert and S. Linkwitz. *Journal of Low Temperature Physics*, **68**, pp. 213–244, (1987)

[181] A. Luck, M. Winterstetter, U. Weiss and C. H. Mak. *Physical Review E*, **58**, pp. 5565–5573, (1998)

[182] D Porras and JI Cirac. *Physical Review Letters*, **92**, p. 207901, (2004)

[183] A. Lemmer, C. Cormick, D. Tamascelli, T. Schaetz, S. F. Huelga and M. B. Plenio. *New Journal of Physics*, **20**, p. 073002, (2018)

[184] R Puebla, J Casanova, O Houhou, E Solano and M Paternostro. *Physical Review A*, **99**, p. 032303, (2019)

[185] R. Puebla, G. Zicari, I. Arrazola, E. Solano, M. Paternostro and J. Casanova. *Symmetry-Basel*, **11**, (2019)

[186] M Pino and JJ García-Ripoll. *New Journal of Physics*, **20**, p. 113027, (2018)

[187] D. Xu and K. Schulten. *Chemical Physics*, **182**, pp. 91–117, (1994)

[188] MJ Tao, NN Zhang, PY Wen, FG Deng, Q Ai and GL Long. *Science Bulletin*, **65**, pp. 318–328, (2020)

[189] M Blume, Vj Emery and A Luther. *Physical Review Letters*, **25**, pp. 450–&, (1970)

[190] M. B. Cibils, Y. Cuche, V. Marvulle, W. F. Wreszinski, J. P. Amiet and H. Beck. *Journal of Physics A - Mathematical and General*, **24**, pp. 1661–1675, (1991)

[191] H. B. Wang, X. Y. Song, D. Chandler and W. H. Miller. *Journal of Chemical Physics*, **110**, pp. 4828–4840, (1999)

[192] Michael Thoss, Haobin Wang and William H. Miller. *The Journal of Chemical Physics*, **115**, pp. 2991–3005, (2001)

[193] G. J. Nan and Z. S. Li. *Computational and Theoretical Chemistry*, **967**, pp. 226–230, (2011)

[194] M. M. Toutounji and G. J. Small. *Journal of Chemical Physics*, **117**, pp. 3848–3855, (2002)

[195] HB Wang, M Thoss and WH Miller. *Journal of Chemical Physics*, **112**, pp. 47–55, (2000)

[196] H. B. Wang and M. Thoss. *New Journal of Physics*, **10**, p. 115005, (2008)

[197] H. B. Wang and M. Thoss. *Chemical Physics*, **370**, pp. 78–86, (2010)

[198] LP Lindoy, B Kloss and DR Reichman. *Journal of Chemical Physics*, **155**, p. 174108, (2021)

[199] LP Lindoy, B Kloss and DR Reichman. *Journal of Chemical Physics*, **155**, p. 174109, (2021)

[200] J Zheng, Y Xie, JW Peng, ZH Han and ZG Lan. *Journal of Chemical Physics*, **162**, (2025)

[201] O Koch, W Kreuzer and A Scrinzi. *Applied Mathematics And Computation*, **173**, pp. 960–976, (2006)

[202] WL Li, WW Xu and TS Chu. *Computational And Theoretical Chemistry*, **1004**, pp. 18–21, (2013)

[203] WL Li, J Zhang and HB Yao. *Acta Physica Sinica*, **62**, p. 124102, (2013)

[204] AUJ Lode, K Sakmann, RA Doganov, J Grond, OE Alon, AI Streltsov and LS Cederbaum. "Numerically-Exact Schrodinger Dynamics of Closed and Open Many-Boson Systems with the MCTDHB Package". *High Performance Computing In Science And Engineering: Transactions Of The High Performance Computing Center, Stuttgart (Hlrs) 2013*, pp. 81–92.

[205] OE Alon and IOP. "Many-body excitation spectra of trapped bosons with general interaction by linear response". *23rd International Laser Physics Workshop (Lphys'14)*. Vol. 594.

[206] M Theisen and AI Streltsov. *Physical Review A*, **94**, p. 053622, (2016)

[207] AUJ Lode, B Chakrabarti and VKB Kota. *Physical Review A*, **92**, p. 033622, (2015)

[208] J Grond, AI Streltsov, AUJ Lode, K Sakmann, LS Cederbaum and OE Alon. *Physical Review A*, **88**, p. 023606, (2013)

[209] R Lin, P Molignini, L Papariello, MC Tsatsos, C Lévêque, SE Weiner, E Fasshauee, R Chitra and AUJ Lode. *Quantum Science And Technology*, **5**, p. 024004, (2020)

[210] AUJ Lode, C Lévêque, LB Madsen, AI Streltsov and OE Alon. *Reviews of Modern Physics*, **92**, p. 011001, (2020)

[211] I Burghardt, K Giri and GA Worth. *Journal of Chemical Physics*, **129**, (2008)

[212] D Picconi, JA Cina and I Burghardt. *Journal of Chemical Physics*, **150**, (2019)

[213] D Picconi, JA Cina and I Burghardt. *Journal of Chemical Physics*, **150**, (2019)

[214] S Römer, M Ruckenbauer and I Burghardt. *Journal of Chemical Physics*, **138**, (2013)

[215] D Picconi and I Burghardt. *Journal of Chemical Physics*, **150**, (2019)

[216] M. Ben-Nun and T. J. Martinez. *Isreal Journal Of Chemistry*, **47**, pp. 75–88, (2007)

[217] T. J. Martinez. *Accounts of Chemical Research*, **39**, pp. 119–126, (2006)

[218] B. Mignolet and B. F. E. Curchod. *Journal of Chemical Physics*, **148**, p. 134110, (2018)

[219] BG Levine, JD Coe, AM Virshup and TJ Martínez. *Chemical Physics*, **347**, pp. 3–16, (2008)

[220] B. F. E. Curchod, W. J. Glover and T. J. Martinez. *Journal Of Physical Chemistry A*, **124**, pp. 6133–6143, (2020)

[221] Y Lassmann and BFE Curchod. *Journal of Chemical Physics*, **154**, p. 211106, (2021)

[222] Lu Wang, Yuta Fujihashi, Lipeng Chen and Yang Zhao. *The Journal of Chemical Physics*, **146**, p. 124127, (2017)

[223] A. S. Davydov. *Physica Status Solidi (B)*, **36**, pp. 211–219, (1969)

[224] Lu Wang, Lipeng Chen, Nengji Zhou and Yang Zhao. *The Journal of Chemical Physics*, **144**, p. 024101, (2016)

[225] L. P. Chen, Y. Y. Yan, M. F. Gelin and Z. G. Lue. *Journal of Chemical Physics*, **158**, p. 104109, (2023)

[226] Y. Tanimura. *Journal of Chemical Physics*, **153**, p. 020901, (2020)

[227] Z. F. Tang, X. L. Ouyang, Z. H. Gong, H. B. Wang and J. L. Wu. *Journal of Chemical Physics*, **143**, p. 224112, (2015)

[228] C. R. Duan, Z. F. Tang, J. S. Cao and J. L. Wu. *Physical Review B*, **95**, (2017)

[229] Q. L. Wang, Z. H. Gong, C. R. Duan, Z. F. Tang and J. L. Wu. *Journal of Chemical Physics*, **150**, (2019)

[230] C. R. Duan, Q. L. Wang, Z. F. Tang and J. L. Wu. *Journal of Chemical Physics*, **147**, (2017)

[231] Lipeng Chen, Maxim F. Gelin and Dmitrii V. Shalashilin. *The Journal of Chemical Physics*, **151**, p. 244116, (2019)

[232] JC SLATER. *Physical Review*, **81**, pp. 385–390, (1951)

[233] V Fock. *Zeitschrift Fur Physik*, **75**, pp. 622–647, (1932)

[234] P Echenique and JL Alonso. *Molecular Physics*, **105**, pp. 3057–3098, (2007)

[235] R Padmanaban and M Nest. *Chemical Physics Letters*, **463**, pp. 263–266, (2008)

[236] JC Slater. *Physical Review*, **34**, pp. 1293–1322, (1929)

[237] P Hohenberg and W Kohn. *Physical Review B*, **136**, B864–+, (1964)

[238] W Kohn and LJ Sham. *Physical Review*, **140**, pp. 1133–&, (1965)

[239] JC Slater. *Physical Review*, **36**, pp. 0057–0064, (1930)

[240] T Kato. *Communications On Pure And Applied Mathematics*, **10**, pp. 151–177, (1957)

[241] FA deSaavedra, E Buendia, FJ Galvez and I Porras. *Journal Of Physics B - Atomic Molecular And Optical Physics*, **29**, pp. 3803–3813, (1996)

[242] PMW Gill. *Advances in Quantum Chemistry*, **25**, pp. 141–205, (1994)

[243] R Ditchfield, Dp Miller and Ja Pople. *Journal of Chemical Physics*, **54**, pp. 4186–+, (1971)

[244] D Casanova and AI Krylov. *Physical Chemistry Chemical Physics*, **22**, pp. 4326–4342, (2020)

[245] H Bethe. *Zeitschrift Fur Physik*, **71**, pp. 205–226, (1931)

[246] L Yue, YJ Liu and CY Zhu. *Physical Chemistry Chemical Physics*, **20**, pp. 24123–24139, (2018)

[247] NJ Mayhall and M Head-Gordon. *Journal of Chemical Physics*, **141**, p. 134111, (2014)

[248] E Monino and PF Loos. *Journal Of Chemical Theory And Computation*, **17**, pp. 2852–2867, (2021)

[249] S Kotaru, S Kähler, M Alessio and A Krylov. *Journal Of Computational Chemistry*, **44**, pp. 367–380, (2023)

[250] V Vanovschi, AI Krylov and PG Wenthold. *Theoretical Chemistry Accounts*, **120**, pp. 45–58, (2008)

[251] D Casanova. *Chemical Reviews*, **118**, pp. 7164–7207, (2018)

[252] Vy Krivnov, Aa Ovchinnikov and Vo Cheranovskii. *Synthetic Metals*, **33**, pp. 65–79, (1989)

[253] WF Zhu, C Empel, S Pelliccia, RM Koenigs, E Proschak and V Hernandez-Olmos. *Journal of Medicinal Chemistry*, **67**, pp. 4322–4345, (2024)

[254] BFE Curchod and AJ Orr-Ewing. *Journal Of Physical Chemistry A*, **128**, pp. 6613–6635, (2024)

[255] NB Bissonnette, KA Ryu, T Reyes-Robles, S Wilhelm, JH Tomlinson, KA Crotty, EC Hett, LR Roberts, DJ Hazuda, MJ Willis, RC Oslund and OO Fadeyi. *ChemBioChem*, **21**, pp. 3555–3562, (2020)

[256] B Cooper, M Tudorovskaya, S Mohr, A O'Hare, M Hanicinec, A Dzarasova, JD Gorfinkiel, J Benda, Z Masín, AF Al-Refaie, PJ Knowles and J Tennyson. *atoms*, **7**, (2019)

[257] S Samukawa and T Mukai. *Journal of Vacuum Science & Technology A*, **17**, pp. 2463–2466, (1999)

[258] M. G. Kong, G. Kroesen, G. Morfill, T. Nosenko, T. Shimizu, J. van Dijk and J. L. Zimmermann. *New Journal Of Physics*, **11**, p. 115012, (2009)

[259] Nagendra Kumar Kaushik, Sander Bekeschus, Hiromasa Tanaka, Abraham Lin and Eun Ha Choi. *Applied Sciences-Basel*, **11**, (2021)

[260] Y. Kim, S. Kim, H. Kang, S. You, C. Kim and H. Chae. *Acs Sustainable Chemistry & Engineering*, **10**, pp. 10537–10546, (2022)

[261] Haruhiko Fukaya, Taizo Ono and Takashi Abe. *The Journal of Physical Chemistry A*, **105**, pp. 7401–7404, (2001)

[262] J Kim, HJ Kang, Y Kim, M Jeon and H Chae. *Plasma Processes And Polymers*, **21**, p. 2300216, (2024)

[263] S You, JH Kim and CK Kim. *Korean Journal Of Chemical Engineering*, **39**, pp. 63–68, (2022)

[264] Y Kondo, K Ishikawa, T Hayashi, Y Miyawaki, K Takeda, H Kondo, M Sekine and M Hori. *Japanese Journal Of Applied Physics*, **54**, p. 040301, (2015)

[265] Evan E. Bolton, Jie Chen, Sunghwan Kim, Lianyi Han, Siqian He, Wenyao Shi, Vahan Simonyan, Yan Sun, Paul A. Thiessen, Jiyao Wang, Jian Yu Bo Zhang and Stephen H. Bryant. *Journal of Cheminformatics*, **3**, p. 32, (2011)

[266] G. Christopoulou, A. Freibert and G. A. Worth. *Journal of Chemical Physics*, **154**, p. 124127, (2021)

[267] Kuljeet Kaur, Théo Sépulcre, Nicolas Roch, Izak Snyman, Serge Florens and Soumya Bera. *Phys. Rev. Lett.*, **127**, p. 237702, (2021)

[268] Alexander Miessen, Pauline J. Ollitrault and Ivano Tavernelli. *Phys. Rev. Res.*, **3**, p. 043212, (2021)

[269] H. Dekker. *Physica A*, **141**, pp. 570–574, (1987)

[270] F. Giraldi and F. Petruccione. *International Journal of Quantum Information*, **10**, p. 1241001, (2012)

[271] Sai-Yun Ye. "Coherent Effects in Dispersive Quantum Dynamics". Thesis. 2012.

[272] J Tennyson, S Mohr, M Hanicinec, A Dzarasova, C Smith, S Waddington, BQ Liu, LL Alves, K Bartschat, A Bogaerts, SU Engelmann, T Gans, AR Gibson, S Hamaguchi, KR Hamilton, C Hill, D O'Connell, S Rauf, K van 't Veer and O Zatsarinny. *Plasma Sources Science & Technology*, **31**, (2022)

[273] MJ Kushner. *Journal Of Physics D - Applied Physics*, **42**, p. 194013, (2009)